

Debonding Resistance of CHS Wrapped Composite X-Joints

He, P.

DOI

[10.4233/uuid:3ad94ee9-07fd-47f9-a766-843a91830534](https://doi.org/10.4233/uuid:3ad94ee9-07fd-47f9-a766-843a91830534)

Publication date

2023

Document Version

Final published version

Citation (APA)

He, P. (2023). *Debonding Resistance of CHS Wrapped Composite X-Joints*. [Dissertation (TU Delft), Delft University of Technology]. <https://doi.org/10.4233/uuid:3ad94ee9-07fd-47f9-a766-843a91830534>

Important note

To cite this publication, please use the final published version (if applicable).
Please check the document version above.

Copyright

Other than for strictly personal use, it is not permitted to download, forward or distribute the text or part of it, without the consent of the author(s) and/or copyright holder(s), unless the work is under an open content license such as Creative Commons.

Takedown policy

Please contact us and provide details if you believe this document breaches copyrights.
We will remove access to the work immediately and investigate your claim.

Debonding Resistance of CHS Wrapped Composite X-Joints

Debonding Resistance of CHS Wrapped Composite X-Joints

Dissertation

for the purpose of obtaining the degree of doctor

at Delft University of Technology

by the authority of the Rector Magnificus, Prof.dr.ir. T.H.J.J. van der Hagen,

Chair of the Board for Doctorates,

To be defended publicly on

Tuesday 19 September 2023 at 12:30 o'clock

by

Pei HE 何培

Master of Engineering in Architectural and Civil Engineering

Tongji University, China,

Born in Chongqing, China

This dissertation has been approved by the promotor

Composition of the doctoral committee:

Rector Magnificus	Chairperson
Prof.dr. M. Veljkovic	Delft University of Technology, promotor
Dr. M. Pavlovic	Delft University of Technology, copromotor

Independent members:

Prof.dr. T. Keller	École Polytechnique Fédérale de Lausanne
Prof.dr. J. Ramôa Correia	Universidade de Lisboa
Prof.dr.ir. E. Schlangen	Delft University of Technology
Prof.dr. X. Zhao	The Hong Kong Polytechnic University
Dr.ir. F.P. van der Meer	Delft University of Technology
Prof.dr.ir. M.A.N. Hendriks	Delft University of Technology, reserve member



This research was financially supported by China Scholarship Council.

Key words: Debonding, resistance, CHS, wrapped composite X-joints

Printed by: Ipskamp Printing, The Netherlands

Cover design: Pei He, Paraskevi Karatsi

Copy right @ 2023 by Pei He

ISBN: 978-94-6384-482-6

To my family

谨以此书献给我的家人们

CONTENTS

1. INTRODUCTION	11
1.1 Research background	12
1.2 Definition of research problems.....	13
1.3 Research scope (limitations)	14
1.4 Research objectives.....	14
1.5 Research questions.....	14
1.6 Research methodology	15
1.7 Thesis outline	15
References	17
2. LITERATURE REVIEW	21
2.1 Introduction.....	22
2.2 Application of composites in strengthening hollow sections.....	24
2.3 Fracture behavior of composite-steel bonded interface	30
2.4 Modeling of (complex) composite wrapping and composite- steel interface in CHS joints.....	40
2.5 Debonding crack propagation monitoring using DIC	46
2.6 Size effect in composite-metal bonded joints	47
References	51
3. ULTIMATE LOAD JOINT EXPERIMENTS	63
3.1 Introduction.....	64
3.2 Motivation behind the experimental campaign.....	64
3.3 Overview of CHS joints in the ultimate load joint experiments	66
3.4 Production of CHS joints	69
3.5 Measurement technique	70
3.6 Failure modes of wrapped composite joints.....	72
3.7 Influence of production parameters on the static behavior of wrapped composite joints.....	74
3.8 Static behavior of wrapped composite X-joints	87
3.9 Conclusions.....	108
References	110

4. MATERIAL AND INTERFACE EXPERIMENTS.....	113
4.1 Introduction.....	114
4.2 Material experiments of composites	116
4.3 Interface (debonding) experiments	123
4.4 Discussion of critical SERR.....	152
4.5 Conclusions.....	153
References	155
5. FINITE ELEMENT MODELING OF MATERIAL AND INTERFACE EXPERIMENTS	161
5.1 Introduction.....	162
5.2 Determination of element type and mesh size	163
5.3 FEM of composites	165
5.4 FEM of DCB and ENF tests	171
5.5 Conclusions.....	188
References	189
6. FINITE ELEMENT MODELING OF ULTIME LOAD JOINT EXPERIMENTS.....	193
6.1 Introduction.....	194
6.2 Overview of FE models in simulation of tensile static experiments of wrapped composite 45° X-joints	195
6.3 Modelling strategy	196
6.4 Material models and the interface model.....	203
6.5 Sensitivity analysis of the joint global response to physical parameters.....	207
6.6 Validation of FE models of 45° X joint	211
6.7 Conclusions.....	228
References	230

7. PARAMETRIC STUDY	231
7.1 Introduction.....	232
7.2 Overview of the analyzed parameters and the parametric study (PS) joint FE models	232
7.3 Mesh size and mesh type dependency analysis.....	233
7.4 Influence of interface properties	240
7.5 Influence of wrapping dimensions	243
7.6 Influence of the scale of the joint – Size effect	245
7.7 Conclusions.....	248
References	249
8. CONCLUSIONS AND FUTURE WORK	251
Summary	255
Samenvatting	257
Acknowledgements.....	261
List of publications.....	265
Curriculum Vitae	267

1. INTRODUCTION

This chapter provides the background information on the application of circular hollow sections (CHS) and the concept of wrapped composite joints. The research problems and scope are well defined. Research objectives, questions and methodology are introduced subsequently. Finally, the thesis outline is presented.

1.1 Research background

Circular Hollow Sections (CHS) have been extensively used in engineering structures, as shown in Figure 1-1, due to its high mechanical/cost efficiency, aesthetic, and good durability[1]. However, when applied in off-shore jacket structure and steel bridges where long-term cyclic loading is prevalent, CHS joints, traditionally formed by welds connecting brace (diagonal) to the chord member, encounter severe fatigue problem[2]–[4].

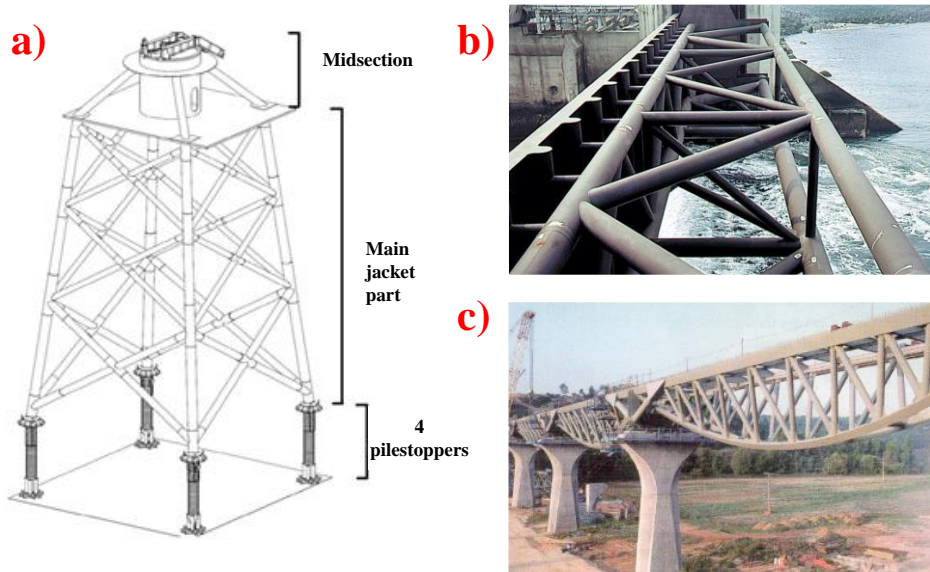


Figure 1-1 Engineering application of CHS in a) off-shore wind turbine jacket supporting structures; b) support structures of hydraulic barriers; c) truss steel bridges (originating from the section library)

The low fatigue endurance of welded CHS joints results from high and complex stress conditions as consequence of: 1) welding residual stresses in the heat affected zone; 2) stress concentrations attributed to fabrication where metallurgical changes occur in welds, heat affected zone and the parent material[5]; 3) geometric peak stresses due to the non-uniform stiffness distribution at the perimeter of the connection[1].

Fiber reinforced polymer (FRP) composites, further referred to as composites, have excellent corrosion and fatigue resistance. With tailorable material properties by choosing the type of fiber (glass or carbon, etc.), resin and ease of providing complex shapes through molding and lamination, composites have potential in application with steel hollow sections, as hybrid joints, in fatigue-dominated loading conditions. Increasing interest of research has been seen in last two decades towards strengthening of existing welded circular hollow section (CHS) joints with composite material. The main focus is on steel T/Y-joints [6]–[18], tubular K joints [19]–[25], and tubular KH-joints [26], [27]. The conclusion of all the previous research studies is that retrofitting

welded CHS joints by composites can enhance loading capacity, decrease the stress concentration factor (SCFs) of those joints substantially, and mitigate unfavorable failure modes such as chord ovalization and punching shear efficiently.

Despite improved static and fatigue behavior of composite-strengthened CHS joints, the large part of load is transferred through welded connection, which remains to be a source of stress concentration and dominated failure under fatigue load. To fully unlock application potential of CHS restricted by current welding technology in many cases, the concept of innovative wrapped composite joints is proposed by TU Delft[28] as an alternative to traditional welded joints, as shown in Figure 1-2. CHS brace members (diagonals) and the chord member in this case are bonded together by composite wrap which can be shaped in an optimal manner to decrease stress concentration at the bonded interface.

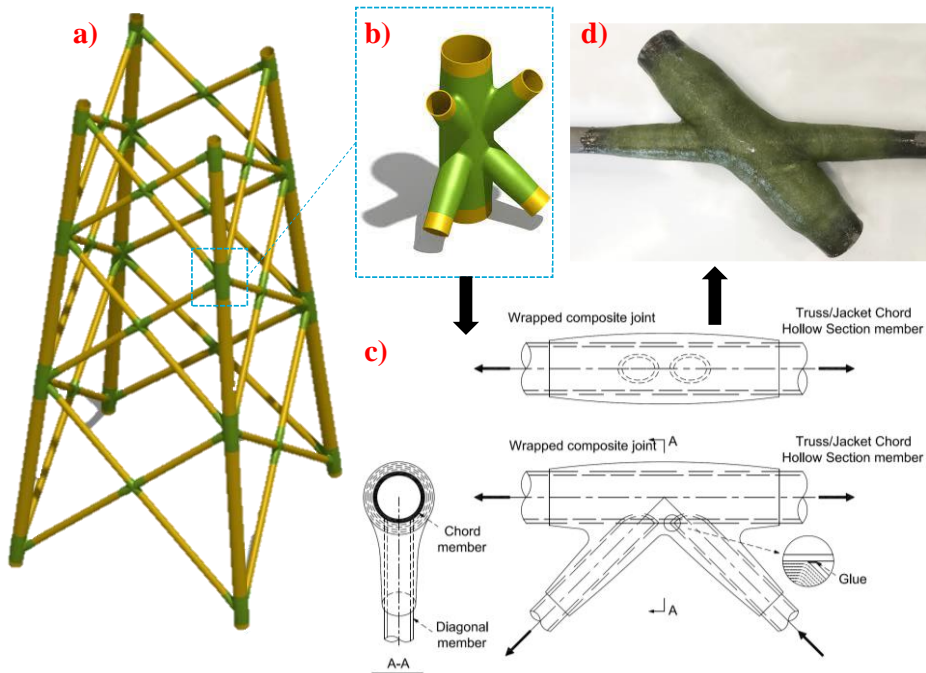


Figure 1-2 a) Off-shore jackets made of wrapped composite joints; b) wrapped composite K-K joint; c) wrapped composite K-joint; d) a 45° small-scale X-joint with Ø 60.3mm braces tested in this research.

1.2 Definition of research problems

Currently, bonded joints are not preferred to be used in the load carrying structures due to its risk of brittle failure. Therefore, the feasibility of applying the innovative wrapped composite K-K joint shown in Figure 1-2 b) to offshore jackets is doubted. Moreover, it is difficult to predict debonding failure in wrapped composite K-K joint attributed to its complexity in failure mechanism as consequence of complex geometry, stress concentrations and size effect. In this research, these two problems must be

answered.

1.3 Research scope (limitations)

Sufficient debonding resistance and its reliable prediction are the prerequisite for application of large-scale bonded joints in load carrying structures. Therefore, understanding debonding failure of wrapped composite joints is the relevant knowledge gap to solve. Wrapped composite K-K joint in offshore jackets is prone to tensile fatigue failure so tensile load scenario is mainly considered. The K-K joint geometry is simplified to K-joint geometry shown in Figure 1-2 c) to limit load conditions to uniplanar tension, aiming to make it easier to understand debonding. Considering limitation of loading protocol and efficiency in lab experiments, the K-joint is designed as 2Y 45° joints with comparable stress concentrations. For simplification of nomenclature in representing test results, the 2Y 45° joints is further named as 45° X-joints, as shown in Figure 1-2 d). Hence, the focus (scope) of this study is on debonding behavior of wrapped composite 45° X-joints under tensile load. To focus on debonding failure, the joint specimens in this study are designed with an empirical margin to prevent ultimate failure by excessive damage in composite material.

1.4 Research objectives

The goal of this research is to understand and predict debonding failure of wrapped composite 45° X-joints subjected to monotonic tensile load. In order to achieve this goal, the following research objectives should be accomplished:

- **Research objective 1:** Identify and explain debonding failure modes and failure process of wrapped composite 45° X-joints under tensile load.
- **Research objective 2:** Understand and estimate influence of size-effect on debonding resistance of wrapped composite joints.
- **Research objective 3:** Develop a numerical model to predict debonding resistance of wrapped composite 45° X-joints loaded in tension.

1.5 Research questions

Based on the proposed research objectives, the following research questions should be addressed:

- **Research question 1:** How is the tensile resistance of joints influenced by initiation and propagation of debonding? Are wrapped composite joints prone to brittle debonding?
- **Research question 2:** Is debonding failure of the joints dominated by mode I, mode II or mixed-mode interface failure?
- **Research question 3:** Which failure mode is dominating the resistance of wrapped composite joints loaded in tension: interface or substrate failure? Is fiber bridging present in the joints?

- **Research question 4:** How are the ultimate resistance, ductility and elastic load limit of the joints influenced by interaction of debonding failure modes on braces and on the chord member of the joints at different scales?
- **Research question 5:** What are the fracture properties of the composite-steel bonded interface in terms of crack initiation, crack propagation and fiber bridging?
- **Research question 6:** Which model can be used to represent non-linear behavior of steel-composite interface in mode I and mode II dominated failure?
- **Research question 7:** How can the model for composite-steel bonded interface developed based on fracture mechanics tests be implemented to simulate debonding behavior of the joints loaded in tension? Can the proposed interface model effectively account for size-effects in wrapped composite joints?

1.6 Research methodology

At the joint level, the monotonic ultimate tensile load joint experiments with different joint sizes are conducted to identify the debonding failure modes of wrapped composite 45° X-joints. At the material level, the fracture mechanics experiments, including the double cantilever beam (DCB) test and the end notched flexure (ENF) test, are used to determine the fracture mechanical properties of the composite-steel bonded interface in terms of toughness, crack initiation and crack propagation. The material coupon experiments are carried out to obtain mechanical properties of composite material used in the joints. Digital image correlation (DIC) technique is used in the material, fracture mechanics and joint experiments to measure the damage development and to identify debonding failure process.

Numerical finite element modeling (FEM) is used at the scale of the interface fracture mechanics experiments to develop interface model which can replicate mode I and mode II fracture behavior. FEM is developed at the joint level incorporating the interface model to help understand debonding failure process of wrapped composite joints and to predict resistance. The FE model at the joint level is first cross-validated with the joint experiments at different scales and then used in the parametric study to investigate the influence of geometry (size and wrapping length) on the failure modes and resistance of the joints.

1.7 Thesis outline

The thesis consists of 8 Chapters which are arranged as follows:

Chapter 1 serves as the general introduction to the research background, research problems, research scope, research objectives, research question and research methodology.

Chapter 2 presents the literature review on application of composites for strengthening welded tubular joints, fracture behaviour of bi-material interface, method to model complex composite wrapping and composite-steel bonded interface in strengthened CHS joints, debonding crack propagation monitoring by DIC, and size

effect in composite-metal bonded joints.

Chapter 3 gives the ultimate load test results of wrapped composite 45° X-joints loaded in tension/compression, and wrapped composite 90° X-joints loaded in bending. The tensile behavior of wrapped composite 45° X-joints and the bending behavior of wrapped composite 90° X-joints are compared to the welded joint counterparts. Wrapped composite 45° X-joints in small-scale and medium-scale are tested in tension to investigate size effect. The governing failure modes of wrapped composite X-joints are identified.

Chapter 4 shows the results of fracture mechanics tests (DCB, 3ENF and 4ENF tests) to quantify the fracture toughness at crack initiation/propagation and the fracture process zone (FPZ) length of composite-steel bonded interface in pure mode I and mode II. The results of the composite material tests including tensile, compressive and in-plane shear coupon test are also presented.

Chapter 5 shows the numerical results of the DCB and ENF tests based on the developed modelling strategy. The element type and mesh, composite layup orientation, boundary conditions, contact interaction, and analyses method are introduced. The traction-separation laws in mode I, mode II and mixed-modes are determined through the iterative fitting procedure and validated by comparing both global response and the local failure process.

Chapter 6 shows the development of the joint model and the numerical results of the wrapped composite 45° X-joints in small-scale and medium-scale under tensile load. The modification of the modeling strategy is conducted to consider the differences in geometry complexity and debonding process. The joint FE model is validated by good matches to the test results in terms of global response and the failure process which is presented by the FEA.

Chapter 7 presents the results of parametric study concerning the influence of wrapping length, wrapping thickness and the geometric size on the static resistance of wrapped composite 45° X-joints under tensile load. Mesh dependency is also investigated in this Chapter.

Chapter 8 summarizes the key conclusions and indicates the recommendation for future work.

It should be noted that understanding how debonding of the large-scale joints can be modelled by the interface model and how the initiation and propagation are influenced by size effects will contribute to other structural engineering research fields.

References

- [1] J. Wardenier, *Hollow Section in Structural applications*. CIDECT, 2010. doi: 10.1007/978-94-011-5856-5_6.
- [2] N. Van Vuong and M. H. Quan, “Fatigue analysis of jacket support structure for offshore wind turbines,” *J. Sci. Technol. Civ. Eng. - HUCE*, vol. 13, no. 1, pp. 46–59, Jan. 2019, doi: 10.31814/STCE.NUCE2019-13(1)-05.
- [3] S. C. Siriwardane, N. D. Adasooriya, and D. Pavlou, “Fatigue Strength Curve for Tubular Joints of Offshore Structures under Dynamic Loading,” *Dynamics*, vol. 1, no. 1, pp. 125–133, 2021, doi: 10.3390/dynamics1010007.
- [4] N. Shabakhty and S. S. Tabatabaei, “Sensitivity of fatigue assessment for offshore jacket platform to different pile–soil–structure interaction models,” *Ships Offshore Struct.*, vol. 17, no. 10, pp. 1–18, 2022, doi: 10.1080/17445302.2021.1979919.
- [5] L. D. Alain Nussbaumer, Luis Borges, *Fatigue Design of Steel and Composite Structures: Eurocode 3: Design of Steel Structures, Part 1-9 Fatigue; Eurocode 4: Design of Composite Steel and Concrete Structures*. John Wiley & Sons, 2012.
- [6] Z. G. Xiao and X. L. Zhao, “CFRP repaired welded thin-walled cross-beam connections subject to in-plane fatigue loading,” *Int. J. Struct. Stab. Dyn.*, vol. 12, no. 1, pp. 195–211, 2012, doi: 10.1142/S0219455412004653.
- [7] J. Aguilera and A. Fam, “Bonded FRP Plates for Strengthening Rectangular Hollow Steel Section T-Joints against Web Buckling Induced by Transverse Compression,” *J. Compos. Constr.*, vol. 17, no. 4, pp. 421–432, 2013, doi: 10.1061/(asce)cc.1943-5614.0000311.
- [8] H. Nassiraei and P. Rezaadoost, “Stress concentration factors in tubular T/Y-joints strengthened with FRP subjected to compressive load in offshore structures,” *Int. J. Fatigue*, vol. 140, no. May, p. 105719, 2020, doi: 10.1016/j.ijfatigue.2020.105719.
- [9] H. Nassiraei and P. Rezaadoost, “Parametric study and formula for SCFs of FRP-strengthened CHS T/Y-joints under out-of-plane bending load,” *Ocean Eng.*, vol. 221, no. May 2020, p. 108313, 2021, doi: 10.1016/j.oceaneng.2020.108313.
- [10] A. Sadat Hosseini, M. R. Bahaari, and M. Lesani, “Formulas for Stress Concentration Factors in T&Y Steel Tubular Joints Stiffened with FRP under Bending Moments,” *Int. J. Steel Struct.*, vol. 22, no. 5, pp. 1408–1432, 2022, doi: 10.1007/s13296-022-00651-w.
- [11] J. Aguilera and A. Fam, “Retrofitting tubular steel T-joints subjected to axial compression in chord and brace members using bonded FRP plates or through-wall steel bolts,” *Eng. Struct.*, vol. 48, pp. 602–610, 2013, doi: 10.1016/j.engstruct.2012.09.018.
- [12] M. Lesani, M. R. Bahaari, and M. M. Shokrieh, “Numerical investigation of FRP-strengthened tubular T-joints under axial compressive loads,” *Compos. Struct.*, vol. 100, pp. 71–78, 2013, doi: 10.1016/j.compstruct.2012.12.020.

- [13] M. Lesani, M. R. Bahaari, and M. M. Shokrieh, "Experimental investigation of FRP-strengthened tubular T-joints under axial compressive loads," *Constr. Build. Mater.*, vol. 53, pp. 243–252, 2014, doi: 10.1016/j.conbuildmat.2013.11.097.
- [14] M. Lesani, M. R. Bahaari, and M. M. Shokrieh, "FRP wrapping for the rehabilitation of Circular Hollow Section (CHS) tubular steel connections," *Thin-Walled Struct.*, vol. 90, pp. 216–234, 2015, doi: 10.1016/j.tws.2014.12.013.
- [15] A. S. Hosseini, M. R. Bahaari, and M. Lesani, "SCF distribution in FRP-strengthened tubular T-joints under brace axial loading," *Sci. Iran.*, vol. 27, no. 3 A, pp. 1113–1129, 2020, doi: 10.24200/SCI.2018.5471.1293.
- [16] A. Sadat Hosseini, M. R. Bahaari, and M. Lesani, "Parametric Study of FRP Strengthening on Stress Concentration Factors in an Offshore Tubular T-Joint Subjected to In-Plane and Out-of-Plane Bending Moments," *Int. J. Steel Struct.*, vol. 19, no. 6, pp. 1755–1766, 2019, doi: 10.1007/s13296-019-00244-0.
- [17] A. Sadat Hosseini, M. R. Bahaari, and M. Lesani, "Stress concentration factors in FRP-strengthened offshore steel tubular T-joints under various brace loadings," *Structures*, vol. 20, no. April, pp. 779–793, 2019, doi: 10.1016/j.istruc.2019.07.004.
- [18] A. Sadat Hosseini, M. R. Bahaari, and M. Lesani, "Experimental and parametric studies of SCFs in FRP strengthened tubular T-joints under axially loaded brace," *Eng. Struct.*, vol. 213, no. October 2019, p. 110548, 2020, doi: 10.1016/j.engstruct.2020.110548.
- [19] C. P. Pantelides, J. Nadauld, and L. Cercone, "Repair of Cracked Aluminum Overhead Sign Structures with Glass Fiber Reinforced Polymer Composites," *J. Compos. Constr.*, vol. 7, no. 2, pp. 118–126, 2003, doi: 10.1061/(asce)1090-0268(2003)7:2(118).
- [20] J. D. Nadauld and C. P. Pantelides, "Rehabilitation of Cracked Aluminum Connections with GFRP Composites for Fatigue Stresses," *J. Compos. Constr.*, vol. 11, no. 3, pp. 328–335, 2007, doi: 10.1061/(asce)1090-0268(2007)11:3(328).
- [21] C. P. Pantelides, "Rehabilitation of cracked aluminum components using fiber-reinforced polymer (FRP) composites," *Rehabil. Met. Civ. Infrastruct. Using Fiber Reinf. Polym. Compos. Types Prop. Test. Methods*, pp. 201–214, 2014, doi: 10.1533/9780857096654.2.201.
- [22] A. Fam, S. Witt, and S. Rizkalla, "Repair of damaged aluminum truss joints of highway overhead sign structures using FRP," *Constr. Build. Mater.*, vol. 20, no. 10, pp. 948–956, 2006, doi: 10.1016/j.conbuildmat.2005.06.014.
- [23] Y. Fu, L. Tong, L. He, and X. L. Zhao, "Experimental and numerical investigation on behavior of CFRP-strengthened circular hollow section gap K-joints," *Thin-Walled Struct.*, vol. 102, pp. 80–97, 2016, doi: 10.1016/j.tws.2016.01.020.
- [24] L. Tong, G. Xu, X. L. Zhao, H. Zhou, and F. Xu, "Experimental and theoretical studies on reducing hot spot stress on CHS gap K-joints with CFRP strengthening," *Eng.*

Struct., vol. 201, no. October, p. 109827, 2019, doi: 10.1016/j.engstruct.2019.109827.

[25] G. Xu, L. Tong, X. L. Zhao, H. Zhou, and F. Xu, “Numerical analysis and formulae for SCF reduction coefficients of CFRP-strengthened CHS gap K-joints,” *Eng. Struct.*, vol. 210, no. February, p. 110369, 2020, doi: 10.1016/j.engstruct.2020.110369.

[26] E. Zavvar, A. Sadat Hosseini, and M. A. Lotfollahi-Yaghin, “Stress concentration factors in steel tubular KT-connections with FRP-Wrapping under bending moments,” *Structures*, vol. 33, no. June, pp. 4743–4765, 2021, doi: 10.1016/j.istruc.2021.06.100.

[27] A. Sadat Hosseini, E. Zavvar, and H. Ahmadi, “Stress concentration factors in FRP-strengthened steel tubular KT-joints,” *Appl. Ocean Res.*, vol. 108, no. September 2020, 2021, doi: 10.1016/j.apor.2021.102525.

[28] M. Pavlovic, M. Veljkovic, and P. Bogers, “Method for making a virgin joint between two separate structural hollow sections, and such a virgin joint,” 11,542,708, 2019 [Online]. Available: <https://patents.google.com/patent/US11542708B2/en>

2. LITERATURE REVIEW

This chapter provides an overview of current research studies in the literature relevant to the present work. Section 2.2 summarizes the current state of research studies on the application of composites in strengthening hollow sections. Section 2.3 presents an overview of theoretical, experimental and numerical approaches used to investigate the fracture behavior of composite-steel bonded interface. In Section 2.4, the current approaches to modelling the complex wrapping geometry are summarized from the literature. Additionally, Section 2.5 discusses debonding crack propagation in experiments monitored by digital image correlation (DIC). The concept of size effect in composite-metal bonded joints is introduced in Section 2.6.

2.1 Introduction

Fatigue is one of the common grounds for the failure of tubular welded joints after a long period of service life[1]. It is a mechanism whereby cracks grow in a structure under fluctuating stress. Final failure generally occurs when the reduced cross section becomes insufficient to carry the load without rupture. Generally the fatigue cracks start at locations with high stress peaks. In welded circular hollow section (CHS) joints, there are two sources of high stress peaks: a) discontinuities at local notches, e.g. at the toes of butt welds and at the toes and roots of fillet welds, where sharp changes of direction occur[2], see Figure 2-1a); b) geometric peak stresses due to the non-uniform distribution at the perimeter of the connection resulting from local bending of the thin-walled CHS sections and ovalization in the welded intersection area, see Figure 2-1b) [3]. Such high stress peaks lead to limited fatigue endurance of CHS welded joints which are extensively used in the jacket structures of off-shore wind turbines[4]–[6].

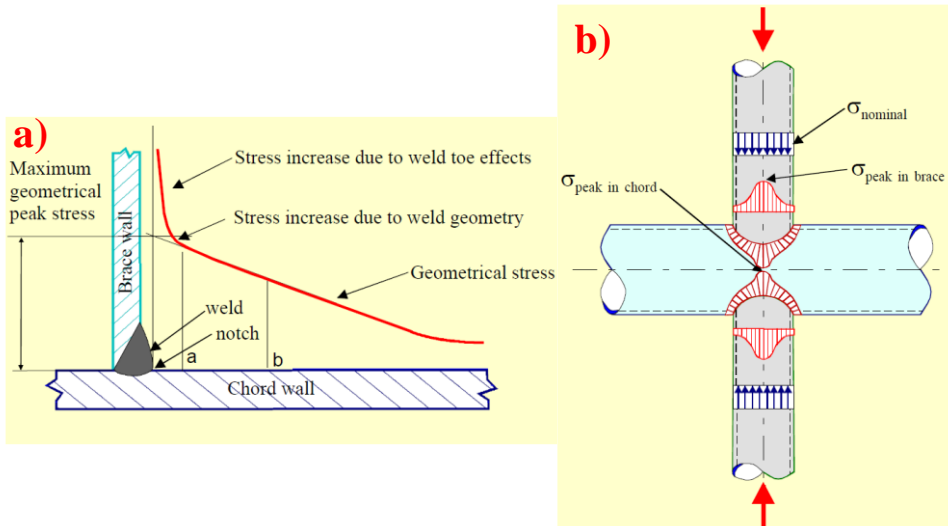


Figure 2-1 a) Peak stress due to weld discontinuity; b) Geometric stress distribution in an axially loaded X joint of circular hollow sections [3]

A composite material is a combination of two or more distinct materials into one with the intent of suppressing undesirable properties of the constituent materials in favour of desirable properties[7]. More specific, fiber polymer composites (a.k.a. Fiber Reinforced Polymer – FRP) further referred to as composites, are typically fabricated using a polymer matrix, such as epoxy, vinyl ester, or polyester and reinforced with various grades of carbon, glass, and/or aramid fibers[8]. Over the past two decades, composites are extensively used in numerous fields, e.g. aerospace[9]–[14], maritime[15]–[18], automotive[19] and civil industries[20], [21], attributed to the following advantages to help improve the performance of traditional material based structures: a) high strength-to-weight ratio; b) excellent fatigue and corrosion resistance; c) design flexibility due to tailorable material properties.

The properties of the composite material necessarily depend on the properties of the

fibers and the resins, types of reinforcement, fiber volume fraction, the orientations of the fibers in the composite with respect to the direction of loading, .etc. Fiber provide the dominant load bearing function and stiffness of composite material due to its high ultimate strength and relatively high modulus of elasticity. Fibers are surrounded by the polymer resin (matrix) which fixes the fibers in designed arrangement, transfers the forces between fibers, prevents buckling of fibers and protects them from environmental effects. Figure 2-2 shows the schematic stress-strain characteristics of composite material given as the synergy of its constituents. As for E-glass fibers used in this research, its stiffness is approximately 70 GPa, the strength is around 2750 MPa and the ultimate strain is approximately 4%. Stiffness and strength of polymer resin are an order of magnitude lower compared to fibers. Elastic modulus is in the range of 2-4 GPa, while the strength is approximately 20-80 MPa.

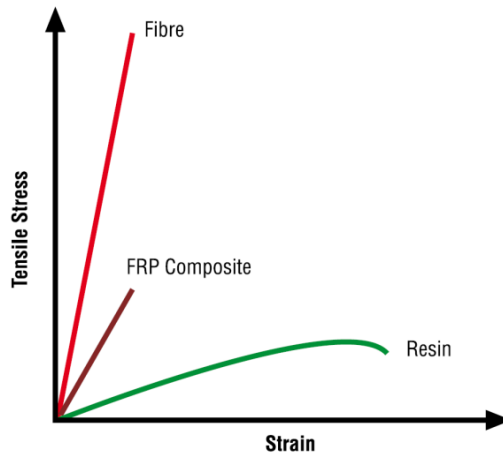


Figure 2-2 Stress-strain curve of composite material given as a synergy of the components[22]

In the current studies, the composites have been extensively used for strengthening of hollow sections or welded tubular joints to increase their static resistance or decrease the SCFs, see more details in section 2.2. But welding still transfer the main load in the strengthened joints which is the main source of stress concentrations and the fracture. When applying composites to the tubular joints, the fracture properties of the composite-steel bonding should be investigated. Calculation of the strain energy release rate (SERR), mode partitioning, experimental and numerical method of bi-material bonded interface are review in section 2.3. Current method of modeling composites with complex geometry and composite-steel bonding in CHS joints are introduced in section 2.4 and its limitations are clarified. Digital image correlation (DIC) can be used to monitor debonding crack propagation between composite and the substrates. The corresponding studies are overview in section 2.5 and they are all focused on the composites with very thin thickness. As a quasi-brittle material, strong energetic size effect is expected in composite-steel interface. The related research studies are summarized in section 2.6 as references to study size effect in wrapped composite joints.

2.2 Application of composites in strengthening hollow sections

2.2.1 Application of composites in strengthening hollow section members

Since the beginning of 21st century, the research area in terms of strengthening of steel hollow section members using composite material has been rapidly developing. Some research studies focused on retrofitting tension or compression columns by composites. Shaat and Fam[23] conducted axial compression test on short and long square hollow section columns retrofitted with CFRP sheets and found that the increase of axial load capacity is maximum 18% for short columns and is 13% to 23% for long columns. The highest gain was associated with three layers applied on four sides. The same authors[24] developed an analytical model for slender steel hollow section columns strengthened with higher modulus CFRP sheet, which considers material and geometric non-linearity, through thickness residual stress, initial column imperfection, and the contribution of CFRP sheets. It could predict the load versus axial and lateral displacements relationship. A limiting strain of 0.13% was adopted in the model for the CFRP in compression.

Zhao et al. [25] and Tao et al. [26] performed tests on concrete-filled steel hollow section short columns strengthened by CFRP. The dominating failure mode was found to be CFRP rupture at outward mechanism locations, which was also observed by Shaat and Fam[23] in their unfilled long column tests. In the test done by Zhao et al. [25], The increase in load carrying capacity was found to be 5%–22% when one CFRP layer was used. The increase in load carrying capacity became 20%–44% when 2 layers of CFRP were applied. It was found that the larger the diameter-to-thickness ratio, the greater the increase in load carrying capacity. Tao et al. [26] found that a lower increase in load carrying capacity due to CFRP strengthening was achieved for concrete-filled rectangular hollow sections, although a similar increase in ductility was found for both CHS and RHS. Teng and Hu[27] investigated the axial compressive behavior of FRP-confined steel tubes and found that the ductility of the steel tube can be greatly enhanced with the provision of a thin FRP jacket. But when the jacket thickness reaches a threshold value for which inward buckling deformations dominate the behavior, further increases in the jacket thickness do not lead to significant additional benefits as the jacket provides little resistance to inward buckling deformations. In addition, finite elements results showed that FRP jacketing is also an effective strengthening method for thin steel cylindrical shells against local elephants' foot buckling failure at the base.

Duell et al. [28] modeled steel pipes containing defect geometries with FRP repairs and the results were compared to field test. It was found that the defect width around the circumference had little impact on the ultimate rupture pressure of the repaired vessel, but influenced the stress state in the underlying pipe substrate. Fernando et al.[29] found that the end-bearing capacity of a RHS steel tube can be substantially increased through local strengthening using bonded CFRP plates. Haedir and Zhao[30] conducted axial compression test on ten short cold-formed steel CHS columns with externally bonded orthogonal CFRP sheets and found that CFRP sheets delayed the buckling of steel tube while the bare steel tube buckled at its ultimate load. Narmashiri and Mehrmiz[31] used

CFRP sheets to strengthen steel hollow pipe sections and found that when the hollow section was wrapped with two layers of CFRP there was a 20% increase in load bearing capacity.

Some other researchers investigated the flexure behavior of hollow section beams strengthened by composites. Seica et al. [32] conducted four point bending tests on circular steel tubes strengthened by CFRP sheets wrapped and cured in air and underwater. The improvements of the flexural stiffness and the ultimate strength were found in the wrapped beams regardless of the wrapping and curing environments. However, the composite members wrapped and cured underwater were not able to attain the flexural capacity of those cured in air. Haedir et al.[33], [34] conducted tests on class 4 CHS beams strengthened by CFRP sheets. It has been shown that a class 4 section can be upgraded to a class 2 section if CFRP strengthening is applied in both longitudinal and hoop directions. The hoop layers played a more important role in enhancing the rotation behavior of the steel crosssection, thus delaying failure due to local buckling. Meanwhile, the longitudinal layers played a more important role in increasing the bending moment capacity, due to the contribution of the CFRP in the tension zones. Photiou et al.[35] studied strengthening of artificially degraded steel RHS beams under four point bending. Two types of upgrading systems were adopted. One utilized flat plate GFRP and CFRP prepregs bonded only to the tension flange while the other one utilized U-shaped GFRP prepregs, which were bonded to the tension flange and were extended up on the web. It was concluded that provided the ultimate strains in the normal modulus carbon fibers are not exceeded and the bonding mechanisms between the first FRP layer and the steel surface are sufficient, the steel beam can be deformed well into its plastic region; the U-shaped system had the ability to contain the failure and to provide a degree of stiffening even after substantial damage had taken place.

2.2.2 Application of composites in strengthening welded tubular joints

Welded tubular joints are prone to failure under cyclic loading. Results of finite element analysis of tubular T-joints[36] indicates that the critical point for the peak hot spot stresses is located on the saddle position when subjected to pure axial loading. Conversely, in the case of pure in-plane bending loading, the critical point occurs almost midway between the saddle and the crown. Wang and Chen[37] investigated failure of welded tubular T-joints under cyclic loading and concluded that the energy dissipation is mainly by plastic deformation of the chord wall under axial load while by plastic deflection of the brace under in-plane bending load. The primary failure of the joints is weld cracking in tension and excessive plastic deformation of the chord wall in compression. For in-plane bending failure modes are punching shear and chord plastification accompanied by ductile fracture of the welds.

Strengthening and retrofitting is needed for welded tubular joints to increase their lifespan and fatigue life. The conventional methods to strengthen tubular joints are by filling with grout[38]–[40], chord reinforcement, adding collar plate or ring stiffeners, as shown in Figure 2-3. The fatigue life of grout filled joints was found to get increased compared to the original joints[38], but practical difficulties exist in terms of filling grout

in offshore tubular joints[39]. In addition, the effectiveness of strengthening depends on the early-age cycling during grout cure, grout shrinkage, radial pre-stress, temperature and surface finish[40] which are not easy to be controlled. Chord reinforcement was found to be effective in improving static strength of tubular joints[41], [42], but it is only suitable when the brace diameter is much smaller than the chord one and the reinforced thickness should not exceed twice of its original thickness. This is because the large ratio of brace to chord diameter or large ratio of local to global chord thickness makes the chord behave just like a bending beam, and no local buckling occurs on the chord surface. In this case, the failure mode of the chord is flexure yielding, which has no relation to the local chord thickness[41]. The collar plate reinforced tubular joints can absorb more energy than the unreinforced joints and the collar-plate reinforcement can change the failure location from the intersection region to the weld toe of the collar plate to the chord surface[43]. An increase of ultimate strength of up to 295% for double collar plate reinforced tubular T and Y joints was found compared to the unreinforced joints[44]. The internal ring stiffeners placed in tubular joints lead to the disposition of the peak stress concentration factor along the weld toe[45] and a new set of SCF parametric equation was developed for the fatigue design of internally ring-stiffened KT-joints[46], [47]. The experimental study[48] found that the external ring stiffeners greatly enhance the tubular joint compressive strength. The joint strength increases significantly as the size of the stiffener increases. The reinforcement effect is more dependent on the stiffener length than on the stiffener height [49]. However, corrosion is a major factor in the utilization of collar plates or ring stiffeners in reinforcement. Placing of stiffeners in the existing structures is a challenging job [50].

An alternative to the conventional strengthening methods is to apply composites in retrofitting welded tubular joints. Tubular joints of in-service structures have complex geometry where composites application is more efficient and convenient than traditional metallic-based reinforcing methods. It is more practical to apply hand layup method in which soft fiber sheets are in situ laminated, than to employ prefabricated rigid FRP plates [51], [52]. Relevant research of composites application on strengthening welded tubular joints were summarized as below according to the joint geometries.

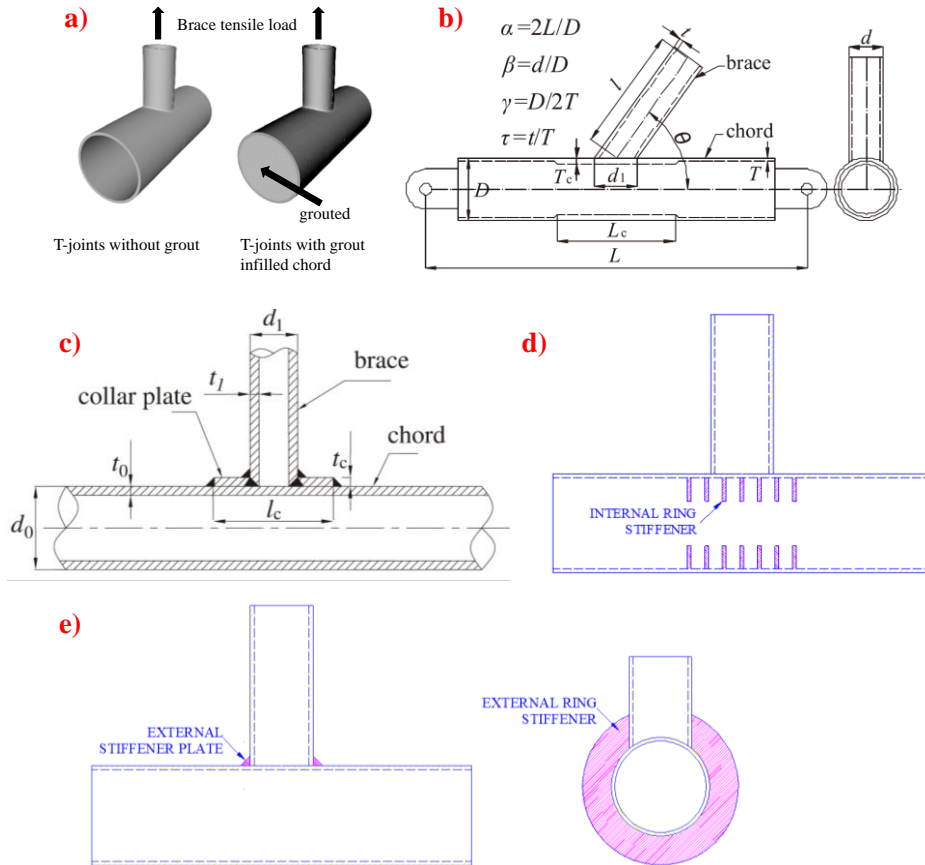


Figure 2-3 Conventional methods for strengthening of welded tubular joints: a) filling grout[38]; b) chord reinforcement[41]; c) adding collar plate[43]; d) adding internal ring stiffener[50]; e) adding external ring stiffener[50]

(1) Tubular butt joints: The behavior of CFRP strengthened butt-welded very high strength (VHS) steel circular hollow section joints was investigated by the axial tensile experiments conducted on a total of 21 specimens [53]. The results indicated that the load carrying capacity of the joints was enhanced by 85% using the CFRP and Araldite 420 epoxy system. The full yield capacity of VHS steel tubes was recovered. An effective bond length of 75 mm was found for the Araldite 420 bonded CFRP system.

(2) Tubular T-/Y-joints: A pilot fatigue test was conducted to explore the effective method of applying CFRP patches on a damaged steel T-joint of square hollow sections (SHS), and early debonding resulting from peeling effect was analyzed and fixed out for further research on repair of three fatigue-cracked RHS-to-RHS cross-beam connections [52]. GFRP sheets were bonded to the intersection of the rectangular hollow section T-joints against web buckling. The results demonstrated the effectiveness of externally bonded FRP plates in stabilizing thin webs of high strength steel (HSS) sections, and generally the FRP plating technique is more effective than the through-wall bolting

technique especially at higher axial loading in chord[54], [55]. The numerical and experimental work were conducted on GFRP wrapped CHS T-/Y-joints sustained to axial compressive load, with the tested T-joint specimen in wrapping shown in Figure 2-4 a) and the comparison of chord deflections without and with wrapping after compression test shown in Figure 2-4 b) and c). It was found that the state of stresses, deformations and ovalization of the wrapped joint have a descending trend up to 50% of the original joint[56]–[58]. SCF values in FRP strengthened tubular T-joints subjected to the three main loading conditions were studied to investigate the affectability of joints from FRP parameters. Three different types of FRP materials were used, and a reduction of around 50% in the SCF was observed for the Carbon/Epoxy layup with 1-mm thickness[59], [60]. A rather sophisticated numerical study on the effect of FRP parameters such as thickness, fibers orientation and strengthening material was performed on two benchmark specimens under various brace loading, and recommendations were given for practical FRP lay-up on tubular T-joints[61][62]. Subsequently, the similar research was extended to the tubular Y-joints in terms of influence of strengthening parameters on the SCFs[63]–[65].

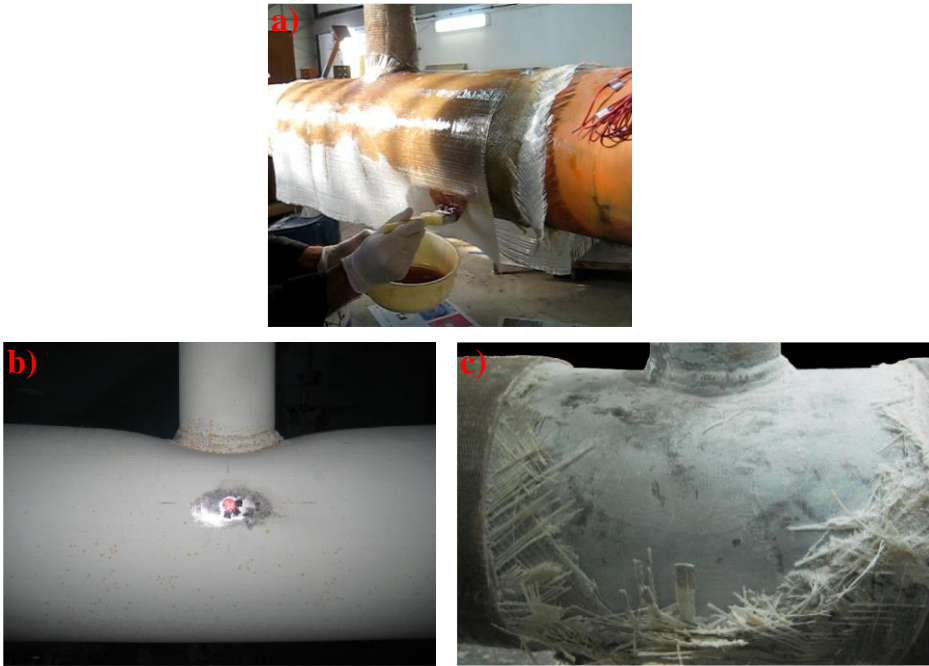


Figure 2-4 a) GFRP wrapping on tested CHS T-joint specimen and differences in chord deflection in b) original and c) wrapped specimens[57]

(3) Tubular K-/KT-joints: GFRP composites were applied to repair fatigue-cracked CHS aluminum truss K-joint of overhead sign structures, and both static tensile and fatigue experiments were conducted to demonstrate the effect of GFRP application in terms of ultimate capacity and fatigue life[66]–[68]. An innovative FRP installation method was proposed to repair fatigue damaged CHS aluminum K-joint of highway

overhead sign structures, and the results of static tensile experiments showed that full strength of the joints was restored using CFRP, whilst only 70% of strength restored using GFRP[69]. More recently in 2014, Fu et al.[70] improved the strengthening technique for CHS K-joints on the basis of work in [69]. A combined use of bidirectional and unidirectional CFRP sheets significantly improved the load-bearing capacity of undamaged steel CHS gap K-joints tested in static force in braces. Figure 2-5 shows installation of one layer of chord laminate made of two patches of L-shaped bi-directional CFRP. The same strengthening method is utilized in fatigue experiments of CHS-CFRP gap K-joints and it was found that the maximum SCFs were reduced by 20% in the chord while by 15% in the brace[71]. The 3D FE model was verified by the experimental results in [71] and the parametric study indicates that the wrapping length has a negligible effect on SCF reduction coefficient if the bond length requirement is met[72]. The parametric study based on the validated FE models indicated that the SCF values of tubular KT-joints could be lowered by 30 to 55 percent through FRP strengthening, and the fatigue design formulas were developed in terms of axial and bending load[73], [74].

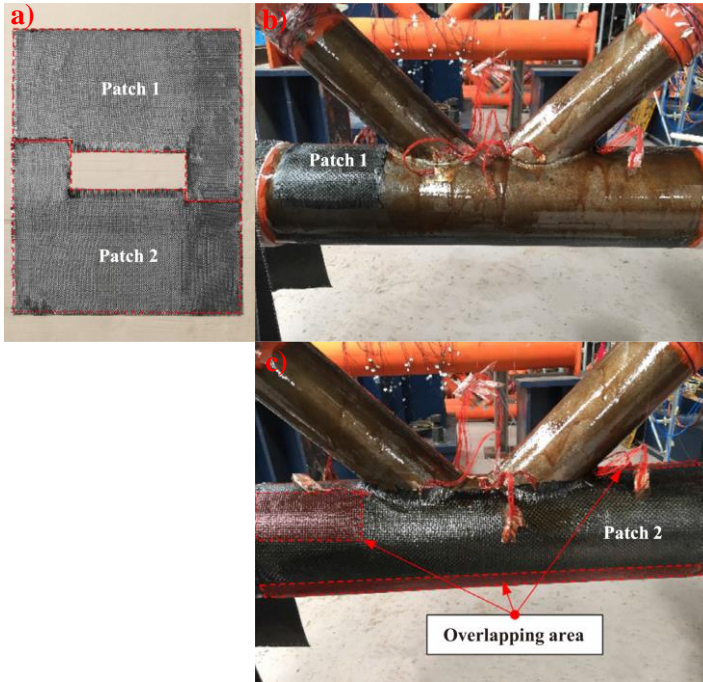


Figure 2-5 Installation of chord CFRP (one layer): a) two patches of L-shaped bidirectional CFRP; b) the first patch of L-shaped bidirectional CFRP; c) the second patch of L-shaped bidirectional CFRP.

Despite improved static behavior of composites strengthened welded tubular joints, main load is still carried through welded connection, which remains to be a source of stress concentration and brittle failure under fatigue load. The influence of welds on the mechanical performance of tubular joints can be eliminated if the load transfer is only through bonding between composites and steel hollow section members. Zhao et al.[53],

[75] conducted axial tensile tests on very high strength (VHS) steel circular butt joints connected by CFRP bonding (no welding is applied). The effective bond length, the strain distribution along the bond length and across CFRP layers are investigated. Unfortunately, no further research studies were carried out to investigate their bonding capacity compared to welded connections, and the debonding mechanism. To fully unlock application potential of CHS restricted by current welding technology in many cases, the concept of innovative wrapped composite joints is proposed by TU Delft as an alternative to traditional welded joints, and a series of experimental and numerical work is conducted[76]–[80]. The details of the static behavior of wrapped composite joints will be thoroughly presented in this doctoral dissertation.

2.3 Fracture behavior of composite-steel bonded interface

2.3.1 Failure modes of FRP-steel bonded joints

The possible failure modes in the general FRP-steel bonded joints can be categorized as below (see the schematic view in Figure 2-6):

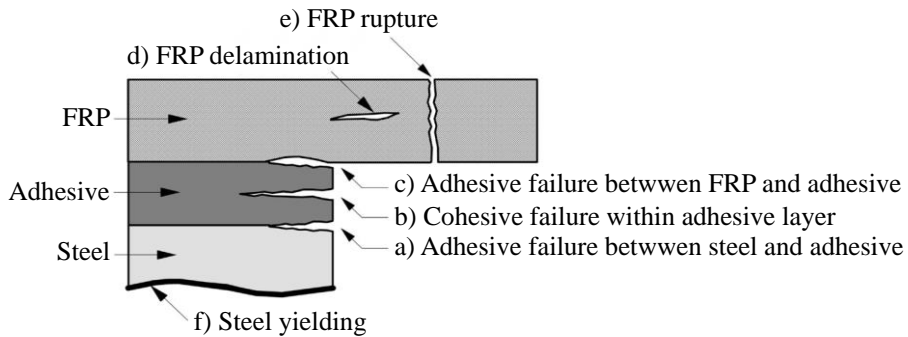


Figure 2-6 Schematic view of failure modes of general FRP-steel bonded interface[81]

- a) Adhesive failure between steel adherend and the adhesive;
- b) Cohesive failure within adhesive layer;
- c) Adhesive failure between FRP adherend and the adhesive;
- d) FRP delamination;
- e) FRP rupture;
- f) steel yielding;

In the innovative wrapped composite joints, thickness of adhesive layer is negligible such that no obvious distinction can be observed between failure modes a), b) and c). Therefore, they can be combined as the failure mode of debonding. Similarly, FRP delamination and FRP rupture can be combined as failure of composites. Based on the simplification, three main failure modes exist in wrapped composite joints: 1) debonding of composite-steel bonded interface; 2) Failure of composite laminate; c) steel yielding. It was found in the current study that debonding of the composite-steel bonded interface is the governing failure mode of wrapped composite joints[78]. Therefore, it is

imperative to understand fracture behavior of composite-steel bonded interface.

2.3.2 Fracture mechanics concepts

- **Fracture modes**

An interface crack can propagate in three different fracture modes in fracture mechanics: opening (mode I), in-plane shear (mode II) and out-of-plane shear (mode III)[82], as shown in Figure 2-7. In the case of quasi-isotropic laminate, the fracture behavior in mode II and mode III is identical. Therefore, the focus of research shifts towards the fracture properties of mode I and mode II.

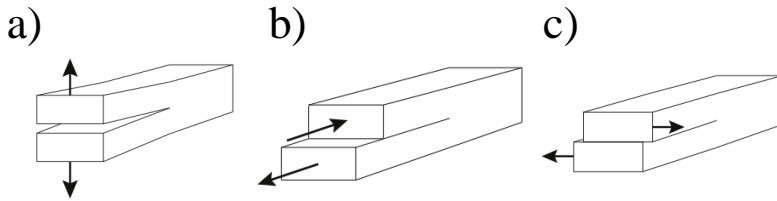


Figure 2-7 The fracture modes of the bonded interface – a) mode I: opening; b) mode II: in-plane shear; c) mode III: out-of-plane shear

- **Crack driving force**

There are three forms of crack driving force pursued to predict the onset and propagation of cracking: 1) stress intensity factor (SIF); 2) strain energy release rate (SERR); 3) J-integral. The concept of SIF K was introduced by Irwin in 1957 with a focus on the near-tip stress and displacement fields[83]. It particularly describes the singular stress and displacement fields in front of the crack tip. It can be written as[84], [85]:

$$K = \sigma \sqrt{\pi a} f(a/W) \quad \text{Equation 2-1}$$

where $f(a/w)$ is a specimen geometry dependent function of the crack length a , and the specimen width W , and σ is the applied stress. The concept of SIF is frequently applied to characterize the crack growth behavior in the domain of Linear Elastic Fracture Mechanics (LEFM) and it is difficult to calculate K for inhomogeneous composites. J-integral has also been applied as the crack driving force to account for the failure behavior of the ductile adhesive in bi-material bonded joints[86], [87]. In order to avoid the complexity of calculating the stress singularity at the bi-material interface, the strain energy release rate G is regularly chosen as the crack driving force[88]. The validity of SERR is also confined to crack problems where the extent of the inelastic processes is much smaller than the relevant geometric length scales, and calculation of total SERR is essential in the fracture analysis of a bi-material interface fracture. Unlike the near tip stress field method discussed for K , the concept of SERR associates the crack growth with the energy variation of the system containing a growing crack. The total SERR, G_{total} , is defined as the release of strain energy per unit crack growth area:

$$G_{total} = \frac{1}{B} \left(\frac{dU_e}{da} - \frac{dU_s}{da} \right) \quad \text{Equation 2-2}$$

where U_e is the external work performed and U_s is the strain energy. B corresponds to the specimen width and a is the crack length. Generally the total SERR can be calculated by two means: Irwin's crack closure integral[89] and the compliance method[90]. The crack closure integral method assumes that the work necessary to extend the crack is equal to the work required to close the crack to its original length, and can be expressed as:

$$G_I = \text{Lim}_{\Delta \rightarrow 0} \frac{1}{2\Delta} \int_0^{\Delta} \sigma_{yy}(\Delta - r) \delta_y(r) dr \quad \text{Equation 2-3}$$

$$G_{II} = \text{Lim}_{\Delta \rightarrow 0} \frac{1}{2\Delta} \int_0^{\Delta} \sigma_{xy}(\Delta - r) \delta_x(r) dr \quad \text{Equation 2-4}$$

where Δ is a small crack extension, σ_{xy} and σ_{yy} are the shear and normal tractions, respectively; r refers to the distance ahead of the crack tip; δ_x and δ_y are the displacement jump at a distance r behind the crack tip along the x (mode II) and y (mode I) directions, respectively. The crack closure integral was modified in 1977[91] for the numerical Virtual Crack Closure Technique (VCCT) method which has been extensively applied to calculate the total SERR and perform mode partitioning for adhesively bonded joints. The Irwin-Kies equation is used to calculate the total SERR in the compliance method:

$$G_{total} = \frac{P^2}{2B} \frac{dC}{da} \quad \text{Equation 2-5}$$

where P corresponds to the applied load and C refers to the compliance of the specimen containing a crack length a . Different methods exist for calculation of the compliance in which the compliance calibration method (CCM) is the most intuitive method where the function $C=f(a)$ is derived experimentally and then differentiated with respect to the crack length a . Two forms of the function are normally used:

$$C = C_0 + C_1 a^n \quad \text{Equation 2-6}$$

$$C = C_0 + C_1 a + C_2 a^2 + C_3 a^3 \quad \text{Equation 2-7}$$

where $C_{i=0,1,2,3}$ are constants that can be derived by curve fitting either Equation 2-6 or Equation 2-7. The exponent n in Equation 2-6 is usually 3[12] in accordance with the theoretically obtained compliance functions of a beam theory. The CCM requires continuous and accurate measurements of crack length a measurements during testing, which are not easy to obtain. As a result, important errors can occur during fracture characterization of bonded joints[92]. On the other hand, it was found that CCM cannot be used for the mode partitioning of mixed-mode results as is the case for the asymmetric and layered joint configuration[93]. Another method called the Global Method was

proposed by Williams[90] where the SERR is calculated by application of conventional beam theory, as shown in Figure 2-8. The total SERR can be obtained based on Equation 2-2 and shown in Equation 2-8 below:

$$G_{total} = \frac{1}{16BEI} \left[\frac{M_1^2}{\xi^3} + \frac{M_2^2}{(1-\xi^3)} - (M_1 + M_2)^2 \right] \quad \text{Equation 2-8}$$

in which M_1 and M_2 are the bending moments applied to the upper and lower sections respectively. B , E and I is the width, the axial Young's modulus and the second moment of area, respectively. $\xi = h_1/2h$. The global method assumes that the crack lies between the adherends with the same material and is extended to solve the crack propagation between dissimilar materials. The total SERR in the Extended Global Method (EGM) can be expressed as below:

$$G_{total} = \frac{6}{B^2} \left[\frac{M_1^2}{E_1 h_1^3} + \frac{M_2^2}{E_2 h_2^3} - \frac{(M_1 + M_2)^2}{E (h_1 + h_2)^3} \right] \quad \text{Equation 2-9}$$

Where E_1, E_2 is the axial modulus of the upper and lower adherend, respectively. The EGM is suitable for application in the bi-material cracking investigation and is also used in this research to calculate SERR of the composite-steel bonded interface.

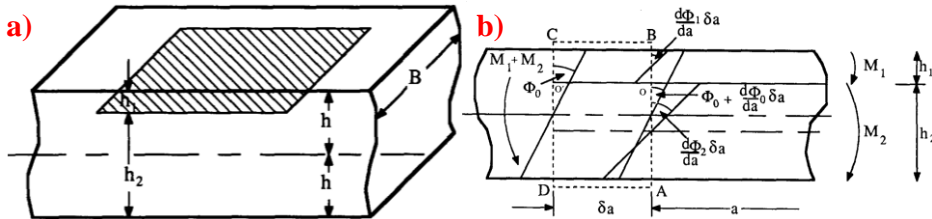


Figure 2-8 a) Geometry of the cracked specimen; b) crack tip contour with rotations[90]

• **Mode partitioning**

Most bi-material interface problems are inherently mixed-mode problems as a result of loading asymmetry and material asymmetry across the interface[94]. As discussed in the preceding sections, the total SERR is relatively easy to calculate using the EGM. On the other hand, the total SERR should be partitioned into mode I and mode II components. William proposed the analytical partitioning method of the mixed mode with two assumptions[90]: 1) pure mode I loading requires two opposite moments of the same value applied to the two arms, $\beta=1$ in Figure 2-9; 2) pure mode II is obtained when the curvature of the two arms is the same, resulting in $\psi = (1-\xi)^3/\xi^3$ with $\xi = h_1/(h_1+h_2)$. The applied moments can be decomposed into two moments corresponding to pure mode I and pure mode II loading cases:

$$M_1 = M_I + M_{II} \quad \text{Equation 2-10}$$

$$M_2 = -M_I + \psi M_{II} \quad \text{Equation 2-11}$$

Substituting Equation 2-10 and Equation 2-11 into Equation 2-8 leads to decomposition of the total SERR into:

$$G_I = \frac{M_I^2}{BEI} \frac{1+\psi}{16(1-\xi)^3} \quad \text{Equation 2-12}$$

$$G_{II} = \frac{M_{II}^2}{BEI} \frac{3(1-\xi)}{16\xi^3} (1+\psi) \quad \text{Equation 2-13}$$

where $E=E_1=E_2$ is the longitudinal Young's modulus in the case of bonding with same material and I is the reference moment of inertia of the bonded part. In the case of bonding with dissimilar material, the equivalent bending stiffness ratio should be defined based on the flexure stiffness of each arm[93], [95] as shown in Equation 2-14.

$$\psi = \frac{E_2 I_2}{E_1 I_1} \quad \text{Equation 2-14}$$

It has been proved that the assumption made in the Williams portioning method for obtaining pure mode I SERR is not accurate[96]. It is only reasonable for the symmetric case[97]. To overcome the identified deficiency, the strain-based mode partitioning method[98] was proposed by modifying the condition for mode I SERR motivated by the strain-based design of bi-material double cantilever beam for pure mode I loading[82]. As illustrated in Figure 2-9, in order to have the same strain distribution at the faying surfaces of the two arms for the pure mode I SERR, β is expressed as

$$\beta = \frac{E_2 h_2^2}{E_1 h_1^2} \quad \text{Equation 2-15}$$

The strain-based mode partitioning is suitable for composite-metal interface and is also used in this research to calculate the SERR in the pure mode.

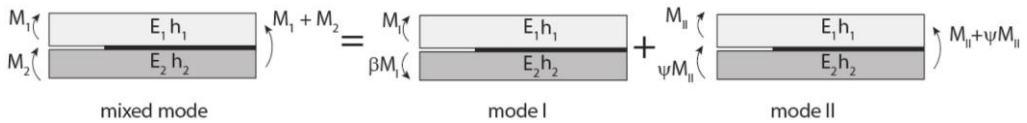


Figure 2-9 Illustration of loading in the mode partitioning method[99]

2.3.3 Bi-material interface testing

• Mode I testing

The double cantilever beam (DCB) specimen configuration has been extensively applied to obtain fracture toughness or investigate the fatigue behavior under mode I loading of composites and adhesively bonded joints[99]. Currently, standard mode I

fracture test methods[100], [101] are only available for joints with the same adherend material. Experimental and numerical work has been carried out by many researchers for bonded joints with symmetric DCB (same material and same thickness) configuration[102]–[105].

The fracture behavior and correspondent critical fracture energy might be dependent on the materials of two adherends when performing fracture test of bi-material DCB joints. In this case, the standard DCB specimens has to be adapted[82] to the general DCB configuration illustrated in Figure 2-10. The mode I testing of the bi-material interface crack is initially based on the DCB specimens designed for cracks between two adherends with the same flexural stiffness which bend symmetrically under a pair of opening loads. This design criterion can be expressed mathematically as below:

$$E_1 I_1 = E_2 I_2 \quad \text{Equation 2-16}$$

Where E and I denotes the longitudinal Young's modulus and the moment of inertia, respectively. The subscripts 1 and 2 denotes the two different adherends, respectively. This design criterion has been followed by some researchers for testing composite-metal bonded interfaces[106]–[110], but the mode II fracture component was found in the numerical results indicating failure of this criterion in guaranteeing pure mode I loading condition[107], [108]. Therefore, another design of DCB configuration is based on the criterion that the two arms have the same longitudinal strain distribution at the faying surfaces. This is proposed to remove the in-plane sliding associated with the mode II fracture components[82]. This design criterion can be described by the following equation:

$$E_1 h_1^2 = E_2 h_2^2 \quad \text{Equation 2-17}$$

Research on bi-material DCB joint design following Equation 2-17 is not extensive as the one following the same flexure rigidity but the limited research[82], [111]–[113] agrees that the mode II fracture component is sufficiently suppressed when Equation 2-17 is followed in designing the bi-material DCB specimens.

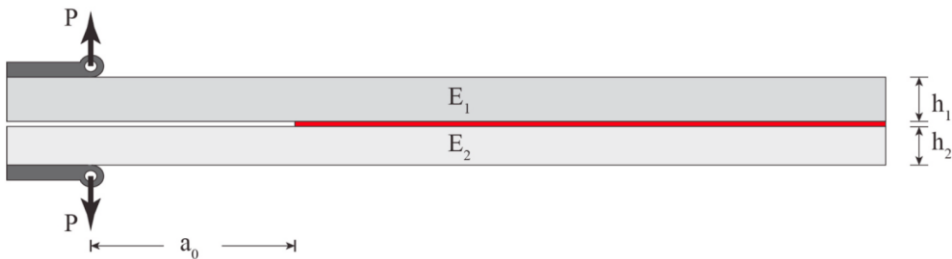


Figure 2-10 Illustration of a general DCB specimen[99]

- **Mode II testing**

The significance of mode II interface crack problem is justified by the fact that most bonded joints are designed to transmit loads in the form of shear[99]. The three-

point end notched flexure (3ENF) test has been used by many researchers to investigate delamination propagation in laminated composites. The current standard of 3ENF test is only suitable for unidirectional composite specimens with symmetric geometry [114]. The standard configuration of the 3ENF test is adapted to the general configuration shown in Figure 2-11 for application for bi-material interface problem. Compared to the mode I interface crack problem in bi-material specimens, less work in terms of mode II interface problem between two dissimilar materials can be found from current literature. Ning et al.[115] used the standard 3ENF configuration that comprises two adherends of the same thickness to investigate the mode II fracture toughness of CFRP-aluminum interface without providing any information on the mode mixity. Ouyang and Li[116] proposed a bi-material 3ENF specimen configuration described by Equation 2-17 to ensure the pure mode II based on their previous work on developing pure mode I in the DCB configuration[111], [112]. It was found that[111], [112], [116] Equation 2-17 is a decoupling condition such that mode I loading does not cause tangential deformation components related to mode II fracture behavior. Besides this, the mode II loading does not cause normal deformation components related to mode I fracture behavior. Other researches designed the bi-material 3ENF specimen by matching the stiffness of upper and lower adherends as depicted by Equation 2-16[117]–[120]. They did not conduct detailed analysis to prove the mode I fracture component was not presented in the studies.

The main drawback of the 3ENF configuration is the inherent instability of the crack propagation. An alternative test configuration, namely the four-point end notched flexure (4ENF) test, was proposed[121] for stable cracking propagation in mode II. The 4ENF specimen configuration is shown in Figure 2-12. Unfortunately, there is no current literature found in terms of mode II bi-material interface problem.

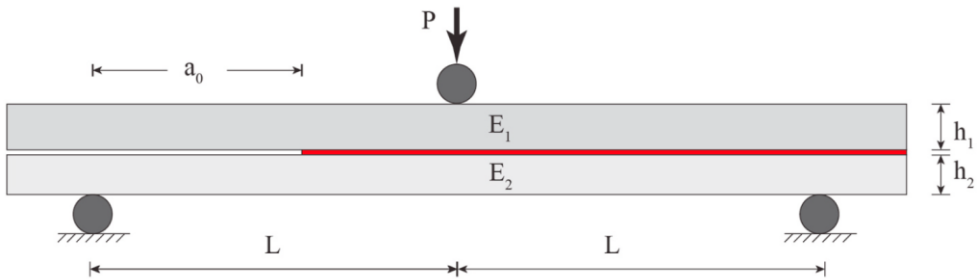


Figure 2-11 Illustration of a generic 3ENF configuration [99]

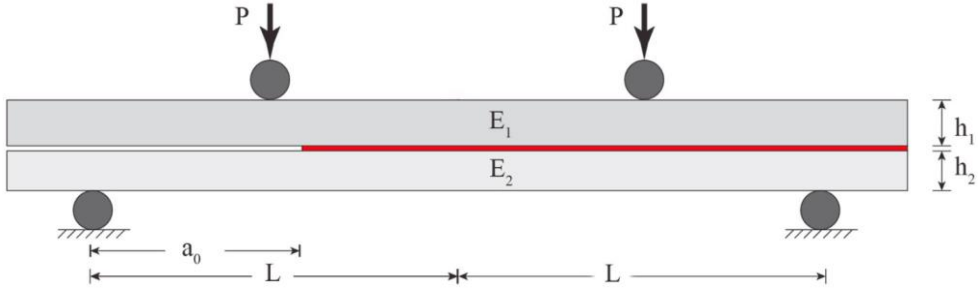


Figure 2-12 Illustration of a 4ENF configuration

- **Mixed-mode testing**

Adhesively bonded joints are normally subjected to mixed mode loading and it is well known that the fracture toughness, $G_{\text{total}} = G_I + G_{II}$, is a function of the mode I, mode II fracture components and their ratio[99]. The mixed mode bending (MMB) test configuration has been extensively used for studying mixed mode failure in symmetric bonded joints and has been adopted in bi-material bonded joints as well. The general MMB test setup is depicted in Figure 2-13. It was first proposed by Reeder and Crews[122], [123] and has been standardized for specimens with symmetric adherends[124]. Technically, all mode mixities can be achieved with this test setup by changing the loading moment arm. For this reason, the MMB test is widely employed for characterizing crack growth in bi-material joints[99]. Shahverdi and Cassilopoulos et al.[93], [95], [125], [126] have employed the MMB test to study the mixed mode fracture in asymmetric pultruded GFRP joints where the EGM was used to separate the SERR components for pure mode I and mode II. Arouche and Wang et al.[98] also employed the MMB test to study the crack propagation at bi-material CFRP-steel bonded interface. The specimen was designed according to Equation 2-17 to match the longitudinal strains such that pure mode I loading is generated at the pair of opposite moment while pure mode II is obtained by having the same curvature in the two adherends.

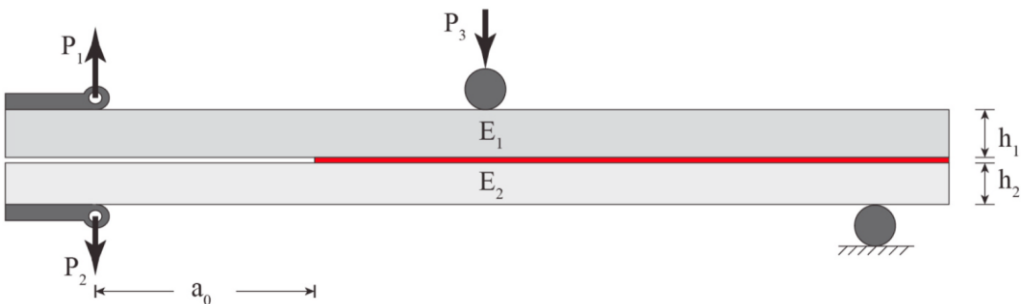


Figure 2-13 Illustration of the MMB configuration

2.3.4 Numerical simulation of interface fracture

Linear elastic fracture mechanics (LEFM) is a useful tool for solving fracture

problems provided a crack-like notch or flaw exists in the body and the nonlinear zone, namely the fracture zone, ahead of the crack tip is negligible[127], i.e., the notch root tip and the real crack tip shown in Figure 2-14 overlap. However, for ductile metals or cementitious materials, the size of the fracture zone – due to plasticity or micro-cracking – is not negligible compared to other dimensions of the cracked geometry. Moreover, even for brittle material where the fracture zone can be lumped into a single point, the presence of an initial crack is needed for LEFM to be applied. This means that bodies with blunt notches – but no cracks – cannot be analyzed with LEFM[127].

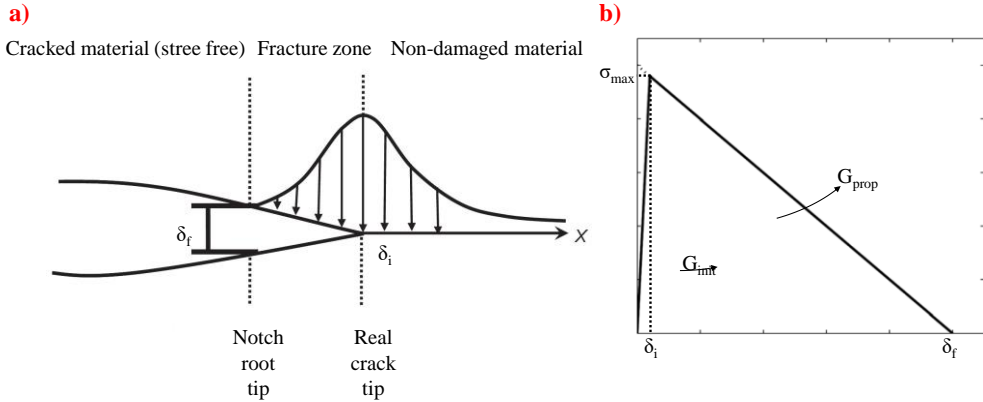


Figure 2-14 Illustration of a): the fracture process zone and b) cohesive parameters in a bi-linear CZM

The non-linear fracture zone can be approximated in conjunction with computational techniques by utilizing the concept of a cohesive zone model (CZM) pioneered for concrete by Hillerborg under the name of fictitious crack model[128] to surmount the above-mentioned difficulties. The constitutive behavior of the cohesive zone, a.k.a. fracture zone or fracture process zone (FPZ), is defined by the traction-separation law, a.k.a. the cohesive law, derived from laboratory tests. In the traction-separation relation, the traction across the cohesive surface reaches a peak value with increasing separation and then decreases until vanishing eventually[129], as shown in Figure 2-14. δ_i and δ_f refers to the critical separation values to reach crack initiation and crack propagation (failure of the fracture process zone). The area under the traction-separation law until δ_i corresponds to the fracture toughness or the critical SERR in terms of crack initiation G_{init} , while the area of the whole traction-separation law corresponds to the fracture toughness or the critical SERR in terms of crack propagation G_{prop} . The distance between the real crack tip and the notch root tip is identified as the length of the fracture process zone (FPZ).

The shape of the cohesive law is highly dependent on the material property, the layout configuration, the surface preparation of the bonded material, etc. Various traction-separation laws have been utilized in the open literature, as shown in Figure 2-15. The bi-linear cohesive law is the simplest and most widely used traction-separation relation and other cohesive laws, i.e. tri-linear, trapezoidal, exponential and polynomial

laws, are also applied according to the material or interface properties.

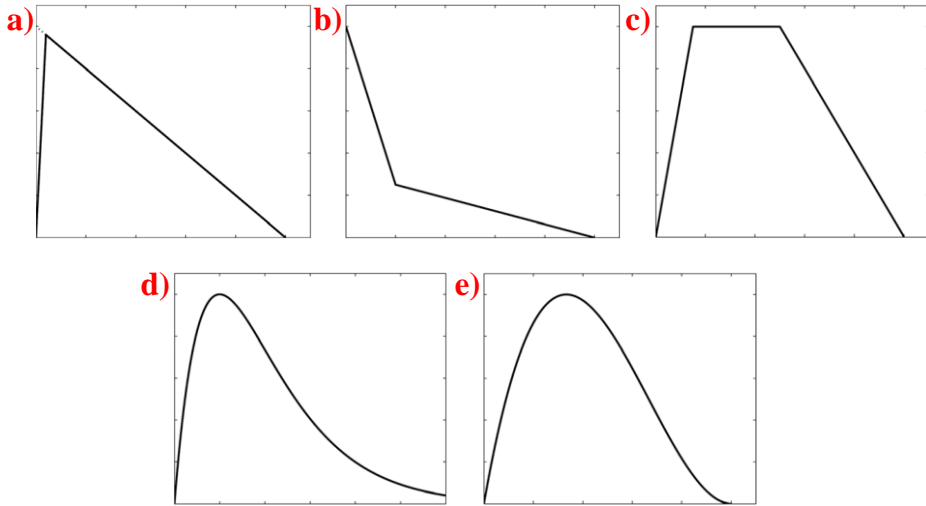


Figure 2-15 Normally used traction-separation laws: a) bi-linear; b) tri-linear; c) trapezoidal; d) exponential; e) cubic polynomial

The CZM has been extensively applied in the research in terms of numerical simulation of delamination in laminated composites. Shahverdi and Vassilopoulos et al.[93], [95], [125] used an exponential bridging law to simulate bridging behavior in mode I fracture of asymmetric adhesively-bonded pultruded composite joints. Molares et.al[130] and Rarani et.al[131] applied the tri-linear cohesive law to simulate the mode I delamination process. Joki et.al simulated the delamination incorporating lar scale bridging behavior by the trapezoidal cohesive law. Unluckily, there is limited research studies in terms of applying cohesive zone model in simulation of composite-steel bonded interface.

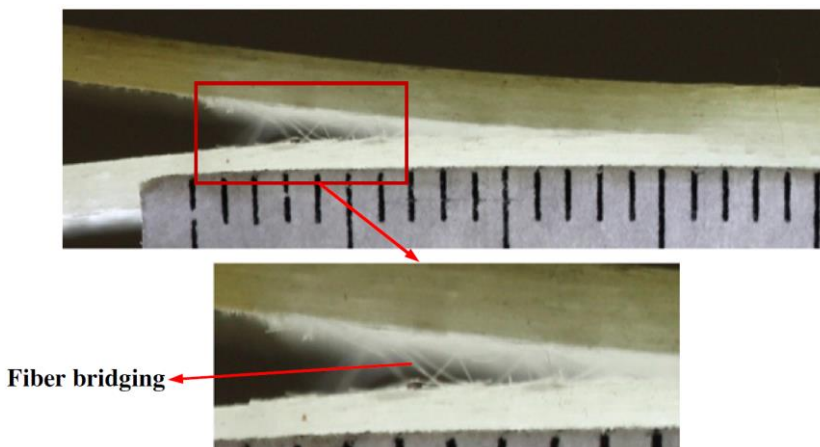


Figure 2-16 Fiber bridging during delamination of laminated composites[132]

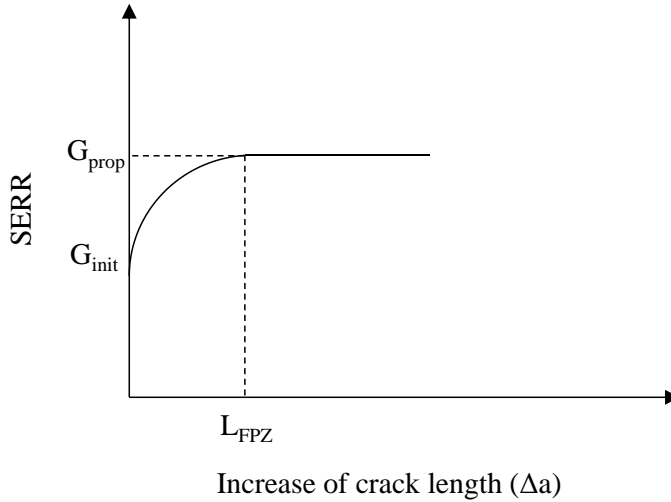


Figure 2-17 A schematic R-curve

In the delamination problem of composites, the existence of fiber bridging, as shown in Figure 2-16, results in significant increase of the fracture toughness and relatively long fracture process zone. The feature that the strain energy release rate (SERR) as the crack advances is known as the resistance curve (R-Curve)[132], as shown in Figure 2-17. The R-curve can be identified as the material property of the composites or the bonded interface such that the length of FPZ remains constant and the crack propagation proceeds by a steady state or a self-similar crack growth involving simultaneous propagation of both crack tips[132].

In the context of describing mixed mode fracture problems, two terminologies are frequently used in literature: mixed mode ratio and mode mixity. Mixed mode ratio is normally referring to the ratio of the mode II fracture toughness G_{II} , to the total fracture toughness, G_{total} , i.e., G_{II} / G_{total} . Shahverdi et al.[125] conducted MMB test of adhesively-bonded pultruded GFRP joints and found out that the fracture toughness follows a polynomial relation as the mixed mode ratio increases from pure mode I to mode II.

2.4 Modeling of (complex) composite wrapping and composite-steel interface in CHS joints

It is essential to accurately model the behavior of composites and the composite-steel bonded interface when composites are used to wrap CHS joints. The corresponding modeling strategies were proposed by some researchers mentioned in Section 2.2.2 when they investigated the application for composite wrapping in strengthening welded tubular joints[56]–[64], [70], [72]–[74].

Lesani et al.[56]–[58] used ABAQUS software package to simulate behavior of FRP-strengthened CHS T/Y-joints under axially compressive load. The tubular joints were modeled as three-dimensional structures with shell elements. The FRP wrapping was modeled with shell elements as a skin stretched on the tube surfaces by sharing

interface nodes, see Figure 2-18. A perfect bond state was considered without modeling of cohesive/adhesive element at the FRP and the steel substrate interface and this assumption was validated against the experimental results accordingly. For the FRP, the Hashin damage criteria were utilized for strength assessment and damage evolution was considered in the analyses to consider the post-damage behavior of the FRP element[57]. In this research, the thickness of FRP wrapping on brace, chord and the brace/chord intersection is 4, 6 mm and 10 mm, respectively. Exceeding 6 mm FRP thickness on the steel tubes was not considered since the thicker composites have different behavior and also it is not cost effective in practical application of strengthening[56].

Hosseini et al. built the numerical model by ABAQUS software package to investigate influence of FRP material on SCF values in tubular T-joints[59]–[62] where the model geometry was exactly the same as the experimental specimens tested by Lesani et al.[56]. The shell element used in the numerical work of Lesani et al.[56] was replaced by the 3D solid element C3D20 in modeling the geometry of tubes and weld profile, in order to achieve more accurate and detailed stress distribution at the joint intersection zone. FRP wrapping was still modelled by shell element but the element type S4R was used which is a 4-node doubly curved thin or thick shell with reduced integration. FRP wrapping performed in the model as covering layer of the joint and the shell elements were stretched on the tube surfaces as a skin by sharing interface nodes. Alike in the studies of Lesani et al.[56], the FRP-steel interface was considered as a perfect bond state without utilization of cohesive/adhesive element. The finite element model is shown in Figure 2-19.

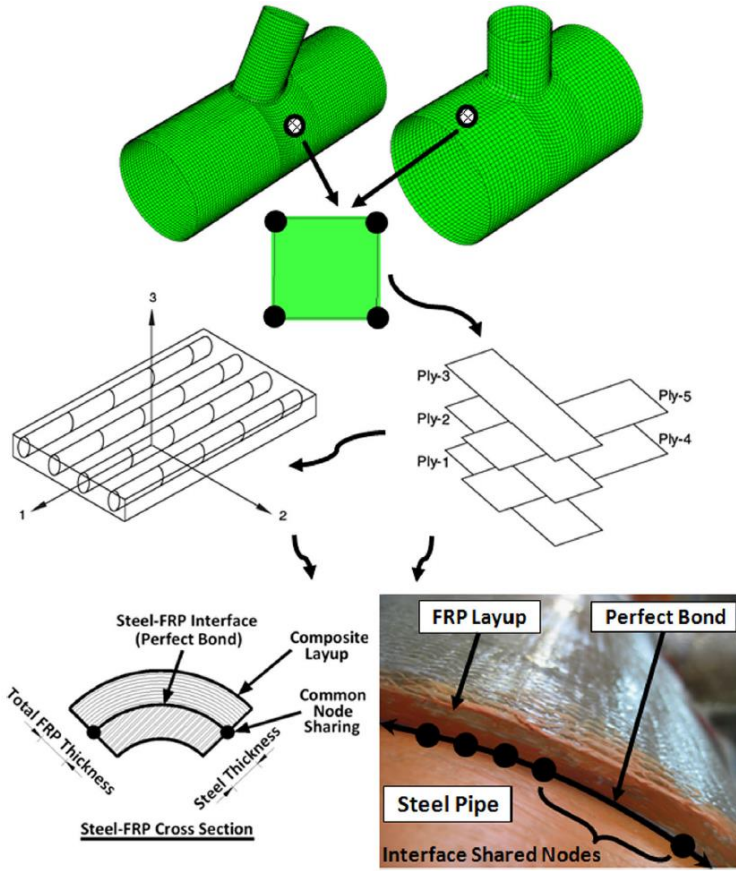
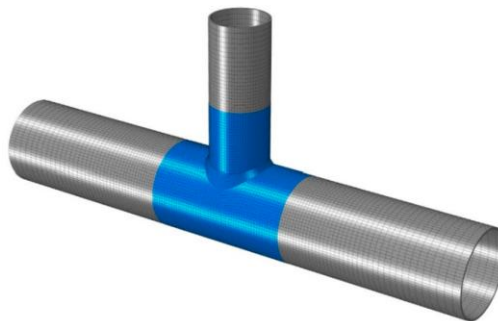


Figure 2-18 Graphical presentation of modeling FRP wrapping and FRP-steel bonding[58]



(a)

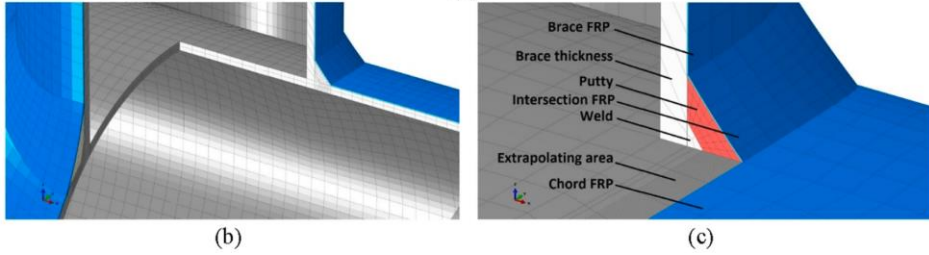


Figure 2-19 Finite element mode of the tested T-joint specimens: a) Isometric view; b) sections cuts at crown and saddle points; c) Mesh enlargement view[62]

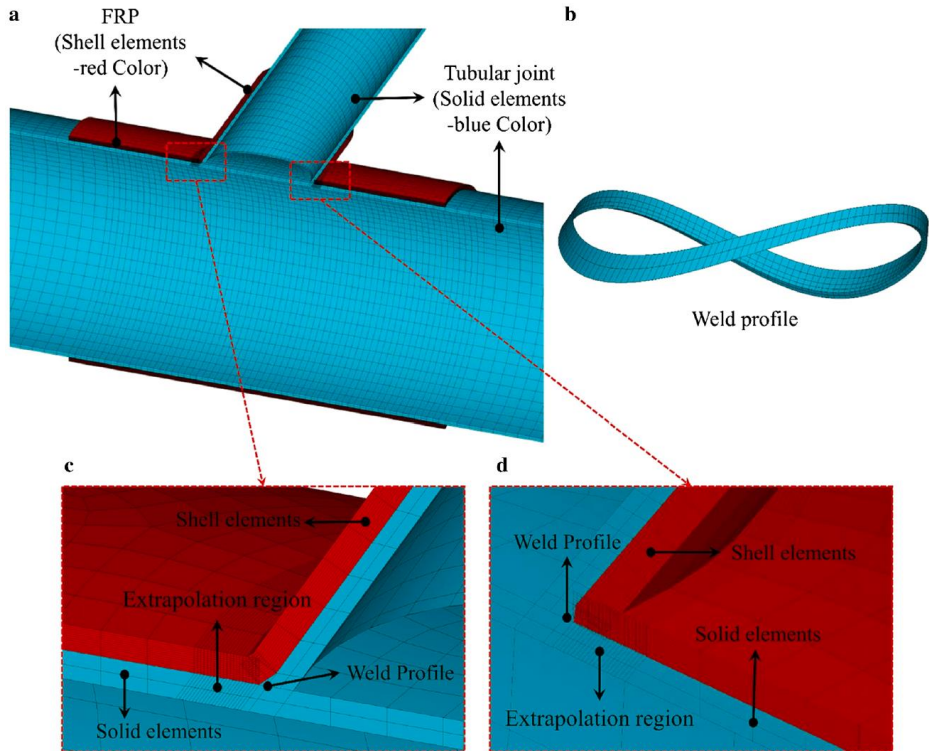


Figure 2-20 The FE model of tubular Y-joints using the sub-zone method: a) the regions adjacent to the joint intersection; b) spatial 360° volume of weldment; c) and d) the enlarged brace-to-chord intersection region[63]

Nassiraei et al.[63], [64] also performed numerical investigation into SCF values of FRP-strengthened T/Y-joints based on the results from open literature. ANSYS software package was utilized for the simulation where the element type SOLID186 was used to model tubes and weld profile while the SHELL281 element was used to model FRP layers. A sub-zone mesh technique was used to guarantee the mesh quality where the entire model is divided into several different regions according to the computational requirements. The mesh of every region is generated separately using different densities and then mesh of full model is generated by merging the meshes of all the sub-

regions[63]. The behavior of the FRP-steel interface was defined to be always bonded simulated by the ANSYS contact ability. The outer surfaces of CHS members were chosen as the contact surface and inner surfaces of the FRP sheets were selected as the target surface. The flexible-to-flexible surface-to-surface contact elements were used to simulate the interaction[64]. The FE model of the strengthen tubular Y-joints are shown in Figure 2-20.

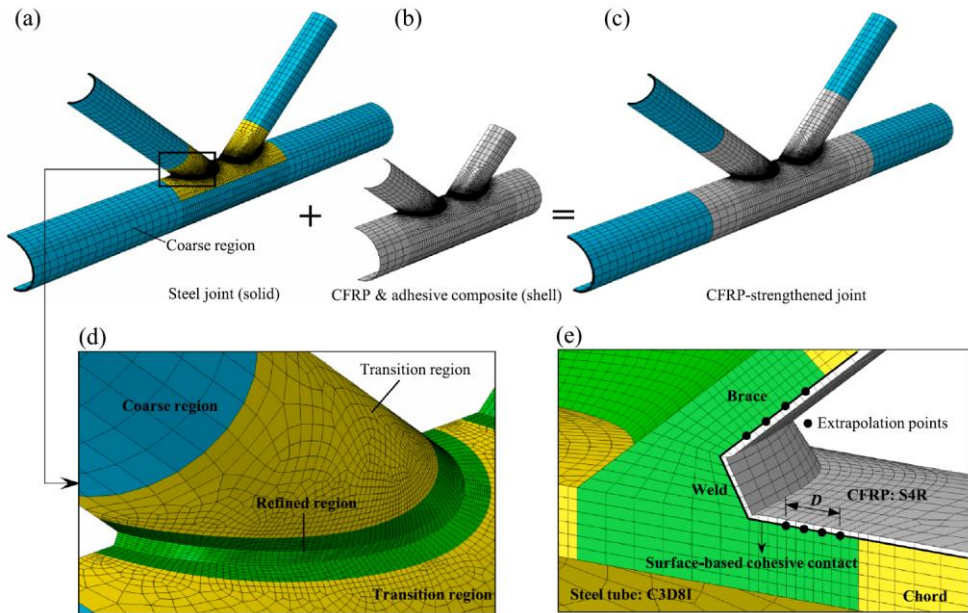


Figure 2-21 The FE model of a CFRP-CHS K-joint [72]

Lewei Tong et al.[70], [72] conducted numerical simulation in terms of static and fatigue behavior of CFRP-strengthened CHS gap K-joints, with the FE model built in ABAQUS software package shown in Figure 2-21. The steel members and the welding were modeled with 3D solid element and a linear solid element C3D8I was used to model steel tubes which is better at gloving the convergence problem that occurs in contact analysis than a quadratic element such as C3D20R. To balance the computational cost and accuracy, the meshes near the weld intersection line were refined, see Figure 2-21 d). The CFRP sheets were modeled using the shell element S4R, and the Hashin damage criteria and damage evolution were combined to analyze post-damage behavior of the composites. The perfect bonding was assumed in majority of bonding area between CFRP wrapping and steel substrate, as per reference[56] without adhesive elements while the surface-based cohesive contact was applied to the interface between CFRP-brace and at the intersection areas where debonding was observed.

Zavvar et al. investigated SCFs in steel tubular KT-joints with FRP-wrapping and built the FE model with ABAQUS software package, as shown in Figure 2-22. The 3D solid element C3D20 was used to model steel members and the shell element S4R

sharing nodes with the 3D solid element was utilized to model CFRP. A perfect bond state was considered proved by Lesani et al[56]–[58].

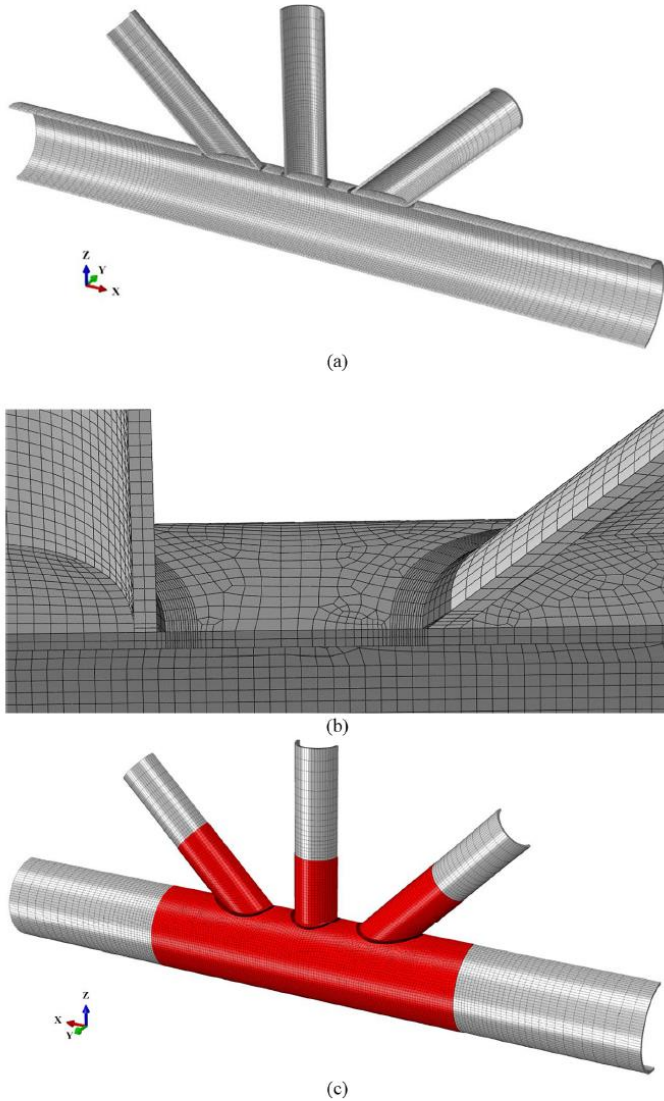


Figure 2-22 a) Isometric view of the KT-joint FE model; b) Mesh enlargement at the intersection zone; c) FRP shell elements sharing nodes with steel solid elements[73]

It can be concluded from the current modelling strategies in literature that the composite wrapping were all modelled by shell elements. This is suitable for the FRP-strengthened tubular joints where the weld still transferred the main load such that thickness of wrapping is relatively small especially at the intersection region (no more than 10 mm) due to limited numbers of wrapping plies. However, this is not applicable in the case of wrapping composite joints with wrapping thickness significantly larger than that in strengthened joints. Using shell element to model behavior of thick and

curved geometry is difficult and inaccurate so an alternative method should be proposed. On the other hand, the perfect bond state was assumed in the majority of the current studies, which cannot be utilized in wrapped composite joints in which the governing failure mode is debonding of the composite-steel bonded interface. The surface-based cohesive contact is a good option but the constitutive law of the bonded interface should be given correctly.

2.5 Debonding crack propagation monitoring using DIC

The digital image correlation (DIC) technique, as one of the NDT techniques, has been extensively applied for monitoring cracking in physical testing attributed its advantages of non-contact, full field and real-time measurements, and also powerful post-processing analysis. Tracking and image registration techniques are employed in DIC for accurate 2D and 3D measurements of deformations and surface strains of tested specimens. It has been used as a useful tool to monitor the debonding crack propagation between composites and steel/concrete/masonry substrates during the experiments. Ghiassi et al.[133], Zhang et al.[134] and Ali-Ahmad et al.[135] monitored the debonding process between composites and substrates under the monotonic quasi static loads with help of DIC. In their studies, the observed strain distribution can be divided into three main regions (see Figure 2-23): 1) the unstressed region; 2) the stress transfer zone corresponding to the effective bond length; 3) the fully debonded zone. The formula was proposed to approximate strain distribution along the bond length to quantify the three zones. The DIC technique was also utilized in monitoring the debonding crack propagation of the CFRP-steel bonding subjected to fatigue load[136], [137]. In these studies, the debonding length was identified by the strain plateau or by negligible strain gradient. Some other researchers[138], [139] used the artificial delamination crack to validate the surface strain-based crack monitoring method by DIC. The results showed that the location of the artificial delamination can be effectively detected by DIC strain contours. The DIC results were also comparable with results from finite element (FE) models. It is worth noting that the thickness of the material above the delaminated interface may have influence on the monitoring results.

It can be concluded that DIC technique is effective in monitoring the debonding crack propagation between composite and substrates, but the thickness of applied composites is very thin. As for wrapped composite joint with thick and varying thickness, the influence of local material variations of composites on the surface strain distribution can be considerable. In this case, the FEM can be used to validate the feasibility of the DIC monitoring method and determine the debonded area.

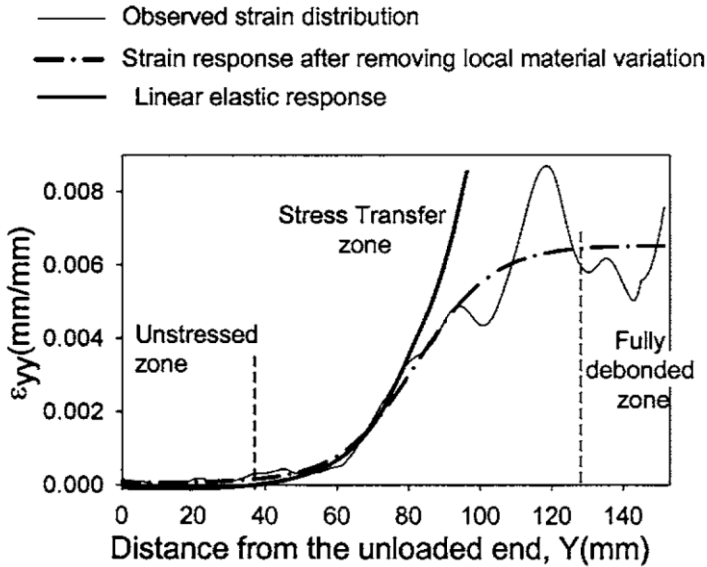


Figure 2-23 Experimental and theoretical strain distribution along FRP sheet at the postpeak part of load response [135]

2.6 Size effect in composite-metal bonded joints

In many situations, the laboratory tests must be conducted on a much reduced scale of the specimens attributed to the cost of failure tests of full scale or larger scale structures. Therefore, it is essential to extrapolate the small-scale test results to the large-scale structures where the size effect needs to be considered. The size effect is defined for geometrically similar structures and represents the effect of structural size D (or characteristic dimension) on a load parameter of the dimension of stress. This parameter is normally chosen as the nominal strength, which is defined as:

$$\sigma_N = \frac{P_{\max}}{bD} \quad \text{Equation 2-18}$$

where P_{\max} is the maximum load, b is the width of the structure in the third dimension and D is the characteristic dimension which can be selected arbitrarily since only the ratio of σ_N values matters. There are two types of size effect: a) the statistical size effect caused by randomness of material strength; b) the energetic/deterministic size effect caused by stress redistributions due to stable propagation of fracture or damage and the inherent energy release[140]. For purely metallic structure, there is no deterministic size effect and the relatively weak statistical size effect is well understood. However, the deterministic size effect is much stronger than the statistical size effect in the quasi-brittle materials like fiber composites[141], as in the case of wrapped composite joints.

The size effect was explained by Bazant[140] using a simply-supported beam as shown in Figure 2-24 a). The response Y (e.g. the maximum stress or the maximum deflection) is a function of the characteristic size (dimension) of D , i.e. $Y = Y_0 f(D)$. Three

structural sizes (1, D and D') are presented and the size 1 is chosen as the reference size. The response for size D and size D' are $Y=f(D)$ and $Y'=f(D')$. If there is no characteristic length, the Equation 2-19 must be satisfied which is a functional equation for the unknown scaling law $f(D)$ having only one solution, namely the power law (Equation 2-20). The s is the constant exponent, and c_1 is a constant implied as a unit of length measurement. For elasticity with a strength limit or plasticity with a yield surface expressed in terms of stresses and strains, $s = 0$ in the power scaling law indicating that there is no characteristic dimension. On the other hand, $s = -1/2$ in LEFM provided that geometrically similar structures with geometrically similar cracks or notches are considered, as shown in Figure 2-24 b).

$$\frac{f(D')}{f(D)} = f\left(\frac{D'}{D}\right) \quad \text{Equation 2-19}$$

$$f(D) = \left(\frac{D}{c_1}\right)^s \quad \text{Equation 2-20}$$

Quasi-brittle materials obey the theory of plasticity or strength theory on a small scale where $s = 0$ while they follow the LEFM on a large scale where $s = -1/2$. As for the sizes in between as shown in Figure 2-24 c), the size effect law was derived[142] for the bridging of plasticity and LEFM:

$$\sigma_N = B\sigma_0 \left(1 + \frac{D}{D_0}\right)^{-\frac{1}{2}} + \sigma_R \quad \text{Equation 2-21}$$

in which B are positive dimensionless constants and D_0 is the constant representing the transitional size at which the power laws of plasticity and LEFM intersect; Usually, the constant $\sigma_R = 0$.

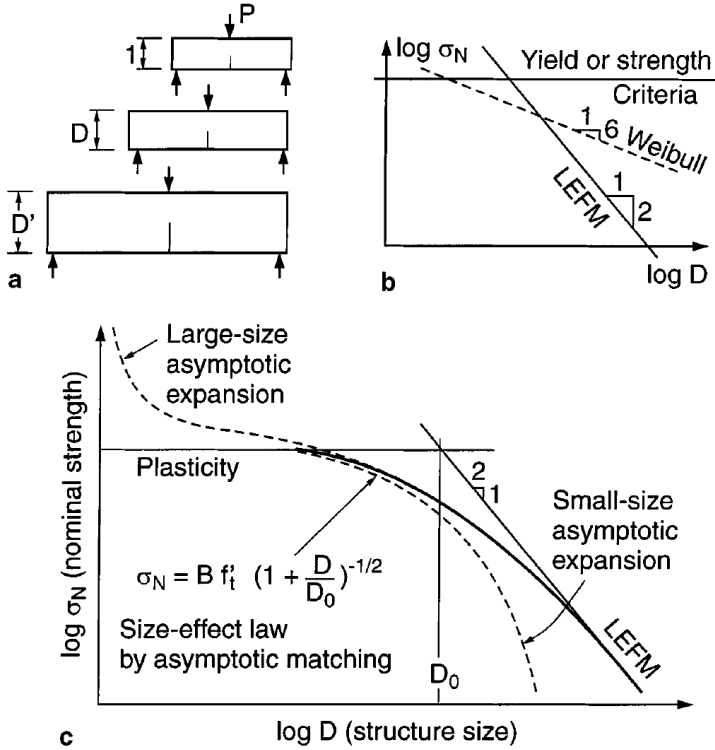


Figure 2-24 a) Geometrically similar structures of different size; b) power scaling law; c) size effect law for quasi-brittle failures bridging the law of plasticity (horizontal asymptote) and the power law of LEFM (inclined asymptote)

Due to the existence of composites, the strong deterministic size effect in composite-metal bonded joints was investigated by some researchers. Yu et al.[141], [143], [144] studied the size effect on the strength of hybrid bi-material joints of steel and fiber composites. Three series of scaled geometrically similar specimens of symmetric double-lap joints with a rather broad size range (1:12) are tested, as shown in Figure 2-25. With the help of asymptotic matching, the general approximate size effect laws for the strength of the 2 types of hybrid metal-composite joints were derived[143] and validated by comparison with size effect experiments[141]. The size effect is depicted in the double-logarithmic graphs of σ_N and D shown in Figure 2-26. It was found that the strength of metal-composite hybrid joints exhibits a strong size effect with more than 50% drop of the strength due to a fourfold increase in size. It is not safe to design large hybrid joints on the basis of classical material failure criteria expressed in terms of stresses or strains, or both[143]. A cohesive layer base on a traction-separation softening law was used by the same authors to simulate the failure of the hybrid joints and good agreement was reached compared to the experiment results[144].

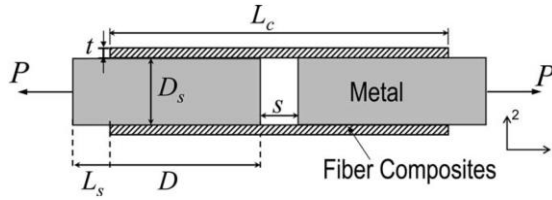


Figure 2-25 Geometry of double-lap hybrid joint[141]

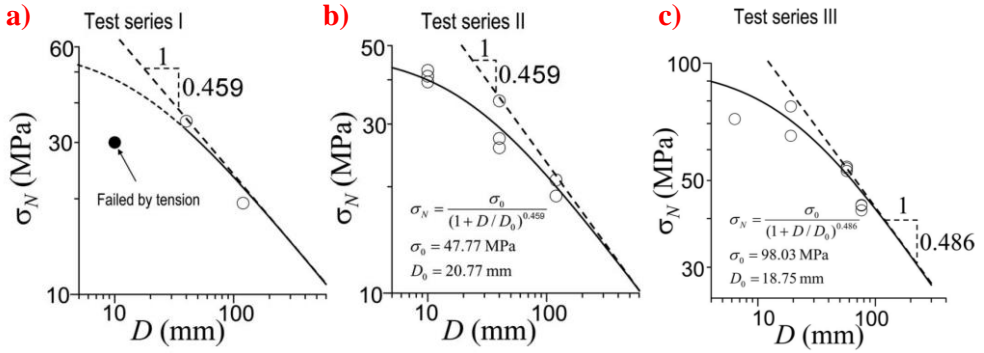


Figure 2-26 Measured nominal strength values compared with optimum fit by size effect formula (solid curves): a) test series 1; b) test series 2 and c) test series 3[141]

References

- [1] A. Stacey and J. V Sharp, “Safety factor requirements for the offshore industry,” *Eng. Fail. Anal.*, vol. 14, no. 3, pp. 442–458, 2006, doi: 10.1016/j.engfailanal.2005.08.003.
- [2] L. D. Alain Nussbaumer, Luis Borges, *Fatigue Design of Steel and Composite Structures: Eurocode 3: Design of Steel Structures, Part 1-9 Fatigue; Eurocode 4: Design of Composite Steel and Concrete Structures*. John Wiley & Sons, 2012.
- [3] J. Wardenier, *Hollow Section in Structural applications*. CIDECT, 2010. doi: 10.1007/978-94-011-5856-5_6.
- [4] N. Van Vuong and M. H. Quan, “Fatigue analysis of jacket support structure for offshore wind turbines,” *J. Sci. Technol. Civ. Eng. - HUCE*, vol. 13, no. 1, pp. 46–59, Jan. 2019, doi: 10.31814/STCE.NUCE2019-13(1)-05.
- [5] S. C. Siriwardane, N. D. Adasooriya, and D. Pavlou, “Fatigue Strength Curve for Tubular Joints of Offshore Structures under Dynamic Loading,” *Dynamics*, vol. 1, no. 1, pp. 125–133, 2021, doi: 10.3390/dynamics1010007.
- [6] N. Shabakhty and S. S. Tabatabaei, “Sensitivity of fatigue assessment for offshore jacket platform to different pile–soil–structure interaction models,” *Ships Offshore Struct.*, vol. 17, no. 10, pp. 1–18, 2022, doi: 10.1080/17445302.2021.1979919.
- [7] B. T. Astorm, *Manufacturing of Polymer Composites*. Routledge, 2018. doi: 10.1201/9780203748169.
- [8] R. Jain and L. Lee, *Fiber Reinforced Polymer (FRP) Composites for Infrastructure Applications*. Springer Science & Business Media, 2012. Accessed: Jan. 11, 2023. [Online]. Available: <http://www.springer.com/series/8584>
- [9] W. Wang, J. A. Poulis, S. Teixeira De Freitas, and D. Zarouchas, “Surface pretreatments on CFRP and titanium for manufacturing adhesively bonded bi-material joints,” in *ECCM 2018 - 18th European Conference on Composite Materials*, Athens, Greece, 2018.
- [10] K. S. G. Krishnan, O. Bertram, and O. Seibel, “Review of hybrid laminar flow control systems,” *Prog. Aerosp. Sci.*, vol. 93, pp. 24–52, 2017, doi: 10.1016/j.paerosci.2017.05.005.
- [11] A. Vlot and J. W. Gunnink, *Fibre Metal Laminates: An Introduction*. Springer-Science+Business Media, B,V, 2001.
- [12] D. Á. Feito, “Fracture mechanics of carbon fibre reinforced plastics to Ti-alloy adhesive joints,” PhD Dissertation, Imperial College London, 2012.
- [13] W. Wang, C. Rans, and R. Benedictus, “Analytical prediction model for non-symmetric fatigue crack growth in Fibre Metal Laminates,” *Int. J. Fatigue J.*, vol. 103, pp. 546–556, 2017, doi: 10.1016/j.ijfatigue.2017.06.035.
- [14] W. Wang, C. Rans, R. C. Alderliesten, and R. Benedictus, “Predicting the influence

of discretely notched layers on fatigue crack growth in fibre metal laminates,” *Eng. Fract. Mech.*, vol. 145, pp. 1–14, 2015, doi: 10.1016/j.engfracmech.2015.06.062.

[15] J. Cao and J. L. Grenestedt, “Design and testing of joints for composite sandwich/steel hybrid ship hulls,” *Compos. Part A Appl. Sci. Manuf.*, vol. 35, no. 9, pp. 1091–1105, 2004, doi: 10.1016/j.compositesa.2004.02.010.

[16] J. Cao, J. L. Grenestedt, and W. J. Maroun, “Testing and analysis of a 6-m steel truss/composite skin hybrid ship hull model,” *Mar. Struct.*, vol. 19, no. 1, pp. 23–32, 2006, doi: 10.1016/j.marstruc.2006.07.001.

[17] M. Saeedifar, M. N. Saleh, S. Teixeira, D. Freitas, and D. Zarouchas, “Damage characterization of adhesively-bonded Bi-material joints using acoustic emission,” 2019, doi: 10.1016/j.compositesb.2019.107356.

[18] M. N. Saleh, M. Saeedifar, D. Zarouchas, and S. T. De Freitas, “Stress analysis of double-lap bi-material joints bonded with thick adhesive,” *Int. J. Adhes. Adhes.*, vol. 97, Mar. 2020, doi: 10.1016/J.IJADHADH.2019.102480.

[19] M. Dlugosch, J. Fritsch, D. Lukaszewicz, and S. Hiermaier, “Experimental investigation and evaluation of numerical modeling approaches for hybrid-FRP-steel sections under impact loading for the application in automotive crash-structures,” *Compos. Struct.*, vol. 174, pp. 338–347, 2017, doi: 10.1016/j.compstruct.2017.04.077.

[20] S. Teixeira de Freitas and J. Sinke, “Failure analysis of adhesively-bonded skin-to-stiffener joints: Metal-metal vs. composite-metal,” *Eng. Fail. Anal.*, vol. 56, pp. 2–13, 2015, doi: 10.1016/j.engfailanal.2015.05.023.

[21] S. Teixeira de Freitas and J. Sinke, “Failure analysis of adhesively-bonded metal-skin-to-composite-stiffener: Effect of temperature and cyclic loading,” *Compos. Struct.*, vol. 166, pp. 27–37, 2017, doi: 10.1016/j.compstruct.2017.01.027.

[22] Gurit Holding AG, “Guide to Composites,” Available URL <http://www.netcomposites.com/> ..., p. 74, 2000, [Online]. Available: <http://www.gurit.com/guide-to-composites.aspx>

[23] A. Shaat and A. Fam, “Axial loading tests on short and long hollow structural steel columns retrofitted using carbon fibre reinforced polymers,” *Can. J. Civ. Eng.*, vol. 33, no. 4, pp. 458–470, 2006, doi: 10.1139/L05-042.

[24] A. Shaat, W. Safwat, E. Sayed, and A. Fam, “Modeling of axially loaded HSS slender steel members retrofitted with composites,” in *Advances in Engineering Structures, Mechanics & Construction*, Springer Netherlands, 2006, pp. 227–238.

[25] Y. Zhao, W. Gu, J. Xu, and H. Zhang, “The strength of Concrete Filled CFRP-Steel Tubes under axial compression,” *Proc. Int. Offshore Polar Eng. Conf.*, vol. 2005, pp. 466–470, 2005.

[26] Z. Tao, L. H. Han, and J. P. Zhuang, “Axial loading behavior of CFRP strengthened concrete-filled steel tubular stub columns,” *Adv. Struct. Eng.*, vol. 10, no. 1, pp. 37–46,

2007, doi: 10.1260/136943307780150814.

[27] J. G. Teng and Y. M. Hu, “Behaviour of FRP-jacketed circular steel tubes and cylindrical shells under axial compression,” *Constr. Build. Mater.*, vol. 21, no. 4, pp. 827–838, 2007, doi: 10.1016/j.conbuildmat.2006.06.016.

[28] J. M. Duell, J. M. Wilson, and M. R. Kessler, “Analysis of a carbon composite overwrap pipeline repair system,” *Int. J. Press. Vessel. Pip.*, vol. 85, no. 11, pp. 782–788, 2008, doi: 10.1016/j.ijpvp.2008.08.001.

[29] D. Fernando, T. Yu, J. G. Teng, and X. L. Zhao, “CFRP strengthening of rectangular steel tubes subjected to end bearing loads: Effect of adhesive properties and finite element modelling,” *Thin-Walled Struct.*, vol. 47, no. 10, pp. 1020–1028, 2009, doi: 10.1016/j.tws.2008.10.008.

[30] J. Haedir and X. L. Zhao, “Design of short CFRP-reinforced steel tubular columns,” *J. Constr. Steel Res.*, vol. 67, no. 3, pp. 497–509, 2011, doi: 10.1016/j.jcsr.2010.09.005.

[31] K. Narmashiri and G. Mehramiz, “Strengthening of steel hollow pipe sections subjected to transverse loads using CFRP,” *Struct. Eng. Mech.*, vol. 60, no. 1, pp. 163–173, 2016, doi: 10.12989/sem.2016.60.1.163.

[32] M. V. Seica and J. A. Packer, “FRP materials for the rehabilitation of tubular steel structures, for underwater applications,” *Compos. Struct.*, vol. 80, no. 3, pp. 440–450, 2007, doi: 10.1016/j.compstruct.2006.05.029.

[33] J. Haedir, M. Bambach, X. Zhao, and R. Grzebieta, “Bending strength of CFRP-strengthened circular hollow steel sections,” in *3rd International Conference on Composites in Civil Engineering*, 2006.

[34] J. Haedir, M. R. Bambach, X. L. Zhao, and R. H. Grzebieta, “Strength of circular hollow sections (CHS) tubular beams externally reinforced by carbon FRP sheets in pure bending,” *Thin-Walled Struct.*, vol. 47, no. 10, pp. 1136–1147, 2009, doi: 10.1016/j.tws.2008.10.017.

[35] N. K. Photiou, L. C. Hollaway, and M. K. Chryssanthopoulos, “Strengthening of an artificially degraded steel beam utilising a carbon/glass composite system,” *Constr. Build. Mater.*, vol. 20, no. 1–2, pp. 11–21, 2006, doi: 10.1016/j.conbuildmat.2005.06.043.

[36] M. Haghpanahi and H. Pirali, “Hot Spot Stress Determination for a Tubular T-Joint under Combined Axial and Bending Loading,” *Int. J. Eng. Sci.*, vol. 17, no. 3, pp. 21–28, 2006.

[37] W. Wang and Y. Y. Chen, “Hysteretic behaviour of tubular joints under cyclic loading,” *J. Constr. Steel Res.*, vol. 63, no. 10, pp. 1384–1395, 2007, doi: 10.1016/j.jcsr.2006.12.002.

[38] W. Shen and Y. S. Choo, “Stress intensity factor for a tubular T-joint with grouted chord,” *Eng. Struct.*, vol. 35, pp. 37–47, 2012, doi: 10.1016/j.engstruct.2011.10.014.

- [39] R. G. Harwood and E. P. Shuttleworth, "Grouted and mechanical strengthening and repair of tubular steel offshore structures," Technical report; Wimpey Offshore, London (United Kingdom), 1988.
- [40] P. Dallyn, A. El-Hamalawi, A. Palmeri, and R. Knight, "Experimental testing of grouted connections for offshore substructures: A critical review," *Structures*, vol. 3, pp. 90–108, 2015, doi: 10.1016/j.istruc.2015.03.005.
- [41] J. Yang, Y. Shao, and C. Chen, "Static strength of chord reinforced tubular Y-joints under axial loading," *Mar. Struct.*, vol. 29, no. 1, pp. 226–245, 2012, doi: 10.1016/j.marstruc.2012.06.003.
- [42] D. P. Yang, Y. B. Shao, F. Le Long, G. Q. Niu, L. Zhang, and J. B. Zhi, "Static strength of RHS T-joints with reinforced chord under in-plane bending load," *Appl. Mech. Mater.*, vol. 488, pp. 790–794, 2014, doi: 10.4028/www.scientific.net/AMM.488-489.790.
- [43] Y. B. Shao, S. T. Lie, S. P. Chiew, and Y. Q. Cai, "Hysteretic performance of circular hollow section tubular joints with collar-plate reinforcement," *J. Constr. Steel Res.*, vol. 67, no. 12, pp. 1936–1947, 2011, doi: 10.1016/j.jcsr.2011.06.010.
- [44] H. Nassiraei, M. A. Lotfollahi-Yaghin, and H. Ahmadi, "Static strength of collar plate reinforced tubular T/Y-joints under brace compressive loading," *J. Constr. Steel Res.*, vol. 119, pp. 39–49, 2016, doi: 10.1016/j.jcsr.2015.12.011.
- [45] H. Ahmadi, M. A. Lotfollahi-yaghin, and S. Yong-bo, "Experimental and Numerical Investigation of Geometric SCFs in Internally Ring-Stiffened Tubular KT-Joints of Offshore Structures," *J. Persian Gulf*, vol. 43, no. 1, pp. 7–8, 2013.
- [46] H. Ahmadi, M. Ali Lotfollahi-Yaghin, S. Yong-Bo, and M. H. Aminfar, "Parametric study and formulation of outer-brace geometric stress concentration factors in internally ring-stiffened tubular KT-joints of offshore structures," *Appl. Ocean Res.*, vol. 38, pp. 74–91, 2012, doi: 10.1016/j.apor.2012.07.004.
- [47] H. Ahmadi, M. A. Lotfollahi-Yaghin, and S. Yong-Bo, "Chord-side SCF distribution of central brace in internally ring-stiffened tubular KT-joints: A geometrically parametric study," *Thin-Walled Struct.*, vol. 70, pp. 93–105, 2013, doi: 10.1016/j.tws.2013.04.011.
- [48] L. Zhu, S. Han, Q. Song, L. Ma, Y. Wei, and S. Li, "Experimental study of the axial compressive strength of CHS T-joints reinforced with external stiffening rings," *Thin-Walled Struct.*, vol. 98, pp. 245–251, 2016, doi: 10.1016/j.tws.2015.09.029.
- [49] L. Zhu, Y. Zhao, S. Li, Y. Huang, and L. Ban, "Numerical analysis of the axial strength of CHS T-joints reinforced with external stiffeners," *Thin-Walled Struct.*, vol. 85, pp. 481–488, 2014, doi: 10.1016/j.tws.2014.09.018.
- [50] P. S. Prashob, A. P. Shashikala, and T. P. Somasundaran, "Review of existing techniques and fibre reinforced polymers used for strengthening tubular joints," *Struct. Monit. Maint.*, vol. 4, no. 3, pp. 255–268, 2017, doi: 10.12989/smm.2017.4.3.255.

- [51] L. C. Bank, *Composites for construction: structural design with FRP materials*. John Wiley & Sons, 2006.
- [52] Z. G. Xiao and X. L. Zhao, “CFRP repaired welded thin-walled cross-beam connections subject to in-plane fatigue loading,” *Int. J. Struct. Stab. Dyn.*, vol. 12, no. 1, pp. 195–211, 2012, doi: 10.1142/S0219455412004653.
- [53] H. Jiao and X. L. Zhao, “CFRP strengthened butt-welded very high strength (VHS) circular steel tubes,” *Thin-Walled Struct.*, vol. 42, no. 7, pp. 963–978, 2004, doi: 10.1016/j.tws.2004.03.003.
- [54] J. Aguilera and A. Fam, “Bonded FRP Plates for Strengthening Rectangular Hollow Steel Section T-Joints against Web Buckling Induced by Transverse Compression,” *J. Compos. Constr.*, vol. 17, no. 4, pp. 421–432, 2013, doi: 10.1061/(asce)cc.1943-5614.0000311.
- [55] J. Aguilera and A. Fam, “Retrofitting tubular steel T-joints subjected to axial compression in chord and brace members using bonded FRP plates or through-wall steel bolts,” *Eng. Struct.*, vol. 48, pp. 602–610, 2013, doi: 10.1016/j.engstruct.2012.09.018.
- [56] M. Lesani, M. R. Bahaari, and M. M. Shokrieh, “Numerical investigation of FRP-strengthened tubular T-joints under axial compressive loads,” *Compos. Struct.*, vol. 100, pp. 71–78, 2013, doi: 10.1016/j.compstruct.2012.12.020.
- [57] M. Lesani, M. R. Bahaari, and M. M. Shokrieh, “Experimental investigation of FRP-strengthened tubular T-joints under axial compressive loads,” *Constr. Build. Mater.*, vol. 53, pp. 243–252, 2014, doi: 10.1016/j.conbuildmat.2013.11.097.
- [58] M. Lesani, M. R. Bahaari, and M. M. Shokrieh, “FRP wrapping for the rehabilitation of Circular Hollow Section (CHS) tubular steel connections,” *Thin-Walled Struct.*, vol. 90, pp. 216–234, 2015, doi: 10.1016/j.tws.2014.12.013.
- [59] A. S. Hosseini, M. R. Bahaari, and M. Lesani, “SCF distribution in FRP-strengthened tubular T-joints under brace axial loading,” *Sci. Iran.*, vol. 27, no. 3 A, pp. 1113–1129, 2020, doi: 10.24200/SCI.2018.5471.1293.
- [60] A. Sadat Hosseini, M. R. Bahaari, and M. Lesani, “Parametric Study of FRP Strengthening on Stress Concentration Factors in an Offshore Tubular T-Joint Subjected to In-Plane and Out-of-Plane Bending Moments,” *Int. J. Steel Struct.*, vol. 19, no. 6, pp. 1755–1766, 2019, doi: 10.1007/s13296-019-00244-0.
- [61] A. Sadat Hosseini, M. R. Bahaari, and M. Lesani, “Stress concentration factors in FRP-strengthened offshore steel tubular T-joints under various brace loadings,” *Structures*, vol. 20, no. April, pp. 779–793, 2019, doi: 10.1016/j.istruc.2019.07.004.
- [62] A. Sadat Hosseini, M. R. Bahaari, and M. Lesani, “Experimental and parametric studies of SCFs in FRP strengthened tubular T-joints under axially loaded brace,” *Eng. Struct.*, vol. 213, no. October 2019, p. 110548, 2020, doi: 10.1016/j.engstruct.2020.110548.

- [63] H. Nassiraei and P. Rezaeidoost, “Stress concentration factors in tubular T/Y-joints strengthened with FRP subjected to compressive load in offshore structures,” *Int. J. Fatigue*, vol. 140, no. May, p. 105719, 2020, doi: 10.1016/j.ijfatigue.2020.105719.
- [64] H. Nassiraei and P. Rezaeidoost, “Parametric study and formula for SCFs of FRP-strengthened CHS T/Y-joints under out-of-plane bending load,” *Ocean Eng.*, vol. 221, no. May 2020, p. 108313, 2021, doi: 10.1016/j.oceaneng.2020.108313.
- [65] A. Sadat Hosseini, M. R. Bahaari, and M. Lesani, “Formulas for Stress Concentration Factors in T&Y Steel Tubular Joints Stiffened with FRP under Bending Moments,” *Int. J. Steel Struct.*, vol. 22, no. 5, pp. 1408–1432, 2022, doi: 10.1007/s13296-022-00651-w.
- [66] C. P. Pantelides, J. Nadauld, and L. Cercone, “Repair of Cracked Aluminum Overhead Sign Structures with Glass Fiber Reinforced Polymer Composites,” *J. Compos. Constr.*, vol. 7, no. 2, pp. 118–126, 2003, doi: 10.1061/(asce)1090-0268(2003)7:2(118).
- [67] J. D. Nadauld and C. P. Pantelides, “Rehabilitation of Cracked Aluminum Connections with GFRP Composites for Fatigue Stresses,” *J. Compos. Constr.*, vol. 11, no. 3, pp. 328–335, 2007, doi: 10.1061/(asce)1090-0268(2007)11:3(328).
- [68] C. P. Pantelides, “Rehabilitation of cracked aluminum components using fiber-reinforced polymer (FRP) composites,” *Rehabil. Met. Civ. Infrastruct. Using Fiber Reinf. Polym. Compos. Types Prop. Test. Methods*, pp. 201–214, 2014, doi: 10.1533/9780857096654.2.201.
- [69] A. Fam, S. Witt, and S. Rizkalla, “Repair of damaged aluminum truss joints of highway overhead sign structures using FRP,” *Constr. Build. Mater.*, vol. 20, no. 10, pp. 948–956, 2006, doi: 10.1016/j.conbuildmat.2005.06.014.
- [70] Y. Fu, L. Tong, L. He, and X. L. Zhao, “Experimental and numerical investigation on behavior of CFRP-strengthened circular hollow section gap K-joints,” *Thin-Walled Struct.*, vol. 102, pp. 80–97, 2016, doi: 10.1016/j.tws.2016.01.020.
- [71] L. Tong, G. Xu, X. L. Zhao, H. Zhou, and F. Xu, “Experimental and theoretical studies on reducing hot spot stress on CHS gap K-joints with CFRP strengthening,” *Eng. Struct.*, vol. 201, no. October, p. 109827, 2019, doi: 10.1016/j.engstruct.2019.109827.
- [72] G. Xu, L. Tong, X. L. Zhao, H. Zhou, and F. Xu, “Numerical analysis and formulae for SCF reduction coefficients of CFRP-strengthened CHS gap K-joints,” *Eng. Struct.*, vol. 210, no. February, p. 110369, 2020, doi: 10.1016/j.engstruct.2020.110369.
- [73] E. Zavvar, A. Sadat Hosseini, and M. A. Lotfollahi-Yaghin, “Stress concentration factors in steel tubular KT-connections with FRP-Wrapping under bending moments,” *Structures*, vol. 33, no. June, pp. 4743–4765, 2021, doi: 10.1016/j.istruc.2021.06.100.
- [74] A. Sadat Hosseini, E. Zavvar, and H. Ahmadi, “Stress concentration factors in FRP-strengthened steel tubular KT-joints,” *Appl. Ocean Res.*, vol. 108, no. September 2020, 2021, doi: 10.1016/j.apor.2021.102525.

- [75] S. Fawzia, R. Al-Mahaidi, X. L. Zhao, and S. Rizkalla, “Strengthening of circular hollow steel tubular sections using high modulus CFRP sheets,” *Constr. Build. Mater.*, vol. 21, no. 4, pp. 839–845, 2007, doi: 10.1016/j.conbuildmat.2006.06.014.
- [76] P. He and M. Pavlovic, “Feasibility of Wrapped FRP Circular Hollow Section Joints,” in *Proceedings of the 17th International Symposium on Tubular Structures*, 2019, pp. 292–299. doi: 10.3850/978-981-11-0745-0_043-cd.
- [77] W. Feng and M. Pavlovic, “Fatigue behaviour of non-welded wrapped composite joints for steel hollow sections in axial load experiments,” *Eng. Struct.*, vol. 249, no. October, p. 113369, 2021, doi: 10.1016/j.engstruct.2021.113369.
- [78] P. He and M. Pavlovic, “Failure modes of bonded wrapped composite joints for steel circular hollow sections in ultimate load experiments,” *Eng. Struct.*, vol. 254, no. August 2021, p. 113799, 2022, doi: 10.1016/j.engstruct.2021.113799.
- [79] P. He, W. Feng, and M. Pavlovic, “Influence of steel yielding and resin toughness on debonding of wrapped composite joints,” *Compos. Struct.*, vol. 312, no. February, p. 116862, 2023, doi: 10.1016/j.compstruct.2023.116862.
- [80] M. P. Weikang Feng, Pei He, “Interfacial fatigue debonding retardation in wrapped composite joints : experimental and numerical study,” *Compos. Struct.*, vol. 319, no. April, p. 117146, 2023, doi: 10.1016/j.compstruct.2023.117146.
- [81] X. L. Zhao and L. Zhang, “State-of-the-art review on FRP strengthened steel structures,” *Eng. Struct.*, vol. 29, no. 8, pp. 1808–1823, 2007, doi: 10.1016/j.engstruct.2006.10.006.
- [82] W. Wang, R. Lopes Fernandes, S. Teixeira De Freitas, D. Zarouchas, and R. Benedictus, “How pure mode I can be obtained in bi-material bonded DCB joints: A longitudinal strain-based criterion,” *Compos. Part B Eng.*, vol. 153, no. July, pp. 137–148, 2018, doi: 10.1016/j.compositesb.2018.07.033.
- [83] G. Irwin, *Analysis of stresses and strains near the end of a crack traversing a plate*. 1957. Accessed: Jan. 18, 2023. [Online]. Available: <https://asmedigitalcollection.asme.org/appliedmechanics/article-abstract/24/3/361/1111028>
- [84] “Mechanical properties of engineered materials | WorldCat.org.” <https://worldcat.org/zh-cn/title/300921090> (accessed Jan. 18, 2023).
- [85] M. Janssen, J. Zuidema, and R. Wanhill, “Fracture Mechanics,” Aug. 2004, doi: 10.1201/9781482265583.
- [86] K. N. Anyfantis, “Finite element predictions of composite-to-metal bonded joints with ductile adhesive materials,” *Compos. Struct.*, vol. 94, no. 8, pp. 2632–2639, 2012, doi: 10.1016/j.compstruct.2012.03.002.
- [87] M. Rask and B. F. Sørensen, “Determination of the J integral for laminated double cantilever beam specimens: The curvature approach,” *Eng. Fract. Mech.*, vol. 96, pp.

- 37–48, 2012, doi: 10.1016/j.engfracmech.2012.06.017.
- [88] R. C. Alderliesten, J. Schijve, and S. van der Zwaag, “Application of the energy release rate approach for delamination growth in Glare,” *Eng. Fract. Mech.*, vol. 73, no. 6, pp. 697–709, 2006, doi: 10.1016/j.engfracmech.2005.10.006.
- [89] G. R. Irwin, “Elasticity and Plasticity,” 1958.
- [90] J. G. Williams, “On the calculation of energy release rates for cracked laminates,” *Int. J. Fract.*, vol. 36, no. 2, pp. 101–119, 1988, doi: 10.1007/BF00017790.
- [91] E. F. Rybicki and M. F. Kanninen, “A finite element calculation of stress intensity factors by a modified crack closure integral,” *Eng. Fract. Mech.*, vol. 9, no. 4, pp. 931–938, 1977, doi: 10.1016/0013-7944(77)90013-3.
- [92] M. F. S. F. de Moura, R. D. S. G. Campilho, and J. P. M. Gonçalves, “Pure mode II fracture characterization of composite bonded joints,” *Int. J. Solids Struct.*, vol. 46, no. 6, pp. 1589–1595, 2009, doi: 10.1016/j.ijsolstr.2008.12.001.
- [93] M. Shahverdi, A. P. Vassilopoulos, and T. Keller, “Mixed-Mode I/II fracture behavior of asymmetric adhesively-bonded pultruded composite joints,” *Eng. Fract. Mech.*, vol. 115, pp. 43–59, 2014, doi: 10.1016/j.engfracmech.2013.11.014.
- [94] J. H.-M. interfaces and undefined 1990, “Mixed mode fracture mechanics of interfaces,” *web-static-aws.seas.harvard.edu*, Accessed: Jan. 19, 2023. [Online]. Available: <http://web-static-aws.seas.harvard.edu/hutchinson/papers/404.pdf>
- [95] M. Shahverdi, A. P. Vassilopoulos, and T. Keller, “Mixed-Mode I/II fracture behavior of asymmetric composite joints,” *Procedia Struct. Integr.*, vol. 2, pp. 1886–1893, 2016, doi: 10.1016/j.prostr.2016.06.237.
- [96] R. A. Schapery and B. D. Davidson, “Prediction of energy release rate for mixed-mode delamination using classical plate theory,” *Appl. Mech. Rev.*, vol. 43, no. 5, pp. S281–S287, 1990, doi: 10.1115/1.3120829.
- [97] J. Wang and P. Qiao, “On the energy release rate and mode mix of delaminated shear deformable composite plates,” *Int. J. Solids Struct.*, vol. 41, no. 9–10, pp. 2757–2779, 2004, doi: 10.1016/j.ijsolstr.2003.11.039.
- [98] M. M. Arouche, W. Wang, and S. T. De Freitas, “Strain-based methodology for mixed-mode I + II fracture : A new partitioning method for bi- material adhesively bonded joints,” *J. Adhes.*, vol. 95, no. 5–7, pp. 385–404, 2019, doi: 10.1080/00218464.2019.1565756.
- [99] W. Wang, S. T. De Freitas, J. A. Poulis, and D. Zarouchas, “A review of experimental and theoretical fracture characterization of bi-material bonded joints,” *Compos. Part B Eng.*, vol. 206, no. October 2020, p. 108537, 2021, doi: 10.1016/j.compositesb.2020.108537.
- [100] ASTM International, “ASTM D5528 - 13: 2014 - Standard Test Method for Mode I Interlaminar Fracture Toughness of Unidirectional Fiber-Reinforced Polymer Matrix

Composites 1,” *West Conshohocken, PA ASTM Int.*, doi: 10.1520/D5528-13.

[101] International Standards Organization, “ISO 15024:2001 Fibre-reinforced plastic composites -- Determination of mode I interlaminar fracture toughness, GIC, for unidirectionally reinforced material,” 2001. <https://www.iso.org/standard/25581.html> (accessed Jan. 20, 2023).

[102] S. Azari, A. Ameli, M. Papini, and J. K. Spelt, “Analysis and design of adhesively bonded joints for fatigue and fracture loading: A fracture-mechanics approach,” *J. Adhes. Sci. Technol.*, vol. 27, no. 15, pp. 1681–1711, 2013, doi: 10.1080/01694243.2012.748434.

[103] G. Ji, Z. Ouyang, G. Li, S. Ibekwe, and S. S. Pang, “Effects of adhesive thickness on global and local mode-I interfacial fracture of bonded joints,” *Int. J. Solids Struct.*, vol. 47, no. 18–19, pp. 2445–2458, 2010, doi: 10.1016/j.ijsolstr.2010.05.006.

[104] M. M. Shokrieh, M. Heidari-Rarani, and M. R. Ayatollahi, “Interlaminar fracture toughness of unidirectional DCB specimens: A novel theoretical approach,” *Polym. Test.*, vol. 31, no. 1, pp. 68–75, 2012, doi: 10.1016/j.polymertesting.2011.08.012.

[105] M. Cabello, A. Turon, J. Zurbitu, J. Renart, C. Sarrado, and F. Martínez, “Progressive failure analysis of DCB bonded joints using a new elastic foundation coupled with a cohesive damage model,” *Eur. J. Mech. A/Solids*, vol. 63, pp. 22–35, 2017, doi: 10.1016/j.euromechsol.2016.12.004.

[106] Z. Jiang, S. Wan, and Z. Wu, “Calculation of energy release rate for adhesive composite/metal joints under mode-I loading considering effect of the non-uniformity,” *Compos. Part B Eng.*, vol. 95, pp. 374–385, 2016, doi: 10.1016/j.compositesb.2016.04.001.

[107] M. Khoshrovan and F. Asgari Mehrabadi, “Fracture analysis in adhesive composite material/aluminum joints under mode-I loading; Experimental and numerical approaches,” *Int. J. Adhes. Adhes.*, vol. 39, pp. 8–14, 2012, doi: 10.1016/j.ijadhadh.2012.06.005.

[108] R. G. Boeman, D. L. Erdman, L. B. Klett, and R. D. Lomax, “A practical test method for mode I fracture toughness of adhesive joints with dissimilar substrates,” *SAMPE-ACCE-DOE Adv. Compos. Conf.*, pp. 1–9, 1999.

[109] K. Shimamoto, Y. Sekiguchi, and C. Sato, “Effects of surface treatment on the critical energy release rates of welded joints between glass fiber reinforced polypropylene and a metal,” *Int. J. Adhes. Adhes.*, vol. 67, pp. 31–37, 2016, doi: 10.1016/j.ijadhadh.2015.12.022.

[110] K. Shimamoto, Y. Sekiguchi, and C. Sato, “The Critical Energy Release Rate of Welded Joints between Fiber-Reinforced Thermoplastics and Metals When Thermal Residual Stress is Considered,” *J. Adhes.*, vol. 92, no. 4, pp. 306–318, 2016, doi: 10.1080/00218464.2015.1031339.

[111] Z. Ouyang, G. Ji, and G. Li, “On approximately realizing and characterizing pure

mode-I interface fracture between bonded dissimilar materials,” *J. Appl. Mech. Trans. ASME*, vol. 78, no. 3, 2011, doi: 10.1115/1.4003366.

[112] Z. Ouyang, G. Ji, G. Li, S. Ibekwe, and S. Pang, “A new idea of pure mode-I fracture test of bonded bi-materials,” in *Proceedings of the ASME 2010 Pressure Vessels & Piping Division / K-PVP Conference*, 2010.

[113] G. Zambelis, T. Da Silva Botelho, O. Klinkova, I. Tawfiq, and C. Lanouette, “Evaluation of the energy release rate in mode I of asymmetrical bonded composite/metal assembly,” *Eng. Fract. Mech.*, vol. 190, pp. 175–185, 2018, doi: 10.1016/j.engfracmech.2017.12.007.

[114] ASTM International, “ASTM D7905/D7905M-14: Standard Test Method for Determination of the Mode II Interlaminar Fracture Toughness of Unidirectional Fiber-Reinforced Polymer,” *West Conshohocken, PA ASTM Int.*, 2014, doi: 10.1520/D7905.

[115] H. Ning *et al.*, “Investigation on mode-II interface fracture toughness of CFRP/Al laminates toughened by VGCF interleaves,” *J. Mater. Sci.*, vol. 50, no. 4, pp. 1915–1923, 2015, doi: 10.1007/s10853-014-8755-5.

[116] Z. Ouyang and G. Li, “Nonlinear interface shear fracture of end notched flexure specimens,” *Int. J. Solids Struct.*, vol. 46, no. 13, pp. 2659–2668, 2009, doi: 10.1016/j.ijsolstr.2009.02.011.

[117] P. Davidson, A. M. Waas, and C. S. Yerramalli, “Experimental determination of validated, critical interfacial modes I and II energy release rates in a composite sandwich panel,” *Compos. Struct.*, vol. 94, no. 2, pp. 477–483, 2012, doi: 10.1016/j.compstruct.2011.08.007.

[118] C. Alía, J. M. Arenas, J. C. Suárez, J. J. Narbón, and R. Ocaña, “ENF test in the adhesive bonding of aluminium-composite joints and evaluation of its reliability with Weibull distribution,” *J. Adhes. Sci. Technol.*, vol. 27, no. 11, pp. 1236–1246, 2013, doi: 10.1080/01694243.2012.736853.

[119] C. Alía, J. M. Arenas, J. C. Suárez, R. Ocaña, and J. J. Narbón, “Mode II fracture energy in the adhesive bonding of dissimilar substrates: Carbon fibre composite to aluminium joints,” *J. Adhes. Sci. Technol.*, vol. 27, no. 22, pp. 2480–2494, 2013, doi: 10.1080/01694243.2013.787516.

[120] J. M. Arenas, R. Ocaña, C. Alía, J. J. Narbón, and M. Islán, “Fracture energy in structural adhesive joints of composite-aluminum under adverse environments conditions,” *J. Adhes. Sci. Technol.*, vol. 28, no. 2, pp. 201–214, 2014, doi: 10.1080/01694243.2013.833404.

[121] R. H. Martin and B. D. Davidson, “Mode II fracture toughness evaluation using four point bend, end notched flexure test,” *Plast. Rubber Compos. Process. Appl.*, vol. 28, no. 8, pp. 401–406, 1999, doi: 10.1179/146580199101540565.

[122] J. H. Crews and J. R. Reeder, “A mixed-mode bending apparatus for delamination testing,” *NASA Ames Res. Cent.*, vol. 1000, 1988.

- [123] J. R. Reeder and J. H. Crews, “Nonlinear Analysis and Redesign of the Mixed-Mode Bending Delamination Test,” *Nasa Tech. Memo.*, vol. 91–19482, no. 102777, pp. 1–44, 1991.
- [124] ASTM-D6671, “Standard Test Method for Mixed Mode I-Mode II Interlaminar Fracture Toughness of Unidirectional Fiber Reinforced Polymer Matrix Composites,” *ASTM Int.*, no. Mode I, p. 15, 2013.
- [125] M. Shahverdi, A. P. Vassilopoulos, and T. Keller, “Mixed-mode quasi-static failure criteria for adhesively-bonded pultruded GFRP joints,” *Compos. Part A Appl. Sci. Manuf.*, vol. 59, pp. 45–56, 2014, doi: 10.1016/j.compositesa.2013.12.007.
- [126] M. Ševčík, M. Shahverdi, P. Hutař, and A. P. Vassilopoulos, “Analytical modeling of mixed-Mode bending behavior of asymmetric adhesively bonded pultruded GFRP joints,” *Eng. Fract. Mech.*, vol. 147, pp. 228–242, 2015, doi: 10.1016/j.engfracmech.2015.08.040.
- [127] M. Elices, G. V. Guinea, J. Gómez, and J. Planas, “The cohesive zone model: Advantages, limitations and challenges,” *Eng. Fract. Mech.*, vol. 69, no. 2, pp. 137–163, 2001, doi: 10.1016/S0013-7944(01)00083-2.
- [128] A. Hillerborg, M. Modeer, and P. E. Petersson, “Analysis of crack formation and crack growth in concrete by means of fracture mechanics and finite elements,” *Am. Concr. Institute, ACI Spec. Publ.*, vol. SP-249, pp. 225–237, 1976.
- [129] P. Papanastasiou and E. Sarris, *Cohesive zone models*. Elsevier Ltd, 2017. doi: 10.1016/B978-0-08-100781-5.00006-3.
- [130] A. Cameselle-Molares, A. P. Vassilopoulos, J. Renart, A. Turon, and T. Keller, “Numerical simulation of two-dimensional in-plane crack propagation in FRP laminates,” *Compos. Struct.*, vol. 200, no. April, pp. 396–407, 2018, doi: 10.1016/j.compstruct.2018.05.136.
- [131] M. Heidari-Rarani, M. M. Shokrieh, and P. P. Camanho, “Finite element modeling of mode I delamination growth in laminated DCB specimens with R-curve effects,” *Compos. Part B Eng.*, vol. 45, no. 1, pp. 897–903, 2013, doi: 10.1016/j.compositesb.2012.09.051.
- [132] M. M. Shokrieh, M. Heidari-Rarani, and M. R. Ayatollahi, “Delamination R-curve as a material property of unidirectional glass/epoxy composites,” *Mater. Des.*, vol. 34, pp. 211–218, 2012, doi: 10.1016/j.matdes.2011.08.006.
- [133] B. Ghiassi, J. Xavier, D. V. Oliveira, and P. B. Lourenço, “Application of digital image correlation in investigating the bond between FRP and masonry,” *Compos. Struct.*, vol. 106, pp. 340–349, 2013, doi: 10.1016/j.compstruct.2013.06.024.
- [134] P. Zhang, D. Lei, Q. Ren, J. He, H. Shen, and Z. Yang, “Experimental and numerical investigation of debonding process of the FRP plate-concrete interface,” *Constr. Build. Mater.*, vol. 235, p. 117457, 2020, doi: 10.1016/j.conbuildmat.2019.117457.

- [135] M. Ali-Ahmad, K. Subramaniam, and M. Ghosn, “Experimental Investigation and Fracture Analysis of Debonding between Concrete and FRP Sheets,” *J. Eng. Mech.*, vol. 132, no. 9, pp. 914–923, 2006, doi: 10.1061/(asce)0733-9399(2006)132:9(914).
- [136] H. T. Wang, G. Wu, Y. Y. Pang, J. W. Shi, and H. M. Zakari, “Experimental study on the bond behavior between CFRP plates and steel substrates under fatigue loading,” *Compos. Part B Eng.*, vol. 176, no. January, p. 107266, 2019, doi: 10.1016/j.compositesb.2019.107266.
- [137] B. Zheng and M. Dawood, “Debonding of Carbon Fiber–Reinforced Polymer Patches from Cracked Steel Elements under Fatigue Loading,” *J. Compos. Constr.*, vol. 20, no. 6, pp. 1–13, 2016, doi: 10.1061/(asce)cc.1943-5614.0000694.
- [138] O. Z. Ajmal, “The use of digital image correlation to monitor delaminations in composite structures,” PhD Dissertation, University of Surrey, 2018.
- [139] G. Szebényi and V. Hliva, “Detection of delamination in polymer composites by digital image correlation-experimental test,” *Polymers*, vol. 11, no. 3, 2019. doi: 10.3390/polym11030523.
- [140] Z. P. Bažant, “Size effect on structural strength: a review,” *Arch. Appl. Mech.*, vol. 69, 1999.
- [141] Q. Yu *et al.*, “Scaling of strength of metal-composite joints-Part I: Experimental investigation,” *J. Appl. Mech. Trans. ASME*, vol. 77, no. 1, pp. 1–8, 2010, doi: 10.1115/1.3172254.
- [142] Z. P. Bažant, “Size Effect in Blunt Fracture: Concrete, Rock, Metal,” *J. Eng. Mech.*, vol. 110, no. 4, pp. 518–535, 1984, doi: 10.1061/(asce)0733-9399(1984)110:4(518).
- [143] J. L. Le, Z. P. Bažant, and Q. Yu, “Scaling of strength of metal-composite joints-Part II: Interface fracture analysis,” *J. Appl. Mech. Trans. ASME*, vol. 77, no. 1, pp. 1–7, 2010, doi: 10.1115/1.3172152.
- [144] Q. Yu, Z. P. Bažant, and J. L. Le, “Scaling of strength of metal-composite joints - Part III: Numerical simulation,” *J. Appl. Mech. Trans. ASME*, vol. 80, no. 5, pp. 1–4, 2013, doi: 10.1115/1.4023643.

3. ULTIMATE LOAD JOINT EXPERIMENTS

This chapter presents the results of the ultimate load experiments conducted on wrapped composite joints, aiming to identify the debonding failure mechanism. In Section 3.7, the results of monotonic tensile tests of wrapped composite A-joints are presented. The aim is to quantify the influence of the production parameters (bonding primer, resin toughness, steel grade) on the debonding resistance.

Moving on to Section 3.8, the failure modes of wrapped composite X-joints subjected to tensile, compressive, and in-plane bending load are characterized. Two scales of X-joints are tested under monotonic tensile load to identify the size effects on the debonding behavior.

In the aforementioned experimental work, the debonding length of the joints is quantified through the analysis of the surface strain monitored using the digital image correlation (DIC) technique.

Part of this chapter has been published as two journal articles:

- [1] P. He, W. Feng, and M. Pavlovic, "Influence of steel yielding and resin toughness on debonding of wrapped composite joints", *Compos. Struct.*, vol. 312, no. February, p. 116862, 2023, doi: 10.1016/j.compstruct.2023.116862.
- [2] P. He and M. Pavlovic, "Failure modes of bonded wrapped composite joints for steel circular hollow sections in ultimate load experiments", *Eng. Struct.*, vol. 254, no. August 2021, p. 113799, 2022, doi: 10.1016/j.engstruct.2021.113799.

3.1 Introduction

Good debonding resistance of the bonded interface is an essential prerequisite for good static behavior of adhesively bonded joints, which can be realized by appropriate surface treatment and selection of adhesives. Surface treatments are often required to provide maximum adhesion strength, not only to remove contaminants, but also to increase the difference in surface energy between adhesive and substrate, so good wetting and adsorption of the adhesive is obtained[1]. Surface treatments for steel include solvent degreasing, abrasion, grit blasting[2]–[6], use of bonding primers[7]–[11], etc. Adhesive types also have a significant influence on the bonding quality. The load-bearing capacity is inevitably affected by ductility of adhesives[12]–[14]. However, current studies are only limited to the influence of surface treatment and adhesive types on the behavior of adhesively bonded joints. Further study is needed to characterize their influence on the behavior of novel wrapped composite joints that are directly bonded (laminated) where thin resin layer plays the role of the adhesive. Moreover, the influence of steel grade on the joint resistance should be investigated where high-strength steel has the potential to enhance bonding resistance by preventing yielding of the steel cross section which showed to interact with the debonding process[15].

Understanding debonding failure of wrapped composite joints is the relevant knowledge gap to solve. A major problem in characterizing debonding behavior is the complexity resulting from the variety of possible failure modes[16]: 1) rupture of composite material; 2) delamination of composites; 3) debonding of the bonded interface; 4) yielding of steel tubes. Therefore, it is imperative to conduct the ultimate load joint experiments to explicitly learn the relevant failure modes of wrapped composite joints. The joints experiments should be conducted prior to the material and interface experiments aiming to provide the opportunity to select which kind of material and interface experiments need to be designed and conducted. Accordingly, the joint experiments are presented first in Chapter 3 followed by relevant material and interface experiments in Chapter 4.

3.2 Motivation behind the experimental campaign

Aiming to quantify and identify the influence of production parameters (i.e., application of bonding primer, polymer resin types and steel grade) on the debonding resistance of wrapped composite joints, A-joint geometry, namely uniaxial splice joint, is chosen and tested in monotonic tensile load until failure. Selection of this uniaxial and axisymmetric geometry is attributed to ease of production, and the opportunity for clear interpretation of mechanical behavior of the bonding in a simple load condition. A-joint specimens wrapped with and without application of the bonding primer are compared to quantify the influence of difference in chemical bonding properties on the debonding resistance of the joint. Three types of thermoset polymer resins designated as resin 1 and 2 – both vinyl-ester based and resin 3 – polyester based, are used in the wrapping procedure to investigate the impact of fracture toughness of resins on the joint resistance. Resin 2 has improved fracture toughness properties compared to resin 1 and resin 3. Mild steel (S355) and high-strength steel (S700) circular hollow sections are used in

production of A-joint specimens to quantify the influence of interaction between debonding and steel yielding on the static resistance of the wrapped composite joints.

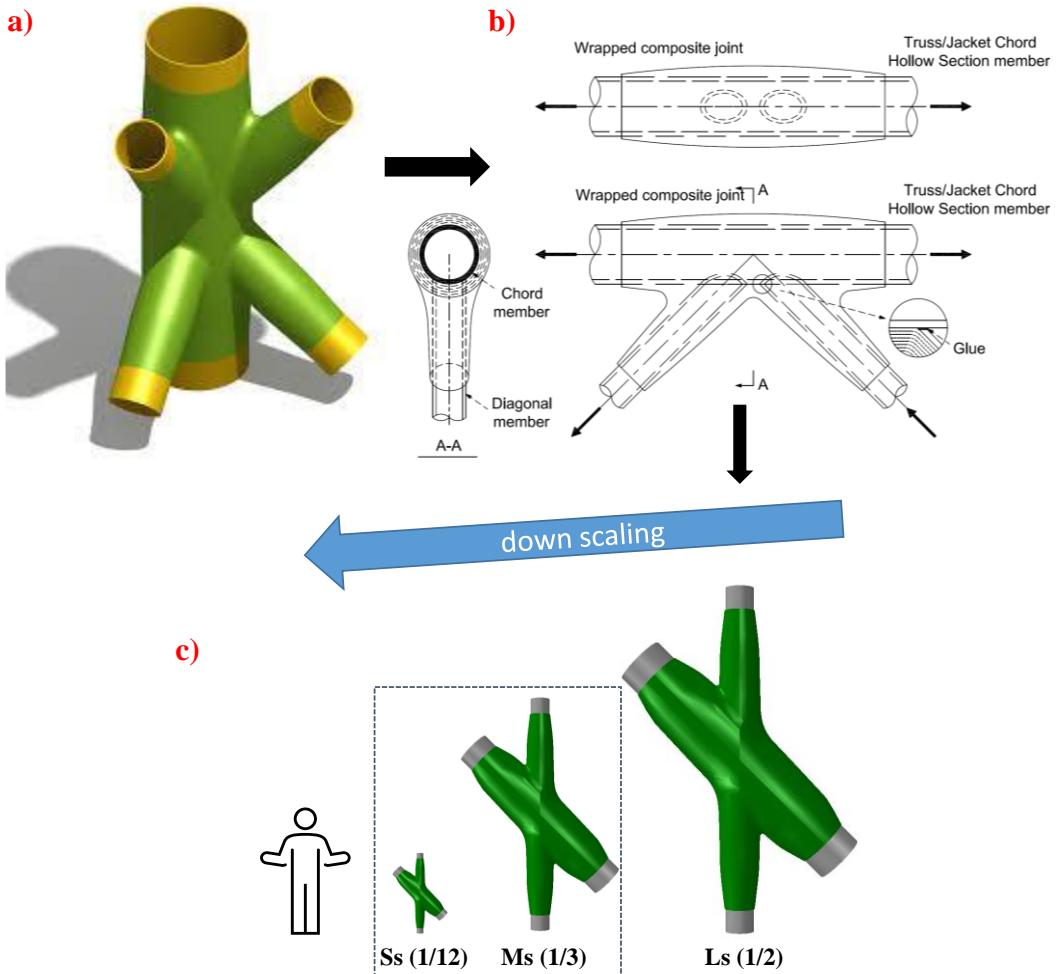


Figure 3-1 Schematic zoom in from full-scale K-K joint to small-scale 45° X-joint: a) full-scale K-K joint; b) full-scale K-joint; c) downscaling from large-scale to small-scale 45° X-joint.

In offshore jackets, wrapped composite K-K joint is prone to tensile fatigue failure while T-T joint suffers from bending fatigue. The K-K joint and the T-T joint geometry are simplified to K-joint and T-joint shapes, respectively, to limit load conditions to uniplanar tension and in-plane bending, aiming to make it easier to understand debonding. In the design of lab experiments, the K-joint geometry is designed as 2Y 45° joints with comparable stress concentration while 2T joints are used which can be regarded as two identical T joints. These two geometries are helpful to set up tensile and in-plane bending experiments, respectively. For simplification of nomenclature in

representing test results, the 2Y 45° joints are further named as 45° X-joints. Similarly, the 2T joints are named as 90° X-joints. Due to limitations of laboratory machines in terms of load capacity and clamping devices, the full-scale geometry of the designed joints is downscaled to 1/12 as the small-scale geometry with diameter ratio $d_1/d_0 = 60/108 = 0.56$. d_1 and d_0 are the diameter of the brace and the chord members, respectively. At small-scale, 45° and 90° X-joints connected by composite wrap and welding are compared in tensile and in-plane bending experiments, respectively, for stiffness, elastic limit and ultimate load comparisons. In addition, medium-scale 45° wrapped composite X-joint is designed by upscaling the brace diameter in small-scale to almost 4 times, reaching 1/3 of the full-scale size. This is to investigate size effect on the debonding behavior of wrapped composite joints.

Figure 3-1 illustrates the schematic zoom-in process, showcasing the design evolution of the wrapped composite K-K joint from its initial form to the small-scale and the medium-scale 45° X-joints in joint experiments. Figure 3-2 shows configuration of the small-scale 45° X-joints used to learn the debonding failure modes and of the small-scale A-joints used to identify influence of production parameters on debonding resistance.



Figure 3-2 Composite wrapped small-scale a) 45° X-joint with Ø 60 mm braces[15] and b) A-joint with Ø 60 mm steel tubes in lab tests[17].

3.3 Overview of CHS joints in the ultimate load joint experiments

Based on the above-mentioned motivation behind the experimental campaign, 7 types of geometries of CHS joints are designed in the ultimate load joint experiments, as summarized in Table 3-1. Geometries with dimensions of CHS joints are shown in Figure 3-3. The main differences of the A-joint geometry in joint type 1 and type 2 as shown in Figure 3-3 a) and Figure 3-3 b), respectively, are the length of the weld at the end detail and the diameter of the steel tubes. Longer weld is used for geometry of joint type 2 where the high strength steel specimens are compared to mild steel specimens. 45° and

90° X joints in small-scale are composed of two CHS 60.3/4 brace members and one CHS 108/5 chord member. 45° X joints in medium-scale consist of two CHS 219/6 brace members and one CHS 324/10 chord member. The joint dimensions in medium-scale are 30% of the real-scale in off-shore jacket supporting structures for wind turbines, where the brace and chord members are typically within 600~1200 mm range in diameter. 45° and 90° X joints in small-scale are connected by either traditional welding technique or by wrapped composite joining (bonding through the composite wrap – i.e., no welding). Chord and brace members in 45° X joints of medium-scale are only connected by wrapped composite joining.

The main objectives of the ultimate load joint experiments are defined:

1) to identify governing failure modes, load transfer mechanism, elastic limit and ultimate load of wrapped composite joints X-joints loaded in tension (45° X-joints), compression (45° X-joints) and in-plane bending (90° X-joints).

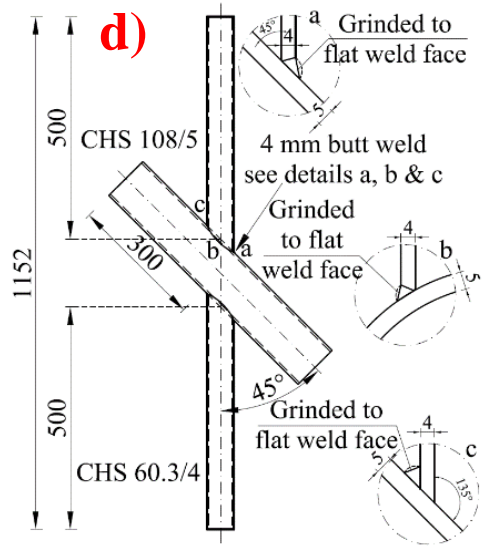
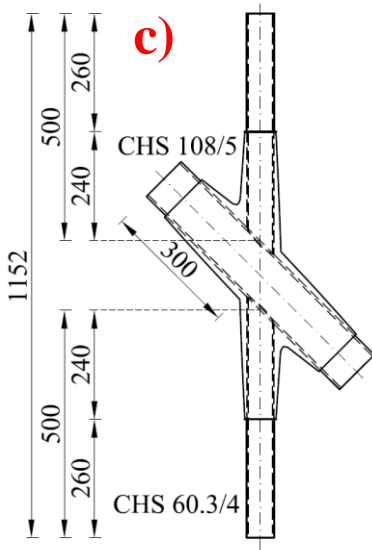
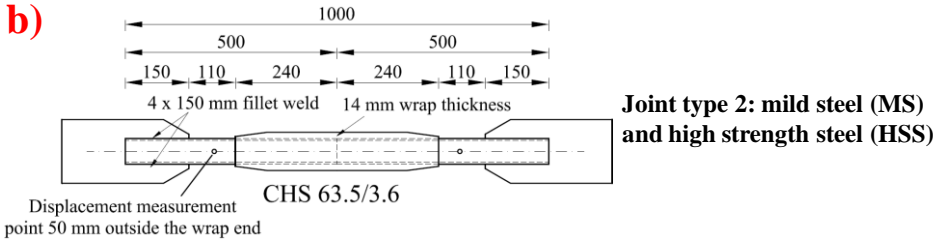
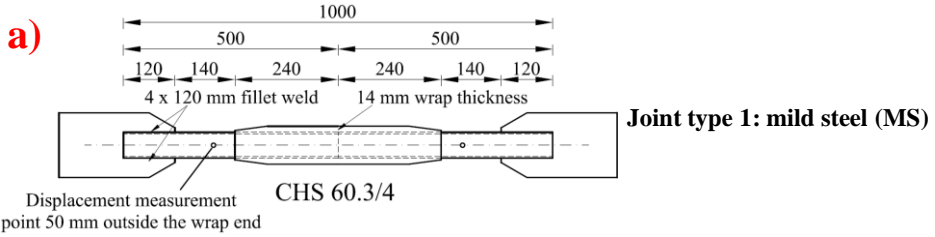
2) to understand differences in failure modes of wrapped composite 45° X-joints at two different scales (small-scale and medium-scale) to investigate size effect on the debonding behavior of wrapped composite joints.

3) to compare tensile static behavior of wrapped composite 45° X-joints vs. welded counterparts and bending static behavior of composite 90° X-joints vs. welded counterparts.

4) to investigate the influence of production parameters on the debonding behavior of wrapped composite joints, including effect of bonding primer, resin toughness and steel yielding.

Table 3-1 Overview of geometries of CHS joints in ultimate load experiments

Joint type	Joint description	Geometry in Figure number
1	Wrapped composite A-joints in small-scale with cross section 60.3/4	Figure 3-3 a)
2	Wrapped composite A-joints in small-scale with cross section 63.5/3.6	Figure 3-3 b)
3	Wrapped composite 45° X-joints in small-scale	Figure 3-3 c)
4	Welded 45° X-joints in small-scale	Figure 3-3 d)
5	Wrapped composite 90° X-joints in small-scale	Figure 3-3 e)
6	Welded 90° X-joints in small-scale	Figure 3-3 f)
7	Wrapped composite 45° X-joints in medium-scale	Figure 3-3g)



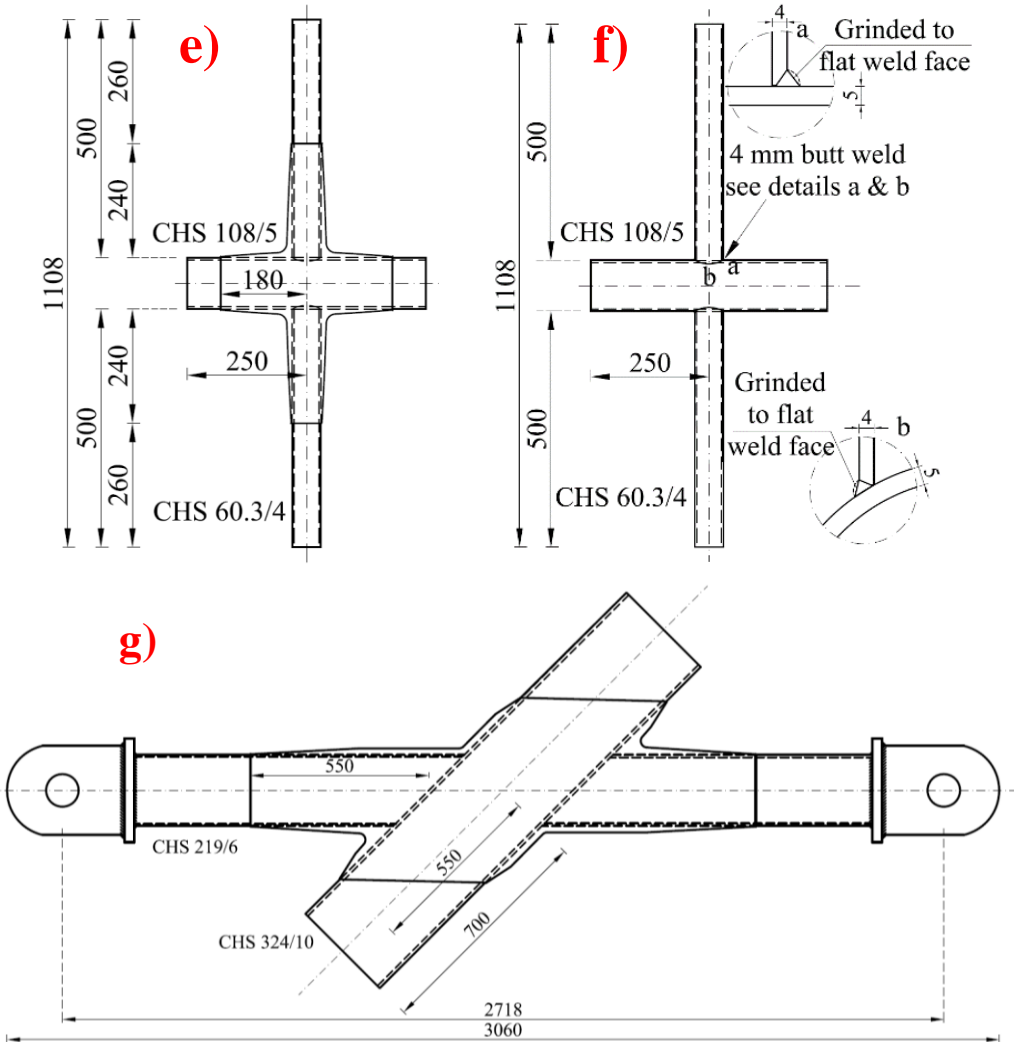


Figure 3-3 Geometries of CHS joints in ultimate load experiments: wrapped composite A-joint with a) type 1 and b) type 2 geometry; wrapped composite c) 45° and e) 90° X-joints in small-scale; welded d) 45° and f) 90° X-joints in small-scale; g) wrapped composite 45° X-joints in medium-scale.

3.4 Production of CHS joints

The CHS profiles of all specimens are made of mild steel with grade S355, except the A-joints made of high strength steel (grade S700). For welded joints, the brace and chord members are connected by single-sided full penetration weld with 4-mm thickness followed by grinding weld toes to improve fatigue endurance, as shown in Figure 3-3. For wrapped composite joints, CHS tubes are connected by E-Glass fiber mixed with thermoset resin with volumetric fraction ranging 30-32% and wrapped (laminated) around steel hollow sections. Three types of thermoset polymer resin (resin 1, resin 2

and resin 3) are used in production of wrapped composite A-joints to investigate its influence on bonding resistance, and the resin leading to optimum bonding quality (resin 2) is used in production of wrapped composite X-joints. It should be noted that the composite wrap is directly bonded on the steel tubes without application of intermediate adhesive layer so that the failure mode related to adhesive is eliminated. Steel tubes are grit blasted and chemically degreased as surface preparation prior to wrapping to ensure good bonding strength between the composite wrap and the steel tubes. The alignment of the steel tubes is controlled to be less than 0.5 mm misalignment. The hand lamination (wrapping) procedure is fulfilled in a couple of steps with quality control to ensure smooth thickness transition, good compaction and avoiding air gaps. The thickness of the composite wrap is maximum at the joint root with a value of 14 mm and 23 mm in small and medium-scale, respectively, and decreases to 0 mm at the end of the bonded connection, see Figure 3-3. No post-curing is applied to the wrapped specimens. The repeatability of the production is assured by using only certified laminators in the factory where the joints are produced. Temperature, humidity, surface roughness and cleans, peroxide type and content, the resin shell and the cleans of the glass fiber and mats are strictly controlled through the quality control and assurance programme.

E-Glass fiber is composed of bidirectional woven fabric and chopped strand mat to perform quasi-isotropic behavior. Mechanical properties of the mild steel and the composite material determined in case of resin 2 are summarized in Table 3-2. The standard tensile/compressive/in-plane shear coupon tests are conducted to obtain these material properties based on ISO standard[18]–[22].

Table 3-2 Mechanical properties of the composite wrap laminate produced with resin 2

Material	Mechanical properties	Average value (and CoV [%])	Standard
Mild steel	Tensile modulus – E	210000 MPa (5.74)	ISO 6892-1[18]
	Yield strength – σ_e	360.91 MPa (4.86)	
Composite	In-plane tensile strength in x/y direction – $f_{x,t}=f_{y,t}$	216 MPa (5.78)	ISO 527-1[19] and 527-2 [20]
	In-plane tensile modulus in x/y direction – $E_{x,t}=E_{y,t}$	11798 MPa (6.37)	
	In-plane compressive strength in x/y direction – $f_{x,c}=f_{y,c}$	200 MPa (3.79)	ISO 14126[21]
	In-plane compressive modulus in x/y direction – $E_{x,c}=E_{y,c}$	12077 MPa (4.50)	
	In-plane shear strength – $f_{xy,v}$	72.2 MPa (2.59)	ISO 14129[22]
	In-plane shear modulus – G_{xy}	3120 MPa (6.81)	

3.5 Measurement technique

Two measurement techniques are used in the ultimate load joint experiments. In experiments of joint type 1, the measurement system based on two Linear Variable Differential Transformers (LVDTs) at front and back is used to capture potential eccentricity and average the data, as shown in Figure 3-4a). The displacement of the A-

joint specimen is equal to the extension of the aluminum bracket clamped to both sides of the CHS members outside the wrapped region by preloading, which is measured by two LVDTs attached through the plastic clip. In experiments of joint type 2~8, the 3-dimensional (3D) Digital Image Correlation (DIC) system is used to measure both longitudinal extension between ends of the specimens and distribution of surface strain of the joints to indirectly track the propagation of the debonding crack, as shown in Figure 3-4b)~e). GOM Aramis adjustable base 12MPx system is used which includes two cameras with 12-megapixel resolution, controller and graphical analysis software to acquire and process test data. It enables recording of strain distribution and crack initiation/propagation on the specimen surface during the experiments, and processing of measurement data with high accuracy and pertinence after the experiments. Two measuring volumes are used corresponding to wrapped composite joints in two geometric scales. The $1900 \times 1400 \times 1400 \text{ mm}^3$ measuring volume is utilized in the medium-scale test, while the $750 \times 610 \times 610 \text{ mm}^3$ measuring volume is used in the small-scale tension, compression and bending tests. Speckle patterns are applied on the specimens' surface by spray method with grain size of approximately 2 and 4 mm in small-scale and medium-scale experiments, respectively. Polarized blue light is used to limit the influence of variation of ambient light on measurement accuracy.

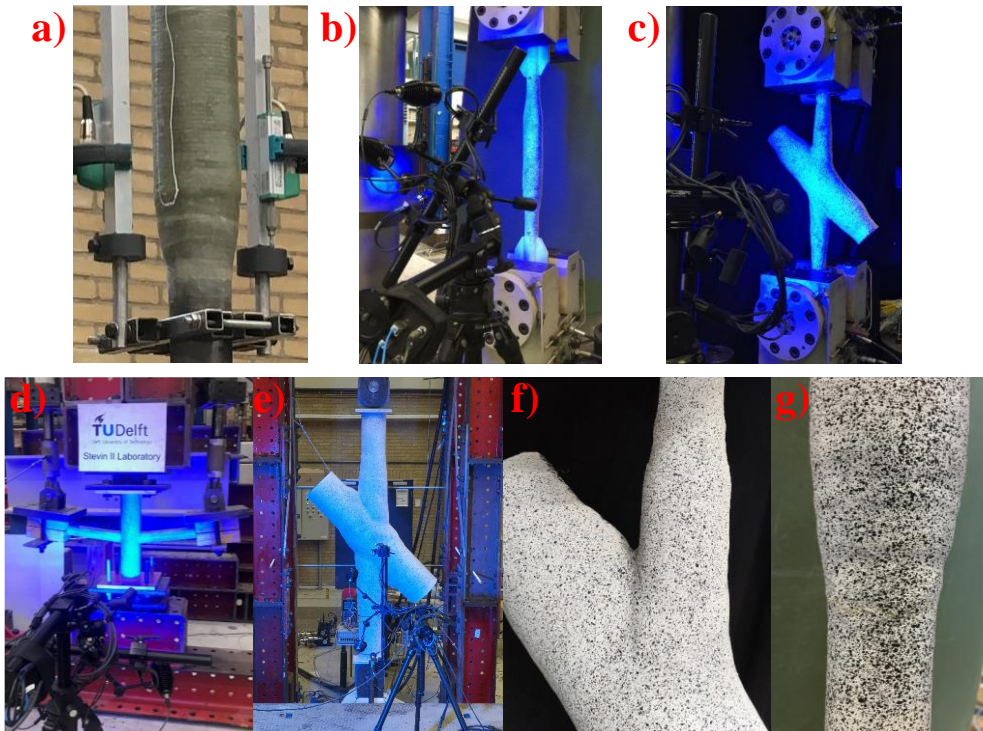


Figure 3-4 Measurement system in ultimate load joint experiments: a) LVDTs and b) 3D DIC used in A-joint tensile tests; 3D DIC used in c) axial and d) bending test of X-joint in small-scale; 3D DIC used in tensile test of e) medium-scale X-joints; speckle pattern on f) small-scale X-joints and g) small-scale A-joints

3.6 Failure modes of wrapped composite joints

Based on the results of the ultimate load joint tests[15], [17], [23]–[26] and the results shown in this Section afterwards, the load transfer mechanism and potential failure scenarios of wrapped composites joints are identified and schematically shown in Figure 3-5. The main load transferring components of the wrapped composite joint are:

- Primary bonded interface in X-joints or bonded interface in A-joints – which connects the brace or CHS member to the composite wrap. The joint load (tension, compression, bending) from the brace or CHS member is transferred to the composite wrap mainly through mode II (shear) interface behavior.
- Composite wrap – which transfers the joint load from the brace or CHS members to another brace or CHS member and to the chord. The load transfer is through complex multi-axial stress state at the meso-scale, scale of the curved laminate.
- Secondary bonded interface in X-joints – which connects the composite wrap to the chord member. The load transfer is through mixed-mode interface behavior, i.e. combination of Mode I (peel) and Mode II/III (shear).

The failure modes of the wrapped composite joint can be divided into four main groups for any general load direction:

1) Failure of the primary bonded interface in X-joint or the bonded interface in A-joint by partial or full debonding. Mode II interface failure is dominant, partially reduced by mode-mixity with Mode I interface stresses at the root due to local bending of the composite wrap and the wrap end due to contraction of the CHS cross section after yielding of steel. The crack initializes at the root of the connection (coincidence of the brace and chord or CHS members) due to stress concentrations and propagates towards the end of the bonded interface. The thickness profile of the composite wrap is tapered towards the wrap end to reduce the shear stress concentrations and peel stresses at the end of the composite wrap.

2) Failure of the composite wrap by fracture involving micro-scale failure modes of the fibers and resin. The failure criterion of composite material was adopted to be 1.2% from looking at the surface strain in DIC results. Given the quasi-isotropic behavior and relatively large thickness of composite wrap laminate used in the joints, the local failure modes of the composite wrap can be characterized as: a) in-plane tensile / compressive / shear failure of the laminate and b) out-of-plane shear / tensile failure of the laminate due to delamination.

3) Failure of the secondary bonded interface in X-joints by debonding of the composite wrap from the steel chord member. The mode-mixity of Mode I and Mode II/III failure behavior at the interface connecting the composite wrap to the chord member will depend on ratio of diameter of the chord and the brace. With smaller brace-to-chord diameter, the peel stresses (Mode I) can turn dominant for example in case of tensile joint load on the brace as the composite wrap is pulled away from the chord.

4) Failure of brace or CHS member by yielding or local buckling next to, or inside the composite wrap. Yielding of the steel inside the composite wrap can promote debonding

on the bonded interface. Yielding of the steel outside, close to the end of composite wrap can initiate debonding crack from the end of the bonded interface.

The interaction of failure modes of separate components can lead in general to two scenarios:

Loss of structural integrity (failure): X-joint: due to full debonding on primary bonded interface in X-joint and bonded interface in A-joint, and/or failure of the composite wrap in a complete circumference around any brace member in X-joint or any CHS member in A-joint; The transfer of the joint loads between the brace or the CHS members and between the chord and the brace members is no longer possible.

Secant stiffness degradation: Partial debonding on the secondary bonded interface in X-joints will not lead to loss of structural integrity of the joint but will result in loss of joint secant stiffness. It will be shown in the results of small-scale and medium-scale experiments of X-joints that debonding on the secondary bonded interface is only partial. Even in the very unlikely event of failure of the entire bonded interface on the chord there would not be loss of structural integrity of the joint. The transfer of the joint load components between the brace members and partially to the chord would still be possible through the composite wrap. Also, partial debonding on primary bonded interface in X-joints and on bonded interface in A-joints leads to reduction of secant stiffness of the joint but not to the loss of the structural integrity.

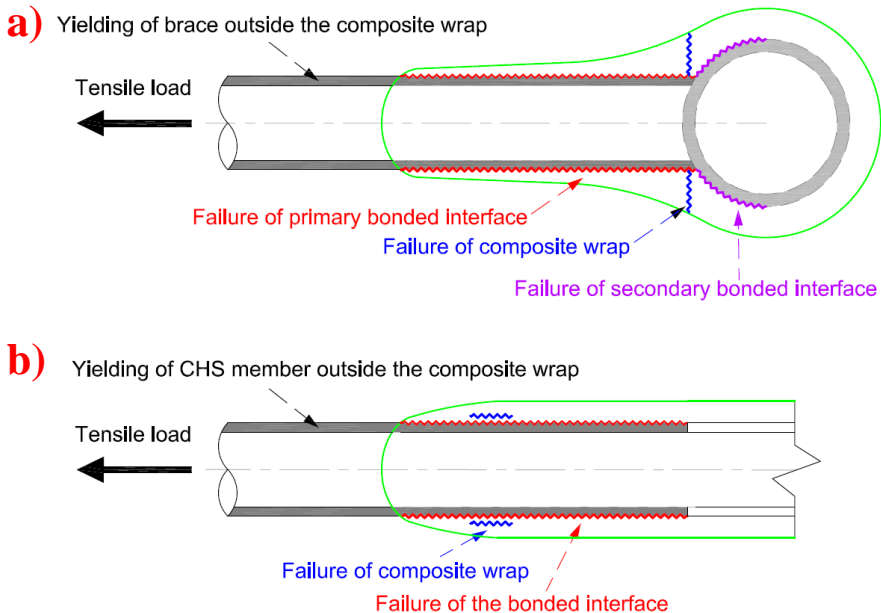


Figure 3-5 Failure modes of wrapped composite a) X-joint and b) A-joint – loaded in tensions as an example

3.7 Influence of production parameters on the static behavior of wrapped composite joints

3.7.1 Test series

6 series of small-scale wrapped composite A-joint specimens are designed for the tensile static experiments, as summarized in Table 3-3, to investigate influence of production parameters (bonding primer, resin toughness and steel yielding) on the debonding resistance of wrapped composite joints. Geometries of the joint specimens with dimensions are shown in Figure 3-3 a) and b). The main differences of the geometry in Figure 3-3 a) and Figure 3-3 b) are in the length of the weld at the end detail and the diameter of the steel tubes. Longer weld is used for series 5 and 6 in which the high strength steel specimens are compared to mild steel specimens. Each series of wrapped composite A-joints tested is accomplished with 3 nominally identical specimens to characterize scattering of static behavior of this new joining technology.

The following naming convention is used for series given in Table 3-3 and used afterwards in analysis of the results: A – Wrapped composite joints, A (uniaxial) geometry; Ss – small-scale; R1, R2, R3 – Resin type used as resin 1, resin 2 and resin 3; PM – with primer / mild steel, NM – no primer / mild steel, PH – with primer / high-strength steel; S1/2/3/etc. - nominally identical specimens, number 1, 2, 3, etc. (S4/5/6 is used in series 5 to distinguish the specimens between series 3 and series 5.)

Table 3-3 Test series and specimen designation of A-joints

Series number	Test series and specimen naming	Resin type	Bonding treatment	Steel Grade	Connection type	Geometry in Figure number
1	A-Ss-R1-NM_S1/2/3	Resin 1	No Primer	S355	Wrapped composite	Figure 3-3 a)
2	A-Ss-R1-PM_S1/2/3	Resin 1	With Primer	S355	Wrapped composite	Figure 3-3 a)
3	A-Ss-R2-PM_S1/2/3	Resin 2	With Primer	S355	Wrapped composite	Figure 3-3 a)
4	A-Ss-R3-PM_S1/2/3	Resin 3	With Primer	S355	Wrapped composite	Figure 3-3 a)
5	A-Ss-R2-PM_S4/5/6	Resin 2	With Primer	S355	Wrapped composite	Figure 3-3 b)
6	A-Ss-R2-PH_S1/2/3	Resin 2	With Primer	S700	Wrapped composite	Figure 3-3 b)

3.7.2 Experimental set-up

The tensile static experiments of wrapped composite A-joints in series 1-4 are conducted in the MTS 647 Hydraulic Wedge Grip with 600 kN loading capacity equipped with hydraulic clamping heads in Stevin lab 2 of TU Delft, as shown in Figure 3-6 a) and b). The axial load on steel tubes is applied through gripping the endplates welded to the joint. Specimens in series 5-6 are tested in the Universal testing Machine (UTM) with 800 kN loading capacity considering the potential enhancement of the static resistance attributed to use of high strength steel, see Figure 3-6 c) and d). Load is applied

by displacement control with rate of 1 mm/min to provide quasi-static loading condition.

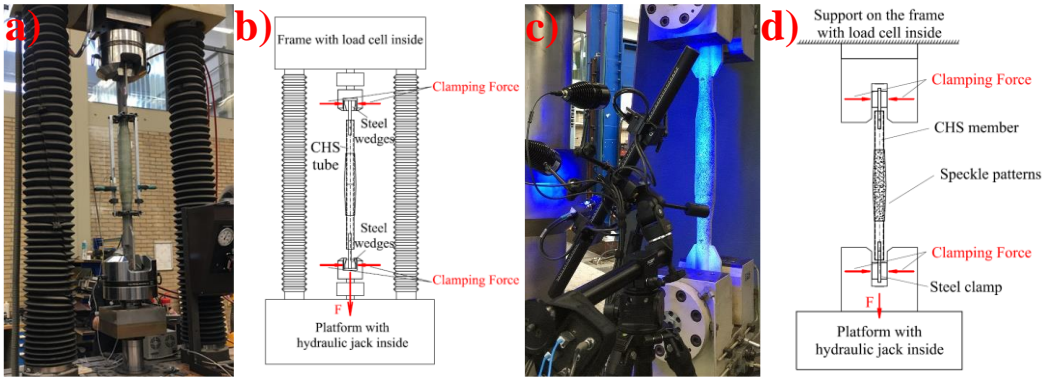


Figure 3-6 Test set-up of wrapped composite A-joints in a) and b) series 1-4 and in c) and d) series 5-6

3.7.3 Overview of test results of wrapped composite A-joints

General overview of all A-joint test results is given in Table 3-4 and Table 3-5. The identification of the failure modes are presented in the follow-up sections and facilitated by analysis of surface strains obtained by 3D DIC measurements in combination with general load-displacement curves. The displacement values in Table 3-4 and Table 3-5 are measured based on the two points 50 mm outside the wrapped region on the two steel members, as indicated in Figure 3-3 a) and b).

All specimens from series 1 to 5 failed by full debonding at the steel-composite interface on one of the steel members preceded by limited or extensive yielding of the steel CHS outside the wrapping area. The debonding initiates and propagates consecutively from the joint root in the middle of the joint towards the wrapping ends. Final debonding failure is due to coalescence of debonding crack from the root and end. The failure process is explained in more detail in section 3.7.7. In series 6 delamination between the first plies next to the interface is dominant failure mode while yielding of the steel CHS is less evident.

The elastic load limit is governed as initiation of debonding from the root of the bonded interface. For each specimen, the elastic limit is determined as the load level at which the secant stiffness decreases 5%.

Table 3-4 Test results of A-joints related to influence of primer and resin

Series	Specimen	Initial stiffness [kN/mm]	Elastic load limit [kN]	Ultimate load [kN]	Displacement at failure [mm]
1	A-Ss-R1-NM_S1	258.5	196.3	319.9	4.0
	A-Ss-R1-NM_S2	262.5	185.2	314.3	1.8
	A-Ss-R1-NM_S3	261.9	198.3	314.0	2.1
	Average (and COV [%])	261.0 (0.67)	193.3 (2.98)	316.1 (0.86)	2.6 (36.99)
2	A-Ss-R1-PM_S1	255.7	189.1	334.7	3.8
	A-Ss-R1-PM_S2	256.7	195.7	327.0	4.4
	A-Ss-R1-PM_S3	252.2	186.8	324.5	3.4
	Average (and COV [%])	254.9 (0.76)	190.5 (1.98)	328.7 (1.32)	3.9 (10.63)
3	A-Ss-R2-PM_S1	251.8	221.5	335.4	5.1
	A-Ss-R2-PM_S2	241.9	221.4	341.2	4.9
	A-Ss-R2-PM_S3	247.8	234.2	334.7	4.8
	Average (and COV [%])	247.2 (1.65)	225.7 (2.66)	337.1 (0.86)	4.9 (2.53)
4	A-Ss-R3-PM_S1	265.8	179	334.4	3.9
	A-Ss-R3-PM_S2	264.8	186.2	324.3	3.7
	A-Ss-R3-PM_S3	266.0	185	325.4	3.6
	Average (and COV [%])	265.5 (0.20)	183.4 (1.72)	328.0 (1.38)	3.7 (3.34)

Table 3-5 Test results of A-joints related to influence of steel grade

5	A-Ss-R2-PM_S4	245.0	225.7	312.4	6.4
	A-Ss-R2-PM_S5	250.1	224.2	306.8	5.8
	A-Ss-R2-PM_S6	254.7	224.4	311.8	6.1
	Average (and COV [%])	249.9 (1.59)	224.8 (0.30)	310.3 (0.81)	6.1 (4.02)
6	A-Ss-R2-PH_S1	241.8	228.4	571.5	6.3
	A-Ss-R2-PH_S2	241.6	228.1	586.3	5.6
	A-Ss-R2-PH_S3	235.1	226.2	471.8	3.8
	Average (and COV [%])	239.5 (1.30)	227.6 (0.41)	543.2 (9.36)	5.2 (20.12)

3.7.4 Influence of bonding primer

Figure 3-7 shows the load-displacement curves of wrapped composite A-joints from series 1 and 2, without and with application of the bonding primer, respectively. Application of the bonding primer helps improve displacement of the joint at failure by 50% and decrease its scattering by 71%. No significant difference (within 5%) is seen in the initial stiffness and elastic load limit because it depends merely on the elastic properties of composite material and steel.

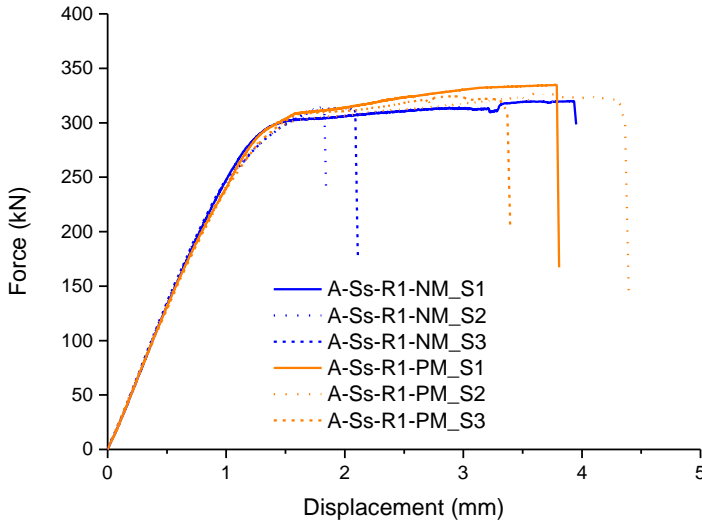


Figure 3-7 Tensile static behavior of wrapped composite A-joints applied with vs without bonding primer

3.7.5 Influence of mechanical properties of polymer resins

Figure 3-8 shows load-displacement curves of wrapped composite A-joint specimens referring to series 2, 3 and 4 produced with three types of resins: resin 1, resin 2 and resin 3, respectively. According to the manufacturers' data, resin 2 exhibits the largest elongation at break compared to resin 1 and resin 3 implying its largest fracture toughness. The joints produced with resin 2 (toughened vinyl ester) show 19%~22% larger elastic load limit and 26%~32% larger displacement at failure, respectively, than the joints produced with resin 1 (regular vinyl ester) and resin 3 (regular polyester).

The fracture toughness of resins has a governing effect on the joints' ultimate displacement (ductility). Larger fracture toughness of resin 2 over the other two resins contributes to less rapid debonding crack propagation in the joint and resulting in larger displacement at failure, thus improved ductility of the joint.

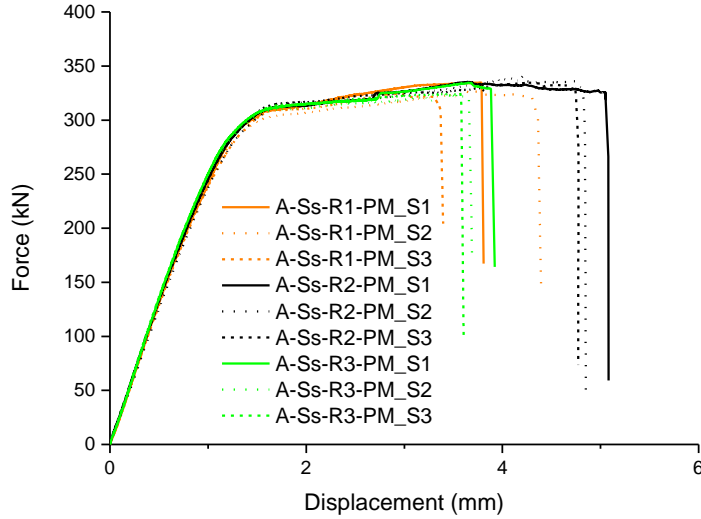


Figure 3-8 Tensile static behavior of wrapped composite A-joints produced with three types of resins

3.7.6 Influence of CHS steel grade

Figure 3-9 depicts the load-displacement behavior of 3 mild steel (MS) vs 3 high strength steel (HSS) wrapped composite A-joint specimens. 75% larger ultimate joint load is observed in HSS joint specimens. The initial stiffness is the same as in case of MS joint specimens. While full debonding on the bonded interface is the governing failure mode of all MS joints, two out of three HSS joints (A-Ss-R2-PH_S1 and S2) fail due to combined debonding and delamination. Still, one of the HSS specimens A-Ss-R2-PH_S3 fails in the same manner as MS specimens, by full debonding, as shown in Figure 3-10. This specimen had lowest resistance in the HSS series experiments.

One of the HSS joints with combined debonding-delamination failure (A-Ss-R2-PH_S1) is cut through its mid-plane after the experiments to investigate the failure process, as shown in Figure 3-11. The cut surface is grinded by sandpaper and polished. The failure is initiated by debonding on the interface at the wrap root (junction of steel tubes) which propagates to a certain length (region a-b in Figure 3-11). At approximately 100 mm of the debonding length the crack transfers into the inter-laminar interface between the first and the second ply of the composite wrap (region c-d). The delamination transfers further into the interface between the 2nd and 3rd ply (e-f), and the final failure is reached by growth of the delamination towards the composite wrap end (point g).

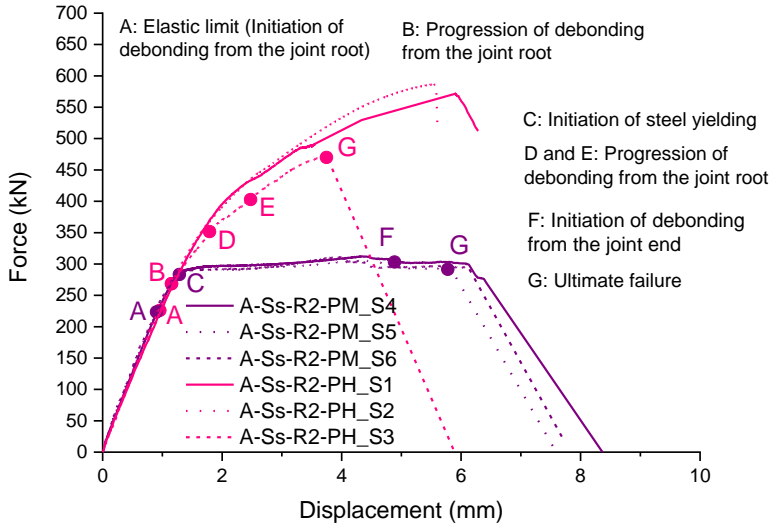


Figure 3-9 Tensile static behavior of MS vs HSS wrapped composite joints

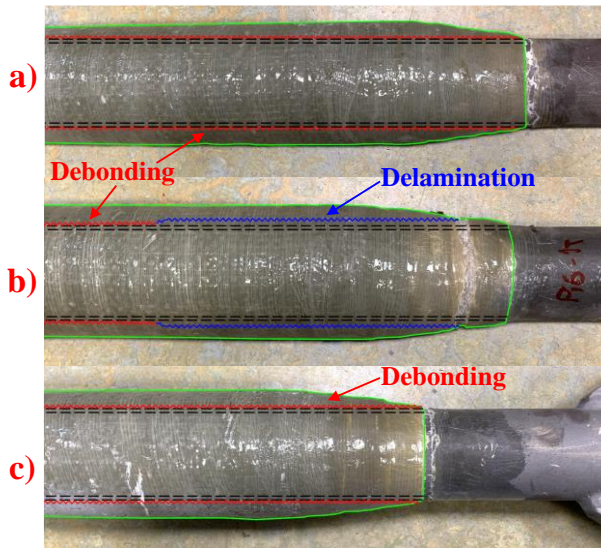


Figure 3-10 Comparison of failure modes between MS and HSS A-joints: a) MS joint fails at the steel-composite bonded interface (full debonding); HSS joint fails due to b) combined debonding and delamination and c) full debonding

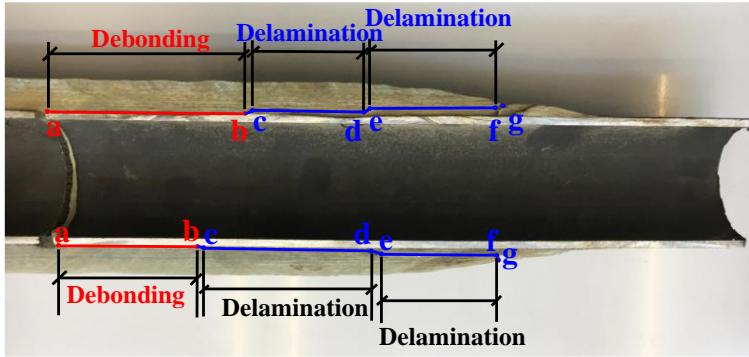


Figure 3-11 Crack path in cut HSS specimen (A-Ss-R2-PH_S1)

3.7.7 Crack propagation in mild steel vs high strength steel A-joint specimens

In the experimental results presented so far for the MS joint specimens, full debonding of the bonded interface is reached after yielding of steel tube. Steel yielding leads to contraction of the steel cross-section outside the wrapped region, resulting in Mode I (peel stress dominated) debonding crack initiation and propagation from the wrap end and finally coalescence with the debonding crack propagated from the wrap root. Therefore, resistance of the bonded interface is limited by yielding of steel. In wrapped composite joints with HSS, yielding and excessive contraction of the steel cross-section outside the composite wrap is excluded. Therefore, debonding at the wrap end is prevented which is the main reason why much larger debonding resistance is reached even though the dimensions of the composite wrap and the surface preparation are the same as in case of MS joint specimens.

In order to substantiate the explained difference in failure behavior, ultrasonic scanning was attempted including phased array alternative to measure the debonding length but unfortunately no useful and conclusive results were obtained. The main reasons for unsuccessful measurements are the relatively large thickness (14mm) curved surface and unclear reflection from steel to composite interface. The analysis of development of debonding cracks in MS and HSS specimens is then performed with help of DIC results. Figure 3-12 gives the explanation of physical analogy that is used to determine the debonding crack length by using longitudinal surface strains obtained from DIC in experiments. In the perfectly bonded state, steel and composite in an arbitrary cross section are connected and carry the external force in a manner of hybrid (composite) circular cross section. The longitudinal strains along the steel tube and the composite wrap are of similar magnitude, as indicated by the blue line. Strains are slightly diminished in the region of the composite wrap due to larger cross section (steel + composite) resisting the external load. Still the distribution of longitudinal surface strain along the longitudinal path is relatively uniform and monotonic. In the partially debonded state, by contrast, a deviation of such monotonic state would exist. In case of debonding at the wrap root an increase of surface strain will occur because in that region the external force is no longer resisted by a hybrid steel + composite cross section but by the composite part of the cross-section only. In similar fashion the surface strains in the

region of debonding at the wrap end would be decreased compared to the bonded area. This is because the composite part of the cross section which is on the outside is debonded and no longer transfers the external load.

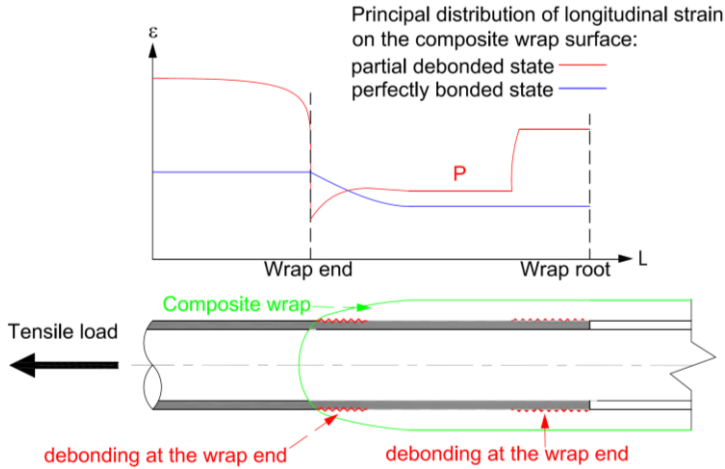


Figure 3-12 Principle of using variation of the distribution of longitudinal surface strains on composite wrap to determine debonding crack length in the embedded bonded interface

Development of surface strains (longitudinal strains) of 2 specimens, A-Ss-R2-PM_S5 and A-Ss-R2-PH_S3, are shown in Figure 3-13 and Figure 3-15, respectively, to characterize the failure process of MS and HSS wrapped composite A-joints. Critical load stages are identified in the load-displacement curves in Figure 3-9 to explain the two different failure processes related to debonding with or without yielding of the steel members. Wrapped composite joints behave elastic in both cases as shown in Figure 3-13a) and Figure 3-15 a) until approximately 225 kN (point A). The end of linear elastic behavior is attributed to initiation of debonding from the joint root between the composite wrap and the steel member due to shear stress on the interface, see Figure 3-13b) and Figure 3-15 b). As for the MS joint, debonding crack propagates steadily from the joint root followed by initiation of steel yielding at the wrap end at 289kN (point C), see Figure 3-13c). Additional debonding crack is initiated from the joint end at 306 kN (point F) when the bonded interface at the wrap end cannot resist the peel stress due to contraction of the steel cross section after yielding (see Figure 3-13d)). Debonding crack then develops significantly to the critical length at 291 kN (point G) and its coalescence with the debonding crack from the wrap root leads to full debonding, as shown in Figure 3-13e). By contrast, debonding crack from the root of the HSS joint consistently propagates (point B, D and E, see Figure 3-15 c), d) and e)) without steel yielding until reaching the critical length at 464 kN (point G, see Figure 3-15 f)) and leads to full debonding of the bonded interface.

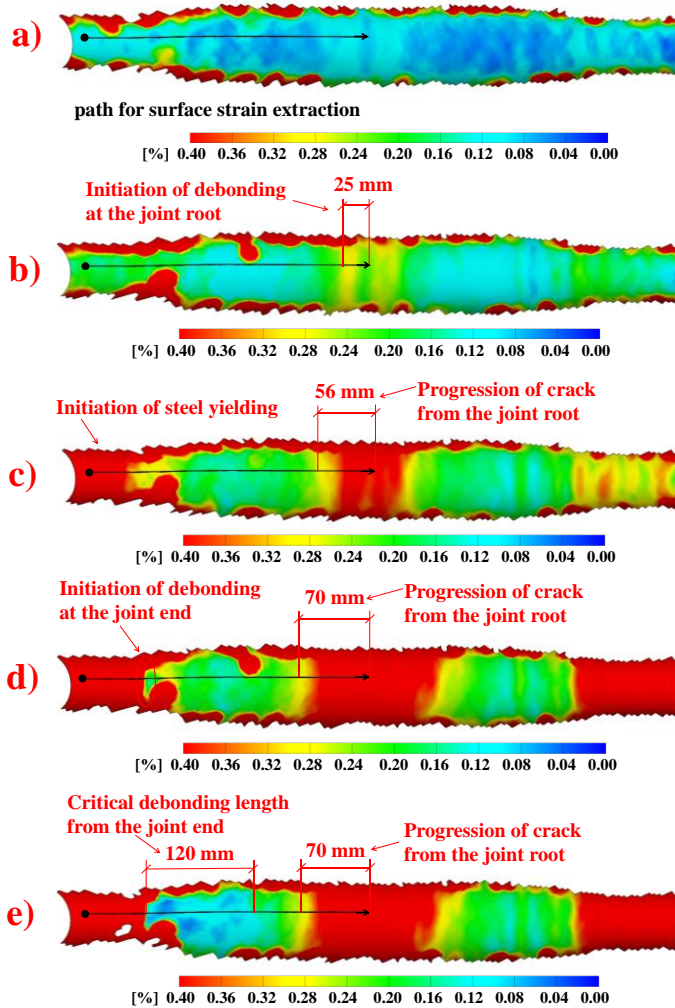


Figure 3-13 Longitudinal surface strains of a mild-steel specimen (A-Ss-R2-PM_S5) at a) linear elastic stage (114 kN); b) initiation of debonding from wrap root – point A (224 kN); c) Initiation of steel yielding – point C (289kN); d) initiation of debonding from the wrap end – point F (306kN); e) Critical debonding length before failure – point G (291kN)

Crack lengths at the characteristic load stages are analyzed along a path which is defined in longitudinal direction, starting at the free end of the composite wrap and ending at the root connection, as indicated in Figure 3-13 and Figure 3-15. The longitudinal surface strains along the path obtained at characteristic loading stages of the MS and HSS joint are shown in Figure 3-14a) and Figure 3-16 a), respectively. The aim is to identify indirectly the debonding crack length by observing local increase or decrease of surface strains at the crack front. To this aim the surface strains at all stages are scaled to strains that would correspond to the elastic load stage in Figure 3-14 b) and Figure 3-16 b) for MS and HSS, respectively. If there were no debonding, delamination, composite cracking and/or steel yielding, the scaled strains at later load stages would be

identical to the reference elastic state. The deviations from such idealistic state are used to identify fronts of the debonding cracks that are observed after cutting of the specimens. The threshold of the strain level to quantify debonding crack length varies from 0.15% to 0.3% while it becomes more or less constant and is approximately 0.1% after strain scaling. These values are chosen on judgment of location of the strains front at which the strain would significantly increase from flat line to higher strain region. This method is verified in the investigation where FE model are used to determine the threshold[26].

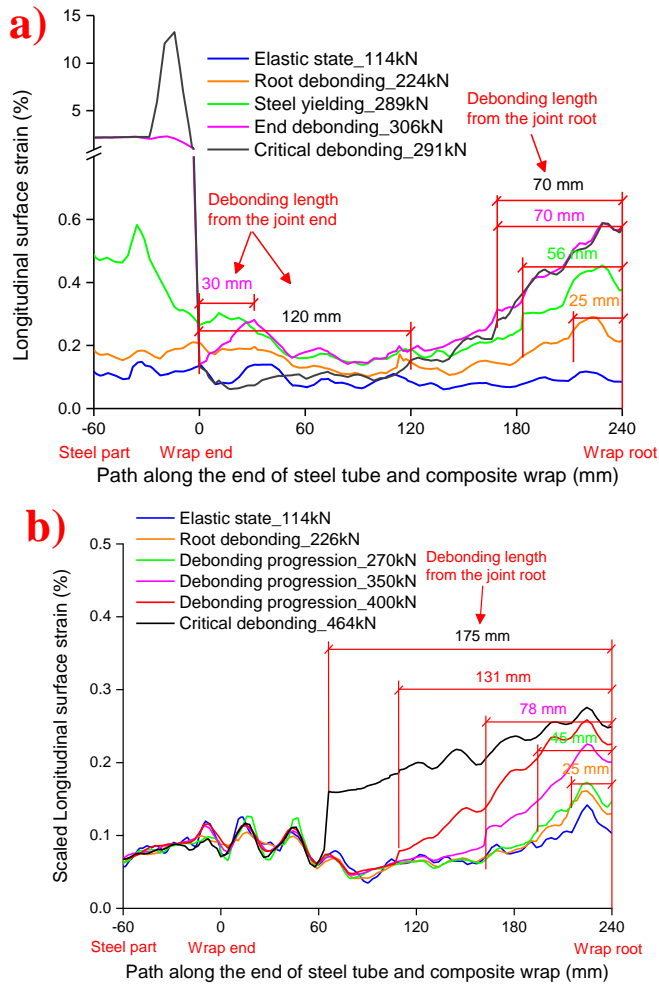


Figure 3-14 a) Absolute and b) scaled surface strains along the end of steel tube and composite wrap of a mild-steel specimens (example of A-Ss-R2-PM_S5)

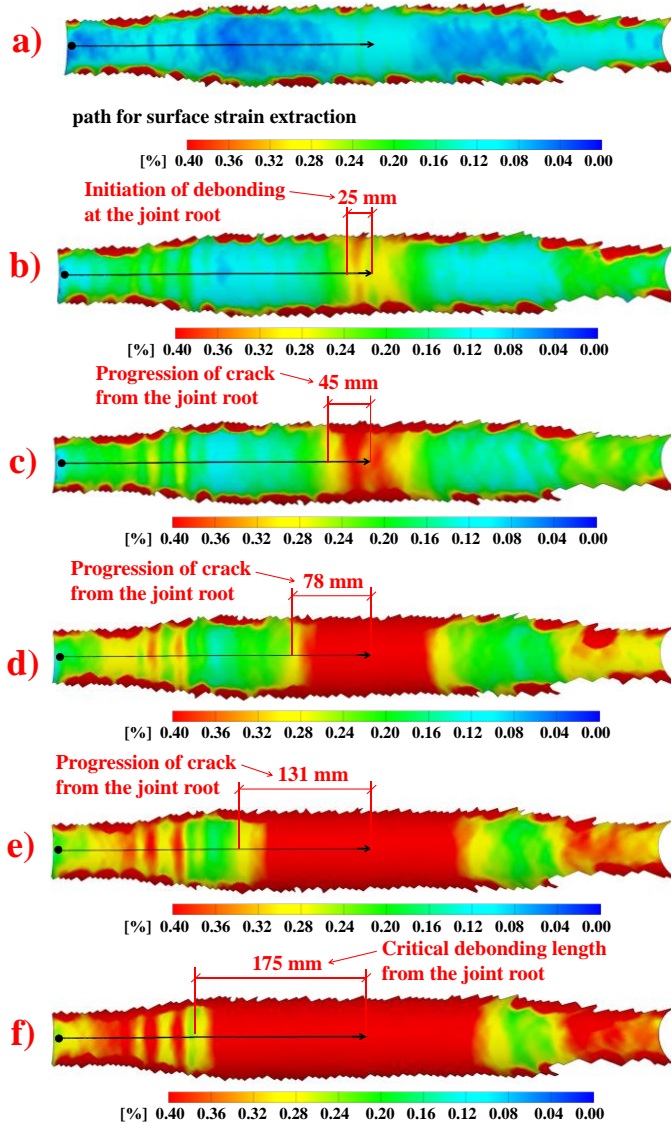


Figure 3-15 Longitudinal surface strains of a high-strength steel specimen (A-Ss-R2-PH_S3) at a) linear elastic stage (114 kN); b) initiation of debonding from wrap root – point A (226 kN); c) Progression of debonding from wrap root – point B (270 kN); d) Progression of debonding from wrap root – point D (350 kN); e) Progression of debonding from wrap root – point E (400 kN); f) Critical debonding length before failure – point G (464kN)

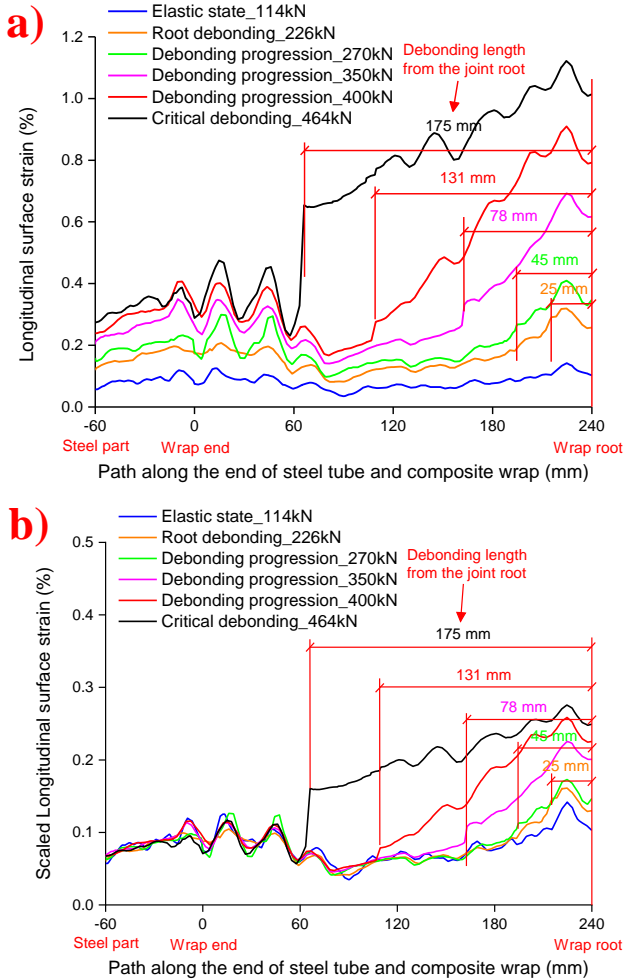


Figure 3-16 a) Absolute and b) scaled surface strains along the end of steel tube and composite wrap of a high strength steel specimens (example of A-Ss-R2-PH_S3)

Surface strains distribute uniformly without steep increase along the path in the linear elastic stage, the load level of 114 kN before point A indicated in Figure 3-9. Significant steep increase of surface strain from 0.1% to 0.3% indicates that debonding is initiated from the wrap root with 25 mm debonding length at load level 225kN (point A). In the MS joint, debonding length at the root steadily increases to 56 mm at 289 kN corresponding to initiation of steel yielding – point C in Figure 3-9, and consistently grows to 70 mm at 306 kN where debonding is initiated from the wrap end – point F in Figure 3-9. Debonding crack from the wrap root subsequently stops increasing because all energy is dissipated in propagation of debonding crack from the wrap end. The critical length of the debonding crack of 190 mm (79% of full bonding length) is recorded just before ultimate failure (see Figure 3-14) when the coalescence of the crack initiated at the wrap root and wrap end is reached due to excessive yielding of steel outside the wrap

with approximately 2.2% of plastic strain (see Figure 3-14 a)). Conversely, debonding crack from the root of the HSS joint steadily increases to 45 mm, 78 mm and 131 mm at 270 kN, 350 kN and 400 kN (point B, D and E in Figure 3-9), respectively, without steel yielding and without debonding initiated from the wrap end. The debonding crack subsequently propagates to the critical length of 175 mm (73% of full bonding length) just before ultimate failure (see Figure 3-16). At the wrap end, strain localization is observed due to ply drops during the loading process as presented in Figure 3-16.

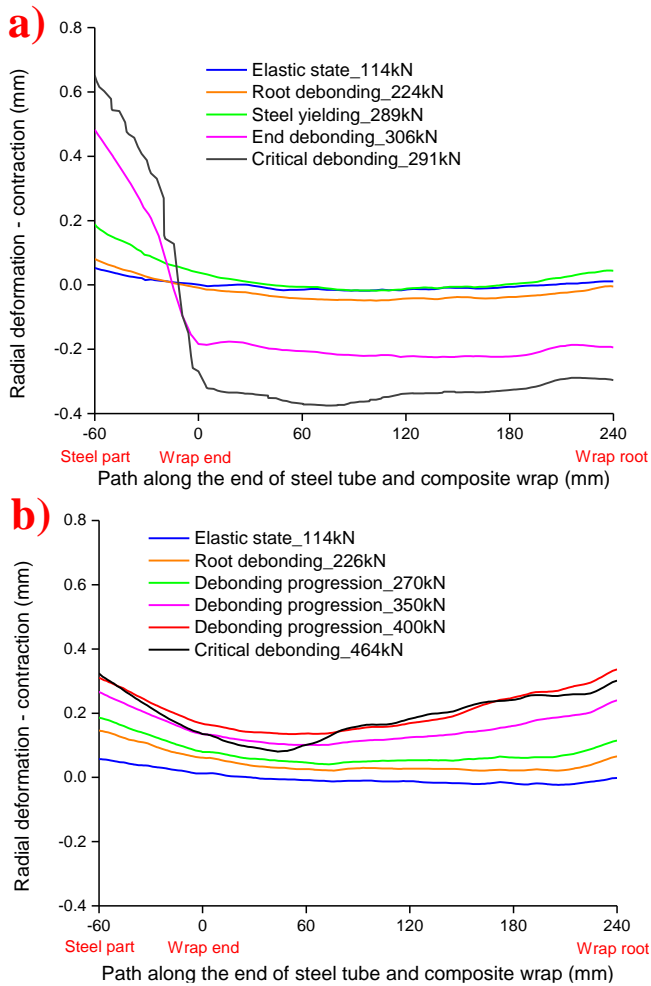


Figure 3-17 Radial deformation of the steel tubes outside the composite wrap indicating the necking behavior in a) mild-steel specimen and b) high strength steel specimen

Development of debonding in MS and HSS joints is compared in Figure 3-18 with respect to the applied load level. The propagation rate of the crack propagating from the wrap root is almost identical for MS and HSS joint until the load level at which steel yielding in MS joint initiates the debonding from the wrap end. Propagation of debonding at the wrap end in MS joints is exhibited at non-increasing load level, however with the

increasing joint displacement, as shown in load-displacement graphs in Figure 3-9. This behavior is attributed to steel CHS yielding as indicated in Figure 3-17a) by contraction (necking) of the steel cross section of MS joints outside the composite wrap. It is shown in section 3.7.5 that more ductile resin would contribute to retarding the propagation of the debonding crack at the wrap end. Development of the debonding crack in the wrap root in the HSS joint is steady until final failure. The debonding from the wrap end is excluded because of absence of steel yielding (necking) in the CHS outside the composite wrap, see Figure 3-17b).

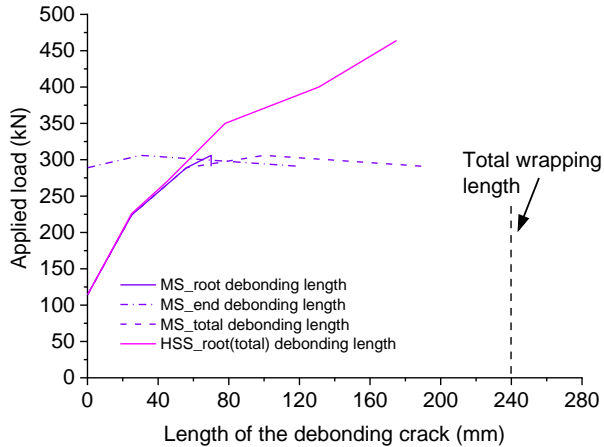


Figure 3-18 Comparison of crack length growth in mild-steel and high strength steel specimens

3.8 Static behavior of wrapped composite X-joints

3.8.1 Test series

In order to characterize the static behavior of wrapped composite X-joints, 6 series of wrapped composite or welded X-joint specimens are designed in the static experiments at various load conditions, as summarized in Table 3-6. Wrapped composite X-joints are produced with mild steel and resin 2. X-joints with two different angles between braces and the chord member: 45° and 90°; in 2 scales: small-scale and medium-scale are tested with 3 load cases applied as tension, compression and in-plane bending. The following naming convention is used for series given in Table 3-6 and used afterwards in analysis of the results: cX45/90 – wrapped composite joint, X geometry at 45°/90° angle; wX45/90 – welded joint, X geometry at 45°/90° angle; Ss, Ms – small-scale and medium-scale, respectively; T, C or B – tension, compression or in-plane bending loading on braces, respectively; S1/2/3/etc. - nominally identical specimens, number 1, 2, 3, etc.

Geometry with dimensions of X-joints in Table 3-6 are shown in Figure 3-3. Each series of wrapped composite joints loaded in tension and compression (series 7, series 9-10) is accomplished with at least 3 nominally identical specimens to characterize scattering of static behavior of this new joining technology. Counterpart welded joints loaded in tension (series 8) are tested with at least 2 nominally identical specimens per

series for comparison reasons. Bending experiment (series 11-12) is accomplished with 2 specimens per series but 4 results are obtained from each series. That is because the clamped boundary conditions with 2 load point set-up allow almost independent test of bending on the left and the right brace members, which is explained in section 3.8.2.

Table 3-6 Test series and specimen designation of X-joints

Series number	Test series and specimen naming	Scale	Load condition	Connection type	Geometry in Figure number
7	cX45-Ss-T_S1/2/3/4/5	Small-scale	Tensile on braces	Wrapped composite	Figure 3-3c)
8	wX45-Ss-T_S1/2	Small-scale	Tensile on braces	Welded	Figure 3-3d)
9	cX45-Ss-C_S1/2/3	Small-scale	Compressive on braces	Wrapped composite	Figure 3-3c)
10	cX45-Ms-T_S1/2/3	Medium-scale	Tensile on braces	Wrapped composite	Figure 3-3g)
11	cX90-Ss-B_S1/2	Small-scale	Bending on braces	Wrapped composite	Figure 3-3e)
12	wX90-Ss-B_S1/2	Small-scale	Bending on braces	Welded	Figure 3-3f)

3.8.2 Experimental set-up

The tensile and compressive experiments of 45° X-joints in small-scale are conducted in the Universal Testing Machine (UTM) with 800kN loading capacity equipped with hydraulic clamping heads in Stevin lab 2 of TU Delft, as shown in Figure 3-19. The axial load on braces is applied through gripping the ends by pairs of preloaded steel clamps with pins inside, as shown in Figure 3-19d), in order to obtain uniform stress distribution in cross section at load introduction. Load is applied by displacement control with rate of 1 mm/min to provide quasi-static loading condition.

The tensile test of 45° X-joints in medium-scale is conducted in the 6-meter-high loading frame with 2.5 MN loading capacity, as shown in Figure 3-20a) and Figure 3-20b). The specimen is pin connected to the loading frame through the ear plates with Ø100 mm cylindrical hole, which are welded through end plates to the braces. Load is applied by controlling the hydraulic jack moving upward, with the displacement control with rate of 1 mm/min to obtain quasi-static loading condition.

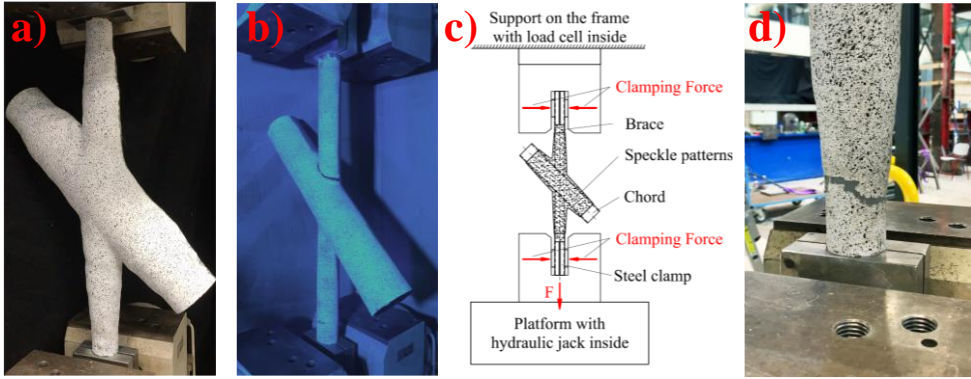


Figure 3-19 Test set-up of small-scale 45° X-joints under tensile/compressive axial load: a) wrapped composite joint; b) welded joint; c) schematic set-up; d) load application at brace end

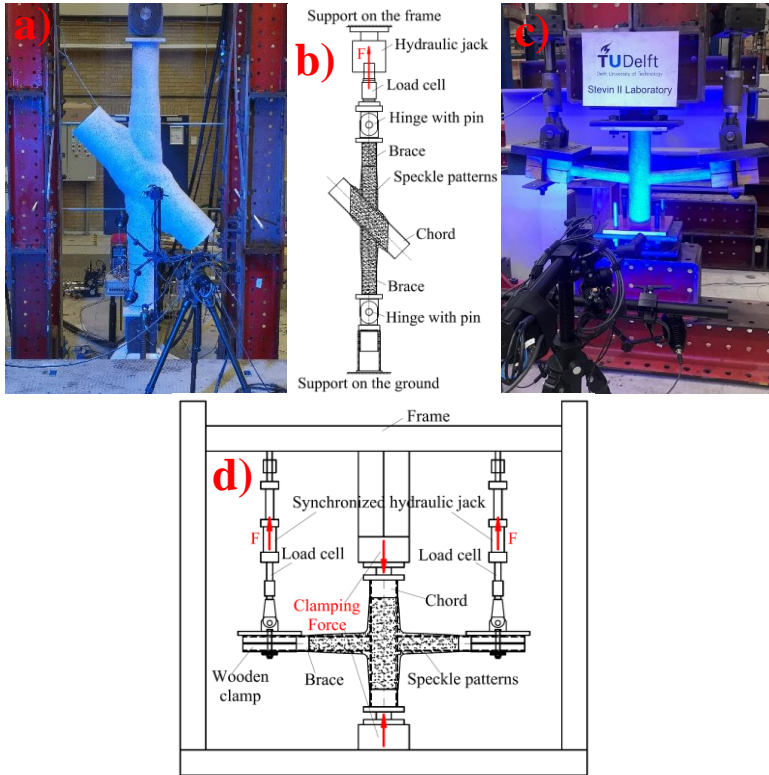


Figure 3-20 a) Configuration and b) schematic set-up of medium-scale 45° X-joints under tensile load; c) configuration and d) schematic set-up small-scale 90° X-joints under in-plane bending load

The in-plane bending load is applied to 90° small-scale X-joint specimens through lateral load on braces. Two synchronized hydraulic jacks with load capacity of 100kN are eccentrically connected to brace ends at 450mm away from the chord center, each. The lateral load on the brace is applied through set of preloaded wooden clamps to

prevent local buckling of the cross section at the load introduction, see Figure 3-20 c) and Figure 3-20 d). The chord member in the middle is fixed to the frame by applying preload at the top and bottom cross section. Such clamped boundary conditions with 2 load point set-up allows independent test of bending on the left and the right brace members. Load is applied simultaneously with displacement control of 1 mm/min. Once one of the connections of the left or the right brace member fails due to excessive bending, the load is continued on the opposite side. Therefore, from one specimen two bending test results are obtained.

3.8.3 Overview of test results of X-joints

General overview of all X-joint test results is given in Table 3-7~Table 3-10. The indicated failure modes and scenarios of failure and stiffness degradation are presented through the experimental results for various load cases and scales. Identification of failure modes is facilitated by analysis of surface strains obtained by 3D DIC measurements in combination with general load-displacement curves.

Table 3-7 Test results of wrapped composite vs welded 45° X-joints in small-scale under tensile load

Specimen	Initial stiffness [kN/mm]	Elastic load limit [kN]	Ultimate load [kN]	Final failure mode
cX45-Ss-T_S1	159.0	183.9	339.5	Full debonding at the primary bonded interface accompanied by yielding on the brace
cX45-Ss-T_S2	163.3	182.2	346.5	
cX45-Ss-T_S3	160.3	180.5	347.4	
cX45-Ss-T_S4	171.9	180.4	346.0	
cX45-Ss-T_S5	170.3	184.9	344.9	
Average (and COV [%])	164.9 (3.15)	182.4 (0.98)	345.7 (1.01)	
wX45-Ss-T_S1	125.6	156.7	334.1	Punching shear failure of the chord next to welds
wX45-Ss-T_S2	129.0	153.3	341.9	
Average (and COV [%])	127.3 (1.37)	155.0 (1.09)	338.0 (1.16)	

Table 3-8 Test results of wrapped composite 45° X-joints in small-scale under compressive load

Specimen	Initial stiffness [kN/mm]	Elastic load limit [kN]	Ultimate load [kN]	Final failure mode
cX45-Ss-C_S1	177.4	215.2	361.2	Local buckling of brace
cX45-Ss-C_S2	177.8	221.3	358.2	Full debonding at the primary bonded interface accompanied by yielding on the brace
cX45-Ss-C_S3	166.0	223.5	361.7	Local buckling of brace
Average (and COV [%])	173.7 (3.14)	220.0 (1.60)	360.4 (0.42)	

Table 3-9 Test results of wrapped composite 45° X-joints in medium-scale under tensile load

Specimen	Initial stiffness [kN/mm]	Elastic load limit [kN]	Ultimate load [kN]	Final failure mode
cX45-Ms-T_S1	349.2	1193	1483	Full debonding at the primary bonded interface
cX45-Ms-T_S2	345.2	1139	1353	Full debonding at the primary bonded interface
cX45-Ms-T_S3	341.5	1053	1640	Full debonding at the primary bonded interface accompanied by yielding on the braces
Average (and COV [%])	345.3 (0.92)	1128 (5.11)	1492 (7.88)	

Table 3-10 Test results of wrapped composite vs welded 90° X-joints in small-scale under in-plane bending load

Specimen	Initial stiffness [kN/mm]	Elastic load limit [kN]	Ultimate load [kN]	Final failure mode
cX90-Ss-B_S1_Left	4.01	10.81	36.59	Fracture of wrap root in the tensile zone
cX90-Ss-B_S1_Right	3.68	10.26	38.03	
cX90-Ss-B_S2_Left	3.63	10.04	33.66	
cX90-Ss-B_S2_Right	3.35	10.10	32.02	
Average (and COV [%])	3.67 (6.42)	10.30 (2.93)	35.07 (6.74)	
wX90-Ss-B_S1_Left	2.29	7.16	18.92	Brace failure next to welds in the tensile zone
wX90-Ss-B_S1_Right	2.41	7.18	18.47	
wX90-Ss-B_S2_Left	2.39	7.19	19.84	
wX90-Ss-B_S2_Right	2.31	7.11	19.61	
Average (and COV [%])	2.35 (2.22)	7.16 (0.43)	19.21 (2.84)	

3.8.4 Small-scale 45° X-joints under tensile load

Figure 3-21 shows the load-displacement curves of 5 wrapped composite joint specimens vs 2 welded counterparts in small-scale loaded in tension. Wrapped composite joint specimens in this case show 30% larger initial stiffness, 18% larger elastic load limit and 3% larger ultimate load resistance than welded counterparts, with low scattering within 0%~5% range. Ultimate displacement at failure is lower compared to welded counterparts, however with less scattering. The elastic load limit of wrapped composite joints (180 kN) is 51% higher than the nominal resistance of the counterpart welded joints (119 kN) calculated according to EN 1993-1-8[27]. Full debonding on the primary bonded interface and final pull-out of steel brace member from the composite wrap is predominant failure mode in wrapped composite joints, See Figure 3-19d). Welded joints are characterized by punching shear failure of the chord next to welds initiating from the joint crown toe and developing into the joint crown heel, see Figure 3-19b).

Figure 3-22 gives the explanation of physical analogy that is used to determine the debonding crack length by using longitudinal surface strains obtained from DIC in experiments. In the perfectly bonded state, steel and composite in an arbitrary cross section are connected and carry the external force in a hybrid manner. The longitudinal strains along the steel brace and the composite wrap are of similar magnitude. Therefore, the distribution of surface strain along the path is relatively uniform with a steady increase towards the root due to local bending caused by transfer of load to the chord. In the partially debonded state, by contrast, an instantaneous jump of surface strain will appear on the surface of composite near the crack tip because there is only composite

material part of the cross section carrying the external load at the debonded part of the primary bonded interface.

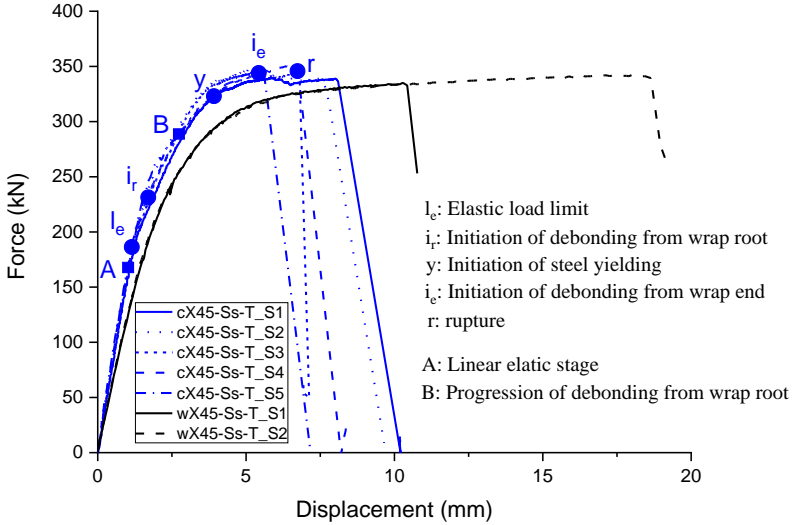


Figure 3-21 Tensile behavior of 45° small-scale wrapped composite joint specimens vs welded counterparts

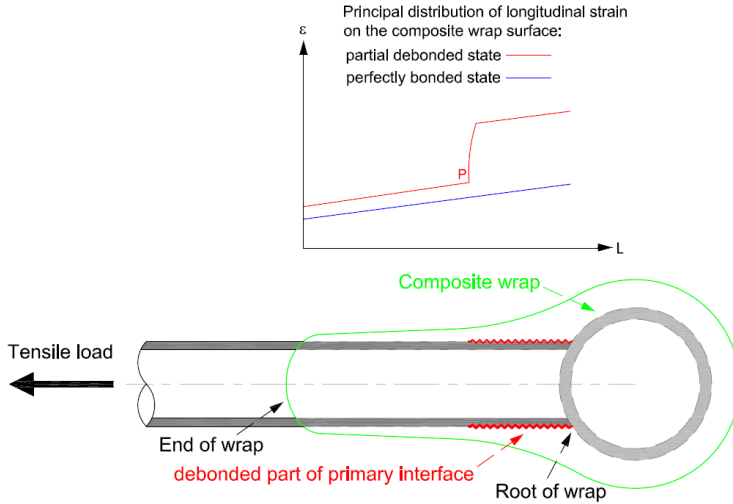


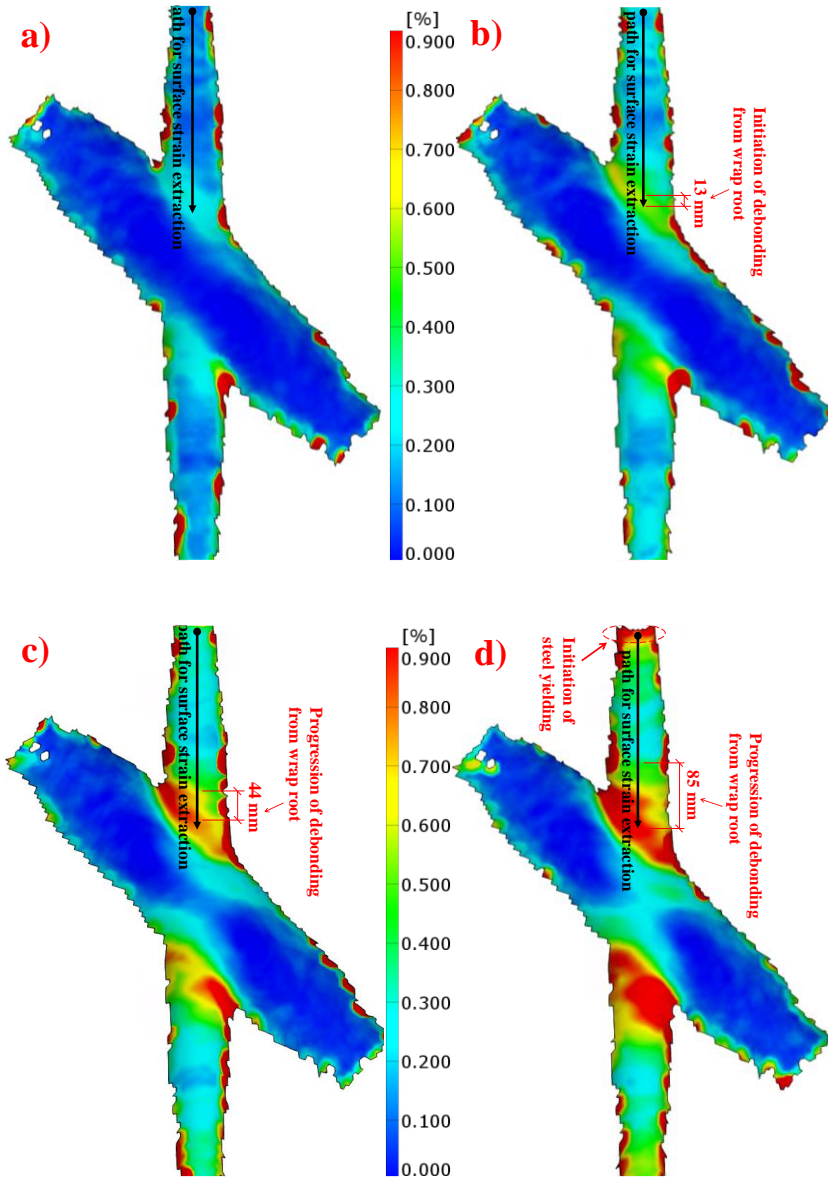
Figure 3-22 The approach of using the distribution of longitudinal surface strains to determine debonding crack length on the brace

Surface strains (principal strains) of a representative wrapped composite joint specimen (cX45-Ss-T_S4) are presented in Figure 3-23 at critical load stages identified in load-displacement curve to explain the failure process. Wrapped composite joints behave elastically as shown in Figure 3-23a) until 180kN (stage i_e) which corresponds to

52% of the ultimate tensile load of 346 kN on braces. The end of linear elastic behavior is attributed to plasticity of the bonded interface on the brace at the wrap root and the local bending of the composite wrap on the chord. Debonding is firstly initiated on the primary bonded interface from wrap root due to shear stress concentrations indicated by the localized increase of surface strains and the occurrence of damaged region at the wrap root shown in Figure 3-23b) – stage **i_r** at 234 kN. Debonding on the chord is initiated simultaneously at stage **i_r** indicated by localized increase of surface strains in Figure 3-23 b) in contrast to Figure 3-23 a) in the region of the composite wrap on the chord next to the brace. This process is gradual in contrast to behavior in tensile experiment at the medium-scale shown later, probably due to size effect that results in more sudden debonding on the chord with a larger energy release in a larger scale. The effect of size on the debonding crack propagation on the brace is investigated in Chapter 7. Debonding crack propagates steadily along the primary bonded interface at stage **B** – 289 kN where the high strain region on the surface and the damaged region at the bonded interface progress from the wrap root, see Figure 3-23 c). Crack propagation continues with further increase of high surface strain regions and the damage areas on the bonded interface illustrated in Figure 3-23 d) at point **y** – 321 kN where the yielding is initiated on the braces outside the composite wrap. Significant progression of debonding from the wrap root continues further at stage **i_e** (341 kN), see Figure 3-23 e). At this stage, additional debonding crack is initiated on the primary bonded interface from wrap end attributed to contraction of steel cross section as a consequence of excessive yielding. The debonding crack propagates significantly from wrap end indicated by the increase of low surface strain region in at the stage **r** (346 kN) prior to the final failure, see Figure 3-23 f). This localizes the fracture process at the end of the composite wrap such that debonding crack stops developing from the wrap root.

A path is defined in the middle of the brace member, starting at the free end of the composite wrap and ending at the root connection to the chord, as indicated in Figure 3-23. The longitudinal surface strains along the path obtained at characteristic loading stages are shown in Figure 3-24. The aim is to identify indirectly the debonding crack length by observing local increase of surface strains at the crack front. Surface strains distribute uniformly, without steep increase along the path, in the linear elastic stage, load level of 170 kN before stage **i_e** indicated in Figure 3-21. Significant steep increase of surface strain from 0.3% to 0.5% indicates that debonding is initiated on the primary bonded interface with 13 mm debonding length at load level 234 kN (stage **i_r**). Debonding length from wrap root steadily increases to 44 mm at the load level 289 kN (stage **B**) and further increases to 85 mm at the load level 321 kN (stage **y**) where yielding is initiated on the brace outside the wrap end. Increase of debonding length (117 mm) is arrested at the load level 341 kN (stage **i_e**) where the debonding from wrap end is initiated and significantly increases to 63 mm at the load level 346 kN (stage **r**). At this stage, debonding crack from wrap end coalesces with the crack from wrap root leading to full debonding. In summary, the gradual loss of secant stiffness during the inelastic stage, between stage **i_r** and stage **y**, is attributed to initiation and growth of the debonding on the secondary bonded interface on the chord and the primary bonded interface from wrap root to 85 mm (35% of full bonding length). The critical length of the debonding crack

on the brace of 181 mm (75% of full bonding length) is recorded just before ultimate failure (stage **r**).



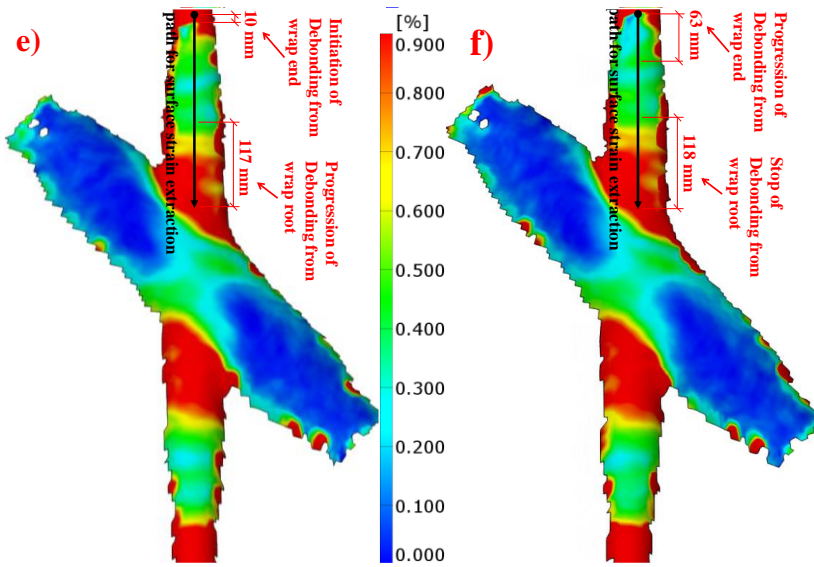


Figure 3-23 Surface strains of cX45-Ss-T_S4 at a) linear elastic state – stage A (170 kN); b) initiation of debonding from wrap root – stage i_r (234 kN); c) Progression of debonding from wrap root – stage B (289 kN); d) initiation of steel yielding – stage y (321kN); e) initiation from wrap end – stage i_e (341kN); f) coalescence of debonding crack from wrap root and wrap end – stage r (346 kN)

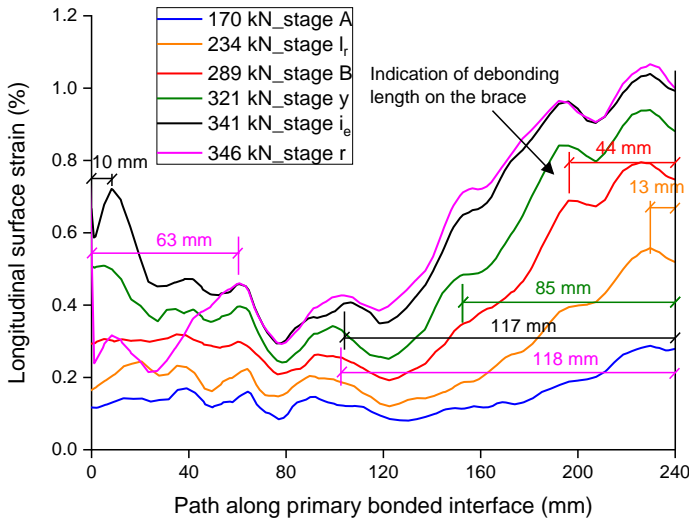


Figure 3-24 Longitudinal surface strains along primary bonded interface at characteristic loading stages – cX45-Ss-T_S4

3.8.5 Small-scale 45° X-joints under compressive load

Figure 3-25 compares the load-displacement curves of wrapped composite joint specimens loaded in compression vs tension (shown in previous section). Wrapped composite joint specimens loaded in compression show 5% larger initial stiffness, 21%

larger elastic load limit and 4% larger ultimate load than in tension. The elastic load limit of wrapped composite joints in compression (215 kN) is 81% higher than the nominal resistance of the counterpart welded joints (119 kN) calculated according to EN 1993-1-8[27]. In the compressive test, all three specimens have the same ultimate load level, and their bonding resistance is all higher than the yielding resistance of the brace cross section confirmed by DIC data. In two out of three specimens (cX45-Ss-C_S1 and C_S3), the bonding resistance is slightly higher, leading to full plastic buckling of the brace cross section outside the wrapped region (see Figure 3-28). By contrast, in specimen cX45-Ss-C_S2, the bonding resistance is a bit lower, allowing the compressive yield strains at the end of the composite wrap to progress inside the composite wrap. Progression of yield strains inside the composite wrap initiates coalescence of the debonding crack from the wrap end and the wrap root, leading to full debonding as in the case of the tensile experiment. Some specimens show slight drops of load in load-displacement curves, which is attributed to the interaction between debonding on the secondary bonded interface and ovalization of the chord due to contact force from the brace.

Surface strains (principal strains) of a representative wrapped composite joint specimen (cX45-Ss-C_S1) are presented in Figure 3-26 at critical load stages identified in load-displacement curves to explain the failure process. The colors in compression DIC images (Figure 3-26) corresponds to the same absolute values of strain as in tension DIC images in Figure 3-23. Additional load transferring mechanism exists in the joints loaded in compression through the direct contact between the brace and the chord member at the root of the joint. This is identified as main reason for higher limit of elastic behavior at 215kN (stage **i_e** in load-displacement curve) compared to joints loaded in tension. The debonding on the secondary bonded interface and the primary bonded interface leads to gradual decrease of secant stiffness from stage **i_r** to stage **y** in the load-displacement curve. Debonding on primary bonded interface, see Figure 3-26 b), is also initiated at slightly higher load level (278 kN, point **i_r**) compared to tensile experiment which is again consequence of partial load transfer through the direct contact inside the joint. Progression of debonding from wrap root is also less compared to tensile specimens at stage **y** (323 kN, Figure 3-26c)) where steel starts to yield. The ultimate load is reached at 361 kN (stage **B**) when local buckling of steel outside of the composite wrap is initiated and leads to reduction of load to 338 kN at stage **C**, see Figure 3-26 d).

The distribution of longitudinal surface strains in Figure 3-27 clearly indicates that in contrast to tensile experiment, the debonding crack in the root of the primary bonded interface is arrested to limited length of 35 mm. The compressive strains at the end of the composite wrap linearly increase as a consequence of local buckling of brace CHS. The steel cross section is expanding in this case which prevents formation of peel stresses at end of the composite wrap.

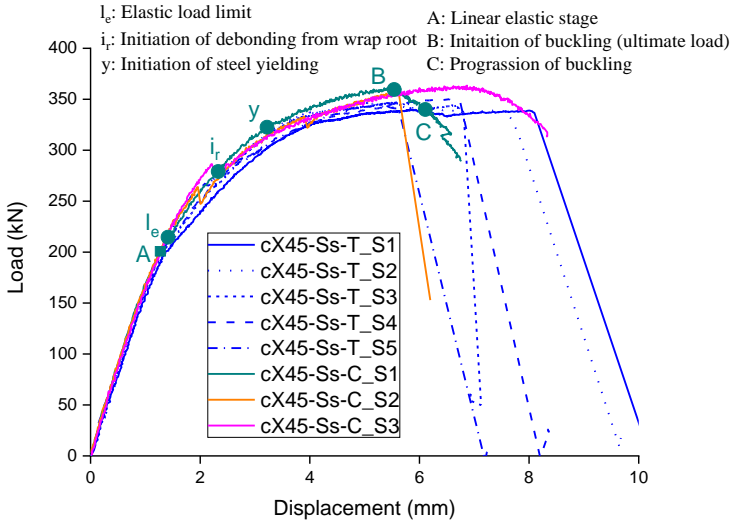
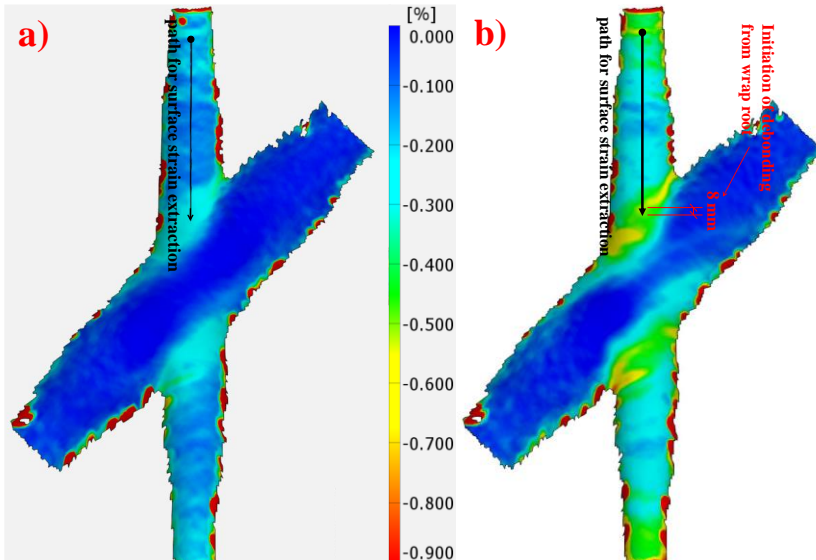


Figure 3-25 Compressive vs tensile behavior of small-scale wrapped composite 45° X-joint specimens



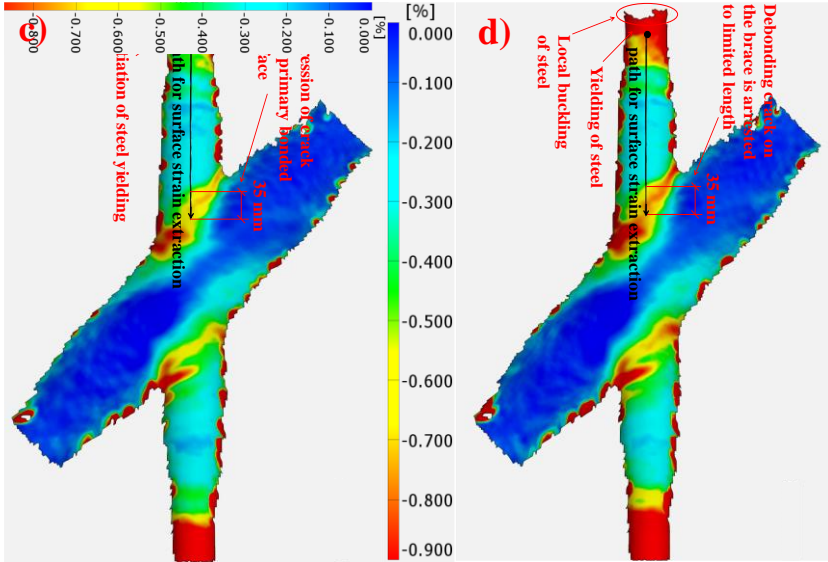


Figure 3-26 Surface strains of cX45-Ss-C_S1 at a) linear elastic state – stage A (200 kN); b) initiation of debonding from wrap root – stage i_r (278 kN); c) initiation of steel yielding – stage y (323 kN); d) local buckling of steel outside composite wrap – stage C (338 kN)

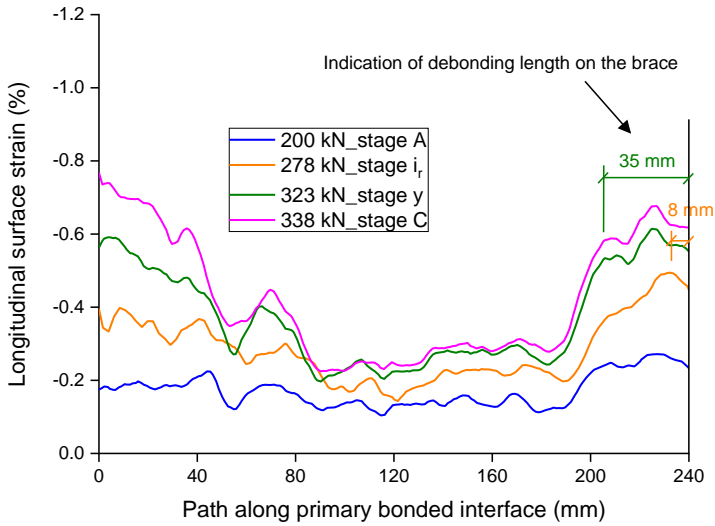


Figure 3-27 Longitudinal surface strains along primary bonded interface at characteristic loading stages – cX45-Ss-C_S1



Figure 3-28 Buckling of brace outside the composite wrap in compressive static test

3.8.6 Medium-scale 45° X-joints under tensile load

Wrapped composite 45° X-joint specimens in medium-scale show linear elastic behavior in axial tension up to a minimum of 1053 kN (64% of the ultimate load), see stage I_e in load-displacement curve of specimen cX45-Ms-T_S3 in Figure 3-29. This elastic load limit of wrapped composite joint is 82% higher than the nominal resistance of the counterpart welded joints (577 kN) calculated according to EN 1993-1-8[27]. Full debonding on the primary bonded interface and final pull-out of steel brace member from the composite wrap is predominant failure mode, accompanied by delamination at the root of wrap and at the end of wrap on brace, as shown in Figure 3-30. Full debonding happens before yielding of the steel brace outside the composite wrap in two out of three specimens (cX45-Ms-T_S1 and S2) while the ultimate load exceeds the yield resistance of steel brace CHS in specimen cX45-Ms-T_S3. The possible reason is the acceptable variability of the debonding resistance within 10%.

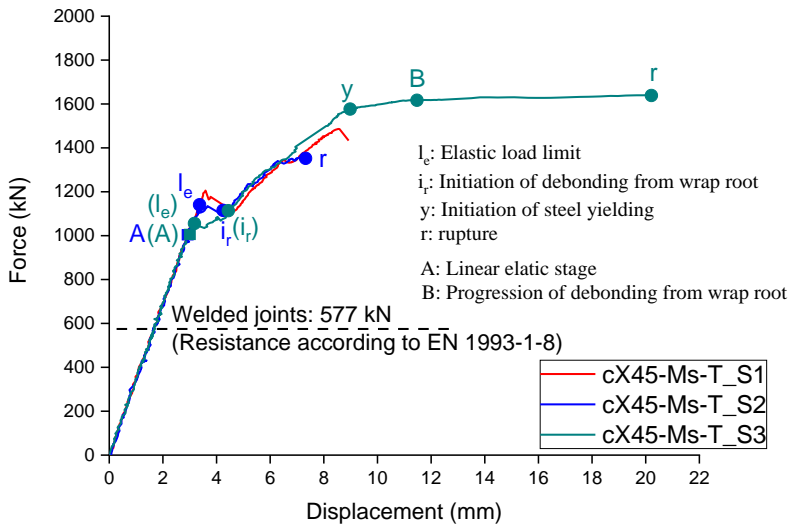


Figure 3-29 Tensile behavior of medium-scale wrapped composite 45° X-joint specimens

Development of surface strains (principal strains) of 2 specimens, cX45-Ms-T_S2 and cX45-Ms-T_S3, are shown in Figure 3-31 and Figure 3-32, respectively. Critical load stages are identified in load-displacement curves to explain the two different failure processes related to final debonding before or after yielding of steel brace. Comparison

between Figure 3-31a) and Figure 3-31b) and between Figure 3-32a) and Figure 3-32b) indicates that the sudden drop of stiffness within 1050~1200kN load range is the consequence of debonding on relatively large area of the chord identified by the local increase of strain on the composite wrap on the chord. This behavior is in contrast to those in small-scale specimens where the stiffness degradation is gradual. The difference in chord debonding behavior between the two scales is probably due to size effect that results in more sudden debonding on the chord with a larger strain energy release in a larger scale. Debonding on the chord is followed by initiation of debonding on the primary bonded interface from wrap root at 1106 kN (stage **i_r**), as shown in Figure 3-31 b) and Figure 3-32 b), respectively. As for the specimen with lower debonding resistance (cX45-Ms-T_S2), the debonding length on the primary bonded interface increases significantly to the critical value (220 mm) leading to final failure at 1353 kN (stage **r**) before yielding of brace CHS, as shown in Figure 3-31 c). By contrast, Figure 3-32 c) indicates that slightly shorter debonding length is reached from wrap root at higher load level (1571kN, stage **y**) where the brace starts to yield in the specimen with larger debonding resistance (cX45-Ms-T_S3). It is followed by final failure with longer critical debonding length (296 mm) reached at 1640 kN (stage **r**) as shown in Figure 3-32 e).

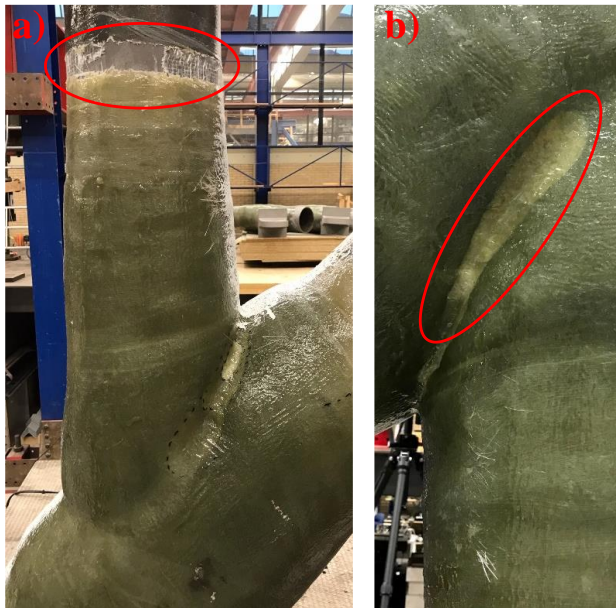


Figure 3-30 Failure patterns on medium-scale wrapped composite 45° X-joint specimens loaded in tension: a) full debonding on the primary bonded interface with delamination at the wrap end; b) delamination at the root of composite wrap

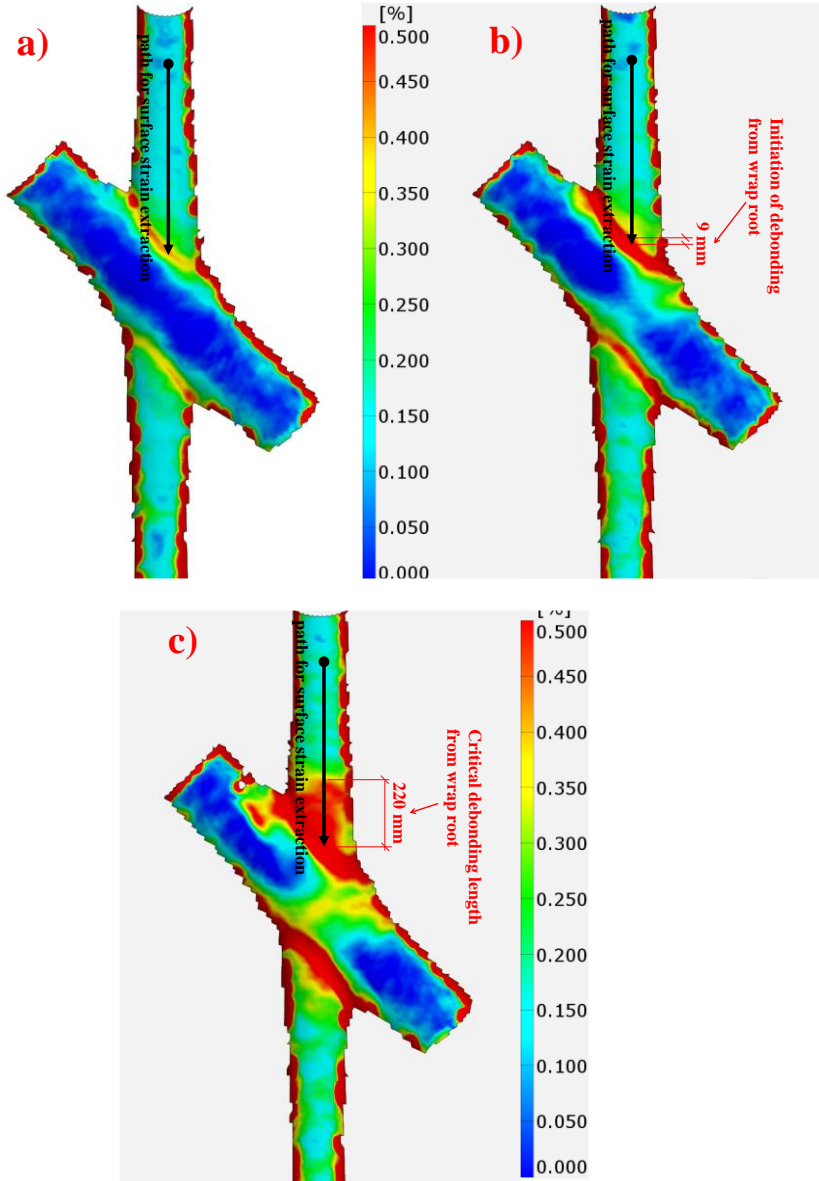
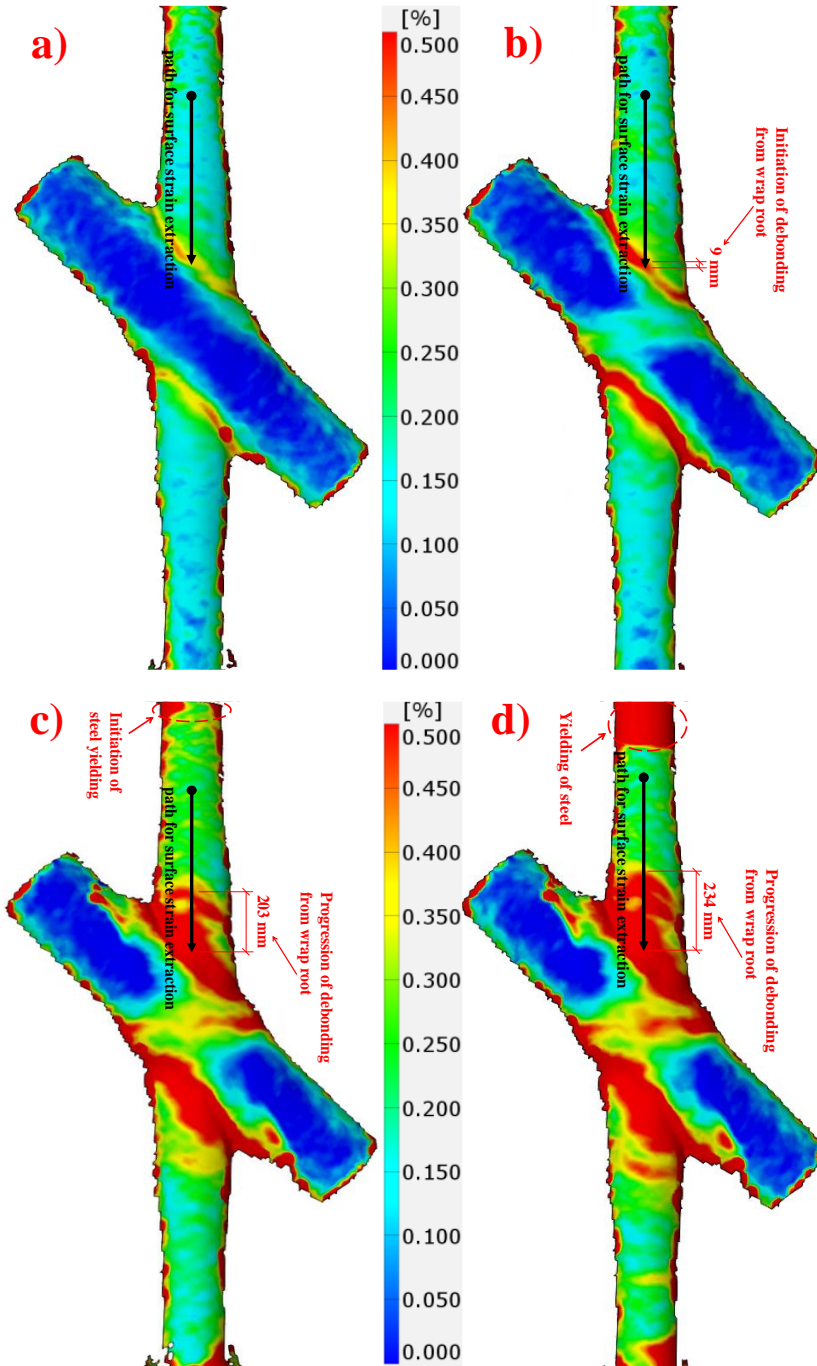


Figure 3-31 Surface strains of cX45-Ms-T_S2 at a) linear elastic state – stage A (1000 kN); b) initiation of debonding from wrap root – stage i_r (1106 kN); c) critical debonding length from wrap root – stage r (1353 kN)



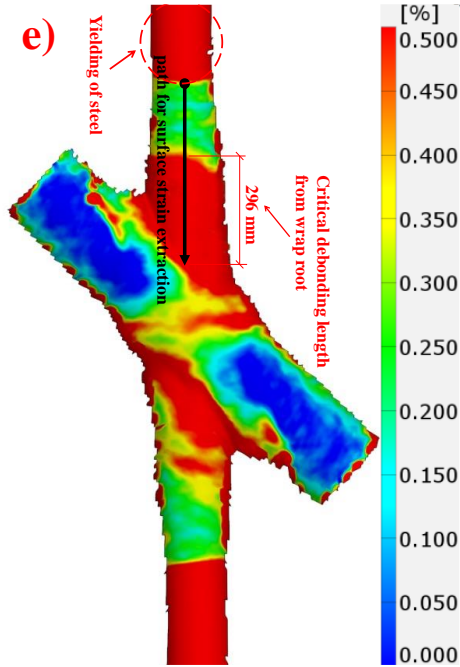


Figure 3-32 Surface strains of cX45-Ms-T_S3 at a) linear elastic state – stage A (1000 kN); b) initiation of debonding from wrap root – stage i_r (1106 kN); c) initiation of steel yielding – stage y (1571 kN); d) Progression of debonding from wrap root – stage B (1618 kN); e) critical debonding length from wrap root – stage r (1640 kN)

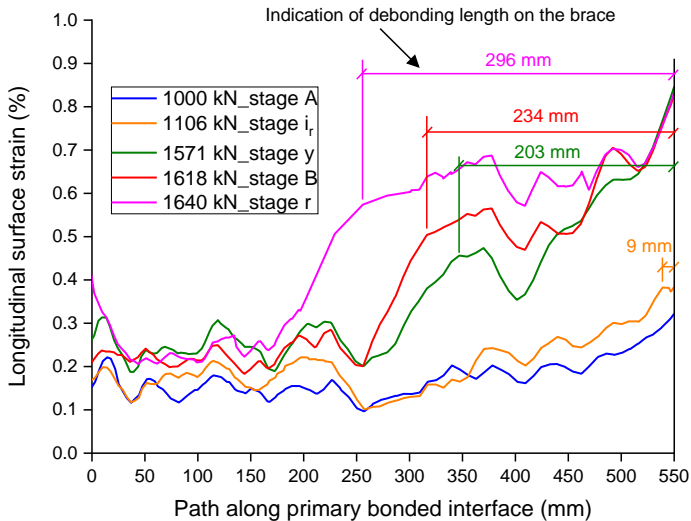


Figure 3-33 Longitudinal surface strains along primary bonded interface of cX45-Ms-T_S3 at characteristic loading stages

Figure 3-33 illustrates longitudinal surface strains of cX45-Ms-T_S3 along the path obtained at critical load stages in Figure 3-32 to indirectly identify the debonding length

on the primary bonded interface. Similar to small-scale tests, strain is relatively uniform in the elastic of medium-scale test. Debonding is initiated with 9 mm cracking length where strain increases considerably to 0.4% at 1248kN (stage **i_r**). Debonding length increases to 203 mm (37%) when yielding of steel is initiated at 1571kN (stage **y**) and subsequently reaches 296 mm (54%) just before final failure at 1640 kN (stage **r**).

3.8.7 Small-scale 90° X-joints under in-plane bending load

Figure 3-34 shows the load-displacement curves of 2 wrapped composite joint specimens vs. 2 welded counterparts (4 results each) in small-scale subjected to in-plane bending load. Wrapped composite joint specimens in this case show 56% larger initial stiffness, 44% larger elastic load limit and 83% larger ultimate load than welded counterparts. The elastic load limit of wrapped composite joints (10 kN) is 6% higher than the nominal load resistance of the counterpart welded joints (9.47 kN), corresponding to the bending moment in the root of the brace calculated according to Wardenier[28]. Fracture of the composite wrap in the complete circumference around the brace member is the predominant failure mode, see Figure 3-35a). Meanwhile, partial debonding on primary bonded interface in the tensile zone and on the joint side and delamination in the compressive zone is observed, as shown in Figure 3-36. Figure 3-35b) indicates that welded specimens are characterized by bending fracture of the brace member next to the welds in the tensile zone, not the failure of the joints. This is confirmed by the fact that the ultimate bending resistance (7.49 kN·m) of the CHS cross section calculated concerning the ultimate strength of steel (590MPa[23]) corresponds to the bending moment in the joint root by applying the ultimate load (19 kN).

Surface strains (Principal strains) of a representative wrapped composite joint specimen (cX90-Ss-B_S2) are presented in Figure 3-37 from DIC results at critical load stages identified in load-displacement curve to explain the failure process. Comparison between Figure 3-37a) and b) indicates that initiation of inelastic behavior of the joint is due to debonding on the secondary bonded interface (chord) in the tensile zone, when transverse bending load reaches 30% of the ultimate load (10kN, stage **A**). Subsequently, debonding on the primary bonded interface in the tensile zone and on the joint side will be initiated and propagate gradually to 80mm (30% of the bonding length) at load level 27kN (stage **B**), as shown in Figure 3-37c). Nevertheless, debonding on the brace will not further develop because fracture of the composite wrap happens in the circumference around the wrap root in the tensile zone and results in final failure at 33kN (stage **C**).

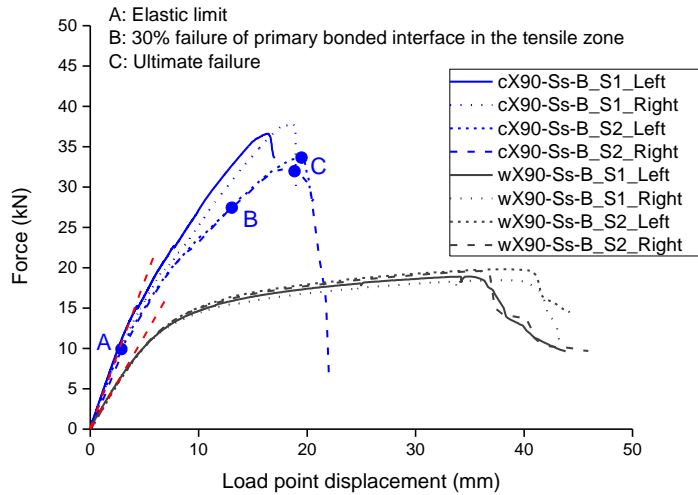


Figure 3-34 Bending behavior of small-scale wrapped composite 90° X-joint specimens vs welded counterparts

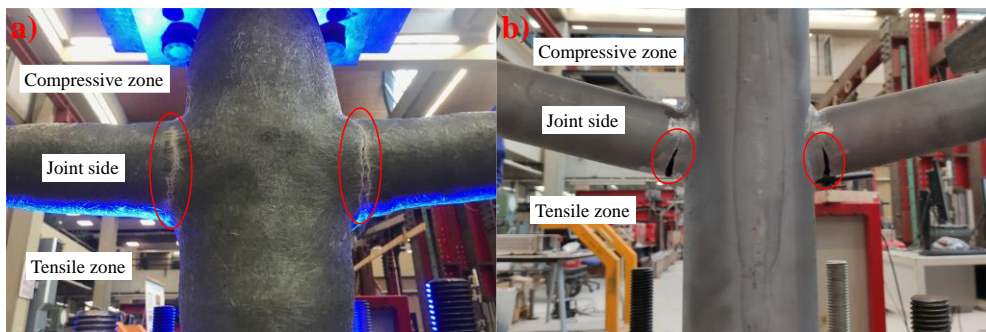


Figure 3-35 Failure pattern on small-scale 90° a) wrapped composite and b) welded X-joint specimens



Figure 3-36 View of cut-plane of small-scale wrapped composite 90° X-joint specimens loaded in bending representing a) debonding on primary bonded interface and fracture of composite wrap on the joint side; b) delamination of composite wrap in the compressive zone

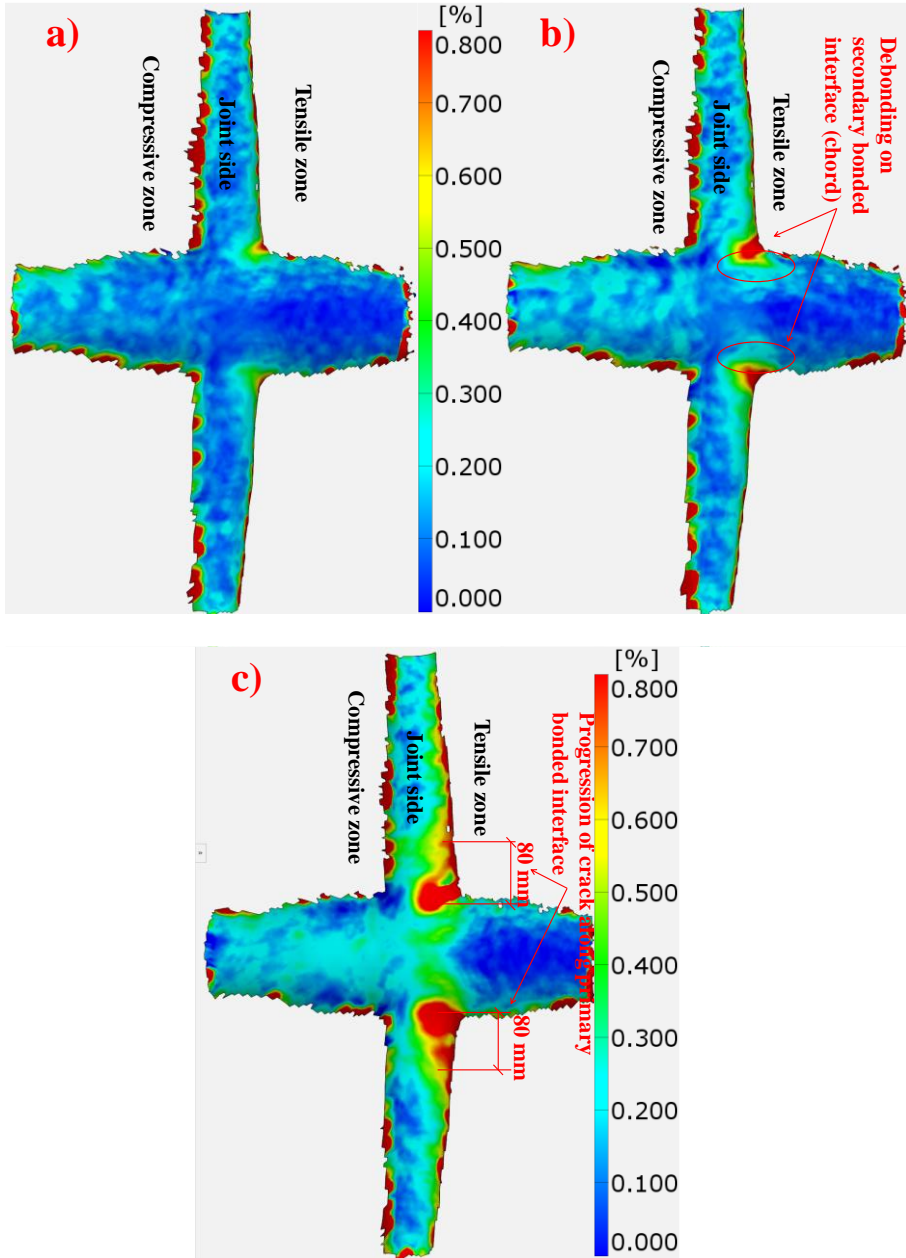


Figure 3-37 Surface strains of cX90-Ss-B_S2 at a) linear elastic state (8kN); b) inelastic state (14kN); c) 30% failure on primary bonded interface – point B (27kN)

3.9 Conclusions

In this Chapter, ultimate load experiments in terms of 6 series of small-scale wrapped composite A-joints and 8 series of X-joints are conducted on 7 types of CHS joint geometries aiming to:

- 1) identify governing failure modes, load transfer mechanism, elastic limit and ultimate load of wrapped composite joints X-joints loaded in tension (45° X-joints), compression (45° X-joints) and in-plane bending (90° X-joints).
- 2) understand differences in failure modes of wrapped composite 45° X-joints at two different scales (small-scale and medium-scale) to investigate size effect on the debonding behavior of wrapped composite joints.
- 3) compare tensile static behavior of wrapped composite 45° X-joints vs. welded counterparts and bending static behavior of composite 90° X-joints vs. welded counterparts.
- 4) investigate the influence of production parameters on the debonding behavior of wrapped composite joints, including effect of bonding primer, resin toughness and steel yielding.

The following conclusions are drawn:

- 1) In tensile, compressive and bending experiments, the ultimate failure load of wrapped composite joints exceeds the yield resistance of the steel brace CHS. Clearly there is opportunity for optimization of composite wrap thickness and length.
- 2) Wrapped composite joints exhibit quasi-ductile failure. The gradual loss of secant stiffness during the inelastic stage is attributed to initiation and growth of partial debonding of the secondary bonded interface on the chord and development of debonding on the primary bonded interface on the brace.
- 3) The final failure of wrapped composite joints is due to full debonding on the brace and pull-out of the steel brace member from the composite wrap in tensile experiments in both small and medium-scales. Partial debonding combined with cracking of the composite material is the governing failure mode in the bending experiment.
- 4) Wrapped composite X-joints in small-scale have 30% to 56% larger joint stiffness, 18% to 44% larger elastic load limit and 3% to 83% larger ultimate load at failure compared to welded counterparts loaded in tension and bending. Wrapped composite 45° X joints in medium-scale (brace diameter 219mm) show linear elastic behavior in axial tension up until a minimum of 1053 kN which is 82% higher than the characteristic resistance of the counterpart welded joints calculated according to EN 1993-1-8.
- 5) Interaction between debonding and steel yielding limits full utilization of the fracture resistance of the bonded interface in the mild steel wrapped composite A-joints. The main reason is initiation and propagation of the debonding crack due to yielding contraction (necking) of the steel-cross section at the wrap end. Wrapped composite A-joints with high strength steel exhibits 75% larger ultimate joint load where steel yielding is prevented.

6) The fracture toughness of polymer resins has a governing effect on the ductility of wrapped composite joints. Larger fracture toughness of the resin helps delay the initiation of debonding crack in mode I from the wrap end due to the steel cross-section contraction.

References

- [1] A. Kwakernaak, J. Hofstede, J. Poulis, and R. Benedictus, *Improvements in bonding metals for aerospace and other applications*, 2nd ed. Elsevier Ltd., 2012. doi: 10.1016/b978-0-12-819140-8.00008-0.
- [2] R. D. Adams, *Adhesive bonding: science, technology and applications*, vol. 48, no. 6. 2021.
- [3] M. Shahid and S. A. Hashim, “Effect of surface roughness on the strength of cleavage joints,” *Int. J. Adhes. Adhes.*, vol. 22, no. 3, pp. 235–244, 2002, doi: 10.1016/S0143-7496(01)00059-8.
- [4] T. Şekerçioğlu, H. Rende, A. Gülsöz, and C. Meran, “The effects of surface roughness on the strength of adhesively bonded cylindrical components,” *J. Mater. Process. Technol.*, vol. 142, no. 1, pp. 82–86, 2003, doi: 10.1016/S0924-0136(03)00463-1.
- [5] K. Uehara and M. Sakurai, “Bonding strength of adhesives and surface roughness of joined parts,” *J. Mater. Process. Technol.*, vol. 127, no. 2, pp. 178–181, 2002, doi: 10.1016/S0924-0136(02)00122-X.
- [6] S. Azari, M. Papini, and J. K. Spelt, “Effect of surface roughness on the performance of adhesive joints under static and cyclic loading,” *J. Adhes.*, vol. 86, no. 7, pp. 742–764, 2010, doi: 10.1080/00218464.2010.482430.
- [7] S. Ebnesaajjad and A. H. Landrock, *Adhesives Technology Handbook*. 2014. doi: 10.1016/B978-0-323-35595-7.00023-1.
- [8] K. W. Allen, *Adhesion and Adhesives.*, vol. 22, no. 5. 1986. doi: 10.1201/9781482269741-24.
- [9] S. RC., *Handbook of surface preparation*. New York, 1974.
- [10] S. C. Aker, “The Function of Adhesive Primers in Adhesive Bonding of Aircraft Structures,” *Appl. Polym. Symp.*, vol. 19, 1972.
- [11] N. J. DeLollis., *Adhesives, adherends, adhesion*. 1980.
- [12] L. F. M. da Silva, T. N. S. S. Rodrigues, M. A. V. Figueiredo, M. F. S. F. de Moura, and J. A. G. Chousal, “Effect of adhesive type and thickness on the lap shear strength,” *J. Adhes.*, vol. 82, no. 11, pp. 1091–1115, 2006, doi: 10.1080/00218460600948511.
- [13] L. Liao, C. Huang, and T. Sawa, “Effect of adhesive thickness, adhesive type and scarf angle on the mechanical properties of scarf adhesive joints,” *Int. J. Solids Struct.*, vol. 50, no. 25–26, pp. 4333–4340, 2013, doi: 10.1016/j.ijsolstr.2013.09.005.
- [14] L. Liao and C. Huang, “Numerical analysis of effects of adhesive type and geometry on mixed-mode failure of adhesive joint,” *Int. J. Adhes. Adhes.*, vol. 68, pp. 389–396, 2016, doi: 10.1016/j.ijadhadh.2015.12.013.
- [15] P. He and M. Pavlovic, “Failure modes of bonded wrapped composite joints for

steel circular hollow sections in ultimate load experiments,” *Eng. Struct.*, vol. 254, no. August 2021, p. 113799, 2022, doi: 10.1016/j.engstruct.2021.113799.

[16] X. L. Zhao and L. Zhang, “State-of-the-art review on FRP strengthened steel structures,” *Eng. Struct.*, vol. 29, no. 8, pp. 1808–1823, 2007, doi: 10.1016/j.engstruct.2006.10.006.

[17] P. He, W. Feng, and M. Pavlovic, “Influence of steel yielding and resin toughness on debonding of wrapped composite joints,” *Compos. Struct.*, vol. 312, no. February, p. 116862, 2023, doi: 10.1016/j.compstruct.2023.116862.

[18] International Standards Organization, “ISO 6892-1 International Standard INTERNATIONAL STANDARD ISO 6892-1:2009(E) Metallic materials — Tensile testing — Part 1: Method of test at room temperature 1,” *Met. Mater.*, vol. 2009, p. 64, 2009.

[19] International Standards Organization, “ISO 527-1:2012 - Plastics - Determination of tensile properties - Part 1: General principles,” 2012, [Online]. Available: www.iso.org

[20] International Standards Organization, “ISO 527-2:1996 – Plastics — Determination of tensile properties – Part 2: Test conditions for moulding and extrusion plastics,” 2009, [Online]. Available: http://www.chemshow.cn/UploadFile/datum/1000/huayangyq2008w_2009420145250792688.pdf

[21] International Standards Organization, “ISO 14126:1999 - Fibre-reinforced plastic composites - Determination of compressive properties in the in-plane direction,” 1999.

[22] International Standards Organization, “ISO 14129: 1997 Fibre-reinforced plastic composites — Determination of the in-plane shear stress/shear strain response, including the in-plane shear modulus and strength, by the plus or minus 45 degree tension test method,” 1997.

[23] M. Liatzouras, “Feasibility of non-welded CHS steel joints adhesively bonded by GFRP,” MSc Thesis, TU Delft, 2018.

[24] M. Pavlovic, M. Veljkovic, and M. Liatzouras, “Wrapped FRP Joints of Steel Hollow Sections,” in *Eighth International Conference on THIN-WALLED STRUCTURES – ICTWS 2018*, Lisbon, Portugal, 2018, pp. 1–11.

[25] P. He and M. Pavlovic, “Feasibility of Wrapped FRP Circular Hollow Section Joints,” in *Proceedings of the 17th International Symposium on Tubular Structures*, 2019, pp. 292–299. doi: 10.3850/978-981-11-0745-0_043-cd.

[26] W. Feng, P. He, and M. Pavlovic, “Combined DIC and FEA method for analysing debonding crack propagation in fatigue experiments on wrapped composite joints,” *Compos. Struct.*, vol. 297, no. March, p. 115977, 2022, doi: 10.1016/J.COMPSTRUCT.2022.115977.

- [27] EN 1993-1-8, “Eurocode 3: Design of steel structures - part 1-8: Design of joints.” CEN, pp. 395–453, 2015. doi: 10.1201/b18121-19.
- [28] J. Wardenier, *Hollow Section in Structural applications*. CIDECT, 2010. doi: 10.1007/978-94-011-5856-5_6.

4. MATERIAL AND INTERFACE EXPERIMENTS

This chapter presents the results of the double cantilever beam (CCB) and the end notched flexure (ENF) tests conducted on the composite-steel bonded interface. The aim is to quantify the fracture properties of the bi-material interface used in the wrapped composite joints. The tri-stage fracture process is identified, encompassing crack initiation, softening, and fiber bridging. A novel approach is proposed, based on the digital image correlation (DIC) technique, to quantify the crack length and the crack tip opening displacement during the experiments. The strain energy release rate (SERR) is calculated using the extended global method (EGM).

The influence of the adherend position in 3ENF tests and the effect of the pure bending moment loading on obtaining the fracture properties of the bi-material interface are discussed.

4.1 Introduction

It was found in Chapter 3 that debonding of the composite-steel bonded interface is the predominant failure mode of wrapped composite joints subjected to axial load[1], [2], as shown in Figure 4-1. It is therefore imperative to understand the fracture behavior of the composite-steel bonded interface as a prerequisite for prediction of the joint resistance. Meanwhile, as the main load transferring component, the material properties of composite wrap should be obtained as the input for finite element analysis. The most explicit way to obtain these properties is to conduct material and interface tests at the material level due to simple geometry and ease of specimen production, ease of test conduction, and the opportunity to investigate failure mechanisms separately.

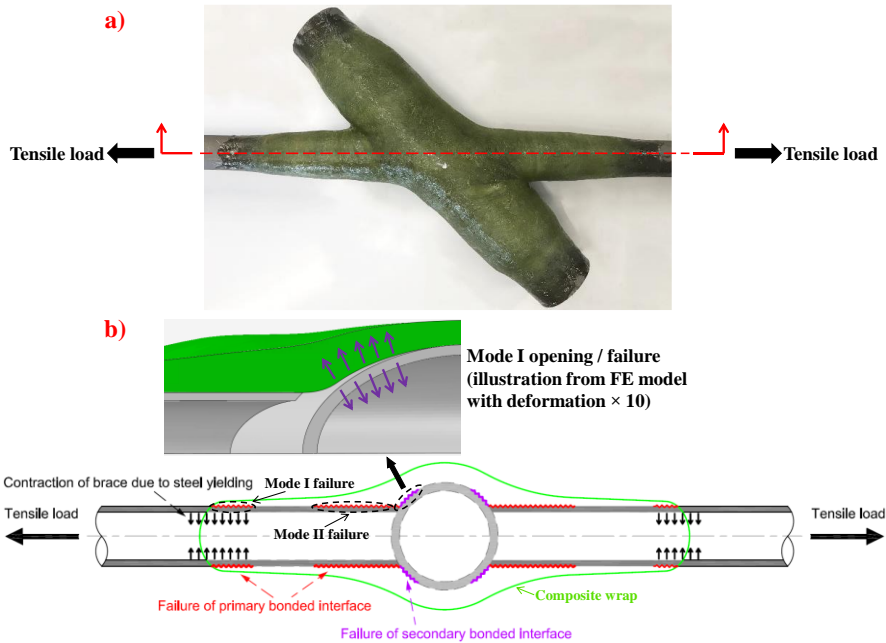


Figure 4-1 a) Wrapped composite joints – a 45° X-joint specimen [1]; b) summary of failure modes and load transfer mechanism of wrapped composite joints loaded in tension [1]

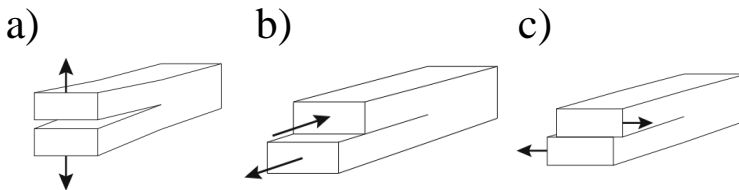


Figure 4-2 a) Fracture modes of the interfacial cracking – a) mode I: opening; b) mode II: in-plane shear; c) mode III: out-of-plane shear

An interfacial crack can propagate in three different fracture modes in fracture mechanics: mode I (opening), mode II (in-plane shear) and mode III (out-of-plane shear),

as illustrated in Figure 4-2. Mode I failure is pronounced at the secondary bonded interface (on the chord) due to local bending of the composite wrap and at the end of the primary bonded interface attributed to contraction of the brace cross section resulting from steel yielding [1]. In comparison, mode II failure is governing at the root of the primary bonded interface (on the brace) leading to coalescence of the debonding crack along the braces, see Figure 4-1 b). The double cantilever beam (DCB) specimen configuration was initially used in the ASTM-D5528 [3] and the ISO 15024 [4] standards for evaluation of delamination in unidirectional composites under mode I loading, and was utilized by many researchers to acquire fracture properties of the adhesively bonded joints[5]–[8]. In comparison, the three-point end notched flexure (3ENF) specimen configuration was initially proposed by Russel [9], [10] and was widely established in the testing standards, such as ASTM D7905 [11], for evaluation of delamination in unidirectional composites under mode II loading. Many researchers used it to acquire mode II fracture properties of the adhesively bonded joints or delamination toughness of composite laminate [12]–[15]. Nevertheless, an important feature of 3ENF configuration is that the crack propagation is generally unstable. Some researchers have found that the stable crack growth can be achieved when the initial crack length is at least 0.7 times of the half span [16], [17]. However, this finding is specific to the delamination crack initiation and propagation at the interply interfaces of the composite laminates or adhesively bonded joints. It is still unknown how to achieve stable crack growth in directly bonded composite-steel interfaces. Additionally, several authors have also reported that 3ENF test allows only the determination of fracture behavior related to crack initiation but not the R-curve behavior [18], [19], which characterizes the crack propagation. As an alternative, the four-point end notched flexure (4ENF) test was proposed to obtain more stable crack growth in mode II loading scenario [20], [21].

It should be noted that all the experimental work mentioned above was based on the symmetric (same material and same thickness) DCB, 3ENF and 4ENF configurations. In the case of asymmetric configurations, with un-even thickness of adherends around the interface and/or dissimilar materials, limited research studies were conducted to investigate fracture behavior of DCB[22]–[27] and 3ENF[28]–[33] specimens. No research studies regarding asymmetric 4ENF specimens are reported - to the best of the author's knowledge. The fracture behavior of an asymmetric composite-metal bonded interface is complex due to the following three reasons: a) the inherently existed mode mixity as result of loading asymmetry and material asymmetry across the interface[34]; b) dependency of interfacial fracture behavior on the material and surface treatment of the adherends, types of resin and adhesive; c) non-linear behavior of the interface attributed to plastic deformation of metal adherend where linear elastic fracture mechanics (LEFM) may not apply. To alleviate the mode mixity attributed to the in-plane sliding, the design of bi-material DCB and ENF configurations based on the criterion that the two bending arms have the same longitudinal strain at the faying surfaces was proposed [25], [26], [32], [35], [36].

This Chapter focuses on the acquisition of material properties of composite wrap by testing composite coupon specimen configuration, and acquisition of mode I and

mode II fracture behavior of glass fiber composite-steel bonded interface by testing DCB, 3ENF and 4ENF specimen configuration. Such bonded interface is utilized in the innovative non-welded wrapped composite joints. However, the developed results and methods are applicable to other connections where composite is directly bonded to steel (excluding adhesive) by wet lamination or other suitable application techniques. Novel approach to analyze 2D DIC measurement data was developed to obtain the crack length and the crack tip opening displacement (CTOD) during the tests. The strain energy release rate (SERR) was calculated by extended global method (EGM) from experiments.

4.2 Material experiments of composites

Due to quasi-isotropic property of the composite laminate used in wrapped composite joints, the tensile, compressive, and in-plane shear behavior should be identified through the corresponding material coupon experiments of composites. The identification includes E-modulus, strength and non-linear behavior in tensile, compressive and in-plane shear direction.

4.2.1 Specimens and materials

3 series of composite coupon specimens are designed in the material experiments, as summarized in Table 4-1. Geometry with dimensions of the coupons in Table 4-1 are determined based on the ISO standards[37]–[39] and are shown in Figure 4-3. Each series of coupons is accomplished with 5 nominally identical specimens to characterize scattering of the material properties. Following naming convention is used for test series given in Table 4-1 and used afterwards in analysis of the results: cT, cC, cIPS – tensile, compressive, in-plane shear coupons of composites, respectively; 1/2/3/4/5 – nominally identical coupons, number 1, 2, 3, 4, 5, etc.

Table 4-1 Overview of series and dimensions of composite coupon specimens (unit: mm)

Test series	Specimen	Material type	Standard for test design
1	cT- 1/2/3/4/5	Composite	ISO 527-1 [37]
2	cC-1/2/3/4/5	Composite	ISO 14126 [39]
3	cIPS-1/2/3/4/5	Composite	ISO 14129 [38]

The composite coupons used in the material experiments were manufactured by hand-lamination in a wet-layup process using E-glass fiber plies and a vinyl ester thermoset resin (resin 2 used in Chapter 3). The hand lamination is performed in a controlled factory environment at room temperature and humidity conditions with quality control to ensure good compaction and avoiding air gaps. The E-glass fiber plies are composed of bidirectional woven fabrics and chopped strand mat, and the composite laminate presents a fiber volumetric fraction ranging 30%~32%. The laminated plate was left for curing at a controlled environment of temperature and humidity and no post-curing was applied.

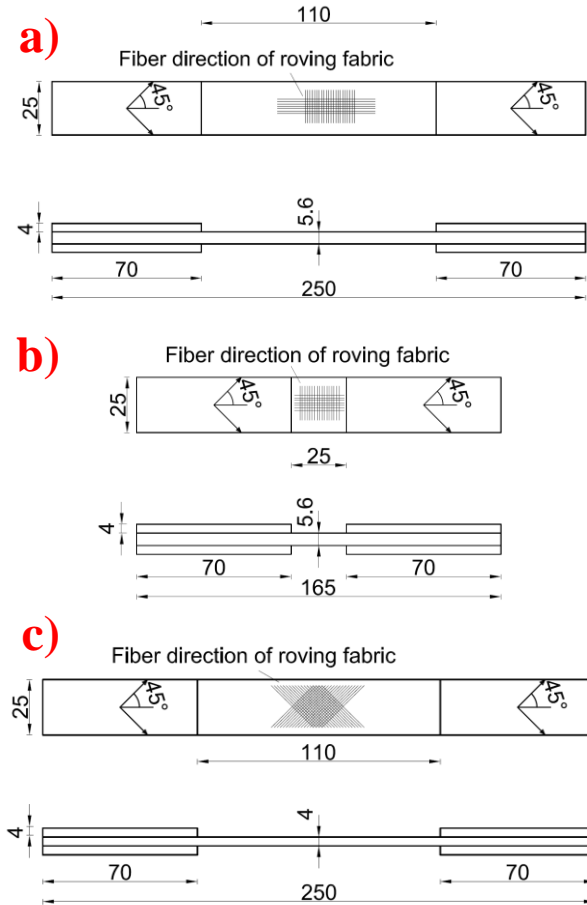


Figure 4-3 Geometry with dimensions of composite specimens in a) tensile, b) compressive and c) in-plane shear coupon experiments

4.2.2 Experiment and measurement set-up

The material coupon tests are conducted in the INSTRON 1251 tensile and compressive press, as shown in Figure 4-4 a) and b). It is equipped with a load cell with 100 kN capacity in static loading and 200 kN in dynamic loading. The axial load is applied through gripping the composite material tabs with $\pm 45^\circ$ fiber orientation at ends by the wedges. Load is applied by displacement control with rate of 2 mm/min in tensile and in-plane shear experiments, respectively, whilst 0.3 mm/min in compressive experiments, to provide quasi-static loading conditions. Measurement of the material experiments are performed by the 3-dimensional (3D) digital image correlation (DIC) system including two cameras with 12-megapixel resolution due to availability of set-up, as shown in Figure 4-4 c). A thin layer of white matt paint was coated to the side surface of the specimens followed by a sprayed black speckle pattern to create the measurement surface for DIC analysis. A polarized blue light was used during the test to provide steady illumination conditions for accurate measurements. After tests, the test

data can be processed in the GOM Aramis graphical analysis software with high accuracy and pertinence after the experiments.

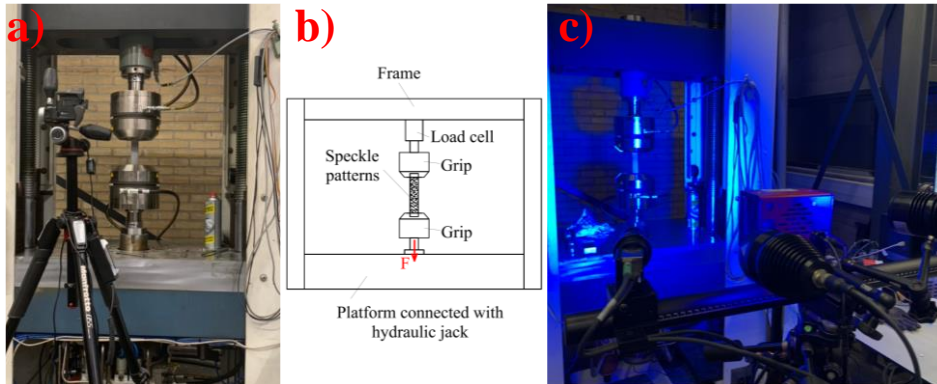


Figure 4-4 Composite coupon experiments conducted in a) the INSTRON 1251 tensile and compressive press illustrated in b) the schematic view; c) the 3D-DIC measurement system

4.2.3 Overview of material coupon test results

General overview of all test results is given in Table 4-2. The indicated failure modes and scenarios of failure process are presented through the experimental results. More detailed analysis is explained in the subsequent subsections.

Table 4-2 Overview of material coupon test results

Specimen	Tensile modulus [MPa]	Tensile strength [MPa]	Strain at failure [%]	Poisson's ratio (ν_{12})	Failure mode
cT-1	12050	197.39	1.95	0.15	Failure of laminate away from the tab
cT-2	12562	221.84	2.39	0.15	
cT-3	10866	231.58	2.61	0.14	Failure of laminate in the middle
cT-4	12365	215.57	2.32	0.13	Failure of laminate away from the tab
cT-5	11148	214.49	2.36	0.15	
Average (and COV [%])	11798 (6.37)	216.17 (5.78)	2.33 (10.23)	0.147 (6.49)	
Specimen	Compressive modulus [MPa]	Compressive strength [MPa]	Strain at failure [%]	-	Failure mode
cC-1	12720	201.21	1.75		Delamination within the gauge length
cC-2	11916	198.12	1.63		
cC-3	12555	196.97	1.85		
cC-4	11764	191.96	1.63		
cC-5	11432	212.29	1.82		
Average (and COV [%])	12077 (4.50)	200.11 (3.78)	1.73 (6.03)		
Specimen	Shear modulus [GPa]	Shear strength [MPa]	Strain at failure [%]	-	Failure mode
cIPS-1	2.94	72.04	0.050		In-plane shear failure in the middle
cIPS-2	3.04	69.56	0.042		
cIPS-3	3.22	74.30	0.046		
cIPS-4	2.96	71.43	0.044		
cIPS-5	3.45	73.60	0.047		
Average (and COV [%])	3.12 (6.81)	72.19 (2.58)	0.046 (6.90)		

4.2.4 Tensile coupon tests of composites

Figure 4-5 shows the stress-strain curves of 5 tensile coupons of composite material.

It can be seen that composite material shows quasi-brittle behavior under tensile load up to final rupture. Measurable non-linear deformation can be quantified prior to failure. A representative coupon as shown in Figure 4-6 indicates the final failure mode of tensile rupture of composite material.

The tensile strains are determined using two virtual extensometers through the GOM graphic software, one 40mm in the longitudinal axis and one 20mm in the transverse direction, positioned at the middle of the coupons. The tensile modulus ($E_{x,t}$) was determined by applying a least squares linear regression analysis on the stress strain curve on the strain interval $0.05\% \leq \epsilon \leq 0.25\%$ [37]. The tensile strength is calculated as $f_{x,t} = F_m/A$, where F_m is maximum force obtained during the loading history. The strain at failure (ϵ_m) is obtained as the strain corresponding to the point where tensile strength is reached[37]. The Poisson's ratio is determined by plotting the change in width against the change in thickness of the coupon, according to the extensometer's measurements, and applying a least squares linear regression fit on the strain interval.

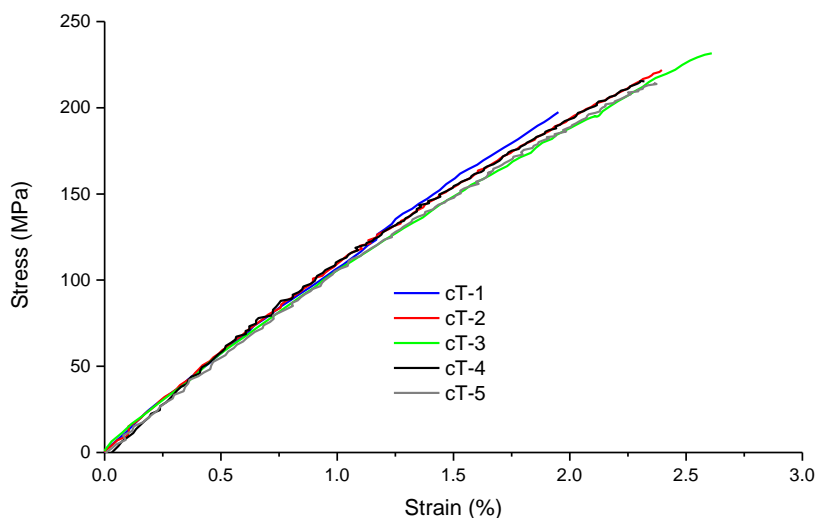


Figure 4-5 Stress-strain curves of composite material under axial tensile load



Figure 4-6 Failure mode of tensile rupture of composite material in tensile coupon tests

4.2.5 Compressive coupon tests of composites

Figure 4-7 shows the stress-strain curves of 5 composite material coupons subjected to axial compressive load. Composite material exhibits a comparable elastic modulus in axial tension and compression, with difference within 2%. Additionally, 7% lower

strength and 35% lower strain at failure are observed in the compressive experiments compared to tensile experiments, attributed to compressive buckling of the fibers forming kink bands and premature failure. The final failure mode of the coupon is delamination within the gauge length, as shown in Figure 4-8.

The compressive modulus is defined as $E_{x,c} = (\sigma''_c - \sigma'_c) / (\varepsilon''_c - \varepsilon'_c)$, where σ''_c is the compressive stress at $\varepsilon''_c = 0.25\%$, and σ'_c is the compressive stress at $\varepsilon'_c = 0.05\%$. The compressive strength is calculated as $f_{x,c} = F_m / (b \cdot h)$ [39]. Strains are calculated along the loaded surface of the coupon through the virtual extensometers in GOM graphic software, similarly as in the tensile experiments.

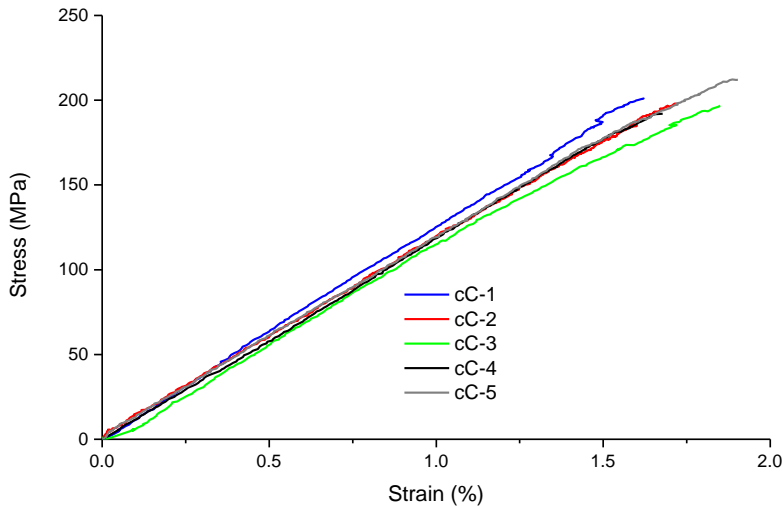


Figure 4-7 Stress-strain curves of composite material under axial compressive load



Figure 4-8 Failure mode of delamination of composite material in compressive coupon test

4.2.6 In-plane shear coupon tests of composites

The stress-strain curves of 5 composite material coupons subjected to in-plane shear load are shown in Figure 4-9. The failure mode is overstretching of the fibers in the $\pm 45^\circ$ direction followed by the final failure, as illustrated in Figure 4-10.

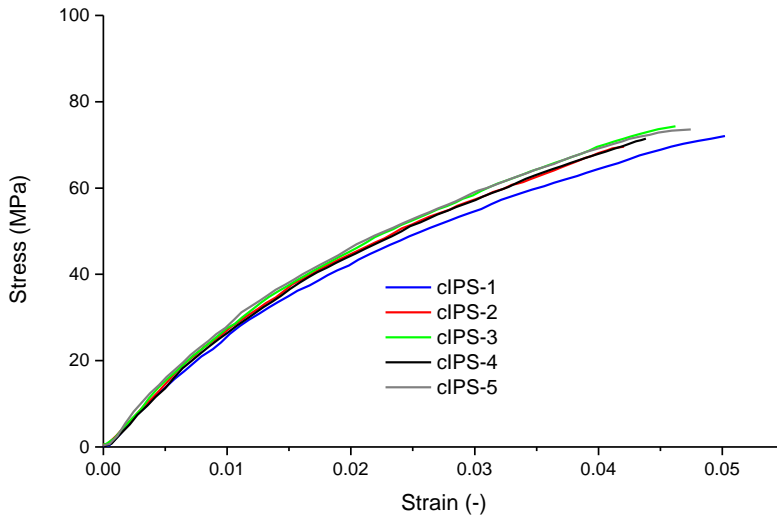


Figure 4-9 Stress-strain curves of composite material under in-plane shear load

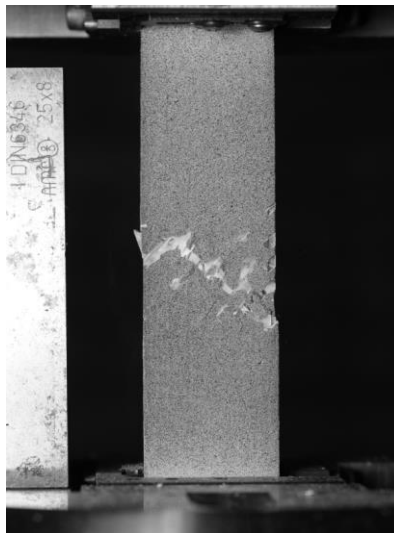


Figure 4-10 Failure mode of composite material in the in-plane shear coupon test

The shear modulus G_{xy} is calculated as the slope of the stress-strain curve within the range of 0.001~0.005 shear strain. The shear strength during the experiment is calculated as $f_{xy,y} = F_m/(2 \cdot b \cdot h)$, where F_m is the maximum attained load during the loading history, and b and h represent the width and the thickness of the coupon, respectively[38]. The in-plane shear strain of the coupon is calculated as $\gamma_{12} = \varepsilon_x - \varepsilon_y$ where ε_x and ε_y are the strains obtained using virtual extensometers in the middle of the coupon during the DIC post-processing analysis, respectively.

4.3 Interface (debonding) experiments

The quasi-isotropic properties of composite material used in the wrapped composite joints leads to identical fracture properties of composite-steel bonded interface in mode II and mode III. Consequently, the main objective of the interface (debonding) experiments presented here is to understand and quantify the mode I and mode II fracture behavior of the used metal-composite interface.

4.3.1 Specimens and materials

1 Series of DCB tests (series 4) are performed to characterize and quantify the mode I fracture behavior of the composite-steel bonded interface with configuration illustrated in Figure 4-11. In contrast, 3 series of 3ENF and 4ENF tests are performed to characterize the mode II fracture behavior. 3ENF specimens with composite laminate positioned as the upper and the lower adherend are illustrated in Figure 4-12 a) and Figure 4-12 b) and tested in test series 5 and test series 6, respectively, to study the influence of adherend position on the mode II behavior of composite-steel bonded interface. 4ENF specimens with composite laminate served as lower adherend (with respect to direction of the applied load) are illustrated in Figure 4-12c) and tested in test series 7 to investigate the effect of a different loading scenario on the mode II fracture process of composite-steel bonded interface. Each test series is accomplished with at least 3 nominally identical specimens to characterize scattering of the material properties. The mode I test specimens are named as DCB-S1/2/3 where S refers to static test and 1/2/3 refers to specimen number 1, 2, 3, respectively. In comparison, the naming convention of the mode II test specimens refers to the testing method (3ENF/4ENF), position of the composite laminate (CU, CL – composite laminate served as upper or lower adherend, respectively), and the specimen number (S1/2/3/etc.).

In DCB tests (series 4) the steel is positioned as the upper adherend with thickness $h_{\text{steel}} = 3$ mm while the composite laminate is located as the lower adherend with thickness $h_{\text{composite}} = 7.62$ mm. The adherend length L and width B is 180 mm and 20 mm, respectively, and the pre-crack is inserted with length $a_0 = 60$ mm. The pre-crack length a_0 is defined as the distance between the section of the applied load and the pre-crack tip. The loading pin with length $L_p = 25$ mm is bonded to the upper and lower adherends for load transfer. The overview of the dimensions of the DCB specimens are summarized in Table 4-3.

Overview of the dimensions of the 3ENF and 4ENF specimens are shown in Table 4-4. h_{steel} and $h_{\text{composite}}$ refer to the thickness of steel and composite laminate adherend, respectively, while the specimen length, specimen width and the span length are designated as l , B and $2L$, respectively, see Figure 4-12. The pre-crack length a_0 is defined as the distance between the support roller (pin) and the pre-crack tip while the distance of the two loading pins in 4ENF specimens is designated as d .

The composite-steel bonded plates were manufactured by hand-lamination in a wet-layup process. Test coupons were cut from the laminated composite-steel plates using water jet. Surface treatment of the steel plate, grade S355, included grit blasting and degreasing by acetone. A non-adhesive Teflon based tape with 32 μm thickness was

placed at the steel plate end before lamination to create a pre-crack. Subsequently, the hand lay-up lamination was performed using E-glass fiber plies and a vinyl ester thermoset resin (resin 2) in a controlled factory environment at room temperature and humidity conditions with quality control to ensure good compaction and avoiding air gaps. The E-glass fiber plies use is the same as the material used in the composite coupon experiments. The laminated plate was left for curing at a controlled environment of temperature and humidity and no post-curing was applied. It should be noted that the composite laminate was directly bonded on the steel plate without application of intermediate adhesive layer so that the thickness of the adhesive layer is negligible.

The 3ENF (test series 5 and 6) and DCB/4ENF specimens (test series 4 and 7) were produced in 2 different batches. 3ENF specimens were produced first with low roughness of steel adherend. Subsequently, DCB and 4ENF specimens were designed with decreased thickness of steel adherend and were produced with higher roughness of steel adherend, aiming to increase the bonding properties. In 4ENF tests, the mode II crack is initiated by the shear strains at the crack which are proportional to the difference in longitudinal strains at the interface in the steel and composite adherends. Both adherends follow same curvature due to bending. Therefore, decreasing the thickness of steel adherend relative to the thickness of the composite adherend helps reducing the longitudinal strain in the steel adherend at the crack tip, thereby reducing the yielding of steel during initiation or crack propagation process.

Table 4-3 Test series and dimensions of DCB specimens (unit: mm)

Test series	Specimen	h_{steel}	$h_{\text{composite}}$	L	B	a_0	L_p
4	DCB-S1/2/3	3	7.62	180	20	60	25

Table 4-4 Overview of test series and dimensions of 3ENF and 4ENF specimens (unit: mm)

Test series	Specimen	h_{steel}	$h_{\text{composite}}$	l	$2L$	B	d	a_0
5	3ENF-CU-S1/2/3/4/5	4	12.3	220	180	25	-	30
6	3ENF-CL-S1/2/3	4	12.3	220	180	25	-	30
7	4ENF-CL-S1/2/3	3	7.6	180	120	20	70	40

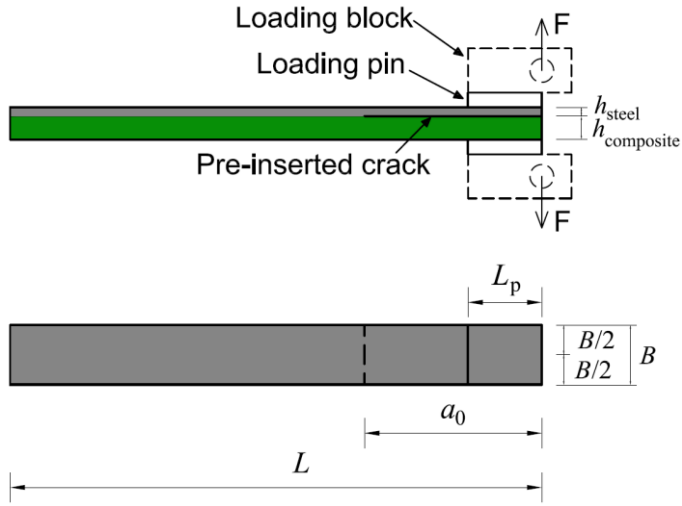
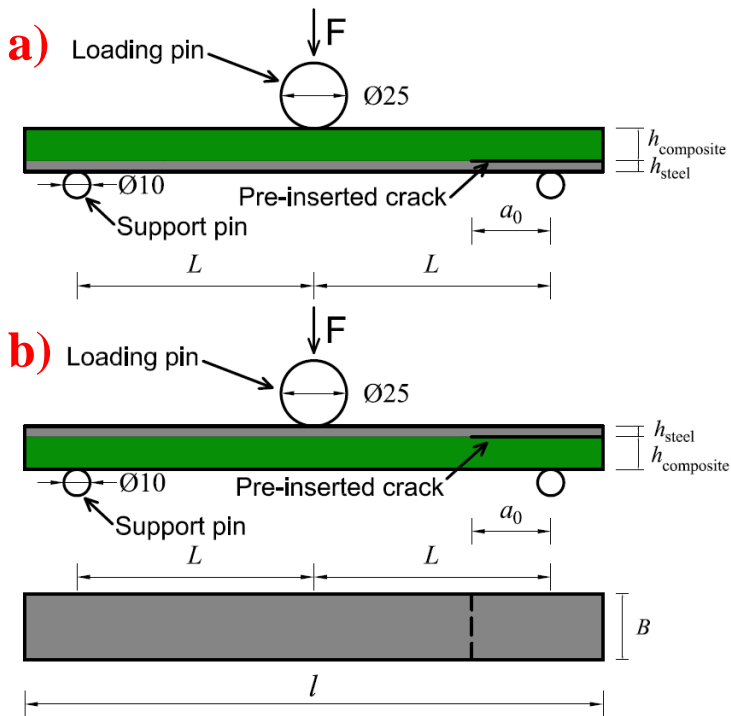


Figure 4-11 Composite-steel DCB specimens



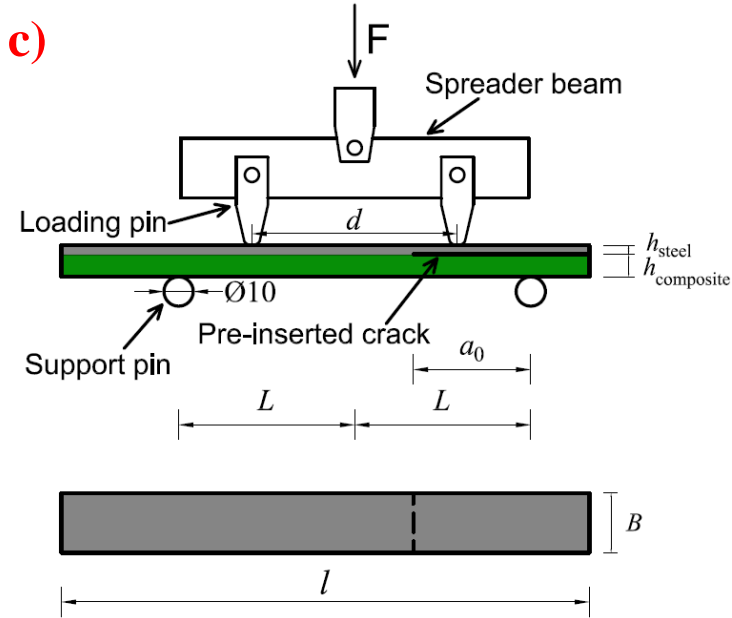


Figure 4-12 Composite-steel mode II fracture test specimens: a) 3ENF specimens with composite as upper adherend; b) 3ENF specimens with composites as lower adherend; c) 4ENF specimens with composite as lower adherend

4.3.2 Experiment and measurement set-up

All 4 series of interface tests were conducted in the UTM 25 universal testing machine with a 15kN load cell, as shown in Figure 4-13. In DCB tests, the specimen is connected to the fixture through the pin connection at the upper and lower adherend, see Figure 4-13 a). The specimens remain supported on the test frame and are connected to the fixture through either one cylindrical loading pin in 3ENF tests (see Figure 4-13 b)) or two arc-edged loading pins symmetrically bolted to a spreader beam in 4ENF tests (see Figure 4-13 c)). The crack driving force F is applied through the hydraulic jack to the upper adherend at a constant displacement rate of 1 mm/min.

Prior to the tests, the specimens were coated on the side to measure the full field displacements around the crack path using a 2-dimensional (2D) digital image correlation (DIC) system. A thin layer of white matt paint was coated to the side surface of the specimens followed by a sprayed black speckle pattern to create the measurement surface for DIC analysis. A camera with 51-megapixel resolution was set to take photos of the specimens at a frequency 1/3 Hz and a polarized blue light was used during the test to provide steady illumination conditions for accurate measurements. A calibration block with a length of 30 mm was placed on the specimen to provide a reference length for the DIC measurements, as shown in Figure 4-14 and Figure 4-15. After the tests, the photos were imported into the GOM Correlate Pro software to track and measure the deformation of the specimens based on the surface component built at the reference stage, see Figure 4-14 and Figure 4-15.

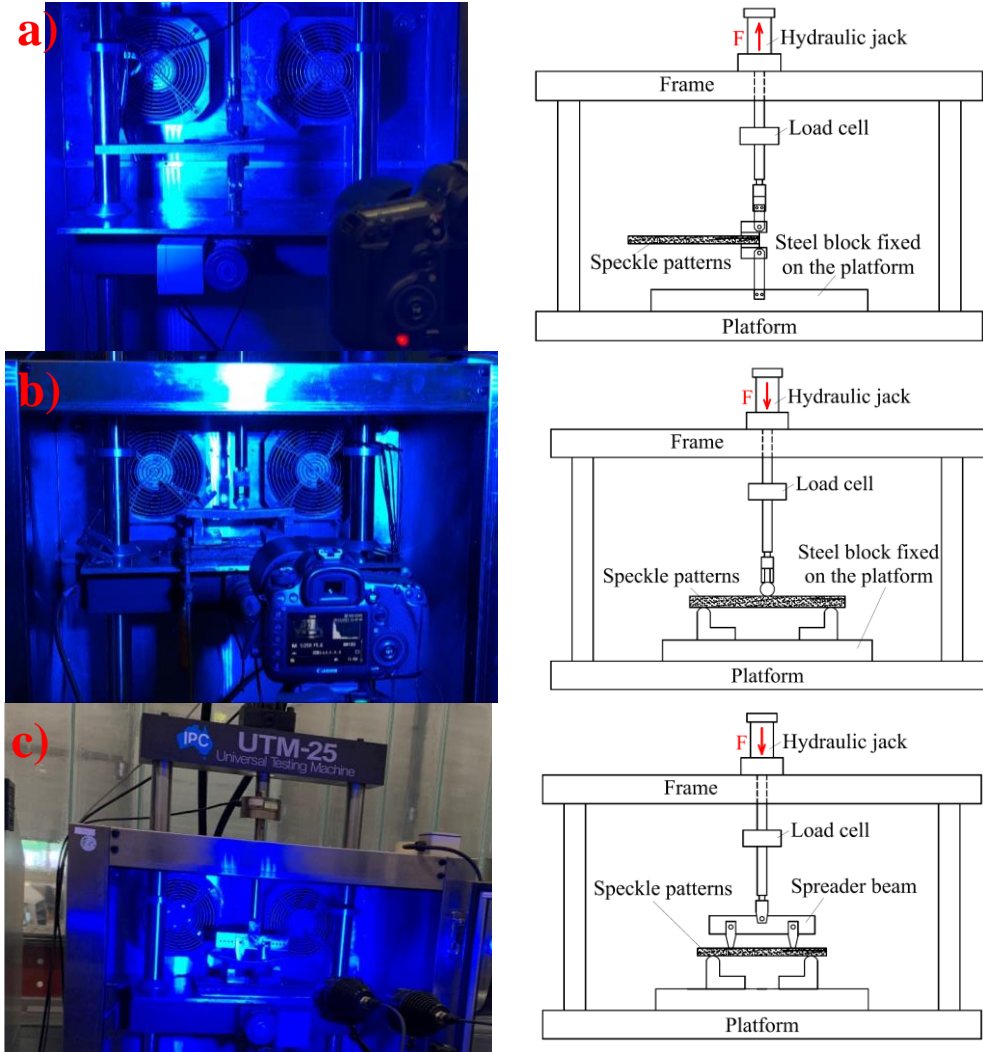


Figure 4-13 Configuration and schematic view of a) DCB, b) 3ENF and c) 4ENF test set-up

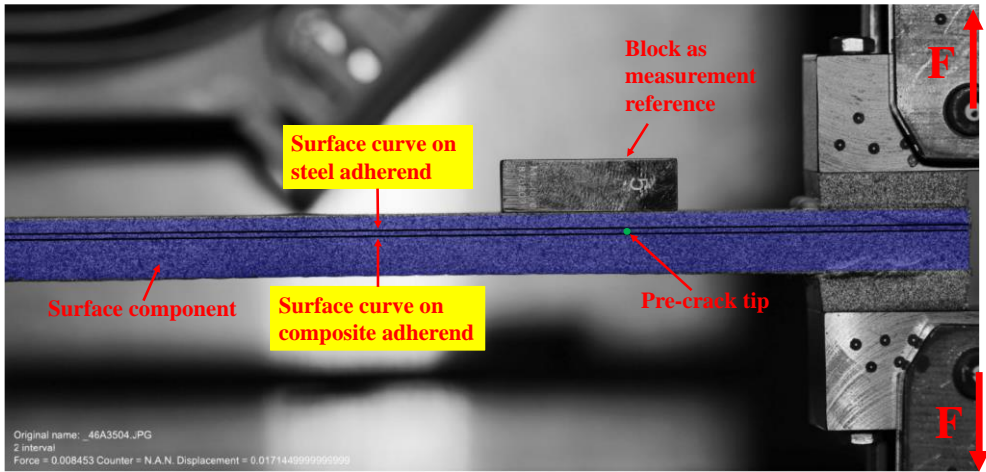


Figure 4-14 DIC analysis in GOM Correlate Pro software – DCB specimens

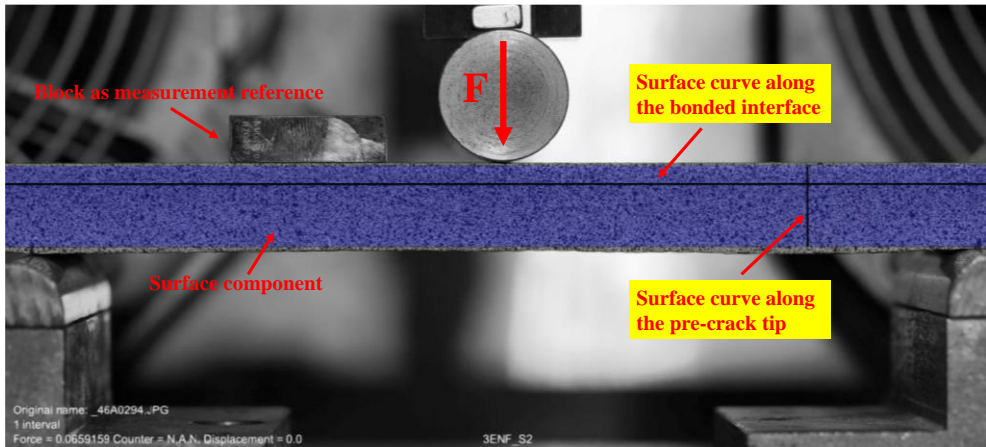


Figure 4-15 DIC analysis in GOM Correlate Pro software – 3ENF specimen as an example

4.3.3 Mode I and mode II fracture process of composite-steel bonded interface represented by a four-linear traction-separation law

Due to improved fracture toughness of resin, enhanced steel surface roughness and existence of fiber bridging, the fracture process of the composite-steel bonded interface does not follow the assumption of LEFM. On the contrary the non-linear behavior near or around the interface, with fracture process zone (FPZ) encompassing various stages of fracture process development, is formed as shown in Figure 4-16 a) for mode I and Figure 4-17 a) for mode II. The relation between the traction and the crack tip opening displacement (CTOD) of the pre-crack tip within the FPZ is defined here by a four-linear traction-separation law illustrated in Figure 4-16 b) for mode I and Figure 4-17 b) for mode II, respectively. Such set-up of the traction-separation law is explained here through physics-based considerations and assumptions. The interface model is then

phenomenologically validated in Chapter 5 through detailed comparison of global and local behavior in the experiments and FE analysis of DCB, 3ENF and 4ENF configurations, by looking at load-displacement response, crack propagation and CTOD development.

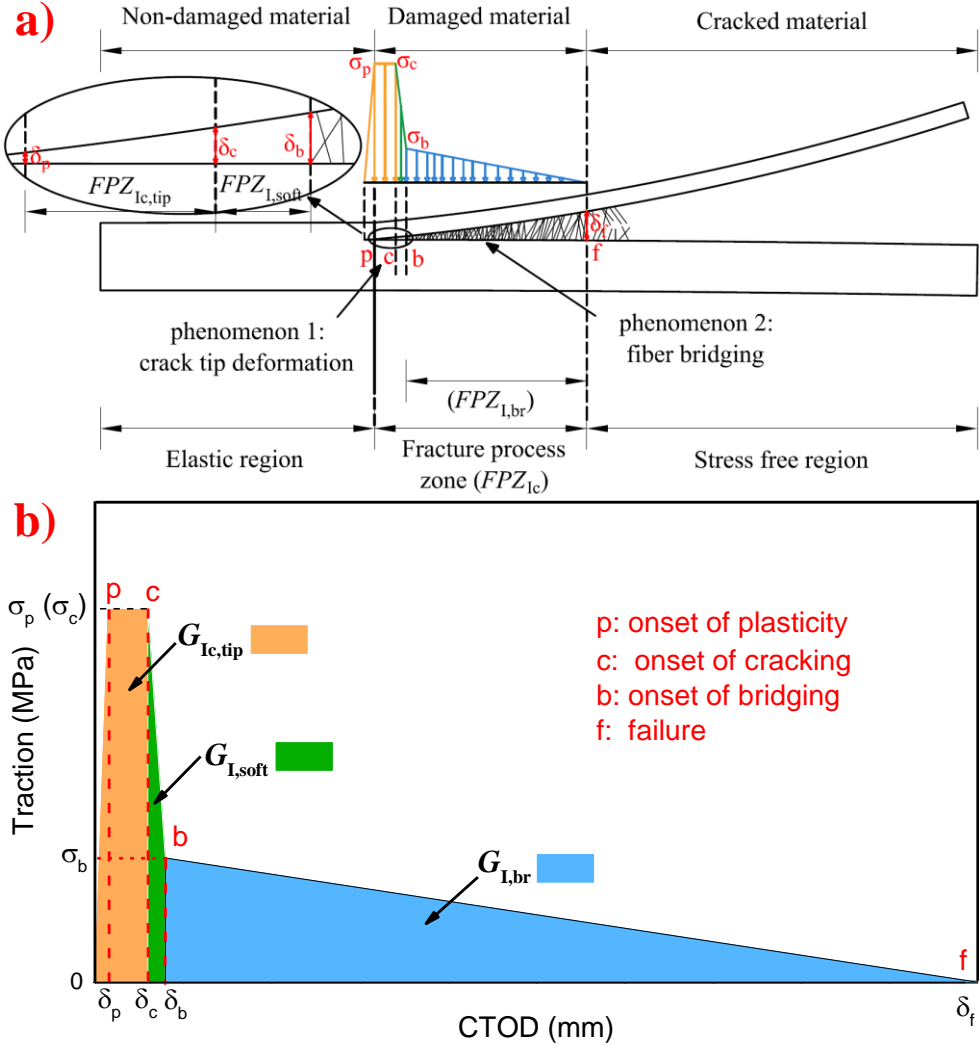


Figure 4-16 Mode I fracture process of composite-steel bonded interface illustrated by a) schematic diagram and described by b) the four-linear traction-separation law

Four critical stages are defined for further explanation: “p” – onset of plasticity; “c” – onset of cracking; “b” – onset of fiber bridging; “f” – failure. Two out of three distinct phenomena described in the fracture process are consistent with the current literature[40]–[42]: phenomenon 1 – crack tip deformation and phenomenon 3 – fiber bridging, indicated by orange and blue regions, respectively, in Figure 4-16 a) and Figure 4-17 a). In addition, phenomenon 2, defined here as softening corresponding to green

regions, is introduced in between to consider the contribution of mechanical interlocking of the resin embedded in the rough steel surface.

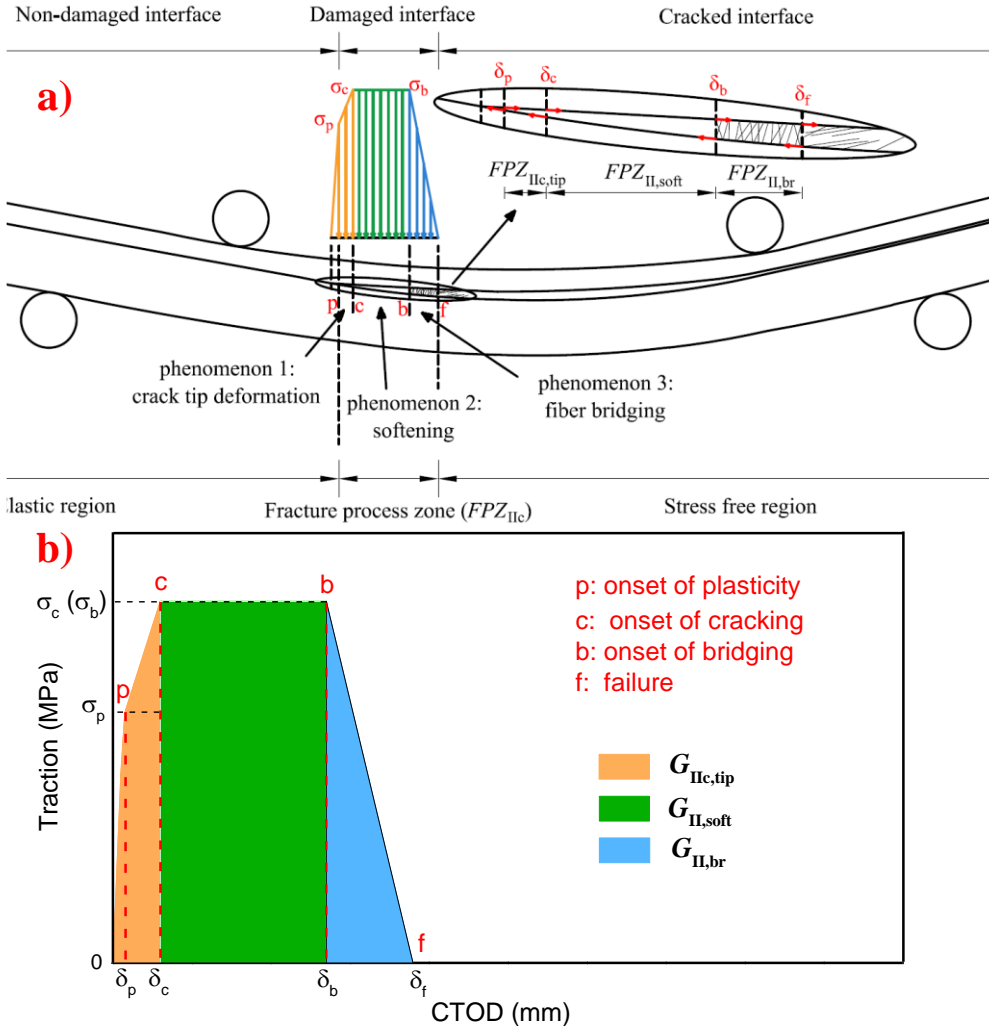


Figure 4-17 Scheme of mode II fracture process of composite-steel bonded interface – 4ENF specimen as an example; b) four-linear traction-separation law to describe the mode II fracture process

In the beginning of the fracture process the cohesive traction increases linearly until reaching σ_p at stage “p” referring to onset of plasticity where the traction keeps constant ($\sigma_p = \sigma_c$) in mode I while increases at a slower pace in mode II, until reaching σ_c at stage “c” corresponding to onset of cracking. The nonlinearity between stage “p” and stage “c” is attributed to micro-fracture of resin within the cavities of the steel surface roughness. Value of σ_c is assumed larger in mode II compared to mode I hypothetically attributed to more resistance to the fracture of resin in the shear mode resulting from restraint of

chopped strand mat and the rough steel surface near the interface. The SERR dissipated to reach stage “c” (the orange area) is defined as the critical SERR for crack initiation or crack tip fracture resistance[40]–[42] with the symbol $G_{Ic,tip}$ in mode I and $G_{IIc,tip}$ in mode II, respectively. The distance between point at stage “p” and point at stage “c” on the interface (see detail cut-out in Figure 4-16 a) and Figure 4-17 a)) is defined as the FPZ length related to crack initiation designated as $FPZ_{Ic,tip}$ in mode I and $FPZ_{IIc,tip}$ in mode II, respectively.

Subsequently, in mode I fracture process, the tractions drop significantly from stage “c” to stage “b”, see Figure 4-16 a). On the contrary, the traction remains constant ($\sigma_c = \sigma_b$) as the CTOD increases until stage “b” in mode II failure, see Figure 4-17 a). The softening phenomenon between stage “c” and stage “b” is hypothetically attributed to pull-out of resin from valleys in the micro profile of steel surface roughness. The resistance of the resin embedded in the steel surface valley against the pull-out force is weak in mode I, while engaging in such mechanical interlocking load transfer provides a significant amount of fracture toughness in mode II fracture. The SERR dissipated from stage “c” to stage “b” is defined as the SERR due to softening (the green area) with the symbol of $G_{I,soft}$ in mode I and $G_{II,soft}$ in mode II, respectively. The distance between point at stage “c” and point at stage “b” on the interface is defined as the FPZ length related to softening designated as $FPZ_{I,soft}$ in mode I and $FPZ_{II,soft}$ in mode II, respectively. The toughness in the softening of mode I is negligible due to weak mechanical interlocking, i.e., pull-out resistance, in the mode I opening. In the current literature, $G_{I,soft}$ and $FPZ_{I,soft}$ are considered as part of $G_{Ic,tip}$ and $FPZ_{Ic,tip}$, respectively[42], [43]. Conversely, in softening of mode II failure, pull-out of resin from valleys in the micro profile of steel surface roughness engaged in mechanical interlocking load transfer provides a significant amount of toughness. Therefore, contribution of softening phenomenon is suspected to be significant and distinct in mode II fracture process. $G_{II,soft}$ and $FPZ_{II,soft}$ is proposed in such tri-staged model, opposed to usually considered[42], [43] dual-stage model considering initiation and fiber bridging behavior only.

The softening is followed by fiber bridging where the traction values decrease gradually from σ_b at stage “b” to 0 at stage “f” and the corresponding SERR dissipated is defined as the SERR corresponding to fiber bridging (the blue area) with the symbol of $G_{I,br}$ in mode I and $G_{II,br}$ in mode II, respectively. The distance between point on the interface at stage “b” and point at stage “f” is defined as the FPZ length related to fiber bridging designated as $FPZ_{I,br}$ in mode I and $FPZ_{II,br}$ in mode II, respectively. When stage “f” is reached, the fracture surface is completely separated at the pre-crack tip and the SERR attains a constant value in an R-curve referred to as the critical SERR for crack propagation or steady state fracture resistance[40], [41], [43] designated as G_{Ic} in mode I and G_{IIc} in mode II, respectively. The distance between point on the interface at stage “p” and at stage “f” is defined as the FPZ length related to crack propagation designated as FPZ_{Ic} in mode I and FPZ_{IIc} in mode II, respectively. The critical SERR for crack propagation and the fracture process zone length related to crack propagation based on Figure 4-16 a) and Figure 4-17 a) are defined as:

$$G_{Ic} = G_{Ic,tip} + G_{I,soft} + G_{I,br} \quad \text{Equation 4-1}$$

$$G_{IIc} = G_{IIc,tip} + G_{II,soft} + G_{II,br} \quad \text{Equation 4-2}$$

$$FPZ_{Ic} = FPZ_{Ic,tip} + FPZ_{I,soft} + FPZ_{I,br} \quad \text{Equation 4-3}$$

$$FPZ_{IIc} = FPZ_{IIc,tip} + FPZ_{II,soft} + FPZ_{II,br} \quad \text{Equation 4-4}$$

Figure 4-16 reveals that the largest area underneath the mode I traction-separation law corresponds to fiber bridging ($G_{I,br}$), and the FPZ length related to fiber bridging is the longest as well. This indicates that fiber bridging provides the majority of the fracture resistance to the bonded interface in mode I fracture process. In contrast, Figure 4-17 shows that softening contributes the most ($G_{II,soft}$) to the mode II fracture toughness and fracture process zone length ($FPZ_{II,soft}$). The values in terms of CTOD at the critical stages (“p”, “c”, “b” and “f”) as well as values of the critical SERR ($G_{Ic,tip}$, G_{Ic} , $G_{IIc,tip}$ and G_{IIc}) are used in the defined cohesive laws for the DCB, 3ENF and 4ENF modeling in Chapter 5. These values are obtained through an approach that combines measurements of crack length a and CTOD through analysis of DIC data, along with SERR values calculated using EGM. More details in terms of this approach are given in the follow-up subsection.

4.3.4 Fracture data analysis

4.3.4.1 Determination of critical stages in fracture process

The method to determine critical stages in DCB and ENF tests is explained in Figure 4-18 and Figure 4-19, respectively, using specimen DCB-S2 and 4ENF-CL-S1 as examples. The load-displacement curves (red in DCB and blue in 4ENF) of the specimen are compared to the variations of tangential stiffness in load-displacement response, crack length and CTOD with the applied displacement (in orange), respectively. It can be seen that stage “p”, stage “c” and stage “f” refer to the turning points where decreasing rate of tangential stiffness grows suddenly and meanwhile increasing rate of crack length a and CTOD rises instantly. Stage “p” cannot be determined through observing the increasing rate of crack length a starting to grow after stage “c”. However, it can be determined by good agreement between variation of tangential stiffness and CTOD. It should be noted that the part of the tangential stiffness curve exceeding 7-mm applied displacement in DCB test is not presented in Figure 4-18 a) because big noise is introduced to the stiffness attributed to appearance of the inertia effect during the fiber bridging process. In this case, point “f” refers directly to the peak load point on the load-displacement curve. It can also be seen in Figure 4-18 and Figure 4-19 that this method helps determine stage “f” but cannot identify stage “b” in DCB and 4ENF tests because no sudden increase of crack length or CTOD happens after stage “b” attributed to stable crack growth. On the contrary, it helps determine stage “b” but cannot identify stage “f” in 3ENF tests because the specimens fail immediately after stage “b” attributed to unstable crack growth without reaching stage “f”, see Figure 4-32. Therefore, it can be beneficial to perform both types of ENF tests to better characterize all the stages in the

4-linear traction-separation law.

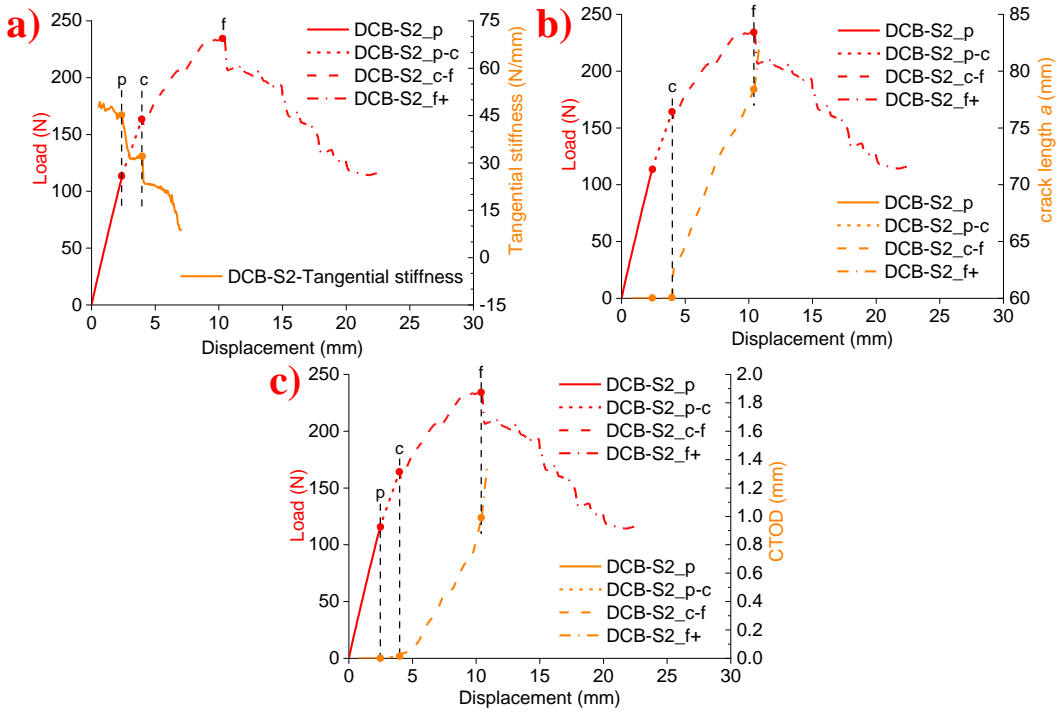


Figure 4-18 Illustration of the method to determine critical points in DCB experiments through a) tangential stiffness, b) crack length a and c) CTOD – an example of specimen DCB-S2 (p, p-c, c-f, f+ corresponds to elastic behavior until point p, point p to point c, point c to point f, after point f, respectively)

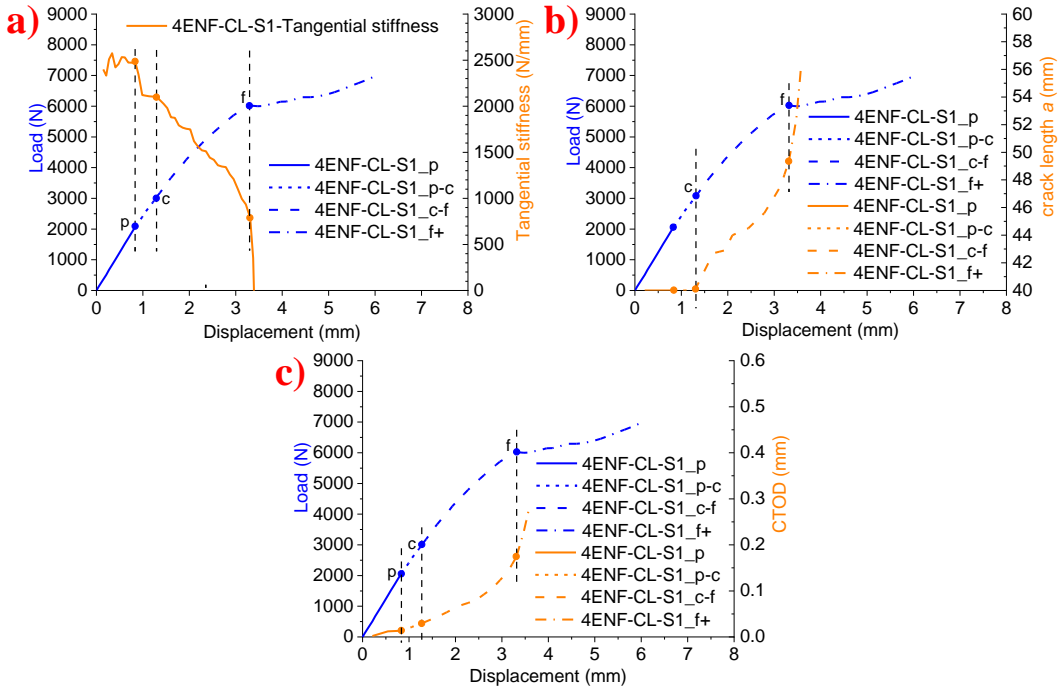


Figure 4-19 Illustration of the method to determine critical stages in 4ENF experiments through a) tangential stiffness, b) crack length a and c) CTOD – an example of specimen 4ENF-CL-S1 (p, p-c, c-f, f+ indicates elastic behavior until stage “p”, stage “p” to stage “c”, stage “c” to stage “f”, after stage “f”, respectively)

4.3.4.2 Determination of crack length a and CTOD

In DCB, 3ENF and 4ENF test the crack length a and the CTOD were determined by analysis of DIC measurement data In GOM Correlate Pro software. In DIC analysis of DCB tests, two surface curves were built on the steel and composite adherends 0.5 mm parallel to the bonded interface (see Figure 4-14) and the vertical displacement along them were read from surface component data. The present crack tip is determined as the location where the relative vertical displacement from the two surface curves starts to deviate, as shown in Figure 4-20. The crack length a is the distance between the section of the applied load and the present crack tip while the CTOD is the subtraction of the vertical displacement from two surface curves at the pre-crack tip location.

However, these two parameters cannot be explicitly measured in 3ENF and 4ENF tests where the direction of the crack opening is parallel to the direction of crack extension. Instead, new “shear strain scaling method” is proposed here to measure the crack length a . It involves building a surface curve along the composite-steel bonded interface (see Figure 4-15) and reading the shear strain from the surface curve data (see Figure 4-21). It can be inferred from the extended global method (EGM) [44], [45] that the significant increase in shear strain from the crack tip to the right support point along the interface is caused by the difference of maximum tensile and compressive strain in

the upper and lower adherend, respectively. Therefore, the present crack tip can be determined indirectly by observing local increase of shear strains along the bonded interface. To eliminate interference of elastic deformation in shear strain increase, and to ensure accuracy in defining the curve path directly on the interface, the shear strains at a later load state are relativized and scaled (the red curve) to shear strains that correspond to a selected reference elastic state (the green curve), as shown in Figure 4-21. If there were no crack extension, the scaled shear strains at a later load state would be identical to the strains at the reference elastic state. The deviations from such idealistic state are used to identify the present crack tip and quantify the crack length a using the strain threshold identified as 0.1% by pin-pointing at which strain level the shear strains significantly increase from a flat, steady, trend to a higher strain distribution trend. The strain threshold depends on the selected reference elastic load level and specimen geometry, therefore, shall be determined for each specific test set-up and selected reference load level. In present study the reference load level for scaling was kept the same.

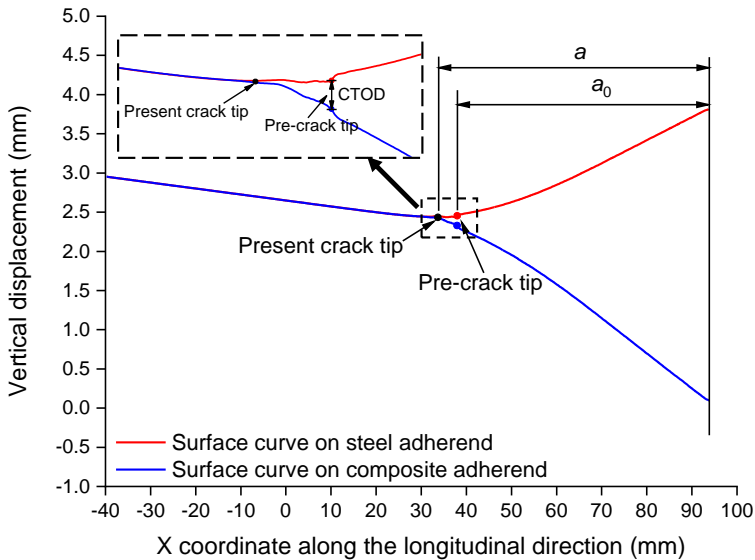


Figure 4-20 Illustration of determination of a and CTOD in DIC – DCB specimens

The CTOD was quantified as well with help of detailed DIC data. The method proposed is by analyzing the horizontal displacement along the height of the specimens at the pre-crack tip as shown in Figure 4-22 where the measurements of displacements were obtained from the vertical surface curve in Figure 4-15. Two parallel straight lines are observed at the steel and composite adherend due to the elastic bending deformation. If there were no slip at the interface related to crack initiation, growth of propagation, the two lines would overlap. Contrarily, once the fracture process starts the CTOD is characterized by shift at the interface between the straight lines fitted to the regions on the upper (steel) and the lower (composite) adherend away from the interface.

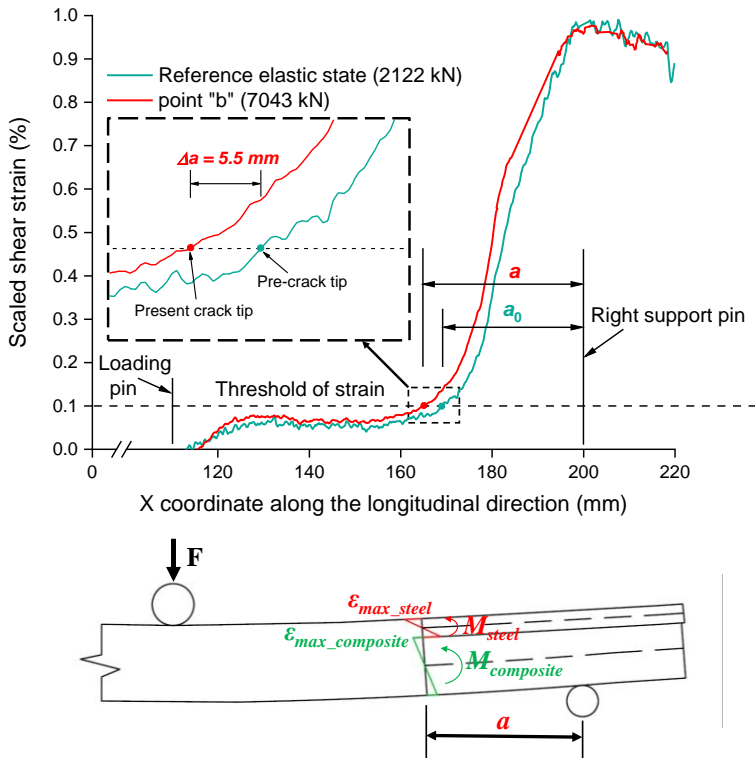


Figure 4-21 Illustration of determination of crack length and growth in DIC using the shear strain scaling method – an example of specimen 3ENF-CL-S2

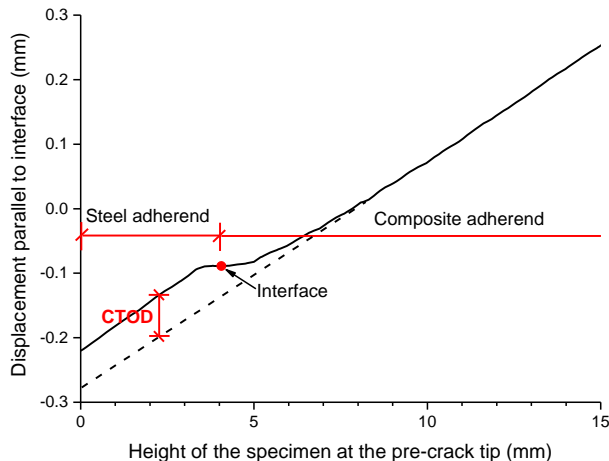


Figure 4-22 Illustration of determination of mode II CTOD by DIC – an example of specimen 3ENF-CL-S2

4.3.4.3 Determination of SERR by EGM

The strain energy release rate (SERR) was calculated using the extended global method (EGM) [44], [45] where the total SERR is:

$$G_{total} = \frac{6}{B^2} \left[\frac{M_{steel}^2}{E_{steel} h_{steel}^3} + \frac{M_{composite}^2}{E_{composite} h_{composite}^3} - \frac{(M_{steel} + M_{composite})^2}{E(h_{steel} + h_{composite})^3} \right] \quad \text{Equation 4-5}$$

where E_{steel} , I_{steel} , $E_{composite}$, $I_{composite}$, E and I are the elastic modulus and the moment of inertia in the section of the crack tip of the steel adherend, composite adherend and the specimen, respectively, see Figure 4-11 and Figure 4-12. M_{steel} and $M_{composite}$ are the bending moments (assumed positive when counterclockwise) of the steel and composite adherend at the crack tip, respectively. The design of DCB and ENF specimens in this study did not satisfy the longitudinal strain based criterion[25], so the equivalent longitudinal strain ratio of the steel and composite adherends was introduced to guarantee pure mode I or pure mode II in mode partitioning of bi-material bonded joints[27]:

$$\beta = \frac{E_{composite} h_{composite}^2}{E_{steel} h_{steel}^2} \quad \text{Equation 4-6}$$

The applied moments can be resolved as:

$$M_{steel} = M_I + M_{II} \quad \text{Equation 4-7}$$

$$M_{composite} = -\beta M_I + \psi M_{II} \quad \text{Equation 4-8}$$

where ψ is defined as the bending stiffness ratio of steel and composite adherends to assure the identical curvature in the two adherends to obtain pure mode II:

$$\psi = \frac{E_{composite} I_{composite}}{E_{steel} I_{steel}} \quad \text{Equation 4-9}$$

Substitution of Equation 4-7 and Equation 4-8 into Equation 4-5 leads to the mode partition of G_{total} into G_I and G_{II} as:

$$G_I = \frac{(\psi M_{steel} - M_{composite})^2}{2B(\beta + \psi)^2} \left(\frac{1}{E_{steel} I_{steel}} + \frac{\beta^2}{E_{composite} I_{composite}} - \frac{(1-\beta)^2}{EI} \right) \quad \text{Equation 4-10}$$

$$G_{II} = \frac{(\beta M_{steel} + M_{composite})^2}{2B(\beta + \psi)^2} \left(\frac{\psi + 1}{E_{steel} I_{steel}} - \frac{(\psi + 1)^2}{EI} \right) \quad \text{Equation 4-11}$$

In the presented DCB tests, $M_{steel} = Fa$, $M_{composite} = -Fa$. Therefore, the SERR in mode I can be calculated as:

$$G_I = \frac{(\psi + 1)^2 F^2 a^2}{2B(\beta + \psi)^2} \left(\frac{1}{E_{steel} I_{steel}} + \frac{\beta^2}{E_{composite} I_{composite}} - \frac{(1-\beta)^2}{EI} \right) \quad \text{Equation 4-12}$$

In the presented 3ENF tests, M_{steel} and $M_{composite}$ are calculated as:

$$M_{steel} = \frac{FaE_{steel}I_{steel}}{EI} \quad \text{Equation 4-13}$$

$$M_{composite} = \frac{FaE_{composite}I_{composite}}{EI} \quad \text{Equation 4-14}$$

where the F is the applied load and a is the present crack length, respectively. Therefore, the SERR in mode II can be calculated as:

$$G_{II} = \frac{F^2 a^2 (\beta E_{steel} I_{steel} + E_{composite} I_{composite})^2}{2B(\beta + \psi)^2 E^2 I^2} \left(\frac{\psi + 1}{E_{steel} I_{steel}} - \frac{(\psi + 1)^2}{EI} \right) \quad \text{Equation 4-15}$$

In the presented 4ENF tests, M_{steel} and $M_{composite}$ are calculated as:

$$M_{steel} = \frac{F(2L-d)E_{steel}I_{steel}}{2EI} \quad \text{Equation 4-16}$$

$$M_{composite} = \frac{F(2L-d)E_{composite}I_{composite}}{2EI} \quad \text{Equation 4-17}$$

where F , L and d are the applied load, half span length, and the distance of the two loading pins, respectively. Therefore, the SERR in mode II can be calculated as:

$$G_{II} = \frac{F^2(2L-d)^2 (\beta E_{steel} I_{steel} + E_{composite} I_{composite})^2}{8B(\beta + \psi)^2 E^2 I^2} \left(\frac{\psi + 1}{E_{steel} I_{steel}} - \frac{(\psi + 1)^2}{EI} \right) \quad \text{Equation 4-18}$$

4.3.5 Results and discussion

4.3.5.1 DCB test results

The load-displacement curves of 3 specimens in DCB tests (test series 4) are shown in Figure 4-24 where the critical stages are identified, and the associated values of applied displacement and load are summarized in Table 4-5. The fracture morphology is shown in Figure 4-23. It can be seen from Figure 4-24 that onset of plasticity (stage “p”) corresponds to the elastic load limit at approximately 120 N followed by crack initiation at approximately 170 N (stage “c”) where the load drops slightly due to softening. Subsequently, the existence of fiber bridging shown in Figure 4-23 a) leads to gradual increase of load until the peak load is reached at stage “f”, where the FPZ for crack propagation is completely formed. It should be noted that stage “b” cannot be obtained from the tests due to the negligible fracture energy accumulated in the softening stage. Figure 4-23 b) and Figure 4-23 c) show the representative fracture morphology of the DCB specimens, and Figure 4-23 d) shows the height profile on the fracture surface of steel adherend obtained from a 3D optical profilometer (Keyence VR6000) with 40×magnification. It can be seen that fiber bridging is really governing in mode I fracture

process.

Table 4-5 Overview of displacement/load values at the critical stages of the fracture process in DCB tests

Specimens	Onset of plasticity (stage “p”)		Onset of stage (point “c”)		Onset of bridging (stage “b”)		Failure (stage “f”)	
	Disp. (mm)	Load (N)	Disp. (mm)	Load (N)	Disp. (mm)	Load (N)	Disp. (mm)	Load (N)
DCB-S1	2.74	133.0	4.14	177.3	-	-	9.60	224.11
DCB-S2	2.42	113.6	3.98	164.3	-	-	10.45	233.62
DCB-S3	2.55	123.4	3.97	165.1	-	-	9.60	236.23
Average (and COV[%])	2.57 (5.11)	123.3 (6.43)	4.03 (1.93)	168.9 (3.51)	-	-	9.88 (4.05)	231.32 (2.25)

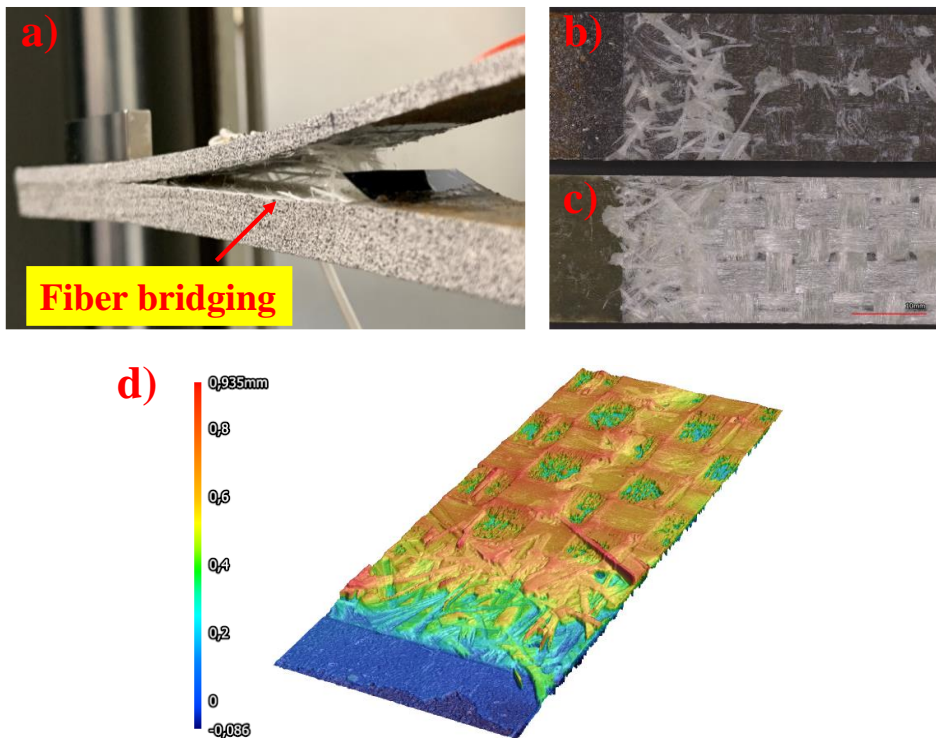


Figure 4-23 Fracture surface morphology: a) fiber bridging observed during loading; b) fracture surface on steel and c) composite adherend; d) 3D scan of the fracture surface on the steel adherend

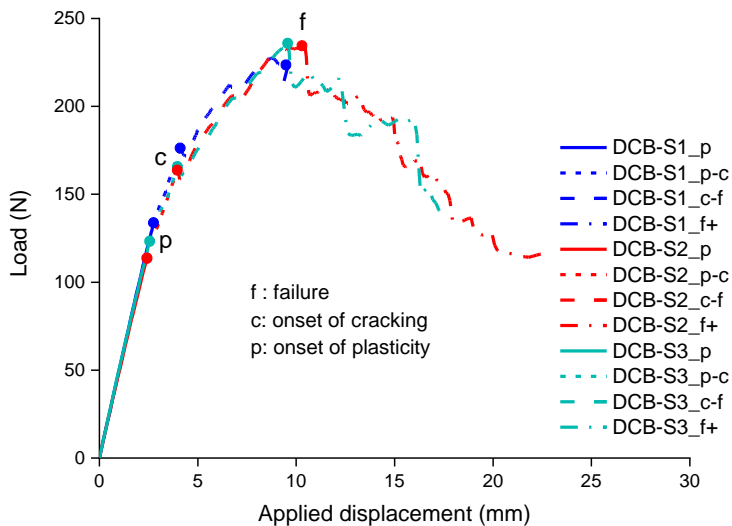


Figure 4-24 Load-displacement response in DCB tests

Figure 4-25 and Figure 4-26 present the crack length a and the CTOD measured during the DCB tests. It can be seen that the pre-crack tip opens at stage “p” but the CTOD is still limited (less than 0.02 mm) until crack initiates at stage “c”. Subsequently, the crack length a and the CTOD develop progressively until stage “f” where these two variables increase at a constant rate. This indicates that FPZ for crack propagation is fully developed, and crack starts to propagate in a stable manner.

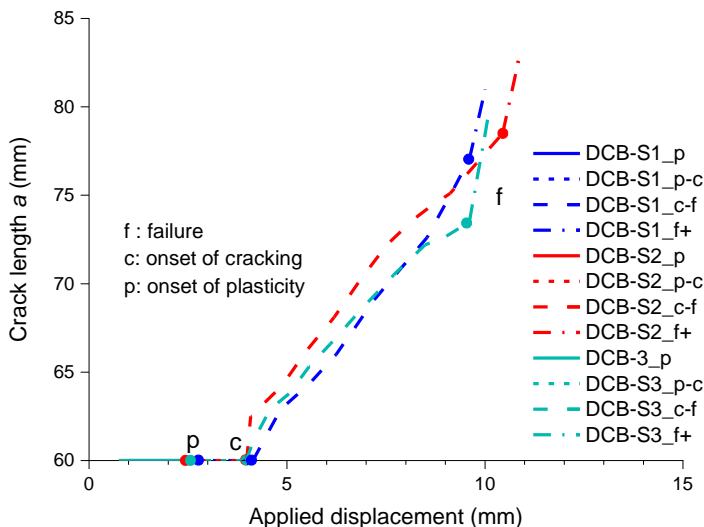


Figure 4-25 The a -displacement relation in DCB tests

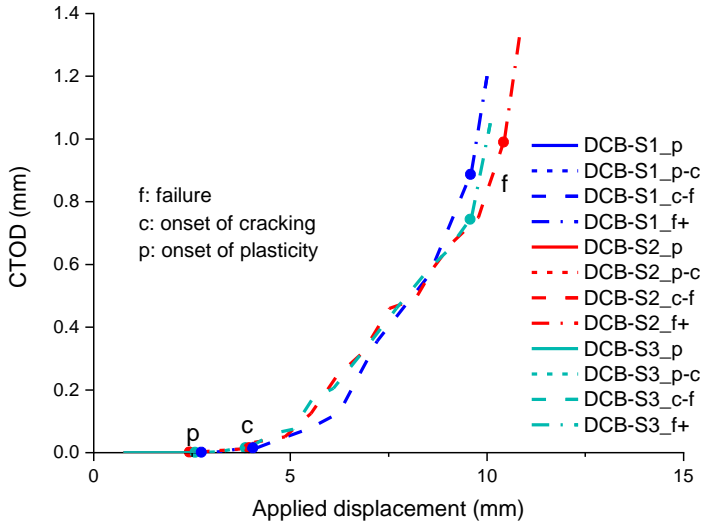


Figure 4-26 CTOD-displacement relation in DCB tests

Based on the EGM, the mode I SERR of the composite-steel bonded interface was calculated and its relation with the crack extension Δa , i.e. the R-curve, is shown in Figure 4-27. It can be seen that the critical SERR for crack initiation $G_{Ic,tip}$ is approximately 0.3 N/mm on average obtained at stage “c” and increases progressively during the fracture process to $G_{Ic} = 1.47$ N/mm on average at stage “f” defined as the critical SERR for crack propagation. The summation of the FPZ length due to softening $FPZ_{I,soft}$ and due to fiber bridging $FPZ_{I,br}$ refers to the distance of X coordinates between stage “c” and stage “f” on the R-curves while $FPZ_{Ic,tip}$ is neglected due to its limited and unmeasurable values. The values of $G_{Ic,tip}$, G_{Ic} and $FPZ_{I,soft} + FPZ_{I,br}$ in 3 DCB specimens are summarized in Table 4-6. The average values of $FPZ_{I,soft} + FPZ_{I,br}$ in mode I fracture is approximately 16 mm.

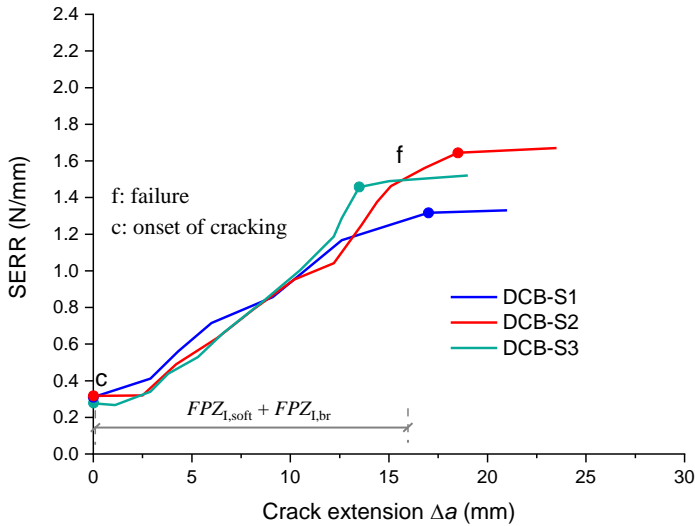


Figure 4-27 R-curves of 3 specimens in DCB tests

Table 4-6 Overview values of fracture resistance and FPZ length in DCB test

Specimens	Critical SERR (N/mm)		$FPZ_{L,soft} + FPZ_{L,br}$ (mm)
	$G_{Ic,tip}$	G_{Ic}	
DCB-S1	0.31	1.32	17.0
DCB-S2	0.32	1.64	18.5
DCB-S3	0.28	1.46	13.5
Average (and COV[%])	0.30 (5.60)	1.47 (8.89)	16.3 (12.83)

4.3.5.2 Test results of 3ENF specimens with composite laminate as upper adherend

The load-displacement curves of five 3ENF specimens tested with composite laminate as upper adherend (test series 5) are shown in Figure 4-28. It shows that non-linearity occurred at approximately 2000 N while the ultimate resistance deviates within the range of 8000~10000 N. Figure 4-29 shows the front view of a characteristic specimen 3ENF-CU-S5 during loading and Figure 4-30 illustrates its fracture morphology after test. It can be seen that migration of the crack happens from the composite-steel bonded interface into the inter-laminar failure plane in the composite adherend directly at the pre-crack tip without initiating and propagating on the bonded interface. The crack transition is attributed to micro cracking of the composite plies close to the bonded interface due to tensile bending when the composite laminate is positioned as the upper adherend. This transition of crack path helps improve the bonding behavior by allowing more energy dissipation but leads to difficulty in obtaining mode II fracture properties of the composite-steel bonded interface.

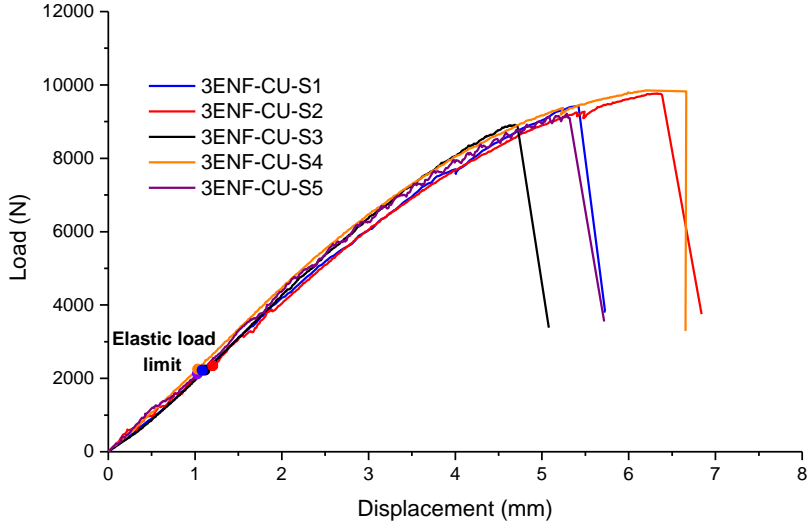


Figure 4-28 Load-displacement response of 3ENF specimens tested with composite laminate as upper adherend

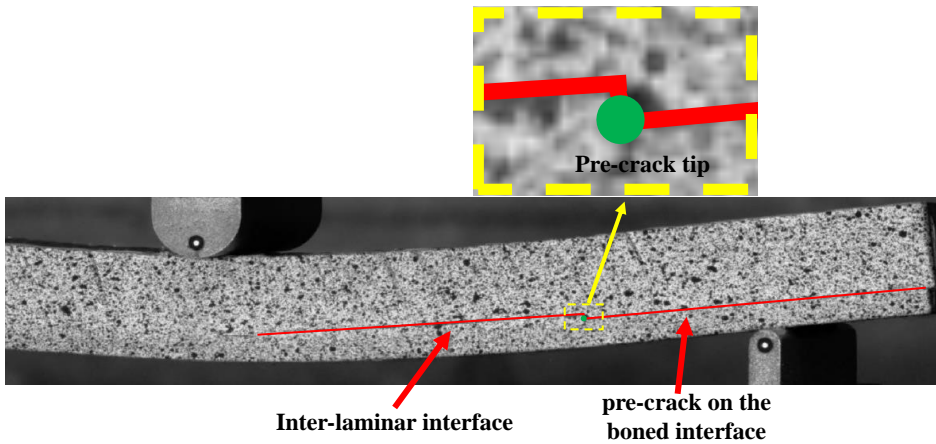


Figure 4-29 Front view of specimen 3ENF-CU-S5 during test indicating the crack transition

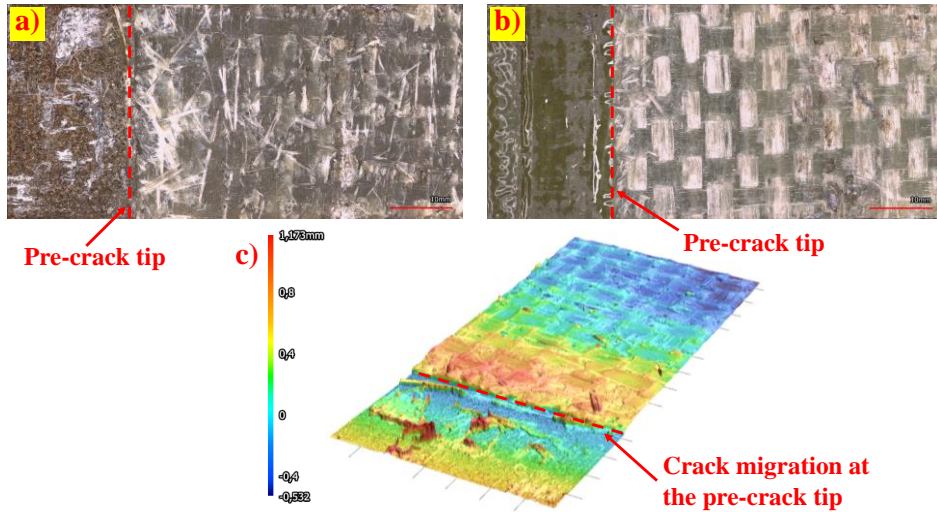


Figure 4-30 Fracture surface morphology of specimen 3ENF-CU-S5: a) fracture surface on a) steel and b) composite adherends; c) 3D scan of the fracture surface on the steel adherend

4.3.5.3 Test results of 3ENF specimens with composite laminate as lower adherend

To prevent crack migration from the bonded interface to the inter-laminar interface, the composite laminate adherend is positioned as the lower adherend in the 3ENF test in test series 6 and the subsequent 4ENF test in test series 7. The aim is to keep composite plies close to the bonded interface in state of longitudinal compression due to the local arm bending moment. The assumption is that the longitudinal compression in combination with the through thickness shear is restraining more the crack development in the composite than the combination of longitudinal tension and through thickness shear. The load-displacement response of the 3ENF specimens in test series 6 is shown in Figure 4-32 where the critical stages (“p”, “c” and “b”) are identified, and the associated values of applied displacement and load are summarized in Table 4-7. The fracture morphology is shown in Figure 4-31. It can be seen from Figure 4-32 that onset of plasticity (stage “p”) corresponds to the elastic load limit at approximately 2000 N followed by crack initiation at approximately 3500 N (stage “c”). Subsequently, softening leads to gradual increase of load until the peak load is reached at stage “b” within the load range of 5500~8000 N, where the bonded interface fails immediately with unstable crack propagation. There are two reasons accounting for the unstable crack propagation: 1) the bending moment at the present crack tip keeps increasing as the crack advances leading to consistently increasing SERR which is unfavourable for stable crack propagation; 2) fiber bridging is negligible on the fracture surface as shown in Figure 4-31 such that the remaining resistance of the interface due to fiber bridging is too small to retain stable crack growth. The fracture morphology in Figure 4-31 clearly shows that crack propagation happened merely on the bonded interface, therefore proving the effectiveness of preventing crack transition by positioning composite laminate as the lower adherend in 3ENF test.

Table 4-7 Overview of displacement/load values at the critical stages of the fracture process in 3ENF test

Specimens	Onset of plasticity (stage “p”)		Onset of cracking (stage “c”)		Onset of bridging (stage “b”)		Failure (stage “f”)	
	Disp. (mm)	Load (N)	Disp. (mm)	Load (N)	Disp. (mm)	Load (N)	Disp. (mm)	Load (N)
3ENF-CL-S1	1.01	2210.02	1.74	3671.28	4.52	7873.33	-	-
3ENF-CL-S2	0.93	2122.93	1.72	3750.41	3.74	7042.56	-	-
3ENF-CL-S3	0.61	1335.2	1.59	3430.8	2.67	5393.6	-	-
Average (and COV[%])	0.85 (20.33)	1889.38 (20.83)	1.68 (3.95)	3617.50 (3.76)	3.64 (20.81)	6769.83 (15.22)	-	-

Figure 4-33 and Figure 4-34 illustrate the development of the crack length a and the CTOD at the pre-crack tip with the increased applied displacement during the tests, respectively. The pre-crack tip starts to open at stage “p” but the opening displacement is limited (less than 0.02 mm) according to DIC measurements. After the crack is initiated at stage “c”, the crack length and crack opening develop steadily until stage “b” where the bonded interface starts to propagate abruptly and fails immediately. Due to unstable crack propagation in 3ENF test, only the part from stage “c” to stage “b” in the R-curves of the tested specimens is obtained based on EGM and is shown in Figure 4-35. The critical SERR for crack initiation $G_{IIc,tip}$ is approximately 0.56 N/mm on average obtained at stage “c” and increases gradually during the fracture process to $G_{IIc,tip} + G_{II,soft} = 3.36$ N/mm on average at stage “b”. The FPZ length related to softening $FPZ_{II,soft}$ is represented by distance between point at stage “c” and point at stage “b” on the R-curves, see Figure 4-35. $FPZ_{IIc,tip}$ is neglected being very short while $FPZ_{IIc,br}$ is unknown in consequence of unstable crack propagation. The values of $G_{IIc,tip}$, $G_{IIc,tip} + G_{II,soft}$, and $FPZ_{II,soft}$ in three 3ENF specimens are summarized in Table 4-8. The average value of $FPZ_{II,soft}$ is approximately 5 mm.

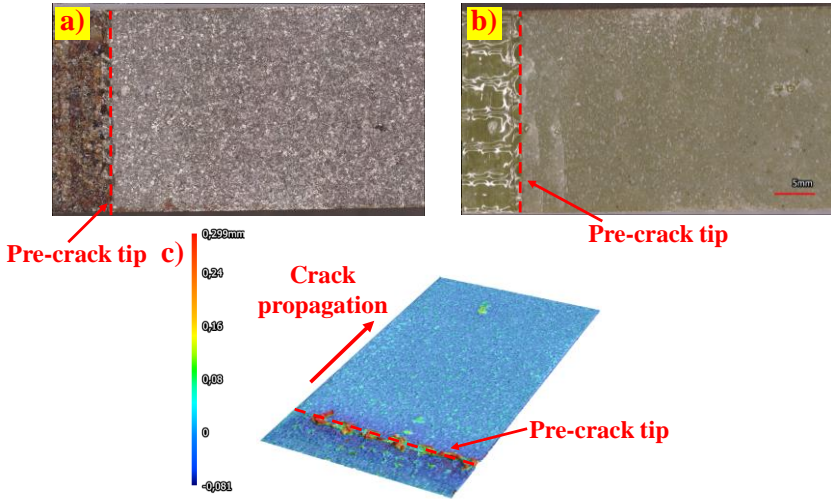


Figure 4-31 Fracture surface morphology of specimen 3ENF-CL-S2: a) fracture surface on a) steel and b) composite adherends; c) 3D scan of the fracture surface on the steel adherend

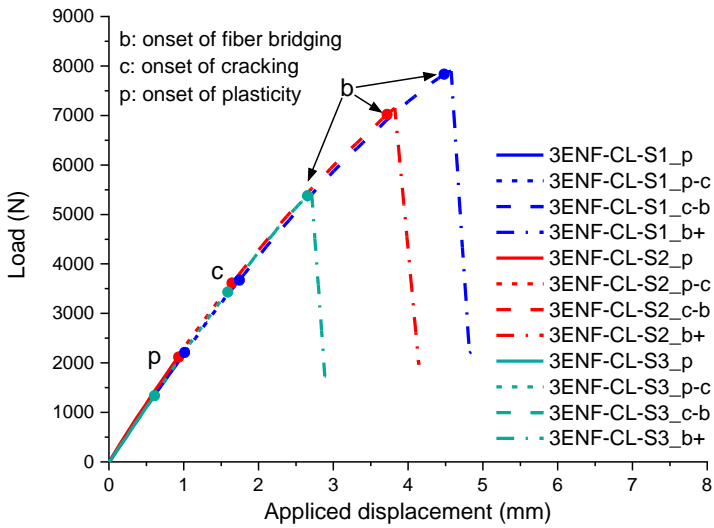


Figure 4-32 Load-displacement response in 3ENF tests with composite laminate as lower adherend

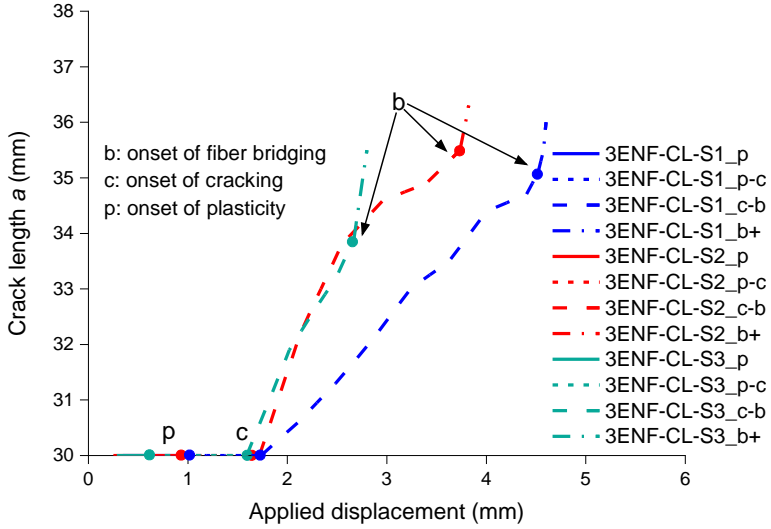


Figure 4-33 The a -displacement relation in 3ENF tests with composite laminate as lower adherend

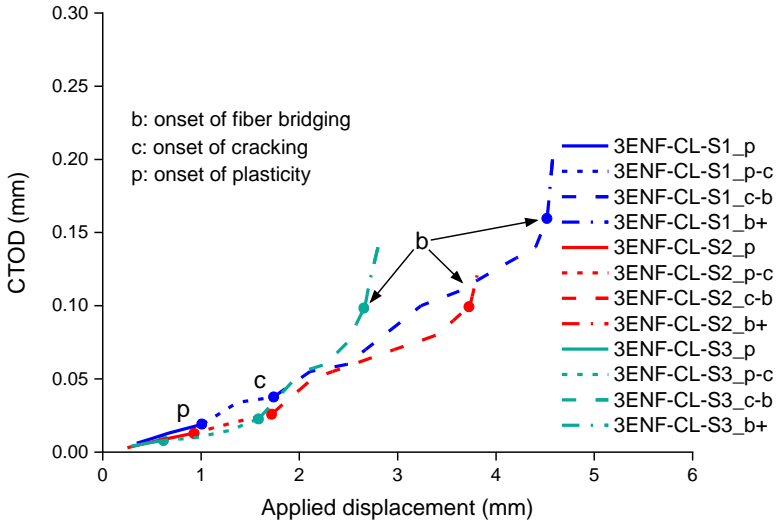


Figure 4-34 CTOD-displacement relation in 3ENF tests with composite laminate as lower adherend

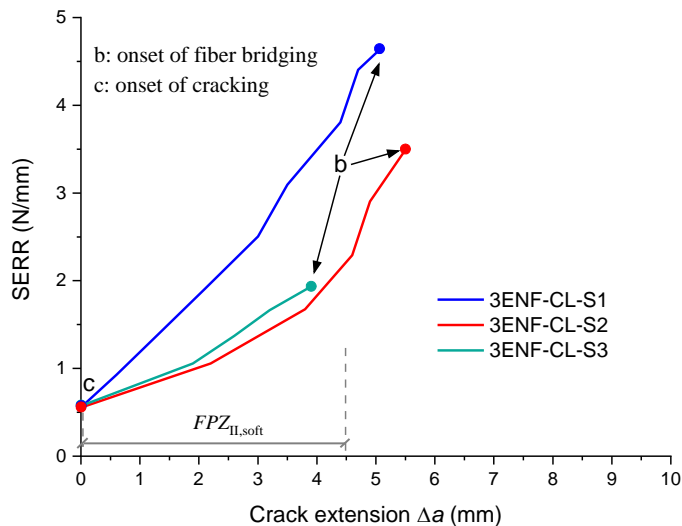


Figure 4-35 R-curves of 3 specimens in 3ENF tests with composite laminate as lower adherend

Table 4-8 Overview values of fracture resistance and FPZ length in 3ENF tests

Specimens	SERR (N/mm)		$FPZ_{II,soft}$ (mm)
	$G_{IIc,tip}$	$G_{IIc,tip} + G_{II,soft}$	
3ENF-CL-S1	0.56	4.66	5.1
3ENF-CL-S2	0.55	3.49	5.5
3ENF-CL-S3	0.57	1.93	3.9
Average (and COV[%])	0.56 (1.46)	3.36 (33.28)	4.8 (14.07)

4.3.5.4 Test results of 4ENF specimens

To prevent unstable crack growth observed in 3ENF tests, 4ENF tests were performed in test series 7. Local bending moments in arms of adherends around the crack tip are constant and independent of the crack length which leads to more stable crack propagation in 4ENF. The load-displacement response of the 4ENF specimens is shown in Figure 4-37 where the critical stages are identified, and the associated values of applied displacement and load are summarized in Table 4-9. The fracture morphology is shown in Figure 4-36. It can be seen in Figure 4-37 that onset of plasticity (stage “p”) corresponds to the elastic load limit at approximately 1700 N followed by crack initiation at approximately 3000 N (stage “c”). Different from 3ENF tests, the applied load increases consistently in 4ENF tests from stage “c” to stage “f” within the load range of 6000–7000 N where the pre-crack tip propagates consistently. This difference can be

explained in two aspects: 1) the bending moment at the present crack tip is independent of the crack length a in 4ENF loading (see Equation 4-17 and Equation 4-18) which is favorable for the stable crack propagation; 2) although fiber bridging in mode II is much less prevalent in 4ENF tests (see Figure 4-36) compared to mode I in DCB tests, it has more ability to engage due to stable propagation than in 3ENF tests (see Figure 4-31).

Table 4-9 Overview of displacement/load values at the critical stages of the fracture process in 4ENF test

Specimens	Onset of plasticity (stage “p”)		Onset of cracking (stage “c”)		Onset of bridging (stage “b”)		Failure (stage “f”)	
	Disp. (mm)	Load (N)	Disp. (mm)	Load (N)	Disp. (mm)	Load (N)	Disp. (mm)	Load (N)
4ENF-CL-S1	0.83	2062.9	1.29	3031.6	-	-	3.31	6020.5
4ENF-CL-S2	0.70	1907.8	1.23	3088.1	-	-	3.46	6261.3
4ENF-CL-S3	0.47	1242.9	1.24	2975.3	-	-	4.44	6958.5
Average (and COV[%])	0.67 (22.33)	1737.9 (20.46)	1.25 (2.09)	3031.7 (1.52)	-	-	3.74 (13.41)	6413.4 (6.20)

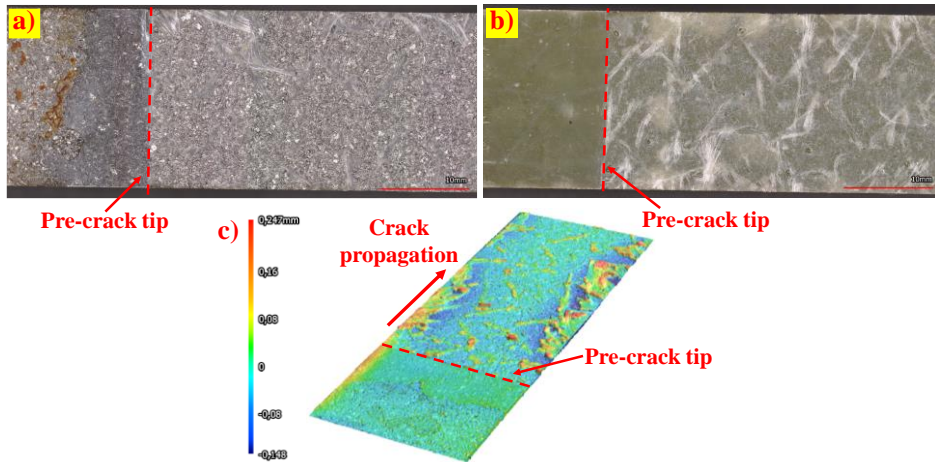


Figure 4-36 Fracture surface morphology of specimen 4ENF-CL-S1: a) fracture surface on a) steel and b) composite adherends; c) 3D scan of the fracture surface on the steel adherend Fracture surface morphology

Figure 4-38 and Figure 4-39 illustrate the development of the crack length a and the CTOD at the pre-crack tip with the increased applied displacement during the tests, respectively. Similar to 3ENF tests, the pre-crack tip starts to open at stage “p” but the opening displacement is limited (less than 0.02 mm). After the crack is initiated at stage “c”, the crack length a and the CTOD develops gradually until stage “f” where these two variables increase at a constant rate. This indicates that FPZ for crack propagation is fully developed, and crack starts to propagate in a stable manner.

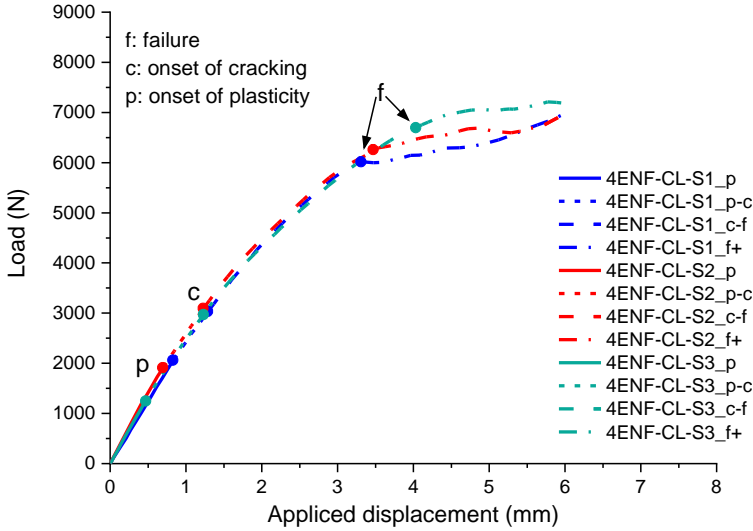


Figure 4-37 Load-displacement response in 4ENF tests

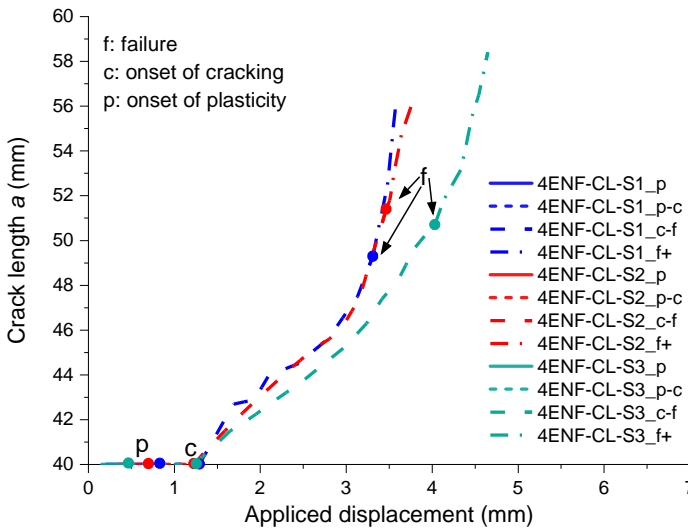


Figure 4-38 The a -displacement relation in 4ENF tests

Based on the EGM, the mode II SERR of the composite-steel bonded interface was calculated and its relation with the crack extension Δa , i.e. the R-curve, is shown in Figure 4-40. It can be seen that the critical SERR for crack initiation $G_{IIc,tip}$ is approximately 0.9 N/mm on average obtained at stage “c” and increases gradually during the fracture process to $G_{IIc} = 5.4$ N/mm on average at stage “f” defined as the critical SERR for crack propagation. The summation of the FPZ length due to softening $FPZ_{II,soft}$ and due to fiber bridging $FPZ_{II,br}$ refers to the distance between point at stage “c” and point at stage “f” on the R-curves while $FPZ_{IIc,tip}$ is neglected being very short. The values of $G_{IIc,tip}$, G_{IIc} and $FPZ_{II,soft} + FPZ_{II,br}$ in three 4ENF specimens are summarized in Table

4-10. The average values of $FPZ_{II,soft} + FPZ_{II,br}$ in mode II fracture is approximately 10 mm.

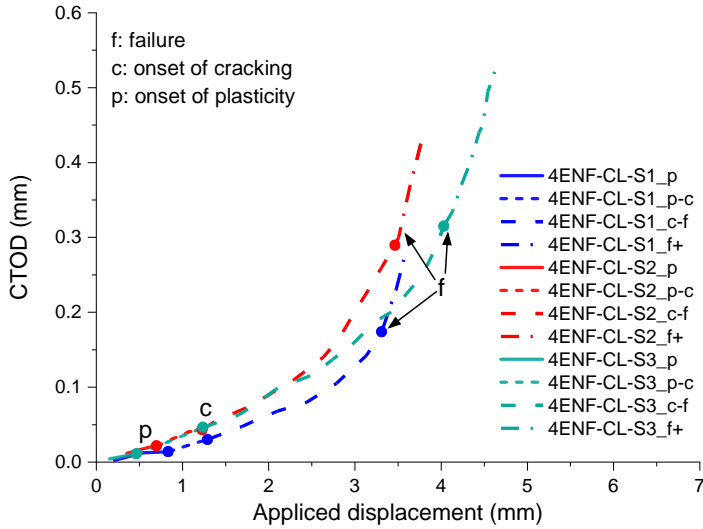


Figure 4-39 CTOD-displacement relation in 4ENF tests

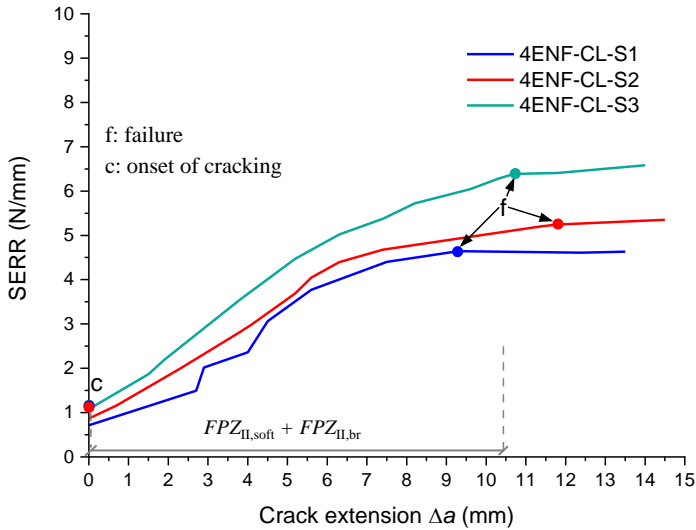


Figure 4-40 R-curves of 3 specimens in 4ENF tests

Table 4-10 Overview values of fracture resistance and FPZ length in 4ENF tests

Specimens	SERR (N/mm)		$FPZ_{II,soft} + FPZ_{II,br}$ (mm)
	$G_{IIc,tip}$	G_{IIc}	
4ENF-CL-S1	0.72	4.64	9.3
4ENF-CL-S2	0.86	5.20	11.4
4ENF-CL-S3	1.08	6.39	10.7
Average (and COV[%])	0.89 (16.71)	5.41 (13.49)	10.5 (8.34)

4.4 Discussion of critical SERR

Based on the aforementioned results in combination with the numerical results from Section 5.4.3, the average values of $G_{Ic,tip}$, $G_{Ic,tip} + G_{I,soft}$ and G_{Ic} in DCB tests, as well as the average values of $G_{IIc,tip}$, $G_{IIc,tip} + G_{II,soft}$ and G_{IIc} in 3ENF and 4ENF tests, are summarized in Table 4-11. Note that differences between the 3ENF and 4ENF critical SERR values are owed to difference in roughness in the two batches and not necessarily due to difference of fracture characterization in those two types of tests. The ratio of critical SERR at crack initiation to crack propagation are further discussed.

It can be seen from Table 4-11 that the critical SERR values at crack initiation contribute merely approximately 20% to those values at crack propagation which is relatively low. Based on the existing literature[45]–[47] this ratio of critical SERR at initiation to propagation is around 40% in mode I and 55% in mode II, respectively. Nevertheless, if the amount of SERR related to softening is included in the critical SERR at crack initiation, the ratio is 40% in DCB and 60% in 4ENF, which are more consistent to the literature results.

DCB experimental and numerical results reveals that crack extension at the end of softening (stage “b”) is 2.5 mm which is 16% of the FPZ length (16 mm). Considering the limited crack extension, inclusion of softening as crack initiation is physically reasonable. However, 4ENF results show that crack extension at stage “b” is 7 mm which is already 67% of the FPZ length (10.5 mm). In this case, considering SERR related to softening as part of the crack initiation is not feasible. Further studies are needed to align the SERR ratio better with the existing research studies.

It should be noted that considering SERR related to softening as part of the critical SERR at initiation in 3ENF tests results in extremely high ratio of it to propagation (96%). This could be attributed to the lower traction values at the softening process as a consequence of low steel surface roughness in the batch of 3ENF specimens compared to 4ENF.

Table 4-11 Overview of critical SERR values of DCB, 3ENF and 4ENF specimens

Interface test scenario	Critical SERR (N/mm)			Ratio of initiation to propagation (%)	
	$G_{Ic,tip}$	$G_{Ic,tip} + G_{I,soft}$	G_{Ic}	$G_{Ic,tip} / G_{Ic}$	$(G_{Ic,tip} + G_{I,soft}) / G_{Ic}$
DCB	0.3	0.56	1.4	21	40
Interface test scenario	Critical SERR (N/mm)			Ratio of initiation to propagation (%)	
	$G_{IIc,tip}$	$G_{IIc,tip} + G_{II,soft}$	G_{IIc}	$G_{IIc,tip} / G_{IIc}$	$(G_{IIc,tip} + G_{II,soft}) / G_{IIc}$
3ENF	0.56	3.35	3.5	16	96
4ENF	0.89	3.25	5.4	16	60

4.5 Conclusions

In this Chapter, 3 series of composite material coupon experiments were conducted to identify its tensile, compressive and in-plane shear behavior. Meanwhile, 4 series of interface (debonding) experiments were employed to understand and quantify the mode I and mode II fracture behavior of the used metal-composite interface. Based on the test results and the discussion, the follow conclusions are drawn:

1) A four-linear traction-separation law is proposed to describe the mode I and mode II fracture behavior of the metal-composite interface. It describes three distinct phenomena: 1) crack tip deformation, 2) softening (newly proposed) and 3) fiber bridging. The fracture morphology indicates that fiber bridging is governing in mode I, but softening phenomenon contributes the most to the fracture toughness in mode II as a consequence of pull-out of resin from valleys in the micro profile of steel surface roughness.

2) No adhesive (interfacial) failure was observed in the considered pure mode I fracture process. The fracture path is through the first ply of the composite adherend (substrate failure) featuring significant fiber bridging behavior. The critical SERR $G_{Ic,tip}$ is 0.3 N/mm on average obtained for crack initiation while the critical SERR G_{Ic} is 1.47 N/mm on average obtained for crack propagation. The average FPZ length corresponding to summation of softening and fiber bridging is approximately 16 mm.

3) To ensure crack propagation on the composite-steel bonded interface instead of transition into the inter-laminar interface due to tensile bending stresses, composite laminate should be designed as the lower adherend (with respect to the load direction) in 3ENF and 4ENF experiments. 3ENF test provides good insight into softening behavior while 4ENF shows to be more useful to quantify fiber bridging.

4) The critical SERR for crack initiation $G_{IIc,tip}$ is within the range of 0.55~1.1 N/mm based on 3ENF and 4ENF results. The critical SERR G_{IIc} is 5.4 N/mm on average for crack propagation while the average fracture process zone (FPZ) length corresponding to summation of softening and fiber bridging is 10.5 mm, based on 4ENF results.

5) An approach is proposed to determine the critical stages of the four-linear

cohesive law through the combination of detailed measurements of crack length and CTOD using 2D DIC, along with SERR values calculated by EGM. A new “shear strain scaling method” is proposed based on DIC measurements to quantify the crack length in the 3ENF and 4ENF tests. DIC sectioning method is introduced and proved to be effective to evaluate usually challenging mode II CTOD.

References

- [1] P. He and M. Pavlovic, “Failure modes of bonded wrapped composite joints for steel circular hollow sections in ultimate load experiments,” *Eng. Struct.*, vol. 254, no. August 2021, p. 113799, 2022, doi: 10.1016/j.engstruct.2021.113799.
- [2] P. He, W. Feng, and M. Pavlovic, “Influence of steel yielding and resin toughness on debonding of wrapped composite joints,” *Compos. Struct.*, vol. 312, no. February, p. 116862, 2023, doi: 10.1016/j.compstruct.2023.116862.
- [3] ASTM International, “ASTM D5528 - 13: 2014 - Standard Test Method for Mode I Interlaminar Fracture Toughness of Unidirectional Fiber-Reinforced Polymer Matrix Composites 1,” *West Conshohocken, PA ASTM Int.*, doi: 10.1520/D5528-13.
- [4] International Standards Organization, “ISO 15024:2001 Fibre-reinforced plastic composites -- Determination of mode I interlaminar fracture toughness, GIC, for unidirectionally reinforced material,” 2001. <https://www.iso.org/standard/25581.html> (accessed Jan. 20, 2023).
- [5] S. Azari, A. Ameli, M. Papini, and J. K. Spelt, “Analysis and design of adhesively bonded joints for fatigue and fracture loading: A fracture-mechanics approach,” *J. Adhes. Sci. Technol.*, vol. 27, no. 15, pp. 1681–1711, 2013, doi: 10.1080/01694243.2012.748434.
- [6] G. Ji, Z. Ouyang, G. Li, S. Ibekwe, and S. S. Pang, “Effects of adhesive thickness on global and local mode-I interfacial fracture of bonded joints,” *Int. J. Solids Struct.*, vol. 47, no. 18–19, pp. 2445–2458, 2010, doi: 10.1016/j.ijsolstr.2010.05.006.
- [7] M. M. Shokrieh, M. Heidari-Rarani, and M. R. Ayatollahi, “Interlaminar fracture toughness of unidirectional DCB specimens: A novel theoretical approach,” *Polym. Test.*, vol. 31, no. 1, pp. 68–75, 2012, doi: 10.1016/j.polymertesting.2011.08.012.
- [8] M. Cabello, A. Turon, J. Zurbitu, J. Renart, C. Sarrado, and F. Martínez, “Progressive failure analysis of DCB bonded joints using a new elastic foundation coupled with a cohesive damage model,” *Eur. J. Mech. A/Solids*, vol. 63, pp. 22–35, 2017, doi: 10.1016/j.euromechsol.2016.12.004.
- [9] A. Russel, “Factors affecting the interlaminar fracture energy of graphite/epoxy laminates,” in *Proc. 4th Int. Conf. Comp. Mater.*, 1982. Accessed: Mar. 08, 2023. [Online]. Available: <https://cir.nii.ac.jp/crid/1573387449040385408>
- [10] A. Russel, “On the measurement of mode II interlaminar fracture energies,” *Def. Res. Establ. pacific, victoria BC*, 1982.
- [11] ASTM International, “ASTM D7905/D7905M-14: Standard Test Method for Determination of the Mode II Interlaminar Fracture Toughness of Unidirectional Fiber-Reinforced Polymer,” *West Conshohocken, PA ASTM Int.*, 2014, doi: 10.1520/D7905.
- [12] M. Todo, P. Y. B. Jar, and K. Takahashi, “Initiation of a mode-II interlaminar crack from an insert film in the end-notched flexure composite specimen,” *Compos. Sci.*

Technol., vol. 60, no. 2, pp. 263–272, 2000, doi: 10.1016/S0266-3538(99)00119-0.

[13] M. F. S. F. de Moura, R. D. S. G. Campilho, and J. P. M. Gonçalves, “Pure mode II fracture characterization of composite bonded joints,” *Int. J. Solids Struct.*, vol. 46, no. 6, pp. 1589–1595, 2009, doi: 10.1016/j.ijsolstr.2008.12.001.

[14] C. C. Chen and D. G. Linzell, “Modeling end notched flexure tests to establish cohesive element Mode II fracture parameters,” *Eng. Fract. Mech.*, vol. 77, no. 8, pp. 1338–1347, 2010, doi: 10.1016/j.engfracmech.2010.03.017.

[15] A. Arrese, N. Carbajal, G. Vargas, and F. Mujika, “A new method for determining mode II R-curve by the End-Notched Flexure test,” *Eng. Fract. Mech.*, vol. 77, no. 1, pp. 51–70, 2010, doi: 10.1016/j.engfracmech.2009.09.008.

[16] L. A. Carlsson, J. W. Gillespie, and R. B. Pipes, “On the Analysis and Design of the End Notched Flexure (ENF) Specimen for Mode II Testing,” *J. Compos. Mater.*, vol. 20, no. 6, pp. 594–604, 1986, doi: 10.1177/002199838602000606.

[17] P. Davies, P. Casari, and L. A. Carlsson, “Influence of fibre volume fraction on mode II interlaminar fracture toughness of glass/epoxy using the 4ENF specimen,” *Compos. Sci. Technol.*, vol. 65, no. 2, pp. 295–300, 2005, doi: 10.1016/j.compscitech.2004.07.014.

[18] B. R. K. Blackman, A. J. Kinloch, and M. Paraschi, “The determination of the mode II adhesive fracture resistance, GIIC, of structural adhesive joints: An effective crack length approach,” *Eng. Fract. Mech.*, vol. 72, no. 6 SPEC. ISS., pp. 877–897, 2005, doi: 10.1016/j.engfracmech.2004.08.007.

[19] A. J. Brunner, B. R. K. Blackman, and P. Davies, “A status report on delamination resistance testing of polymer-matrix composites,” *Eng. Fract. Mech.*, vol. 75, no. 9, pp. 2779–2794, 2008, doi: 10.1016/j.engfracmech.2007.03.012.

[20] R. H. Martin and B. D. Davidson, “Mode II fracture toughness evaluation using four point bend, end notched flexure test,” *Plast. Rubber Compos. Process. Appl.*, vol. 28, no. 8, pp. 401–406, 1999, doi: 10.1179/146580199101540565.

[21] C. Schuecker and B. D. Davidson, “Evaluation of the accuracy of the four-point bend end-notched flexure test for mode II delamination toughness determination,” *Compos. Sci. Technol.*, vol. 60, no. 11, pp. 2137–2146, 2000, doi: 10.1016/S0266-3538(00)00113-5.

[22] M. Khoshravan and F. Asgari Mehrabadi, “Fracture analysis in adhesive composite material/aluminum joints under mode-I loading; Experimental and numerical approaches,” *Int. J. Adhes. Adhes.*, vol. 39, pp. 8–14, 2012, doi: 10.1016/j.ijadhadh.2012.06.005.

[23] K. Shimamoto, Y. Sekiguchi, and C. Sato, “Effects of surface treatment on the critical energy release rates of welded joints between glass fiber reinforced polypropylene and a metal,” *Int. J. Adhes. Adhes.*, vol. 67, pp. 31–37, 2016, doi: 10.1016/j.ijadhadh.2015.12.022.

- [24] K. Shimamoto, Y. Sekiguchi, and C. Sato, “The Critical Energy Release Rate of Welded Joints between Fiber-Reinforced Thermoplastics and Metals When Thermal Residual Stress is Considered,” *J. Adhes.*, vol. 92, no. 4, pp. 306–318, 2016, doi: 10.1080/00218464.2015.1031339.
- [25] W. Wang, R. Lopes Fernandes, S. Teixeira De Freitas, D. Zarouchas, and R. Benedictus, “How pure mode I can be obtained in bi-material bonded DCB joints: A longitudinal strain-based criterion,” *Compos. Part B Eng.*, vol. 153, no. July, pp. 137–148, 2018, doi: 10.1016/j.compositesb.2018.07.033.
- [26] G. Zambelis, T. Da Silva Botelho, O. Klinkova, I. Tawfiq, and C. Lanouette, “Evaluation of the energy release rate in mode I of asymmetrical bonded composite/metal assembly,” *Eng. Fract. Mech.*, vol. 190, pp. 175–185, 2018, doi: 10.1016/j.engfracmech.2017.12.007.
- [27] M. M. Arouche, W. Wang, and S. T. De Freitas, “Strain-based methodology for mixed-mode I + II fracture: A new partitioning method for bi-material adhesively bonded joints,” *J. Adhes.*, vol. 95, no. 5–7, pp. 385–404, 2019, doi: 10.1080/00218464.2019.1565756.
- [28] P. Davidson, A. M. Waas, and C. S. Yerramalli, “Experimental determination of validated, critical interfacial modes I and II energy release rates in a composite sandwich panel,” *Compos. Struct.*, vol. 94, no. 2, pp. 477–483, 2012, doi: 10.1016/j.compstruct.2011.08.007.
- [29] C. Alía, J. M. Arenas, J. C. Suárez, J. J. Narbón, and R. Ocaña, “ENF test in the adhesive bonding of aluminium-composite joints and evaluation of its reliability with Weibull distribution,” *J. Adhes. Sci. Technol.*, vol. 27, no. 11, pp. 1236–1246, 2013, doi: 10.1080/01694243.2012.736853.
- [30] C. Alía, J. M. Arenas, J. C. Suárez, R. Ocaña, and J. J. Narbón, “Mode II fracture energy in the adhesive bonding of dissimilar substrates: Carbon fibre composite to aluminium joints,” *J. Adhes. Sci. Technol.*, vol. 27, no. 22, pp. 2480–2494, 2013, doi: 10.1080/01694243.2013.787516.
- [31] J. M. Arenas, R. Ocaña, C. Alía, J. J. Narbón, and M. Islán, “Fracture energy in structural adhesive joints of composite-aluminum under adverse environments conditions,” *J. Adhes. Sci. Technol.*, vol. 28, no. 2, pp. 201–214, 2014, doi: 10.1080/01694243.2013.833404.
- [32] Z. Ouyang and G. Li, “Nonlinear interface shear fracture of end notched flexure specimens,” *Int. J. Solids Struct.*, vol. 46, no. 13, pp. 2659–2668, 2009, doi: 10.1016/j.ijsolstr.2009.02.011.
- [33] H. Ning *et al.*, “Investigation on mode-II interface fracture toughness of CFRP/Al laminates toughened by VGCF interleaves,” *J. Mater. Sci.*, vol. 50, no. 4, pp. 1915–1923, 2015, doi: 10.1007/s10853-014-8755-5.
- [34] W. Wang, S. T. De Freitas, J. A. Poulis, and D. Zarouchas, “A review of

experimental and theoretical fracture characterization of bi-material bonded joints,” *Compos. Part B Eng.*, vol. 206, no. October 2020, p. 108537, 2021, doi: 10.1016/j.compositesb.2020.108537.

[35] Z. Ouyang, G. Ji, and G. Li, “On approximately realizing and characterizing pure mode-I interface fracture between bonded dissimilar materials,” *J. Appl. Mech. Trans. ASME*, vol. 78, no. 3, 2011, doi: 10.1115/1.4003366.

[36] Z. Ouyang, G. Ji, G. Li, S. Ibekwe, and S. Pang, “A new idea of pure mode-I fracture test of bonded bi-materials,” in *Proceedings of the ASME 2010 Pressure Vessels & Piping Division / K-PVP Conference*, 2010.

[37] International Standards Organization, “ISO 527-1:2012 - Plastics - Determination of tensile properties - Part 1: General principles,” 2012, [Online]. Available: www.iso.org

[38] International Standards Organization, “ISO 14129: 1997 Fibre-reinforced plastic composites — Determination of the in-plane shear stress/shear strain response, including the in-plane shear modulus and strength, by the plus or minus 45 degree tension test method,” 1997.

[39] ISO, “Nen-en-iso 14126,” no. 015, 2023.

[40] R. K. Joki, F. Grytten, B. Hayman, and B. F. Sørensen, “A mixed mode cohesive model for FRP laminates incorporating large scale bridging behaviour,” *Eng. Fract. Mech.*, vol. 239, no. September 2019, p. 107274, 2020, doi: 10.1016/j.engfracmech.2020.107274.

[41] R. K. Joki, F. Grytten, B. Hayman, and B. F. Sørensen, “Determination of a cohesive law for delamination modelling - Accounting for variation in crack opening and stress state across the test specimen width,” *Compos. Sci. Technol.*, vol. 128, pp. 49–57, 2016, doi: 10.1016/j.compscitech.2016.01.026.

[42] A. Comeselle-Molares, A. P. Vassilopoulos, J. Renart, A. Turon, and T. Keller, “Numerical simulation of two-dimensional in-plane crack propagation in FRP laminates,” *Compos. Struct.*, vol. 200, no. April, pp. 396–407, 2018, doi: 10.1016/j.compstruct.2018.05.136.

[43] M. Heidari-Rarani, M. M. Shokrieh, and P. P. Camanho, “Finite element modeling of mode I delamination growth in laminated DCB specimens with R-curve effects,” *Compos. Part B Eng.*, vol. 45, no. 1, pp. 897–903, 2013, doi: 10.1016/j.compositesb.2012.09.051.

[44] A. B. De Moraes and A. B. Pereira, “Mixed mode I + II interlaminar fracture of glass / epoxy multidirectional laminates – Part I : Analysis,” *Compos. Sci. Technol.*, vol. 66, pp. 1889–1895, 2006, doi: 10.1016/j.compscitech.2006.04.006.

[45] M. Shahverdi, A. P. Vassilopoulos, and T. Keller, “Mixed-mode quasi-static failure criteria for adhesively-bonded pultruded GFRP joints,” *Compos. Part A Appl. Sci. Manuf.*, vol. 59, pp. 45–56, 2014, doi: 10.1016/j.compositesa.2013.12.007.

-
- [46] M. Shahverdi, A. P. Vassilopoulos, and T. Keller, “Mixed-Mode I/II fracture behavior of asymmetric adhesively-bonded pultruded composite joints,” *Eng. Fract. Mech.*, vol. 115, pp. 43–59, 2014, doi: 10.1016/j.engfracmech.2013.11.014.
- [47] M. Shahverdi, A. P. Vassilopoulos, and T. Keller, “Mixed-Mode I/II fracture behavior of asymmetric composite joints,” *Procedia Struct. Integr.*, vol. 2, pp. 1886–1893, 2016, doi: 10.1016/j.prostr.2016.06.237.

5. FINITE ELEMENT MODELING OF MATERIAL AND INTERFACE EXPERIMENTS

In this Chapter, a finite element modeling (FEM) strategy for simulating the composites and composite-steel bonded interface using ABAQUS are proposed. The composite material is modeled by solid elements, and its damage is phenomenologically simulated by plasticity. The cohesive zone modeling (CZM) is employed to capture the fracture behavior of the composite-steel bonded interface. A new four-linear traction-separation law is proposed for modeling of the metal-composite interfacial failure. The necessary strain energy release rate (SERR) and the crack tip opening displacement (CTOD) required for calculating the cohesive law are obtained through fracture data analysis in Chapter 4.

The FEM strategy and material input are implemented to model the double cantilever beam (CCB) and the end notched flexure (ENF) tests presented in the previous chapter. The simulation results are validated through a good agreement with the experimental results in both global behavior and local fracture behavior

5.1 Introduction

In Chapter 4, three series of composite material coupon tests were conducted to determine the tensile, compressive, and in-plane shear properties of the composite wrap. Meanwhile, four series of interface (debonding) experiments were employed to understand and quantify the mode I and mode II fracture behavior of the composite-steel bonded interface used in the innovative wrapped composites joints. The fracture properties, i.e., the critical strain energy release rate (SERR) and the fracture process zone (FPZ) length, were quantified. Three distinct phenomena, namely 1) crack tip deformation, 2) softening and 3) fiber bridging, were identified, and a four-linear traction-separation law was proposed to describe the identified fracture process.

It is essential to accurately model the behavior of composite wrap and the composite-steel bonded interface in wrapped composite joints as the prerequisite of predicting its resistance and replicating the debonding process. In the current literature, the composite wrapping was modelled by shell elements[1]–[13]. This is suitable for application in FRP-strengthened tubular joints where the weld still transferred the main load such that thickness of wrapping is relatively small especially at the intersection region (no more than 10 mm) due to limited numbers of wrapping plies. However, this is not applicable in the case of wrapped composite joints with wrapping thickness significantly larger than that in strengthened joints. Using shell element to model behavior of thick and curved geometry is difficult and inaccurate so an alternative method should be proposed.

In the fracture problems of the composite-metal interface where the size of fracture process zone (FPZ) is not negligible attributed to plasticity of adherends due to micro-cracking of resin and fiber bridging, the LEFM cannot be appropriately used for fracture analysis. Instead, the non-linear interface behavior can be approximated with help of the cohesive zone modeling (CZM) [14] where the constitutive behavior of the FPZ is defined by the traction-separation law (cohesive law) derived from laboratory tests. The shape of the cohesive law is highly dependent on the material properties, composite layup, adherend surface treatment, etc. The CZM has been extensively applied in the numerical simulation of delamination in composites[15]–[20]. Unluckily, there is limited research studies in terms of applying cohesive zone model in simulation of composite-steel bonded interface[21].

This Chapter deals with developing the FEM strategy in ABAQUS for simulation of composite wrap and composite-steel bonded interface which is validated in the material level due to simplification of geometry, low calculational cost and the opportunity to simulate the interface fracture modes separately. The material properties of composites obtained in the composite coupon experiments are used as input to simulate its behavior in the FE model. The four-linear traction-separation laws proposed in Chapter 4 will be explained thoroughly as well as the introduction of mode mixity. The modeling approach and the cohesive law are validated by good matches between numerical and experimental results.

5.2 Determination of element type and mesh size

In general composite material can be modeled by any deformable elements in ABAQUS. The selection of finite element types is mainly determined by the types of structures and the types of analysis that is desired. Two categories of elements are normally utilized in numerical simulation of composite structures: 2D shell elements and 3D solid elements. Shell elements allow easy definition of lay-up and geometry of composite material but excludes the possibility to model delamination. In shell elements the thickness is defined through the cross section property which is not suitable for modeling complex and curve-shape composite wrap in wrapped composite joints. The stresses and stiffness in the through-thickness (out-of-plane shear) direction of the composite laminate is not available using shell elements. In the case where contact interactions are modeled as the main failure mechanism, e.g., debonding in wrapped composite joints, the actual thickness of elements is significant where shell element is not suitable.

The disadvantages of modeling by 2D shell elements are partly overcome by using the continuum shell elements, sometimes referred to as 2.5D elements, as shown in Figure 5-1. In continuum shell elements the modeling of the laminate includes real thickness defined by nodal geometry such that contact interactions work properly in simulation. It is useful in the case where thickness of the laminate is varied. However, values of stresses and stiffness in the through-thickness direction (S_{33}) are not accurate in continuum shell element, as well as the out-of-plane shear properties.

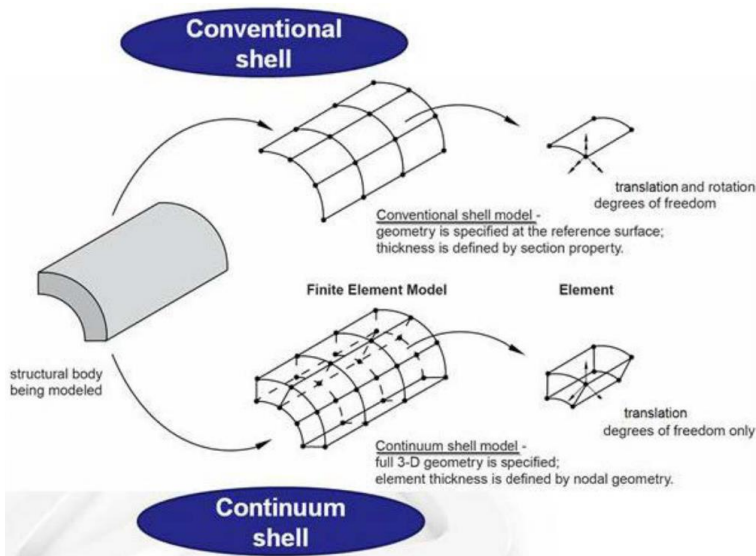


Figure 5-1 Conventional versus continuum shell element[22]

The 3D solid elements are used in simulation of composite wrap in wrapped composite joints, as shown in Figure 5-2, considering its advantage in modeling of

through-thickness behavior over 2D conventional shell and 3D continuum shell elements. The simplification is performed by considering groups of plies by equivalent layers corresponding to wrapping procedure which is explained thoroughly in Chapter 6. The modeling strategy in the material level is consistent to the joint level where 4-node linear tetrahedral elements (C3D4) is used to model composite material, as presented in Figure 5-3. Tetrahedral elements are used as the substitute for hexahedral elements which cannot be used in the curved shape of composite wrap due to difficulty of meshing. Second-order elements capture stress concentrations more effectively and are better for modeling geometric features than first-order (linear) elements, but they require significant calculation costs. Based on the preliminary joint modeling results, linear elements do not significantly result in modeling inaccuracy considering the relatively fine mesh size used in the composite wrap, but enormously enhances modeling efficiency. Therefore, C3D4 elements is used in modeling of composite material, as shown in Figure 5-2 and Figure 5-3. The steel part is meshed with 8-node linear hexahedral element (C3D8) attributed to its simple geometry in wrapped composite joints and DCB/ENF FE models. The global mesh size of composite material and steel is 2 mm according to the results of mesh sensitivity analysis in joint modeling in Chapter 6, which is sufficiently efficient in computational cost but does not sacrifice the accuracy of modeling out-of-plane shear stresses significantly. Local seeds are assigned to the steel plate in DCB/ENF modeling such that 4 elements are present in the through-thickness direction to accurately simulate the bending-dominated deformation, as shown in Figure 5-3 b).



Figure 5-2 Modelling composite wrap of wrapped composite joints using 3D solid elements (4-node linear tetrahedral elements, C3D4)

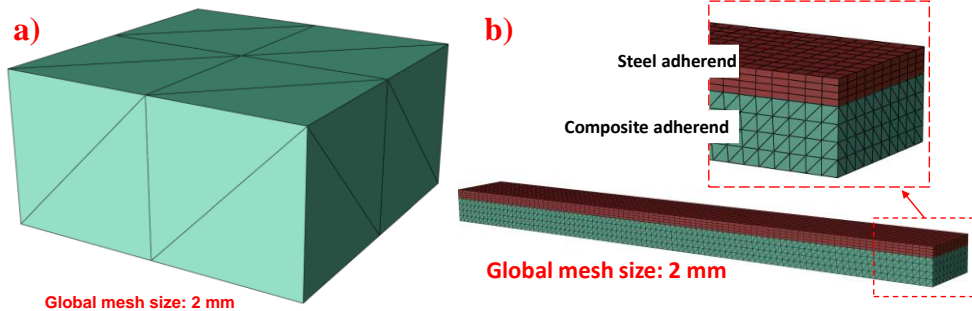


Figure 5-3 Utilization of C3D4 in mesh of composite material and C3D8 in mesh of steel: a) mesh of composite material FE model; b) mesh of interface FE model

5.3 FEM of composites

The composite material is modeled by a cuboid with 4-mm length, 4-mm width and 2-mm height, see Figure 5-3 a) . The aim of this FE model is to justify the FEM strategies introduced to model composites based on the input of material properties from the composite material coupon tests.

5.3.1 Boundary conditions

The displacement/rotation boundary conditions are used in the composite material FE model as shown in Figure 5-4. Two reference points named “Load” and “Hold” are built at the middle of the intersection line between the front and top surface, and between the bottom and back surface, respectively. Displacement controlled failure loading is defined to the reference point “Load” fixed in all degrees of freedom except for the longitudinal translation U1 (1 is designation for the global X direction). The reference point “Hold” is then assigned with a fully fixed boundary condition to simulate the static loading condition. In simulation of axial tensile (compressive) loading, the front and the back surface is kinematically constrained (coupled) to the reference point “Load” applied with positive (negative) U1 displacement and “Hold” fixed completely, respectively, in longitudinal translation U1 and all rotational degrees of freedom. The constraint in the transverse (U2) and through-thickness translation (U3) is released to replicate contract (expansion) of the cross section of composite material due to Poisson Effect, as shown in Figure 5-4 a) and Figure 5-4 b). Similar coupling constraint is applied from the reference point “Load” and “Hold” to the right and the left surface, respectively, in all degrees of freedom to simulate in-plane shear loading, see Figure 5-4 c). Simulation of out-of-plane shear loading is conducted using the same coupling constraint applied to the top and the bottom surface of composite material, see Figure 5-4 d). The obtained longitudinal displacement U1 and the corresponding reaction force (RF1) of the reference point “Load” is divided by the distance between and the cross section area of the constrained surfaces of the composite material part, respectively, to obtain the stress-strain curve in the corresponding loading cases.

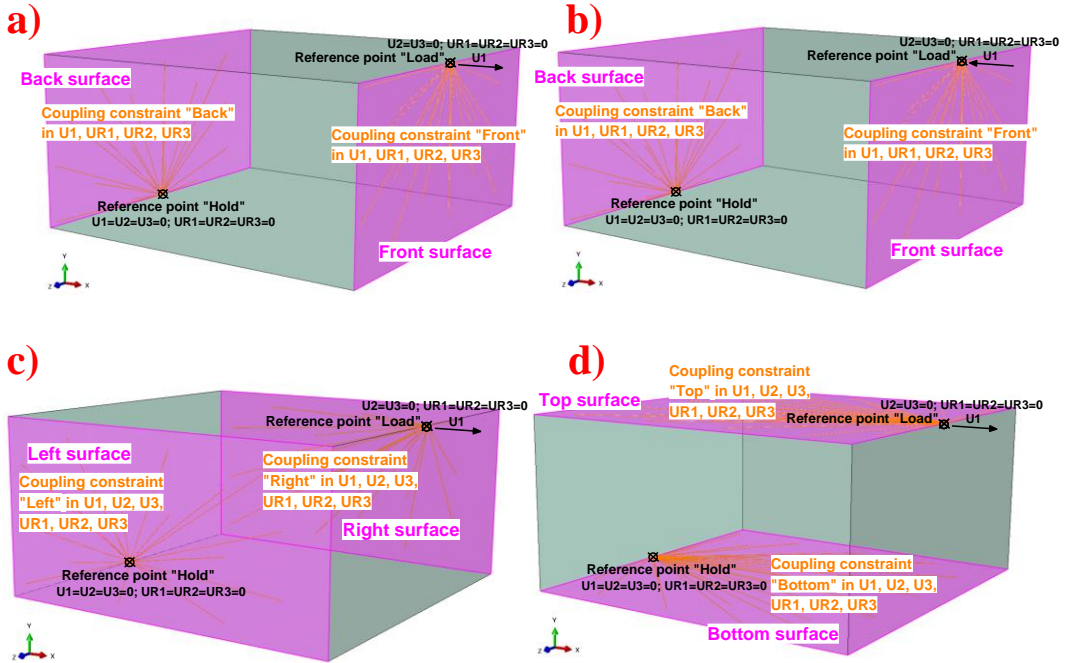


Figure 5-4 Boundary conditions in composite material FE model subjected to a) tension; b) compression; c) in-plane shear and d) out-of-plane shear load

5.3.2 Analyses method

Material nonlinear analysis in modeling of composites and cohesive failure analysis in modeling of interface are performed as quasi-static using the explicit dynamic solver in ABAQUS because it does not have the usual convergence issue as does the implicit static solver. Bottleneck of any explicit dynamic solver is the characteristic size of the smallest finite element in a model, since divided by a wave propagation speed it represents the maximum stable time increment for the integration. Computation time of a real time quasi-static analysis can be inapplicable long. Calculation speed can be increased either by a mass scaling method. This method tends to increase inertia forces in a model, sometimes leading to useless results. A compromise must be found between an acceptable computation time and quality of results, often by analyses for each of the different model set-ups.

Mass scaling with desired time increment of 0.002 sec is used in the modeling of composite material and DCB/ENF experiments. Quality of the results is verified by matching applied and reaction forces in a model for displacement controlled failure loading, as shown in the example of 4ENF modeling results Figure 5-5. Linear matching curve with no fluctuations for the smallest analyzed desired time increment (0.002 s) proves that no inertia effects govern the results.

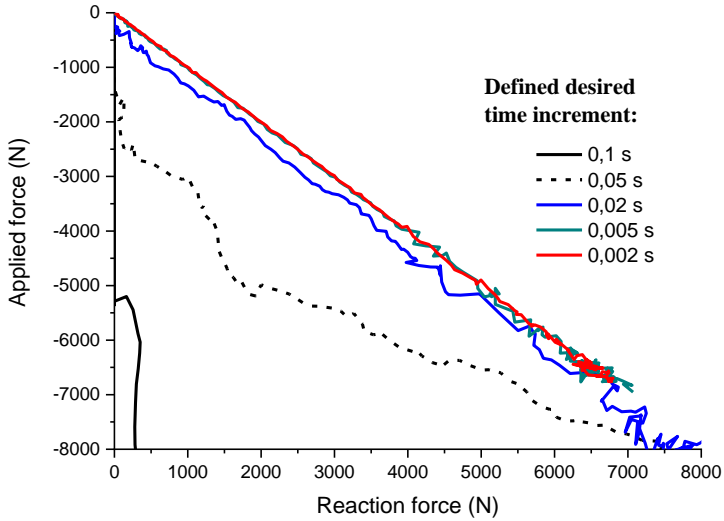


Figure 5-5 Quality of quasi-static solution

5.3.3 Material model of composites

The nature of the composite material used in wrapped composite joints follows a typical stress-strain response of metal specimen which comprises three states of material behavior (see Section 4.2): elasticity, plasticity and damage, as illustrated in Figure 5-6. Therefore, the framework to model linear elastic behavior, plastic behavior and progressive damage in steel are used in modeling of composite material, taking into account the orthotropic properties in different material directions.

Linear elasticity of composite material is defined by “Engineering Constants” considering the orthotropic behavior, and the constitutive law is expressed in Equation 5-1. The subscript 1, 2, 3 represents the principal direction aligned with the fiber, perpendicular to the fiber in plane, and perpendicular to the fiber out of plane, respectively. Three elastic modulus E_1 , E_2 , E_3 , Poisson’s ratios ν_{12} , ν_{13} , ν_{23} , and the shear modulus G_{12} , G_{13} , G_{23} associate with the material’s principal directions. The quasi-isotropic behavior of the composite material determined by the layup composition requires that $E_1 = E_2$, $\nu_{13} = \nu_{23}$ and $G_{13} = G_{23}$. The input of linear elasticity of composite material is the same as the material test results summarized in Section 4.2.3, where E_1 (E_2), ν_{12} , G_{12} are obtained from the ISO standard coupon experiments[23]–[25]. In addition, the elastic modulus in through-thickness tensile and shear behavior is $E_3 = 5000 \text{ N/mm}^2$ and $G_{13} = G_{23} = 2500 \text{ N/mm}^2$, respectively. These values were obtained based on the manufacturer’s data and calculation using classical laminate theory and rule of mixture.

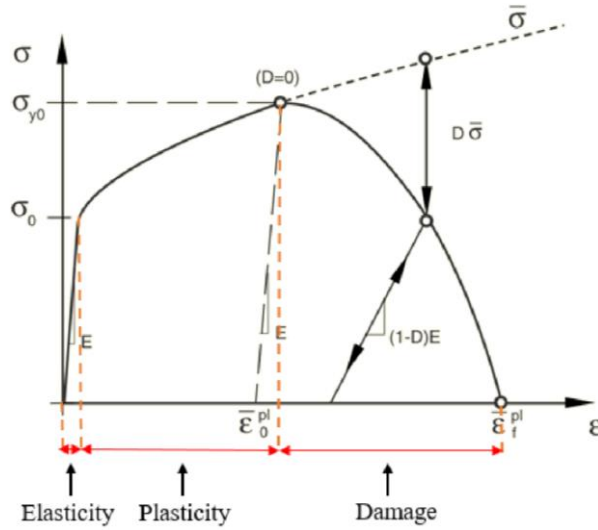


Figure 5-6 The stress-strain response of a typical metal specimen

$$\begin{Bmatrix} \varepsilon_{11} \\ \varepsilon_{22} \\ \varepsilon_{33} \\ \gamma_{12} \\ \gamma_{13} \\ \gamma_{23} \end{Bmatrix} = \begin{bmatrix} 1/E_1 & -\nu_{21}/E_2 & -\nu_{31}/E_3 & 0 & 0 & 0 \\ -\nu_{12}/E_1 & 1/E_2 & -\nu_{32}/E_3 & 0 & 0 & 0 \\ -\nu_{13}/E_1 & -\nu_{23}/E_2 & 1/E_3 & 0 & 0 & 0 \\ 0 & 0 & 0 & 1/G_{12} & 0 & 0 \\ 0 & 0 & 0 & 0 & 1/G_{13} & 0 \\ 0 & 0 & 0 & 0 & 0 & 1/G_{23} \end{bmatrix} \begin{Bmatrix} \sigma_{11} \\ \sigma_{22} \\ \sigma_{33} \\ \sigma_{12} \\ \sigma_{13} \\ \sigma_{23} \end{Bmatrix} \tag{Equation 5-1}$$

Plasticity theories have been developed most intensively for metals, but its fundamental concepts are sufficiently general that model based on these concepts have been developed successfully for a wide range of materials. Anisotropic yield is used in this chapter to simulate the orthotropic softening behavior of composite material. The definition of composite material damage is not provided in this thesis for simplification, as no material failure of composites is observed in the experiments.

5.3.4 Validation of composites FEM

The material model of composite material defined in Section 5.3.3 is input into the composite material FE model to simulate its tensile, compressive, in-plane shear and out-of-plane shear behavior. The numerical material properties are compared to the composite coupon test results to justify the feasibility of the input data. Comparison of the average material property values in experiments vs the material property output in FEM are summarized in Table 5-1 while numerical material stress-strain curves are plotted against the experimental stress-strain curves in Figure 5-7~Figure 5-9 for justification.

It can be seen from Table 5-1 and Figure 5-7~Figure 5-9 that the elastic modulus matches well in tensile, compressive and in-plane shear loading cases, with the deviation

of FEA results from average experimental results all within 10%. The softening behavior also matches well in all loading cases, while the FEA results show more pronounced non-linear behavior after 75 MPa when the material is loaded in compression as illustrated in Figure 5-8. This is because composite material exhibits less non-linearity when subjected to compression compared to tension, as shown in the coupon experiments in Chapter 4. However, the same constitutive law is used in ABAQUS to define the material properties both under tensile and compressive load, leading to overestimation of the non-linear behavior in compression if the material model is input based on the tensile loading scenario. Since the focus of this research is to use plasticity to model softening of composite material in the out-of-plane shear direction aiming to simulate debonding, overestimation of plasticity in compression in the FEA can be acceptable.

Table 5-1 Comparison of elastic modulus of composites in coupon experiments vs FEM ('cT', 'cC', 'cIPS' indicate coupon tension, coupon compression, coupon in-plane shear load scenario, respectively; 'average' indicates the average coupon test results; 'FEM' indicates the modeling output)

Coupon tensile scenario	Tensile modulus [MPa]
cT_average (and COV [%])	11798 (6.37)
cT-FEM	12650
Deviation (%)	7
Coupon compression scenario	Compressive modulus [MPa]
cC_average (and COV [%])	12077 (4.50)
cC-FEM	12851
Deviation (%)	6
Coupon in-plane shear scenario	Shear modulus [GPa]
cIPS_average (and COV [%])	3.12 (6.81)
cIPS-FEM	3.45
Deviation (%)	9

Out-of-plane shear deformation of composite material is considerable, and its input needs to be correctly defined. Unluckily there is no current standard available to obtain the out-of-plane shear properties of composite material through physical experiments. In the current study the out-of-plane shear material input of composites is determined implicitly by iteration in DCB/ENF modeling and in joint modeling. The shear modulus and peak shear stress are 2.50 GPa and 55.65 MPa, respectively.

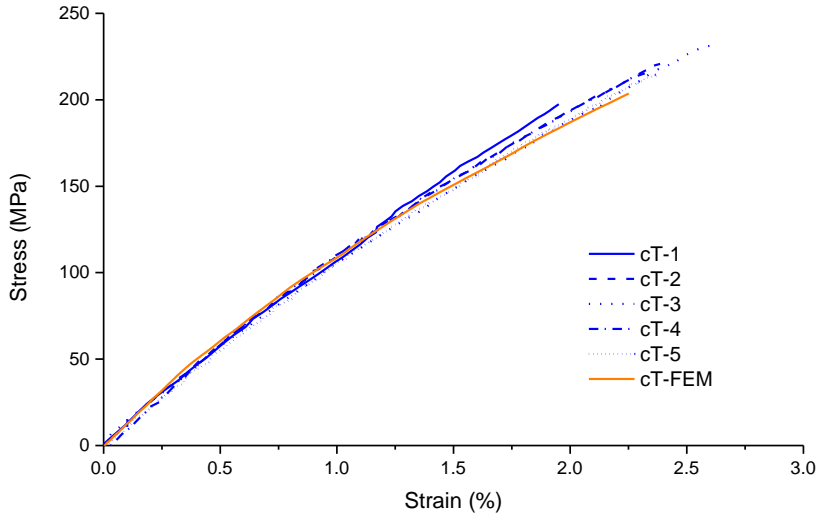


Figure 5-7 Tensile stress-strain behavior of composites from FEM vs from coupon tests

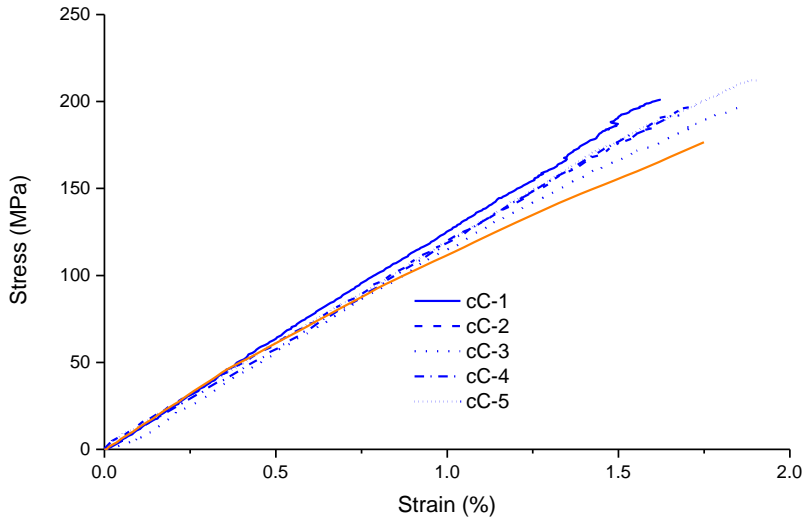


Figure 5-8 Compressive stress-strain behavior of composites from FEM vs from coupon tests

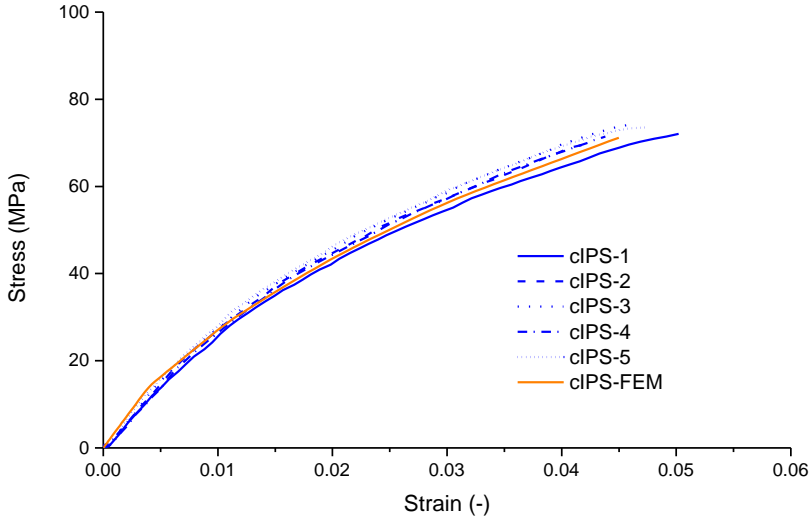


Figure 5-9 In-plane shear stress-strain behavior of composites from FEM vs from coupon tests

5.4 FEM of DCB and ENF tests

The geometry of the DCB, 3ENF and 4ENF FE models are presented in Figure 5-10 where the part in red represents steel adherend while the part in green represents composite material adherend. The hollow cylindrical parts in blue are the loading pin and the support pins.

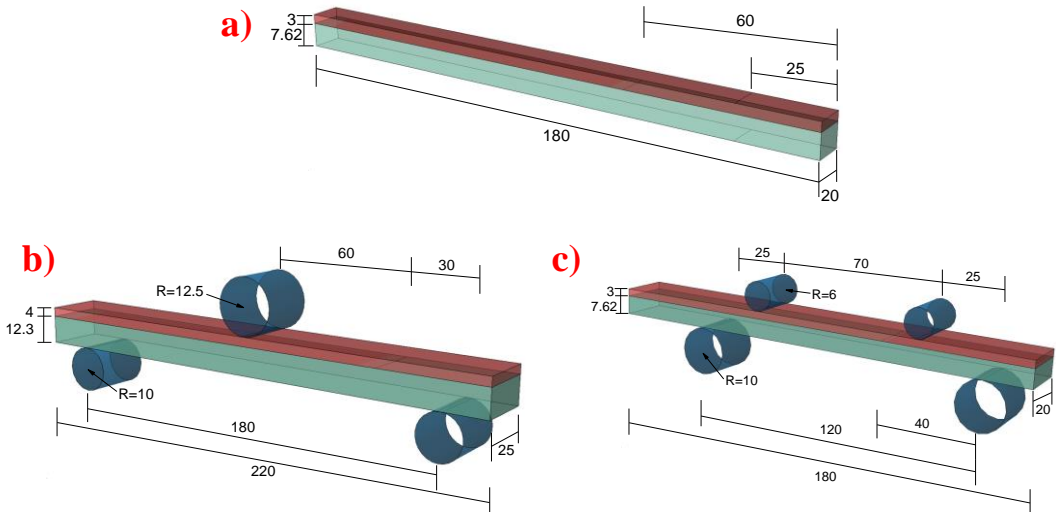


Figure 5-10 Geometries of FE models in simulation of a) DCB, b) 3ENF and c) 4ENF experiments (unit: mm)

The dimensions of the DCB, 3ENF and 4ENF models correspond well to the test series 4, test series 6 and test series 7 presented in Section 4.3, respectively. 3ENF tests with composites as upper adherend are not simulated because of migration of crack into the laminate which could not provide fracture properties of the bonded interface. The aim of interface FEM is to validate the FEM strategies and to validate the proposed cohesive law in modeling fracture process of composite-steel bonded interface by comparing to the interface test results. It should be noted that the selection of element type and mesh size, and utilization of analyses method in the interface FEM have been discussed in Section 5.2.

5.4.1 Boundary conditions

Figure 5-11 a) shows a representation of the boundary conditions applied in the DCB model. The symmetry boundary condition in global Z direction was applied to the back surface of the half model to save computational costs. The area of the steel and composite adherends glued with the loading pin designated as upper surface and lower surface was kinematically constrained (coupled) to the “Load” and the “Hold” reference point in all degrees of freedom, respectively. The crack driving force was applied through positive displacement in vertical translation (U2) to the reference point “Load” fixed in translation in global X and Z direction and rotation in global X and Y direction. The same degrees of freedom were fixed at the reference point “Hold” and the vertical translation U2 was also fixed to simulate the real constraints during the test.

Figure 5-11 b) and Figure 5-11 c) show the boundary conditions applied in the 3ENF model and the 4ENF model, respectively. The loading pin and the support pin were modeled by the cylindrical shell to simulate the sliding between the pins and the specimens due to deflection of the latter observed during the experiments. The outer surfaces of the loading pin and the support pin were kinematically constrained to the “Load” and the “Hold” reference points in all degrees of freedom, respectively. The load in the model was applied through negative displacement in vertical direction (U2) to the reference point “Load” which is fixed in translation in global X and Z direction and rotation in global X and Y direction. In the 4ENF model the translation in global X direction was released at the reference point “load” to allow the translational movement of the spreader beam observed in the experiments. Similarly, all degrees of freedom were fixed at the reference point “Hold” to simulate the constraints during the test.

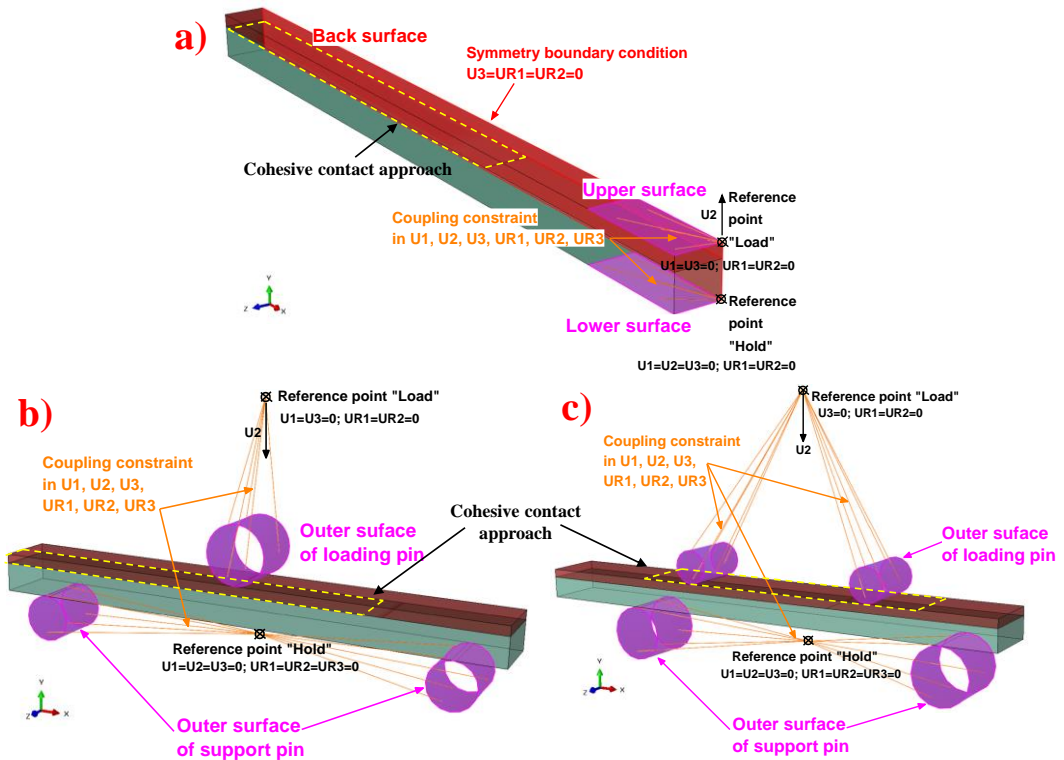


Figure 5-11 Boundary conditions of FE models in simulation of a) DCB, b) 3ENF and c) 4ENF experiments

5.4.2 Contact interactions

ABAQUS Explicit solver provides two algorithms for modelling contact interactions: general contact or contact pairs. In the presented interface FEM process, general contact is utilized attributed to great simplification in contact definitions and the relaxed restrictions on the types of surfaces that can be used in contact. Successful definition of a general contact interaction consists of specifying the contact domain and the mechanical contact property models. In ABAQUS explicit solver self-contact for a default unnamed, all-inclusive surface is automatically defined as the general contact domain which contains all exterior element faces, analytical rigid surfaces and all edges based on beam and truss elements in the model. In addition, contact pairs as a subset of the contact domain can also be specified with distinct contact properties. In the presented DCB, 3ENF and 4ENF models two types of contact property models are assigned globally to the general contact domain: the hard contact model and the friction model. The default hard contact model is illustrated in Figure 5-12 a). When surfaces are in contact, any contact pressure can be transmitted between them. The surfaces separate if the contact pressure reduces to zero and the separated surfaces come into contact when the clearance between them reduces to zero. In DCB modelling the default tangential behavior is defined where the interaction between contacting bodies is frictionless while

in 3ENF and 4ENF modelling the basic Coulomb friction model is used to simulate sliding of the specimen with the loading and the support pins. The Coulomb friction model defines the critical shear stress τ_{crit} , at which sliding of the surfaces starts as a fraction of the contact pressure, p , between surfaces ($\tau_{crit} = \mu p$). The fraction, μ , is known as the coefficient of friction. The stick/slip calculations define a surface in the contact pressure-shear stress space along which a point transitions from sticking to slipping, as shown in Figure 5-12 b).

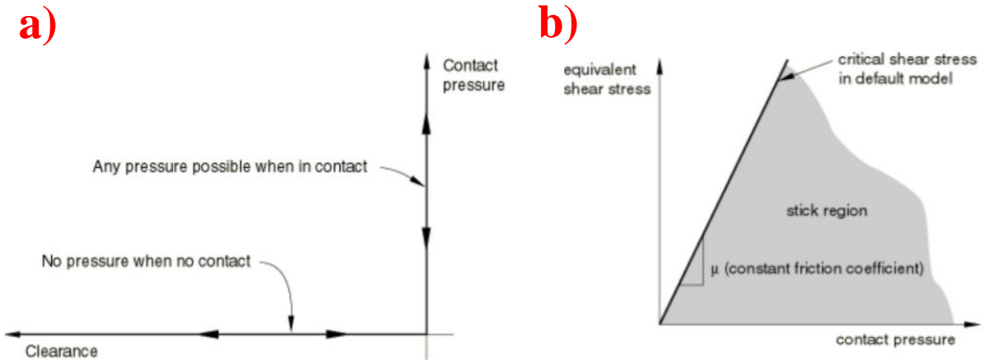


Figure 5-12 Contact property models globally assigned to the general contact domain in the interface models: a) default pressure-overclosure relationship; b) slip regions for the basic Coulomb friction model

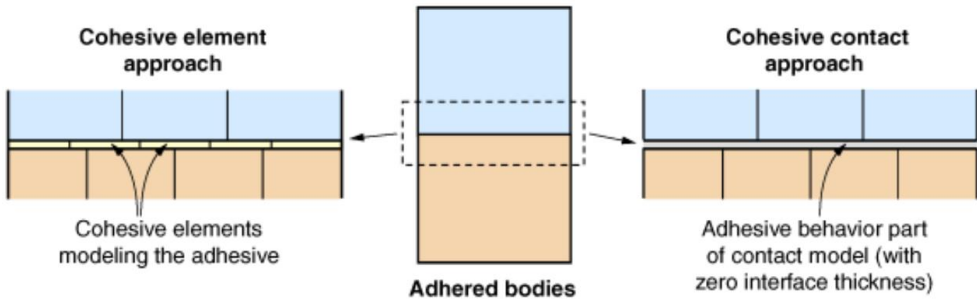


Figure 5-13 Schematic comparison of cohesive element and cohesive contact approaches

To simulate debonding behavior of the composite-steel bonded interface, the cohesive contact approach is used in the DCB, 3ENF and 4ENF models to define the contact model (cohesive zone model) assigned to the individual contact surface pairs, as highlighted in Figure 5-11. Figure 5-13 illustrates the differences between cohesive element and cohesive contact approaches. Cohesive contact approach is primarily intended for situations where the interface thickness is negligibly small as in the case of extremely thin bond line in wrapped composite joints. It is typically easier to define than modeling the interface using cohesive elements and allow simulation of a wider range of cohesive interactions. The cohesive zone model is explained thoroughly in subsection

5.4.3, including the linear elastic traction-separation model, damage initiation criteria and damage evolution laws.

5.4.3 Cohesive zone model (CZM) – the interface model of composite-steel bonding

5.4.3.1 Linear elastic traction-separation behavior

The traction-separation model defines the linear elastic behavior followed by the initiation and evolution of damage. The elastic behavior is written (Equation 5-2) in terms of an elastic constitutive matrix that relates the normal and shear stresses to the normal and shear separations across the bonded interface. The nominal traction stress vector, \mathbf{t} , consists of three components: t_n , t_s and t_t , which represent the normal and the two shear tractions, respectively. The stiffness matrix, \mathbf{K} , consists of nine components with the general form of K_{ij} which is the traction stress in direction i resulting from per unit separation in the direction j . The normal and tangential stiffness components are not coupled in the current modeling: pure normal separation by itself does not give rise to cohesive forces in the shear direction, and vice versa. In other words, only K_{nn} , K_{ss} , K_{tt} are nonzero parameters. The nominal separation vector, δ , represents the normal and shear separations in the three principal directions.

$$\mathbf{t} = \begin{Bmatrix} t_n \\ t_s \\ t_t \end{Bmatrix} = \begin{bmatrix} K_{nn} & K_{ns} & K_{nt} \\ K_{ns} & K_{ss} & K_{st} \\ K_{nt} & K_{st} & K_{tt} \end{bmatrix} \begin{Bmatrix} \delta_n \\ \delta_s \\ \delta_t \end{Bmatrix} = \mathbf{K}\delta \quad \text{Equation 5-2}$$

5.4.3.2 Damage initiation criterion

Damage initiation refers to the beginning of degradation of the cohesive response at a contact point. The process of degradation begins when certain damage initiation criterion defined is satisfied. In the current modeling the quadratic traction criterion is utilized in which damage is assumed to initiate when a quadratic interaction function involving the contact stress ratios reaches a value of 1. This criterion is represented as:

$$\left\{ \frac{\langle t_n \rangle}{t_n^o} \right\}^2 + \left\{ \frac{t_s}{t_s^o} \right\}^2 + \left\{ \frac{t_t}{t_t^o} \right\}^2 = 1 \quad \text{Equation 5-3}$$

where t_n^o , t_s^o and t_t^o represent the peak values of the contact stress when the separation is either purely normal to the interface or purely in the first or the second shear direction, respectively.

5.4.3.3 Damage evolution

Damage evolution law describes the rate at which the cohesive stiffness is degraded once the corresponding initiation criterion is reached. It can be defined by the scalar damage variable, D , representing the overall damage at the contact point. The damage variable initially has a value of 0. If damage evolution is modeled, D monotonically evolves from 0 to 1 upon further loading after the damage initiation. The contact stress components are affected by the damage according to

$$t_n = \begin{cases} (1-D)\bar{t}_n, \bar{t}_n \geq 0 \\ \bar{t}_n, \bar{t}_n \leq 0 \text{ (in compression)} \end{cases} \quad \text{Equation 5-4}$$

$$t_s = (1-D)\bar{t}_s \quad \text{Equation 5-5}$$

$$t_t = (1-D)\bar{t}_t \quad \text{Equation 5-6}$$

where \bar{t}_n , \bar{t}_s and \bar{t}_t are the contact stress components predicted by the elastic traction-separation behavior for the current separations without damage.

5.4.3.4 Four-linear traction-separation law simulating fracture of composite-steel bonded interface

In cohesive zone modeling (CZM) the traction-separation law is defined as the constitutive model describing the traction-separation behavior of the fracture process zone in the wake of the crack tip. Considering the existence of fiber bridging and the mechanical interlocking, a four-linear traction-separation law is proposed in Chapter 4 to simulate encompassing various stages of fracture process of composite-steel bonded interface. Figure 5-14 a) and b) represent the cohesive laws of the composite-steel bonded interface in pure mode I and pure mode II, respectively. Three distinct phenomena are described in the fracture process: crack tip deformation, softening and fiber bridging, distinguished by four critical stages: “p” – onset of plasticity; “c” – onset of cracking; “b” – onset of fiber bridging; “f” – failure. $G_{I,br}$ provides the majority of the fracture toughness in mode I due to fiber bridging whilst $G_{II,soft}$ is most devoted to the fracture resistance in mode II as a consequence of the mechanical interlocking.

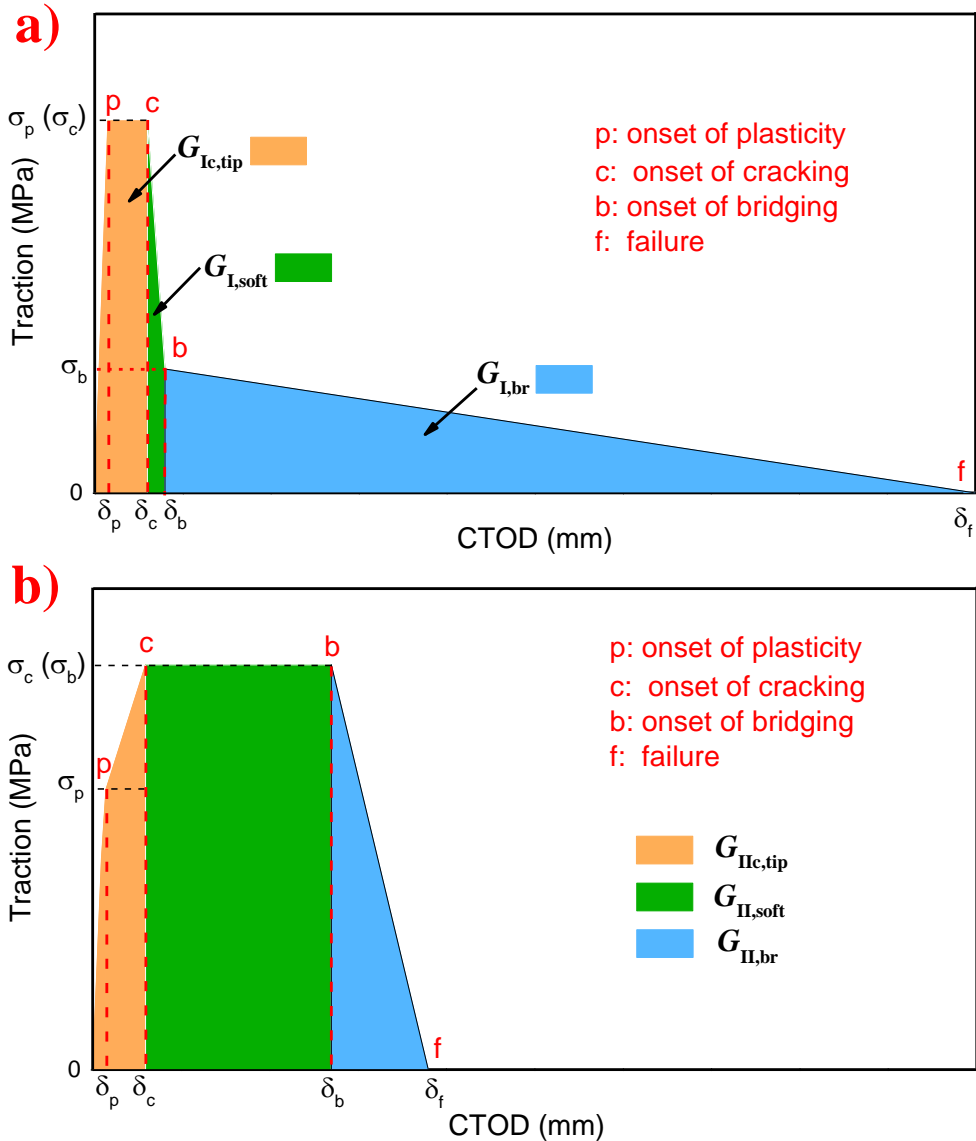


Figure 5-14 Schematic fracture process of composite-steel bonded interface in a) pure mode I and b) pure mode II

The values in terms of CTOD and tractions at the critical stage (“p”, “c”, “b” and “f”) as well as values of the critical SERR ($G_{Ic,tip}$, G_{Ic} , $G_{IIc,tip}$, G_{IIc}) used as the input of cohesive laws for modeling DCB, 3ENF and 4ENF tests are summarized in Table 5-2. The generated cohesive laws for DCB, 3ENF and 4ENF modeling are illustrated in Figure 5-15 and Figure 5-16, respectively. The values in Table 5-2 are obtained based on the average values of the acquired test results which are detailed in Chapter 4. Note that differences between the 3ENF and 4ENF values are owed to difference in roughness

in the two batches and not necessarily due to difference of fracture characterization in those two types of tests.

Table 5-2 Parameters of the four-linear cohesive laws used in modeling DCB, 3ENF and 4ENF tests

FEM scenario	Onset of plasticity - stage "p"		Onset of cracking - stage "c"		Onset of fiber bridging - stage "b"		Failure - stage "f"		Critical SERR	
	δ_p (mm)	σ_p (MPa)	δ_c (mm)	σ_c (MPa)	δ_b (mm)	σ_b (MPa)	δ_f (mm)	σ_f (MPa)	$G_{Ic,tip}$ (N/mm)	G_{Ic} (N/mm)
DCB	0.002	20	0.016	20	0.040	2	0.881	0	0.3	1.4
FEM scenario	δ_p (mm)	σ_p (MPa)	δ_c (mm)	σ_c (MPa)	δ_b (mm)	σ_b (MPa)	δ_f (mm)	σ_f (MPa)	$G_{IIc,tip}$ (N/mm)	G_{IIc} (N/mm)
3ENF	0.0017	17.3	0.027	26	0.132	26	0.148	0	0.56	3.5
4ENF	0.002	20	0.037	30	0.116	30	0.259	0	0.89	5.4

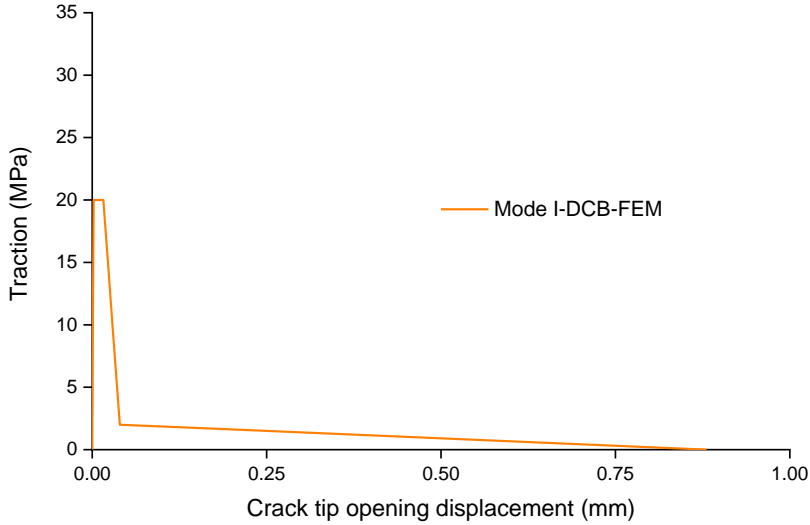


Figure 5-15 Traction-separation laws of pure mode I used in DCB modelling

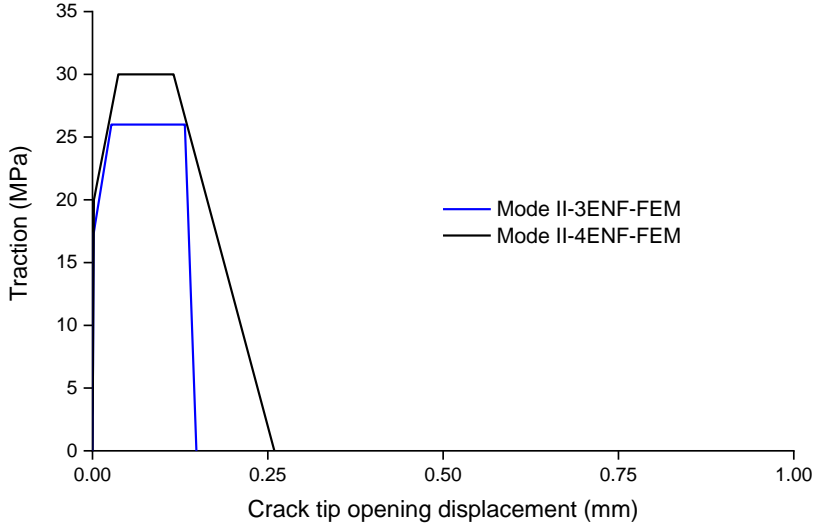


Figure 5-16 Traction-separation laws of pure mode II used in 3ENF and 4ENF modelling

5.4.3.5 Definition of mode mixity

Mode mixity of the interface fracture should be defined in modeling of DCB and ENF experiments due to its prevalent existence in the bi-material fracture behavior. In ABAQUS the data defining the evolution of damage at the cohesive interface can be tabular functions of the mode mixity. The manner in which this dependence is defined can be either based on energy or traction[22]. In this research the mode mixity definition is identified based on energy in ABAQUS due to convenience of description and possibility to be validated by mixed-mode bending (MMB) experiments in the future, as outlined below.

The mode mixity definitions based on energies are as follows:

$$m_1 = \frac{G_n}{G_T} \quad \text{Equation 5-7}$$

$$m_2 = \frac{G_s}{G_T} \quad \text{Equation 5-8}$$

$$m_3 = \frac{G_t}{G_T} \quad \text{Equation 5-9}$$

where G_n , G_s and G_t are the work done by the tractions and their conjugate separations in the normal, first and second shear directions, respectively. $G_T = G_n + G_s + G_t$ is the total strain energy release rate (SERR). It is also useful to define the quantity $G_S = G_s + G_t$ to denote the portion of the total work done by the shear traction and the corresponding separation components. For an energy-based definition of mode mixity,

in the most general case of a three-dimensional state of separation with anisotropic shear behavior, the fracture toughness, G^C , must be defined as a function of $(m_2 + m_3)$ and $[m_3 / (m_2 + m_3)]$. It can be derived based on Equation 5-7~ Equation 5-9 that the quantity $(m_2 + m_3) = G_S / G_T$ is a measure of the fraction of the total separation that is shear, while $[m_3 / (m_2 + m_3)] = G_I / G_S$ is a measure of the fraction of the total shear separation that is in the second shear direction. Considering that mode mixity is identical in the first and the second shear direction attributed to the quasi-isotropic properties of the composite laminate, its definition can be simplified into a two-dimensional problem where SERR is defined as a function of m_2 ($m_3 = 0$). Five mix ratio values of m_2 , i.e., 0 (pure mode I), 0.25, 0.5, 0.7 and 1 (pure mode II), are subsequently used in the current FEM to consider mode mixity. Based on the literature[15], the dependence of SERR on mode mixity does not follow a linear relationship. An exponential relation between interface SERR and the mix ratio is assumed and validated by the interface experiments. The shape of the traction-separation laws at 2 pure modes and 3 mixed modes are shown in Figure 5-17. It can be identified that the portion of the SERR in the softening phenomenon increases as mix ratio changes from pure mode I ($m_2=0$) to pure mode II ($m_2=1$) while the portion of the SERR in the fiber bridging phenomenon decreases. The physical explanation is that the contribution of mechanical interlocking continuously increases from mode I to mode II whilst the fiber bridging effect decreases consistently as observed in Chapter 4 and validated by DCB and ENF modeling in this Chapter.

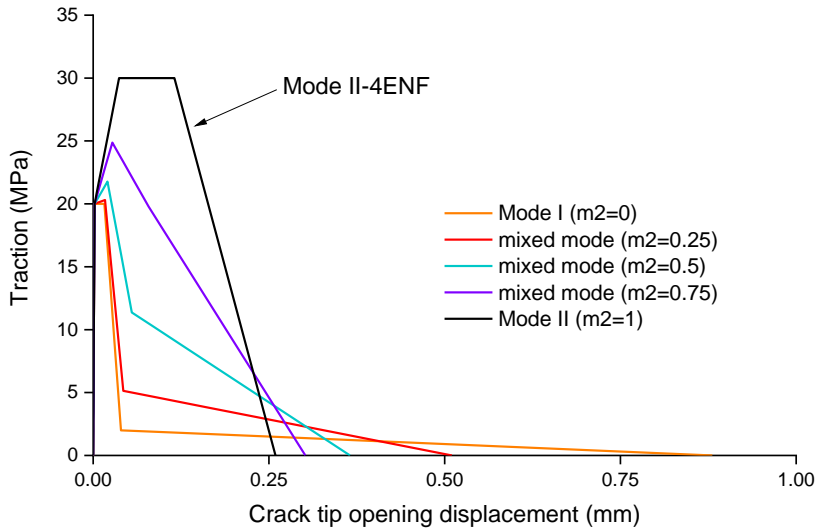


Figure 5-17 Shape of traction-separation laws at mode I, mode II and mixed modes of composite-steel bonded interface

5.4.4 Fracture data analysis

For validation of the interface FEM, the CTOD and the crack length a should be obtained from the FEA and be compared to the values from the experiments. In DCB modeling, the present crack tip is determined as the location where the CSDMG (the

damage variable of the interface) just reaches the input values corresponding to stage “c” indicated as crack initiation, as shown in the front of the yellow contour in Figure 5-18. The CTOD is obtained by subtracting the vertical displacement output in steel and composite adherend at the pre-crack tip.

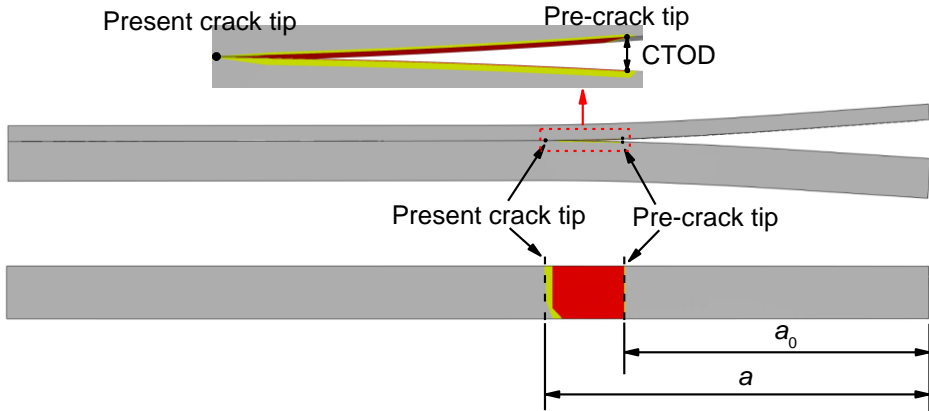


Figure 5-18 Illustration of determination of crack length a and CTOD in DCB FEM

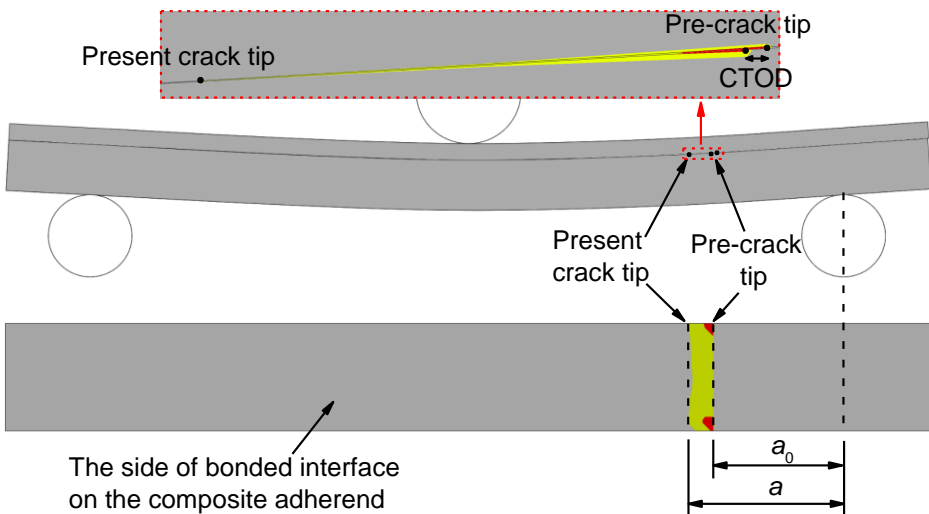


Figure 5-19 Illustration of determination of crack length a and CTOD in 3ENF and 4ENF FEM

In the FEM of 3ENF and 4ENF tests, determination of present crack length is the same as in FEM of DCB tests, as illustrated in Figure 5-19. The CTOD is obtained by subtracting the displacement parallel to the interface on the interface surfaces of steel and composite adherend at the pre-crack tip. The longitudinal position of the present crack tip varies with a convex shape across the DCB specimens (see Figure 5-18) while with a concave shape across the 3ENF and 4ENF specimens (Figure 5-19). This is due to the anticlastic bending of the specimen affected by both material properties (Poisson’s

ratio) and geometry of the specimens[26]–[30].

5.4.5 Validation of DCB and ENF FEM

5.4.5.1 Validation of DCB FEM

It can be seen in Figure 5-20 that the numerical load-displacement curve (black curve) matches well with the testing curves in terms of elastic stiffness, non-linear behavior, ultimate load, and ductility. The values of load and applied displacement at critical stages from FEM are compared to the average values in the experiments, as presented in Table 5-3 where the deviation of these variables compared to average testing results are within 5%. Therefore, it can be concluded that good match is reached in terms of global response in DCB modeling and DCB tests. Figure 5-20 also shows that the load level in DCB numerical curve is larger than those in the experiments curves when the applied displacement value exceeds 15 mm. This is because the crack transfer from the bonded interface into the composite laminate in DCB tests leading to reduction of the bending stiffness while in simulation the crack always propagates on the bonded interface. The numerical load-displacement curve illustrates that stage “b” is reached after stage “c” through only 20 N load increase indicating the softening phenomenon is rather short and the majority of the resistance after crack initiation comes from the fiber bridging until the peak load at stage “f”.

Table 5-3 Displacement/load values at the critical stages of the fracture process in DCB tests vs DCB FEM

Specimens or FE model	Onset of plasticity (stage “p”)		Onset of cracking (stage “c”)		Onset of bridging (stage “b”)		Failure (stage “f”)	
	Disp. (mm)	Load (N)	Disp. (mm)	Load (N)	Disp. (mm)	Load (N)	Disp. (mm)	Load (N)
DCB_aver- age (and COV[%])	2.57 (5.11)	123.33 (6.43)	4.03 (1.93)	168.92 (3.51)	-	-	9.88 (4.05)	231.32 (2.25)
DCB-FEM	2.61	120.77	3.91	172.67	4.95	194.25	9.99	238.78
Deviation (%)	1.6	2.1	3.0	2.2	-	-	1.1	3.2

In Figure 5-21 and Figure 5-22 the crack length a and the CTOD vs applied displacement obtained from the FE model are plotted for comparison with the testing curves. In both figures good matches of the crack length and the CTOD in tests and in FEM are achieved. It can also be seen in Figure 5-21 that the crack extension Δa between point “c” and point “f” obtained from FEM is approximately 16 mm which matches well to the average value from DCB tests. Therefore, it can be concluded that good matches of the failure process are achieved in DCB modeling vs DCB tests.

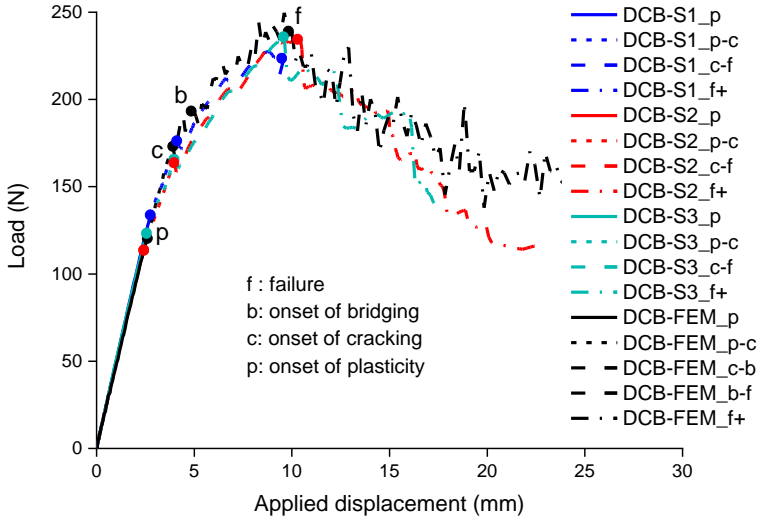


Figure 5-20 Comparison of load-displacement response in DCB test vs modeling

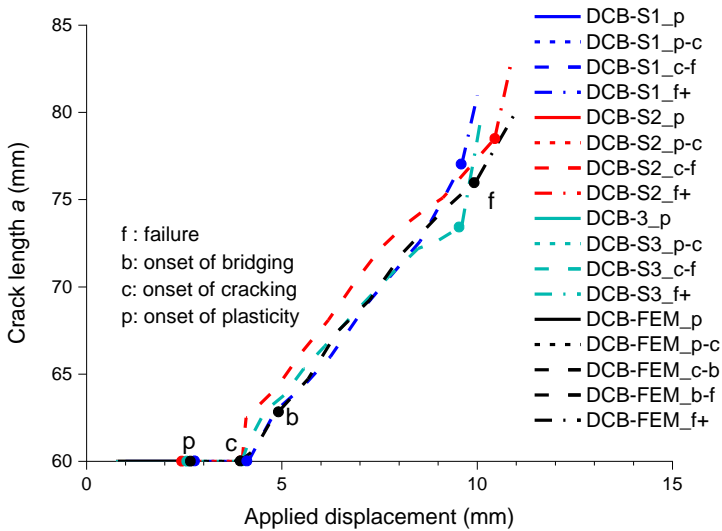


Figure 5-21 Comparison of a-displacement relation in DCB test vs modeling

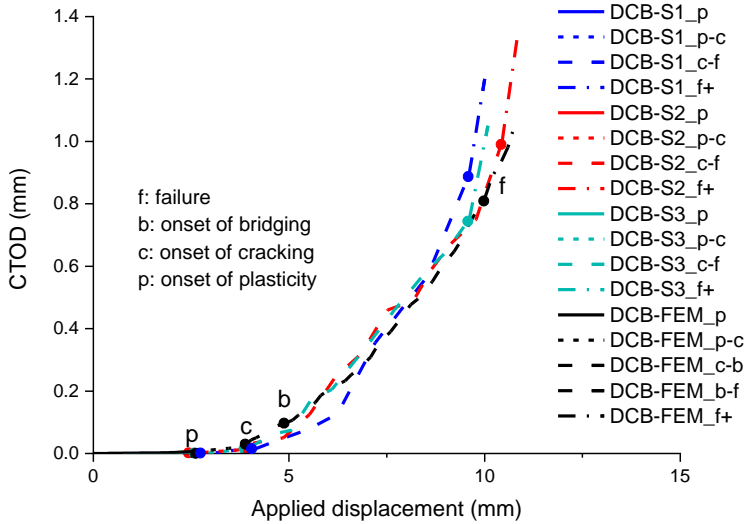


Figure 5-22 Comparison of CTOD-displacement relation in DCB test vs modeling

5.4.5.2 Validation of 3ENF and 4ENF FEM

It can be seen in Figure 5-23 and Figure 5-26 that the load-displacement behavior from the numerical models (black curves) match well with the testing curves in terms of elastic stiffness and non-linear behavior in both 3ENF and 4ENF results. Comparison of load and applied displacement values at critical stages are presented in Table 5-4 and Table 5-5 where the deviation of numerical results from average testing results are within 8%. Therefore, it can be concluded that good match is reached in terms of global response in 3ENF modeling vs 3ENF tests, and in 4ENF modeling vs 4ENF tests. The numerical load-displacement curve in Figure 5-26 illustrates that stage “f” is reached from stage “b” through only 500 N load increase. This indicates that the contribution of fiber bridging to fracture resistance is relatively small and the majority of the resistance after crack initiation comes from the softening phenomenon from stage “c” to stage “b” in mode II failure.

In Figure 5-24~Figure 5-25 and in Figure 5-27~Figure 5-28, the crack length a and the CTOD vs applied displacement obtained from the FE models are plotted and compared with the curves from 3ENF and 4ENF tests, respectively. In both cases good agreement of the crack length and the CTOD in tests and in FEM are achieved. It can also be seen in Figure 5-27 that the crack extension Δa obtained from 4ENF FEM is approximately 11.5 mm which matches well to the average value from 4ENF tests. Therefore, it can be concluded that good agreement of the failure process is achieved in 3ENF modeling vs 3ENF tests, and in 4ENF modeling vs 4ENF tests.

Table 5-4 Displacement/load values at the critical stages of the fracture process in 3ENF tests vs 3ENF FEM

Specimens or FE model	Onset of plasticity (stage “p”)		Onset of cracking (stage “c”)		Onset of bridging (stage “b”)		Failure (stage “f”)	
	Disp. (mm)	Load (N)	Disp. (mm)	Load (N)	Disp. (mm)	Load (N)	Disp. (mm)	Load (N)
3ENF_average (and COV[%])	0.85 (20.33)	1889.4 (20.83)	1.68 (3.95)	3617.5 (3.76)	3.64 (20.81)	6769.8 (15.22)	-	-
3ENF-FEM	0.82	1909.9	1.72	3897.2	3.80	6989.2	-	-
Deviation (%)	3.5	1.1	2.4	7.7	4.4	3.2	-	-

Table 5-5 Displacement/load values at the critical stages of the fracture process in 4ENF tests vs 4ENF FEM

Specimens or FE model	Onset of plasticity (stage “p”)		Onset of cracking (stage “c”)		Onset of bridging (stage “b”)		Failure (stage “f”)	
	Disp. (mm)	Load (N)	Disp. (mm)	Load (N)	Disp. (mm)	Load (N)	Disp. (mm)	Load (N)
4ENF_average (and COV[%])	0.67 (22.33)	1737.9 (20.46)	1.25 (2.09)	3031.7 (1.52)	-	-	3.74 (13.41)	6413.4 (6.20)
4ENF-FEM	0.70	1768.2 ₂	1.34	3174.8	2.82	5528.2	3.45	6084.8
Deviation (%)	4.5	1.7	7.2	4.7	-	-	7.8	5.1

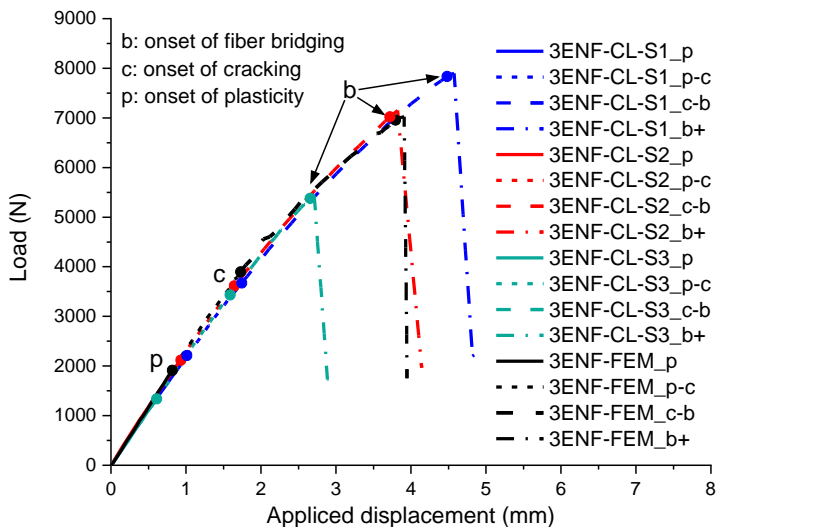


Figure 5-23 Comparison of load-displacement response in 3ENF test vs modeling

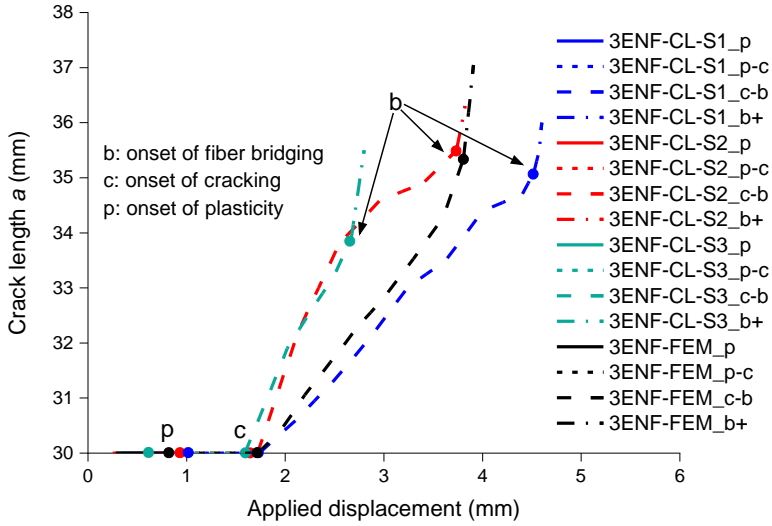


Figure 5-24 Comparison of a-displacement relation in 3ENF test vs modeling

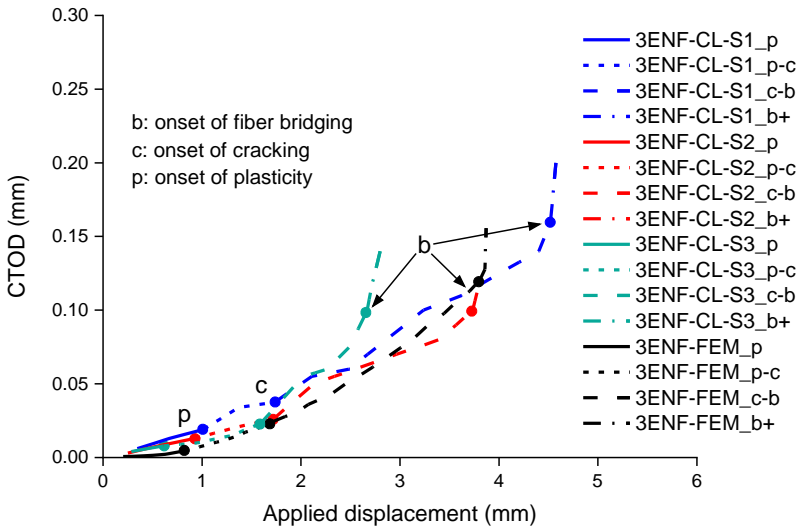


Figure 5-25 Comparison of CTOD-displacement relation in 3ENF test vs modeling

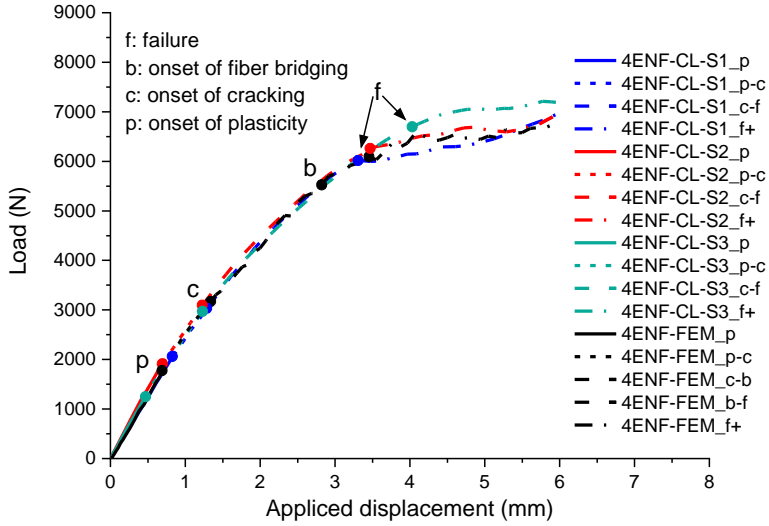


Figure 5-26 Comparison of load-displacement response in 4ENF test vs modeling

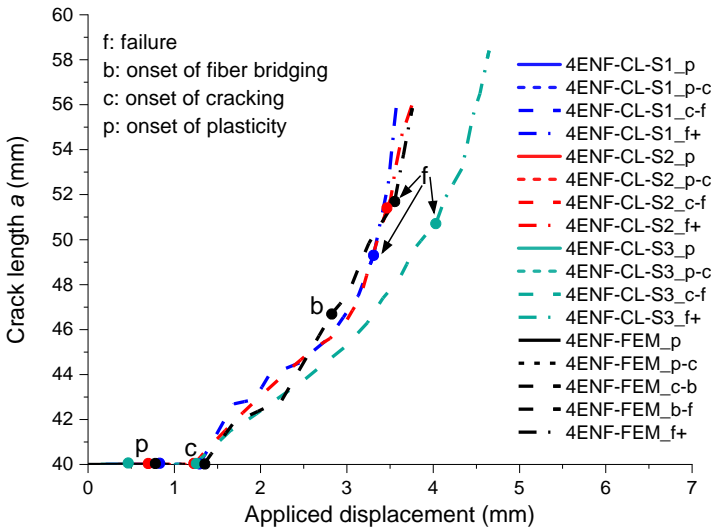


Figure 5-27 Comparison of a-displacement relation in 4ENF test vs modeling

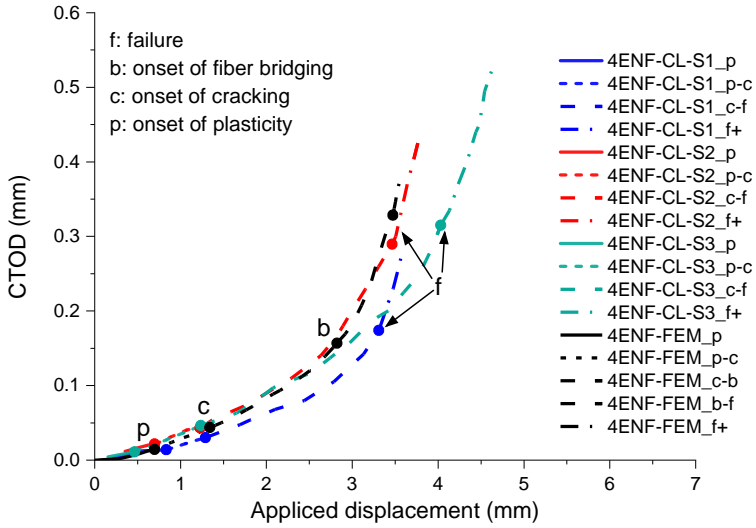


Figure 5-28 Comparison of CTOD-displacement relation in 4ENF test vs modeling

5.5 Conclusions

In this Chapter, the FEM strategy for simulation of composite wrap and composite-steel bonded interface using ABAQUS are proposed. The FE models are built at the material level using composite property input based on composite coupon tests and the interface property input (four-linear traction-separation laws) referring to the interface tests (DCB, 3ENF and 4ENF) conducted in Chapter 4. The numerical results are compared with the experimental results to validate the proposed modelling strategy and the used material input. Based on the numerical results and the discussions, the follow conclusions are drawn:

1) Composites with complex and curved shape as in the case of wrapped composite joints can be modelled by 3D solid 4-node linear tetrahedral element (C3D4) due to its advantage in modelling through-thickness behavior which is significant for modelling of interface debonding.

2) The composite-steel bonded interface with negligible thickness of the adhesive layer can be modelled using the cohesive contact approach where the cohesive zone model is utilized to simulate the fracture process in the wake of the crack tip using a four-linear traction-separation law.

3) The proposed modelling strategy for composites is validated by good matches between the composite coupon tests and the numerical results in terms of the tensile, compressive, and in-plane shear behavior. The modelling strategy for composite-steel bonded interface are justified through the good agreement between the test results and the numerical simulations regarding to DCB, 3ENF and 4ENF scenarios.

References

- [1] M. Lesani, M. R. Bahaari, and M. M. Shokrieh, “Numerical investigation of FRP-strengthened tubular T-joints under axial compressive loads,” *Compos. Struct.*, vol. 100, pp. 71–78, 2013, doi: 10.1016/j.compstruct.2012.12.020.
- [2] M. Lesani, M. R. Bahaari, and M. M. Shokrieh, “Experimental investigation of FRP-strengthened tubular T-joints under axial compressive loads,” *Constr. Build. Mater.*, vol. 53, pp. 243–252, 2014, doi: 10.1016/j.conbuildmat.2013.11.097.
- [3] G. Xu, L. Tong, X. L. Zhao, H. Zhou, and F. Xu, “Numerical analysis and formulae for SCF reduction coefficients of CFRP-strengthened CHS gap K-joints,” *Eng. Struct.*, vol. 210, no. February, p. 110369, 2020, doi: 10.1016/j.engstruct.2020.110369.
- [4] A. Sadat Hosseini, E. Zavvar, and H. Ahmadi, “Stress concentration factors in FRP-strengthened steel tubular KT-joints,” *Appl. Ocean Res.*, vol. 108, no. September 2020, 2021, doi: 10.1016/j.apor.2021.102525.
- [5] E. Zavvar, A. Sadat Hosseini, and M. A. Lotfollahi-Yaghin, “Stress concentration factors in steel tubular KT-connections with FRP-Wrapping under bending moments,” *Structures*, vol. 33, no. June, pp. 4743–4765, 2021, doi: 10.1016/j.istruc.2021.06.100.
- [6] M. Lesani, M. R. Bahaari, and M. M. Shokrieh, “FRP wrapping for the rehabilitation of Circular Hollow Section (CHS) tubular steel connections,” *Thin-Walled Struct.*, vol. 90, pp. 216–234, 2015, doi: 10.1016/j.tws.2014.12.013.
- [7] A. S. Hosseini, M. R. Bahaari, and M. Lesani, “SCF distribution in FRP-strengthened tubular T-joints under brace axial loading,” *Sci. Iran.*, vol. 27, no. 3 A, pp. 1113–1129, 2020, doi: 10.24200/SCI.2018.5471.1293.
- [8] A. Sadat Hosseini, M. R. Bahaari, and M. Lesani, “Parametric Study of FRP Strengthening on Stress Concentration Factors in an Offshore Tubular T-Joint Subjected to In-Plane and Out-of-Plane Bending Moments,” *Int. J. Steel Struct.*, vol. 19, no. 6, pp. 1755–1766, 2019, doi: 10.1007/s13296-019-00244-0.
- [9] A. Sadat Hosseini, M. R. Bahaari, and M. Lesani, “Experimental and parametric studies of SCFs in FRP strengthened tubular T-joints under axially loaded brace,” *Eng. Struct.*, vol. 213, no. October 2019, p. 110548, 2020, doi: 10.1016/j.engstruct.2020.110548.
- [10] A. Sadat Hosseini, M. R. Bahaari, and M. Lesani, “Stress concentration factors in FRP-strengthened offshore steel tubular T-joints under various brace loadings,” *Structures*, vol. 20, no. April, pp. 779–793, 2019, doi: 10.1016/j.istruc.2019.07.004.
- [11] H. Nassiraei and P. Rezaeost, “Stress concentration factors in tubular T/Y-joints strengthened with FRP subjected to compressive load in offshore structures,” *Int. J. Fatigue*, vol. 140, no. May, p. 105719, 2020, doi: 10.1016/j.ijfatigue.2020.105719.
- [12] H. Nassiraei and P. Rezaeost, “Parametric study and formula for SCFs of FRP-strengthened CHS T/Y-joints under out-of-plane bending load,” *Ocean Eng.*, vol. 221,

no. May 2020, p. 108313, 2021, doi: 10.1016/j.oceaneng.2020.108313.

[13] Y. Fu, L. Tong, L. He, and X. L. Zhao, “Experimental and numerical investigation on behavior of CFRP-strengthened circular hollow section gap K-joints,” *Thin-Walled Struct.*, vol. 102, pp. 80–97, 2016, doi: 10.1016/j.tws.2016.01.020.

[14] A. Hillerborg, M. Modeer, and P. E. Petersson, “Analysis of crack formation and crack growth in concrete by means of fracture mechanics and finite elements,” *Am. Concr. Institute, ACI Spec. Publ.*, vol. SP-249, pp. 225–237, 1976.

[15] M. Shahverdi, A. P. Vassilopoulos, and T. Keller, “Mixed-mode quasi-static failure criteria for adhesively-bonded pultruded GFRP joints,” *Compos. Part A Appl. Sci. Manuf.*, vol. 59, pp. 45–56, 2014, doi: 10.1016/j.compositesa.2013.12.007.

[16] M. Shahverdi, A. P. Vassilopoulos, and T. Keller, “Mixed-Mode I/II fracture behavior of asymmetric adhesively-bonded pultruded composite joints,” *Eng. Fract. Mech.*, vol. 115, pp. 43–59, 2014, doi: 10.1016/j.engfracmech.2013.11.014.

[17] M. Shahverdi, A. P. Vassilopoulos, and T. Keller, “Mixed-Mode I/II fracture behavior of asymmetric composite joints,” *Procedia Struct. Integr.*, vol. 2, pp. 1886–1893, 2016, doi: 10.1016/j.prostr.2016.06.237.

[18] A. Cameselle-Molares, A. P. Vassilopoulos, J. Renart, A. Turon, and T. Keller, “Numerical simulation of two-dimensional in-plane crack propagation in FRP laminates,” *Compos. Struct.*, vol. 200, no. April, pp. 396–407, 2018, doi: 10.1016/j.compstruct.2018.05.136.

[19] M. Heidari-Rarani, M. M. Shokrieh, and P. P. Camanho, “Finite element modeling of mode I delamination growth in laminated DCB specimens with R-curve effects,” *Compos. Part B Eng.*, vol. 45, no. 1, pp. 897–903, 2013, doi: 10.1016/j.compositesb.2012.09.051.

[20] M. M. Shokrieh, M. Heidari-Rarani, and M. R. Ayatollahi, “Delamination R-curve as a material property of unidirectional glass/epoxy composites,” *Mater. Des.*, vol. 34, pp. 211–218, 2012, doi: 10.1016/j.matdes.2011.08.006.

[21] E. Martinelli, A. Hosseini, E. Ghafoori, and M. Motavalli, “Behavior of prestressed CFRP plates bonded to steel substrate: Numerical modeling and experimental validation,” *Compos. Struct.*, vol. 207, no. August 2018, pp. 974–984, 2019, doi: 10.1016/j.compstruct.2018.09.023.

[22] D. S. S. Corp., “ABAQUS/Explicit User’s Manual,” 2019.

[23] International Standards Organization, “ISO 527-1:2012 - Plastics - Determination of tensile properties - Part 1: General principles,” 2012, [Online]. Available: www.iso.org

[24] International Standards Organization, “ISO 14129: 1997 Fibre-reinforced plastic composites — Determination of the in-plane shear stress/shear strain response, including the in-plane shear modulus and strength, by the plus or minus 45 degree tension test

method,” 1997.

[25] International Standards Organization, “ISO 14126:1999 - Fibre-reinforced plastic composites - Determination of compressive properties in the in-plane direction,” 1999.

[26] R. K. Joki, F. Grytten, B. Hayman, and B. F. Sørensen, “A mixed mode cohesive model for FRP laminates incorporating large scale bridging behaviour,” *Eng. Fract. Mech.*, vol. 239, no. September 2019, p. 107274, 2020, doi: 10.1016/j.engfracmech.2020.107274.

[27] R. K. Joki, F. Grytten, B. Hayman, and B. F. Sørensen, “Determination of a cohesive law for delamination modelling - Accounting for variation in crack opening and stress state across the test specimen width,” *Compos. Sci. Technol.*, vol. 128, pp. 49–57, 2016, doi: 10.1016/j.compscitech.2016.01.026.

[28] A. Kotousov, P. Lazzarin, F. Berto, and S. Harding, “Effect of the thickness on elastic deformation and quasi-brittle fracture of plate components,” *Eng. Fract. Mech.*, vol. 77, no. 11, pp. 1665–1681, 2010, doi: 10.1016/j.engfracmech.2010.04.008.

[29] Z. Jiang, S. Wan, T. Keller, Z. Fang, and A. P. Vassilopoulos, “Influence of curved delamination front on R-curve of DCB specimen,” *Compos. Struct.*, vol. 227, no. June, p. 111311, 2019, doi: 10.1016/j.compstruct.2019.111311.

[30] B. D. Davidson, “An Analytical Investigation of Delamination Front Curvature in Double Cantilever Beam Specimens,” *J. Compos. Mater.*, vol. 24, no. 11, pp. 1124–1137, 1990, doi: 10.1177/002199839002401101.

6. FINITE ELEMENT MODELING OF ULTIME LOAD JOINT EXPERIMENTS

This chapter is dedicated to modelling debonding behavior of wrapped composite 45° X-joints subjected to the monotonic tensile loads, encompassing both the small-scale and the medium-scale scenarios. The strategy of employing solid elements to model composites in Chapter 5 is implemented and adjusted with varying mesh size to optimize computational efficiency. The four-linear cohesive law, derived from the interface experiments, is further adapted, accounting for statistical uncertainty inherent in the fracture properties of the composite-steel bonded interface. The effect of friction at the bonded interface is considered in the joint modelling to account for the influence of the Poisson's ratio effect and the confinement of the composite wrap.

The joint models are verified through good matches in terms of the global response and failure process with the small-scale and medium-scale 45° X-joints in tensile experiments presented in Chapter 3. The validated joint models gain insight into the failure process of debonding.

6.1 Introduction

In Chapter 4, the mechanical properties of composite material and the composite-steel bonded interface are justified by material and interface experiments. In Chapter 5, those properties are successfully calibrated as material input in finite element modelling (FEM) of interface experiments where the modelling strategy is validated by good matches to the experimental results. The core of the developed FEM strategy can be summarized as follow: 1) Using 3D solid 4-node linear tetrahedral element (C3D4) to model composite material with definition of the composite layup orientation to simulate orthotropic behavior; 2) Utilizing the cohesive contact approach to simulate debonding behavior of the composite-steel bonded interface with introduction of the four-linear traction-separation law to consider mode mixity.

In this chapter, the developed modelling strategy in the material level is used for FEM of wrapped composite joints with calibrated material and interface input to replicate failure process of ultimate load joints experiments presented in Chapter 3. Compared to the material level, the geometry of composites is more complex, more curved, and of considerable size. Therefore, further modification in terms of the modelling strategy should be made to satisfy physical feasibility and computational requirements. The main changes include: 1) the reliability analysis is applied to the determination of the fracture properties of the composite-steel bonded interface used in the joint simulation based on EN 1990[1]; 2) contribution of friction to the debonding resistance of composite-steel bonded interface is considered in FEM of wrapped composite joints as a consequence of contraction of the composites around the steel members due to Poisson's effect while load is applied; 3) variable mesh size is defined in composite wrap to decrease the amount of element and to save computational cost. More details of the changes are explained in the sub-sections below.

In Chapter 3, three types of wrapped composite joints (A-joints, 45° X-joints, and 90° X-joints) are designed and tested in the ultimate load joint experiments, see Table 3-1 and Figure 3-3. Among them the geometry of 45° X-joints is finally selected in FEM of wrapped composite joints, due to the following considerations: a) 45° X-joints resembles K-joints in terms of stress concentration and the D/t ratio and the K-joints are the most prone to axial fatigue failure in offshore jacket structures. FEM of 45° X-joints is the benchmarking work for prediction of resistance of wrapped composite K joints sustained to tensile load; b) fracture of composite laminate is observed in bending test of 90° X-joints, which is not relevant to the aim of avoiding failure of composite material and focusing on experimental characterization and numerical simulation of debonding behavior; c) good matches to the test results of 45° X-joints in 2 geometric scales (small-scale and medium-scale) helps validate the modified modeling strategy used in the joint level, and can be the basis of the subsequent research into size effect. Once the joint FEM strategy and the input of the fracture properties (cohesive zone model) of the bonded interface are validated, the calibrated FE model of 45° X-joints can be used to perform parametric study into the influence of wrapping thickness, wrapping length, and joint size on debonding resistance, therefore providing design recommendations.

6.2 Overview of FE models in simulation of tensile static experiments of wrapped composite 45° X-joints

Corresponding to the ultimate load joint experiments conducted on wrapped composite 45° X-joints, 2 FE models are built to replicate the debonding process of 45° X-joints under tensile static load in small-scale and in medium-scale, respectively, as summarized in Table 6-1. Geometry of the 2 FE models are presented in Figure 6-1. In the medium-scale FE model the blue part and the orange part corresponds to the steel connection plates and the steel ear plate, respectively, for transfer of the tensile load to the brace members. All the dimensions of the circular hollow sections and the composite wrap in the FE models are equal to the values of the tested specimens. The medium-scale geometry is determined by upscaling the chord diameter in small-scale to 3 times, reaching almost 1/4 of the full scale. Similar naming convention as in the ultimate load joint experiments is used for FE models given in Table 6-1 and used afterwards in analysis of the numerical results: cX45 – wrapped composite joint, X geometry at 45° angle; Ss, Ms – small-scale and medium-scale, respectively; T – tension loading on braces; FEM – finite element modelling.

The objectives of the FEM of wrapped composite 45° X-joints under tensile load are defined as below:

- 1) Investigate the influence of considering the statistical uncertainty of the fracture properties of composite-steel bonded interface and the influence of contribution of friction on the debonding resistance of wrapped composite joints.
- 2) Validate the FEM strategy used in the joint level by good matches between numerical and experimental results in both global response and local behavior at two scales.
- 3) Represent the debonding process of wrapped composite 45° X-joints under tensile load which cannot be explicitly obtained in physical tests.
- 4) Determine the principal strain threshold on composite wrap surface which can be used to implicitly quantify the debonding length on the primary bonded interface.

Table 6-1 Overview of FE models in simulation of tensile static test of 45° X joints

FE model type	FE model name	Geometry in Figure number
FE model of small-scale 45° X joints	cX45-Ss-T-FEM	Figure 6-1 a)
FE model of medium-scale 45° X joints	cX45-Ms-T-FEM	Figure 6-1 b)

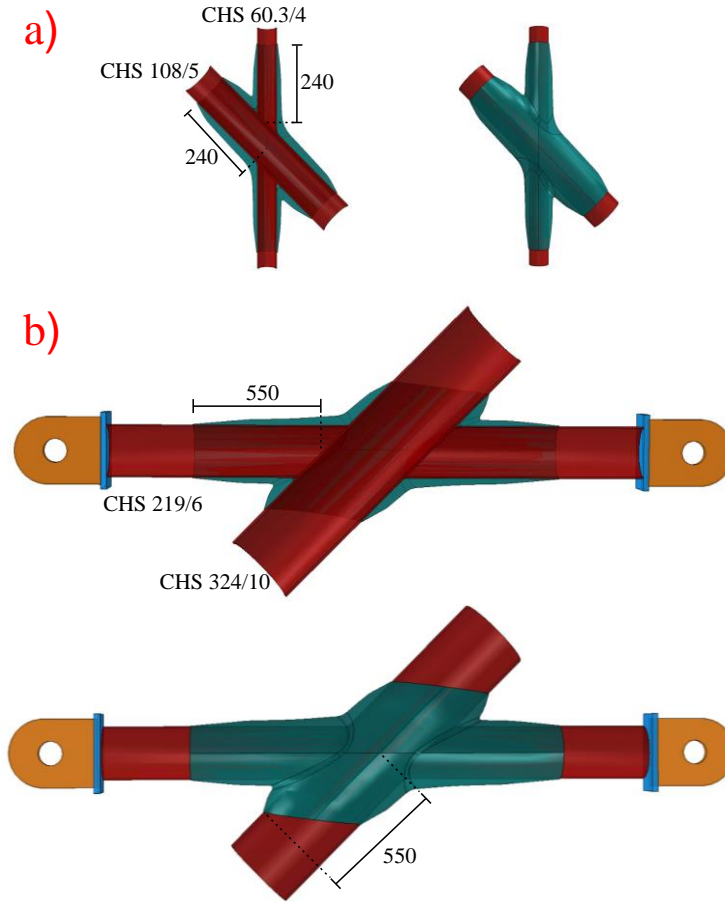


Figure 6-1 Geometries of FE models of wrapped composite 45° X joints in a) small-scale and in b) medium-scale used in simulation of tensile static experiments (unit: mm)

6.3 Modelling strategy

6.3.1 Modeling of layer lay-up, element type and element size

As been explained in the modeling strategy in the material level, the 3D solid elements are used in simulation of composite wrap in wrapped composite joints considering its following advantages over 2D conventional shell element and 3D continuum shell element: 1) the solid element is capable of simulating the real thickness of composite laminate which is suitable for modelling complex and curve-shape composite wrap in wrapped composite joints; 2) values of stresses and stiffness in the through-thickness direction (S33) and in the through-thickness shear (S13) direction can be accurately calculated in 3D solid element. In the case of wrapped composite joints where debonding of the bonded interface is the main failure mechanism, through-thickness shear behavior of composite laminate must be simulated precisely for the load transfer from composite wrap to the unbonded interface; 3) 3D solid element gives

possibility to model delamination within one wrapping layer in the future simulation of wrapped composite joints, while conventional or continuum shell element cannot simulate delamination since there is only one element in the out-of-plane direction. The downside is that using 3D solid element is tedious to define the layered lay-up of composite laminate where the number of elements through the thickness has to coincide with number of plies.

Two simplified strategies are proposed to define the layered lay-up of composite wrap: a) layered method and b) non-layered method. An example of the laminate lay-up in small-scale 45° X joints is illustrated in Figure 6-2 to explain the differences. In the layered method the composite wrap is composed of a couple of wrapping layers, as shown in Figure 6-2a). Each wrapping layer corresponds to one wrapping stage in the production of the joints and includes groups of composite plies. In this method the layered lay-up of composite laminate can be efficiently defined and the delamination within one wrapping layer can be simulated through plasticity the 3D solid element in the through-thickness shear direction. However, the fracture property of the inter-laminar interface between the adjacent wrapping layers should be known and used as interaction input in the joint simulation which is not available in the current stage. On the contrary, in the non-layered method the composite wrap is modeled by one solid part without definition of composite lay-up, as shown in Figure 6-2b). Compared to layered method, it avoids inputting the fracture property of the inter-laminar interface but cannot replicate the position and path of delamination accurately due to lack of details of the composite lay-up. In the tensile experiments of 45° X-joints, no delamination occurs in the composite laminate, so the non-layered method is preferred to model the composite wrap without sacrifice of the modeling accuracy.

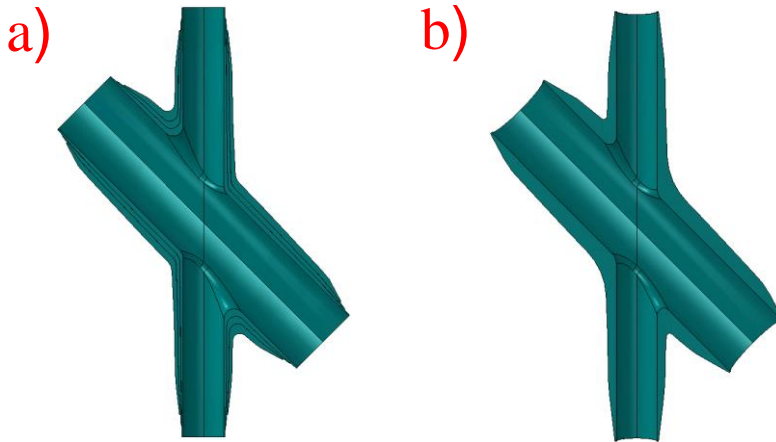


Figure 6-2 Two strategies to define layered lay-up of composite wrap using 3D solid element – an example of small-scale 45° X joints: a) layered method; b) non-layered method

Two types of solid elements are normally used in finite element modeling, i.e., hexahedral element and tetrahedral element. Hexahedral element is preferred to be used in meshing simple geometry and is economic in computational cost because the same degrees of freedom of 1 hexahedral element corresponds to 6 tetrahedral elements. In comparison, tetrahedral element is suitable for meshing complex and curved geometry but the distortion of the element should be well controlled to ensure the mesh quality. Considering the geometry of wrapped composite joints, the hexahedral element is used to mesh steel circular hollow sections while the tetrahedral element is used to mesh composite wrap. In finite element modeling the second-order element captures stress concentrations more effectively and is better for modeling geometric features than the first-order (linear) elements. However, it also incurs a significant increase in calculation costs. Based on the preliminary joint modeling results, linear element does not reduce modeling accuracy considering the relatively fine mesh size used in modeling of composite wrap and steel tubes. Therefore, 4-node linear tetrahedral element (C3D4) and 8-node linear hexahedral element (C3D8) is used in meshing composite wrap and steel members, respectively, as shown in Figure 6-3.

The global mesh size of the joint FE model is determined by trade-off between considerations of simulation accuracy, computational cost, and the dimensions of the joint geometry. Figure 6-3 illustrates the mesh strategy of the FE model using small-scale 45° X-joints as an example where the reference mesh size is 2 mm in meshing steel members and composite wrap. The steel members are meshed with the reference size (2mm) constantly due to limited amount of the hexahedral elements. A local seed of 4 elements is assigned to the through-thickness direction to accurately simulate its bending deformation. On the contrary, two mesh strategies are compared in Figure 6-3 in terms of meshing composite wrap. The first strategy uses the reference size (2mm) constantly in all regions of the composite wrap ensuring modeling accuracy by keeping details of stress concentration in the whole wrap but losing the economy in computation cost especially in the case of larger geometric scale, as shown in Figure 6-3a). The second strategy uses the variable mesh size through the thickness direction where the mesh size is equal to the reference value of 2 mm at the region close to the bonded interface and increases gradually to 8 mm until the outer surface of the composite wrap, as shown in Figure 6-3b). It uses finer mesh around the interface location to accurately capture the stress concentrations as the source of debonding. On the other hand, coarser mesh is used far from the interface location where the stress level is significantly decreased to save the computation cost. Finally, the variable mesh size is selected to be utilized in the joint simulation considering the enhanced computational efficiency without sacrificing modeling accuracy. The numerical results using the two strategies are compared in the section 7.3.1. The variable mesh size is also employed in meshing of medium-scale 45° X-joints where the mesh size of composite wrap is 4 mm close to the bonded interface and increases gradually to 16 mm towards the outer surface.

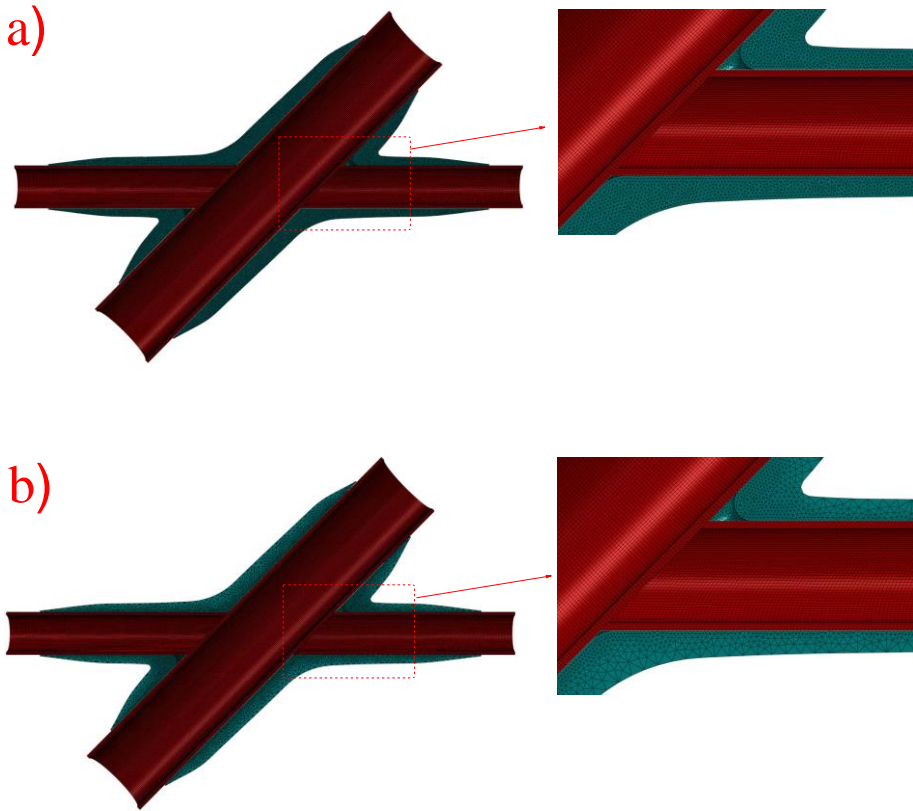


Figure 6-3 Mesh strategies of joint FE modes – an example of small-scale 45° X joints:
 a) constant mesh size in composite wrap; b) variable mesh size in composite wrap

6.3.2 Boundary conditions

The boundary conditions used in the FE models of small-scale and medium-scale 45° X-joints are illustrated in Figure 6-4 b) and Figure 6-5 b), respectively, compared to the experimental set-up shown in Figure 6-4 a) and Figure 6-5 a). In both cases only half of the joint geometry is built to save computational cost and the symmetry boundary condition in global Z direction is applied to mid-plane of the joint with reference to the symmetric tensile load. In the tensile test of small-scale 45° X joints, the load is transferred through gripping the brace members by the steel clamps. Accordingly, a simplified boundary conditions without steel clamps and the inside braces are used in the model since no sliding occurs in between to decrease the stiffness. However, it is not suitable in the case of the medium-scale joint where the stiffness of the ear plates and the connection plates cannot be regarded infinite compared to the joint and should be included in the FE model to ensure the stiffness in the experiments. Two reference points named “Top” and “Bottom” are built at the ends of the top and bottom braces at the edge of the steel clamps in the small-scale model, and at the center of the hollow cylinder of the top and bottom ear plates in the medium-scale model, respectively. The cross section

of the brace end and the hollow cylindrical surface is kinematically constrained (coupled) to the reference point in all degrees of freedom in the small-scale joint model and the medium-scale joint model, respectively, to simulate the same load transfer as in the test. The displacement controlled failure loading is applied by building the displacement/rotation boundary conditions to the reference point “Top” and “Bottom” fixed in all degrees of freedom except for the vertical translation U_2 and the in-plane rotation UR_3 ($2/3$ is designation for the global Y/Z direction). The positive and negative displacement with identical absolute value is simultaneously applied to the “Top” and the “Bottom” reference point, respectively, to simulate the loading scenario as in the test. In the small-scale model the applied displacement and the load is obtained from the displacement and the reaction force of the reference point. In the medium-scale model the load is still obtained from the reference point but the applied displacement is measured from the point approximately 100 mm from the end of the braces to matches the DIC measurements, as shown in Figure 6-5 b).

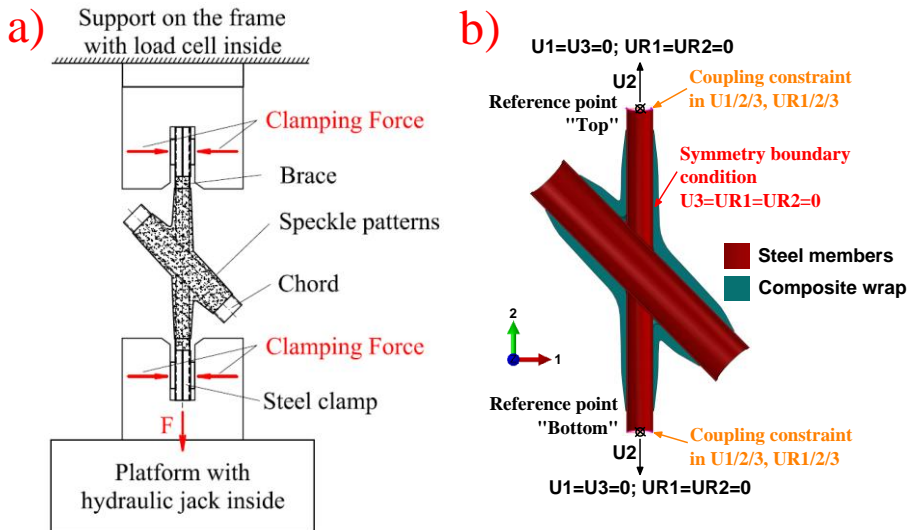


Figure 6-4 Boundary conditions in b) the FE model of small-scale 45° X joints compared to a) the experimental set-up

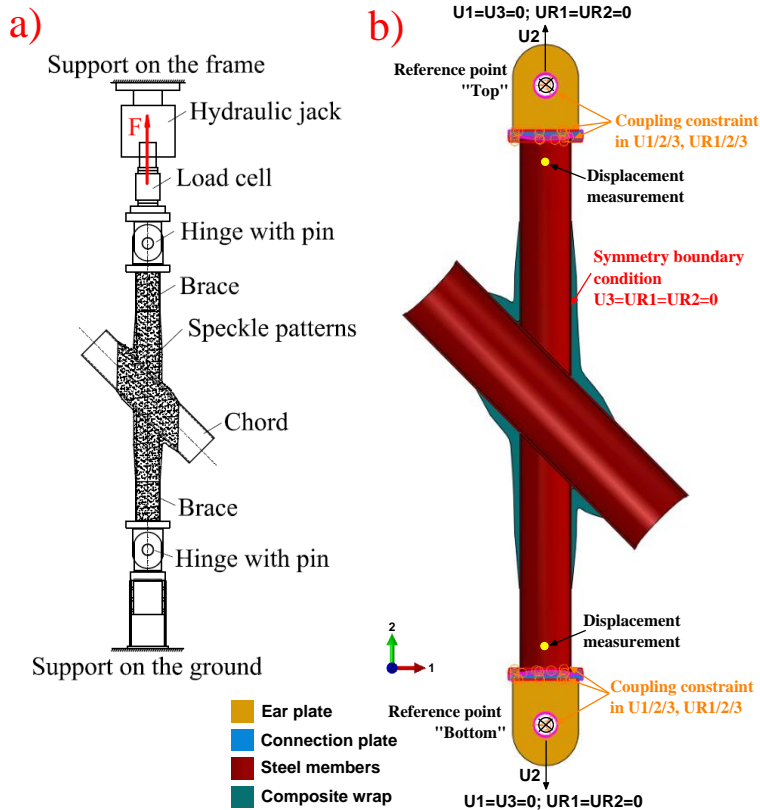


Figure 6-5 Boundary conditions in b) the FE model of medium-scale 45° X joints compared to a) the experimental set-up

6.3.3 Contact interactions

As explained in the Section 5.4.2, the contact interactions in the current FE model are simulated by the general contact algorithm in ABAQUS Explicit solver consisting of specifying the general contact domain with global contact properties and the individual contact pairs with distinct contact properties. Two types of contact property models are assigned globally to the general contact domain: the hard contact model and the friction model. The default hard contact model is illustrated in Figure 6-6a). When surfaces are in contact, any contact pressure can be transmitted between them. The surfaces separate if the contact pressure reduces to zero and the separated surfaces come into contact when the clearance between them reduces to zero. The default tangential behavior is defined where the interaction between contact bodies is frictionless.

The individual contact pairs are defined to simulate the behavior of the bonded interface in the joint model with distinct contact properties which includes hard contact model, the Coulomb friction model and the cohesive zone model (CZM). Different from the material-level model, at the joint level the friction plays a significant role in enhancing the debonding resistance attributed to circumferential contraction applied on

the bonded interface by composite wrap under tensile load due to Poisson's ratio effect. The Coulomb friction model as shown in Figure 6-6b) is used to simulate the improvement of the debonding resistance by friction. It defines the critical shear stress τ_{crit} , at which sliding of the surfaces starts as a fraction of the contact pressure, p , between surfaces ($\tau_{crit} = \mu p$). The fraction, μ , is known as the coefficient of friction (COF). The stick/slip calculations define a surface in the contact pressure-shear stress space along which a point transitions from sticking to slipping. The influence of friction and the measurement of the COF will be explained more thoroughly in Section 6.5.2.

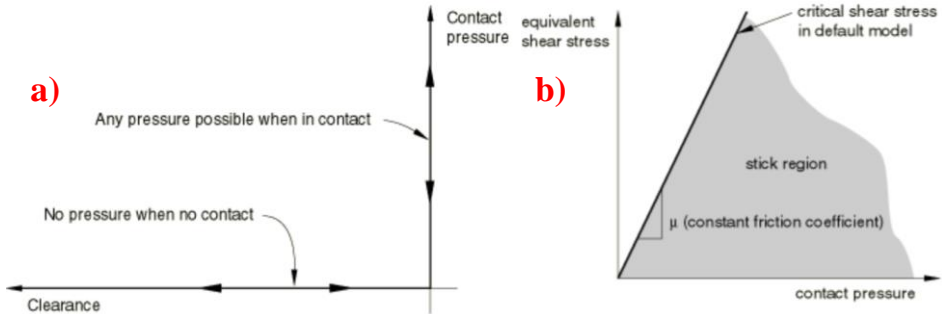


Figure 6-6 The hared contact model and the coulomb friction model used in the joint model[2]: a) default pressure-overclosure relationship; b) slip regions for the basic Coulomb friction model

To simulate debonding behavior of the composite-steel bonded interface, the cohesive-contact approach is used to define the cohesive zone model (CZM) assigned to the individual contact surface pairs. Cohesive contact approach is primarily intended for situations where the interface thickness is negligibly small as in the case of the very thin bond line in wrapped composite joints. It is typically easier to define than modeling the interface using cohesive elements and allows simulation of a wider range of cohesive interactions. The details of the CZM with introduction of four-linear cohesive law are explained thoroughly in subsection 5.4.3. Figure 6-7 illustrates the definition the contact pairs to simulate debonding where the highlighted inner surface of composite wrap and the outer surface of braces and the chord are paired and are assigned with distinct contact properties.

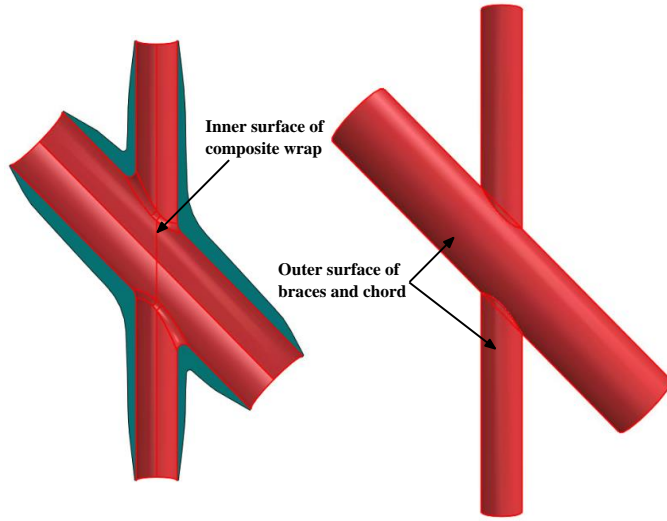


Figure 6-7 Definition of contact pairs to simulate debonding of the bonded interface – an example of small-scale 45° X joint model

6.3.4 Analyses method

Consistent to the numerical simulation of the interface tests in Chapter 5, failure analysis of the joint model is performed as quasi-static using the explicit dynamic solver because it does not have the usual convergence issue as does the implicit static solver. Mass scaling method is also utilized to increase the calculation speed. This method tends to increase inertia forces in a model, sometimes leading to useless results. A compromise must be found between an acceptable computation time and quality of results, often by analyses for each of the different model set-ups.

Mass scaling with desired time increment of 0.002 sec is used in the modeling of wrapped composite joints. Similar to DCB and ENF modeling in Chapter 5, quality of the joint modeling results is verified by matching applied and reaction forces in a model for displacement controlled failure loading. The desired time increment is selected when linear match is reached between input and output forces with no fluctuations. More details can be found in Section 5.3.2.

6.4 Material models and the interface model

6.4.1 Material model of composite material

The material input used in the joint model in this Chapter is the same as used in the material-level FE models which has been calibrated by good matches to the material test results in Table 4-2.

6.4.2 Material model of steel

Non-linear behavior of steel is simulated by plasticity model in ABAQUS. The elastic constants ($E = 210$ GPa, $\nu = 0.3$) and nominal yield and ultimate stress (S355, $f_y = 355$ MPa, $f_u = 510$ MPa) in combination with isotropic hardening are included in the

plasticity model.

6.4.3 Selection of the interface model of composite-steel bonded interface

Debonding of composite-steel bonded interface is simulated by the cohesive zone modeling (CZM) where the traction-separation law is defined to describe the traction-separation behavior of the fracture process zone in the wake of the crack tip. The four-linear traction-separation law is proposed in Chapter 4 and Chapter 5 to simulate the fracture process of the composite-steel bonded interface with three distinct phenomena: 1) crack tip deformation [3]–[5], 2) softening, and 3) fiber bridging [3]. They are distinguished by four critical stages: “p” – onset of plasticity; “c” – onset of cracking; “b” – onset of fiber bridging; “f” – failure. More details of the definition of the CZM and the four-linear cohesive law can be found in Section 4.3.3 and Section 5.3.3.

In Chapter 5, the four-linear traction-separation laws of pure mode I / II used in modeling DCB / ENF tests are determined based on the mean values of the DIC measurements in the 3 tested specimens in each test series. The mean values of the fracture properties of the bonded interface give good matches to the interface experimental results. However, they cannot be used to match and replicate the joint experiment results due to their failure to account for the scatter of test data and the statistical uncertainty associated with the number of tested specimens. Figure 6-8 illustrates a generic normal distribution graph of the material properties where the mean value and the 5% fractile value are indicated. It can be seen that if the mean value of the material property were used for design calculation, the material would fail with 50% probability. EN 1990[1] requires using the characteristic value to achieve the level of reliability which should be defined as the 5% fractile value for design calculations such that in 95% probability the material property is higher than the design values. In the current research, it is unknown how variability of the interface properties influences the overall response of the large and complex joint interface. Therefore, the response of the joint model using both the mean value and the 5% characteristic value of the interface properties are considered and compared. It should be noted that the level of surface treatment and the quality control in production of small-scale and medium-scale wrapped composite 45° X-joints in Chapter 3 is the same as in production of 3ENF specimens in Chapter 5. Consequently, the mode II traction-separation laws in simulation of joint models are determined based on 3ENF test data. Based on EN 1990[1], the characteristic values of the mode II fracture property of the bonded interface in 3ENF tests are derived using the Equation 6-1:

$$X_k = m_k \{1 - k_n V_x\} \quad \text{Equation 6-1}$$

where:

X_k – the characteristic value corresponding to a certain probability (5% in this case) of fractile value;

m_x – Mean value of the n sample results;

k_n – Characteristic fractile factor;

V_X – Coefficient of variation of X ;

The 5% characteristic fractile factor k_n can be determined based on the V_X according to the Table 6-2 in EN 1990[1]. In the current research where the sample number n is 3 and the V_X is known from the test, the $k_n = 1.89$.

The mean values and the 5% characteristic values of the crack tip opening displacement (CTOD) at the critical stages, as well as the critical SERR at crack initiation and crack propagation in mode II failure of 3ENF specimens are summarized in Table 6-3. It should be noted that there is no DCB test available that provides the mode I fracture properties of the bonded interface with nominally comparable production process to 3ENF specimen. An alternative method is therefore proposed to obtain the mean and 5% characteristic parameters in the mode I cohesive law. It assumes the ratio of values of the critical parameters in mode II over those of mode I is the same in the batch of 3ENF and DCB/4ENF. The values of the critical parameters in mode I in the batch of 3ENF specimen can be calculated based the mode II parameters and the ratio. They are also summarized in Table 6-3. The corresponding cohesive laws in mode I and mode II are compared in Figure 6-9 and Figure 6-10, respectively.

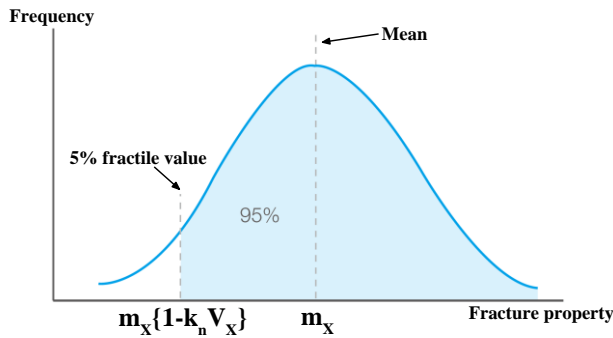


Figure 6-8 The generic normal distribution of material properties[1]

Table 6-2 Values of k_n for the 5% characteristic value

n	1	2	3	4	5	6	8	10	20	30	∞
V_X known	2.31	2.01	1.89	1.83	1.80	1.77	1.74	1.72	1.68	1.67	1.64
V_X unknown	-	-	3.37	2.63	2.33	2.18	2.00	1.92	1.76	1.73	1.64

Table 6-3 Mean values and 5% characteristic values at the critical stages based on DCB and 3ENF test

FEM scenario	Values	Onset of plasticity - stage "p"		Onset of cracking - stage "c"		Onset of fiber bridging - stage "b"		Failure - stage "f"		Critical SERR	
		δ_p (mm)	σ_p (MPa)	δ_c (mm)	σ_c (MPa)	δ_b (mm)	σ_b (MPa)	δ_f (mm)	σ_f (MPa)	$G_{Ic,tip}$ (N/mm)	G_{Ic} (N/mm)
Mode I	Mean	0.0017	17.33	0.012	17.33	0.046	1.73	0.505	0	0.19	0.91
	5% char.	0.0015	14.67	0.012	14.67	0.054	1.47	0.394	0	0.17	0.76
Mode II-3ENF	Mean	0.0017	17.33	0.027	26	0.132	26	0.148	0	0.56	3.5
	5% char.	0.0015	14.67	0.025	22	0.069	22	0.087	0	0.45	1.6

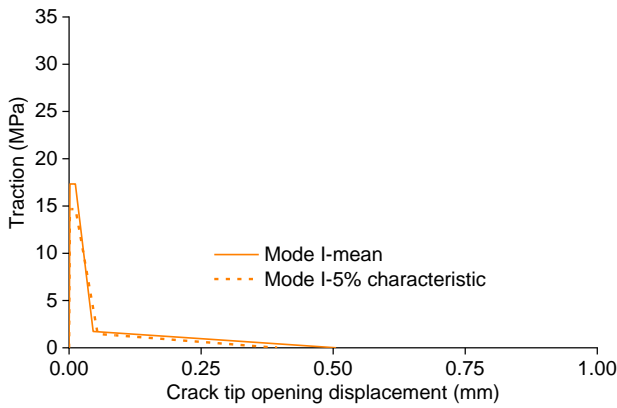


Figure 6-9 Mode I cohesive-law with 5% characteristic fracture properties

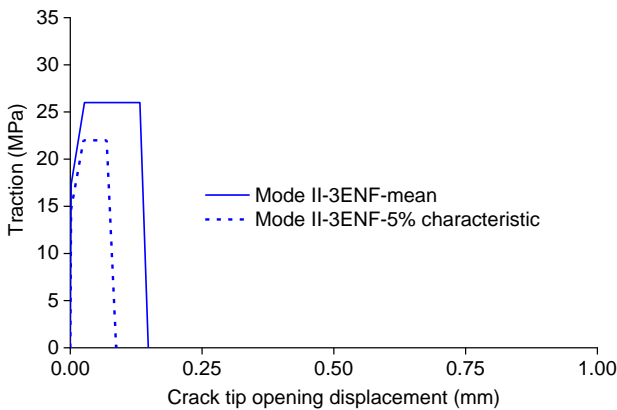


Figure 6-10 Mode II CZM with mean and 5% characteristic fracture properties of 3ENF specimens

The definition of mode mixity in the joint modelling is the same as in the interface modelling explained in Section 5.4.3.5 where five mix ratio (m_2) values, i.e. 0 (pure mode I), 0.25, 0.5, 0.75 and 1 (pure mode II), are used based the values of the SERR. An exponential relation between interface SERR and the mix ratio based on the literature [6] and validated by the interface tests are used. Figure 6-11 shows the shape of traction-separation laws at the 2 pure modes and the 3 mixed modes with 5% characteristic values of the critical parameters used in the modelling of wrapped composite 45° X-joints tested in Chapter 3.

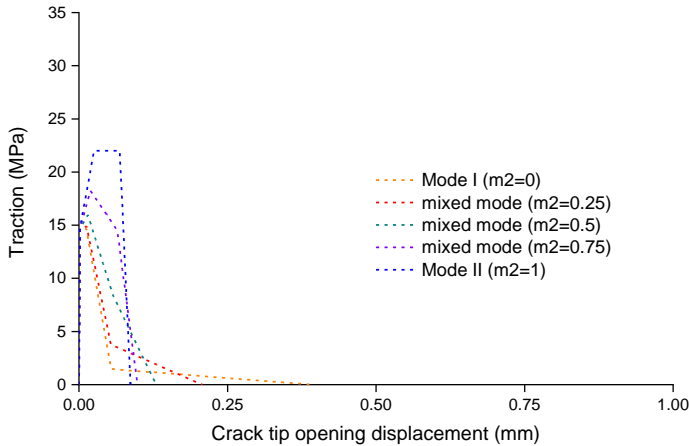


Figure 6-11 Shape of traction-separation laws at mode I, mode II and mixed modes of composite-steel bonded interface (mode I and mode II cohesive laws are based on the 5% characteristic values)

6.5 Sensitivity analysis of the joint global response to physical parameters

In the field of structural reliability or operational safety, mathematical models are used for simulation and for prediction. Models are also used for uncertainty quantification and sensitivity analysis studies[7]. Sensitivity analysis allows the study of how uncertainty in the output of a model can be apportioned to different sources of uncertainty in the model input[8]. Measures of each influential input variable on the response variability provide a deeper understanding of the modeling in order to reduce the response uncertainties in the most effective way[9]–[11]. As been discussed in this Chapter, there are two critical parameters leading to variability in simulation of the debonding resistance of the bonded interface in wrapped composite joints: 1) traction-separation law (CZM) obtained from ENF test; 2) coefficient of friction (COF). The former quantifies the fracture toughness of the bonded interface while the latter helps describe the resistance of the bonded interface to sliding during crack propagation. Influence of the 2 critical parameters on debonding resistance is investigated by sensitivity analysis in the following subsections. The rest of modeling parameters are constant during the sensitivity analysis process to eliminate potential interaction of different input to the modeling output variability.

6.5.1 Influence of the traction-separation laws (CZM)

Due to the identical level of surface treatment and the quality control during the production in 3ENF specimens and small/medium-scale 45° X joints, the traction-separation laws obtained from 3ENF test are used for simulation of the debonding resistance of tested 45° X joints. The joint modeling results with the input of the mean cohesive law and the 5% characteristic cohesive law, as shown in Figure 6-10, are compared to investigate sensitivity of joint resistance to this parameter. In this sensitivity analysis the only variable is the traction-separation law, and no friction is introduced on the bonded interface which will be investigated in the following subsection.

Figure 6-12a) and Figure 6-12b) compares the load-displacement response of the joint models in small-scale and in medium-scale, respectively, with the mean cohesive law and the 5% characteristic cohesive law, to the experiment results. In both geometric scales, the mean CZM and the 5% characteristic CZM give good matches in initial stiffness but the mean CZM underestimates the progression of the non-linearity of the joint after the stiffness starts to degrade. This can be explained in Figure 6-8 where using the mean CZM leads to 50% probability that the real behavior of the bonded interface in experiments is worse than the response of the joint model shown in Figure 6-12. The distinction of the progression of non-linearity between the joint model and the experiment results is even larger in medium-scale joint. On the contrary, the 5% characteristic CZM gives good matches of progression of the non-linear behavior, especially in medium-scale where the load drop (see Figure 6-12b)) appearing at approximately 1200 kN is well-captured. Therefore, the 5% characteristic CZM is used as the benchmark traction-separation law in the following sections related to sensitivity study in terms of COF, the FEA validation, and the parametric study.

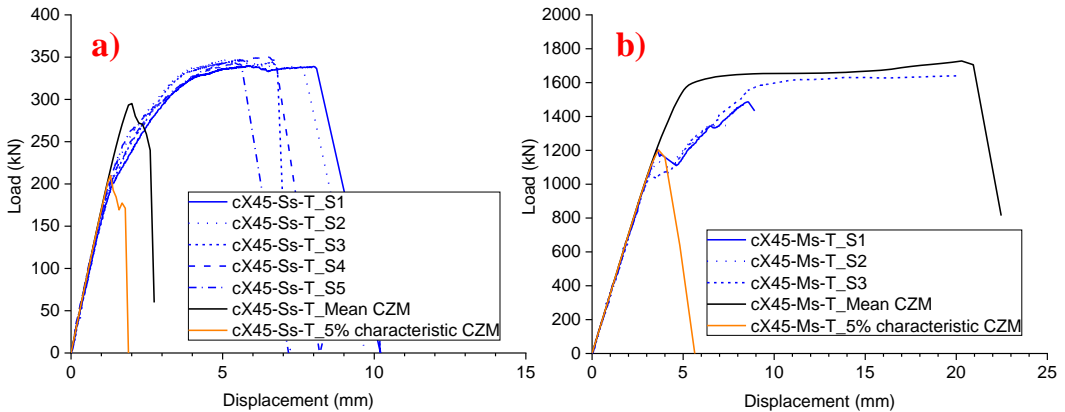


Figure 6-12 Load-displacement response of joint models in a) small-scale and b) medium-scale with input of mean CZM and 5% characteristic CZM

6.5.2 Influence of coefficient of friction (COF)

As illustrated in Figure 6-12, the 5% characteristic CZM is utilized as the benchmark CZM for FEM of 45° X joints due to its effective capturing of the progression of non-linearity. However, the load resistance of the FE model utilizing only CZM to

model the interface behavior is significantly lower than the experimental results, indicating the indispensable contribution of friction on the bonded interface to the debonding resistance. The additional slip resistance provided by friction is the consequence of contraction of the composites around the steel in the debonded region due to Poisson's effects while tensile load is applied, and the consequence of confinement of the composite around steel during curing process. Figure 6-13a) and Figure 6-13b) compares the contour plot of contact pressure (CPRESS) on the bonded interface in the 3ENF FE model and in the small-scale 45° X joint model, respectively, at the peak load in the load-displacement curves. It can be seen that in 3ENF model the value of normal pressure is negative within the fracture process zone in front of the pre-crack tip indicating the trend of separation of the bonded interface attributed to the differences in the curvature. In comparison, in the joint model, approximately 8~10 MPa of normal pressure distributes on the bonded interface between braces and composite wrap where the crack is propagated. Once the normal pressure exists on the bonded interface, the friction would give additional resistance to debonding of the bonded interface.

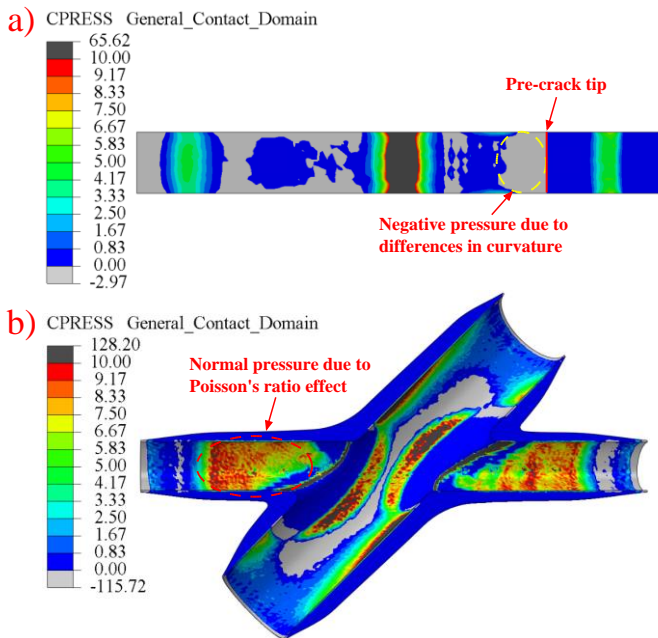


Figure 6-13 Normal pressure on the bonded interface of a) 3ENF model and b) small-scale 45° X joint model at the peak load in load-displacement curves (unit: MPa)

Sensitivity analysis is performed on the small-scale and the medium-scale 45° X joint models to investigate the sensitivity of their load-displacement behavior to the coefficient of friction (COF). The 5% characteristic CZM is used as the benchmark CZM, and the COF is increased from 0 (frictionless) to 0.6 with the increment of 0.1. The load-displacement response of the 45° X joint models in small-scale and in medium-scale is shown in Figure 6-14a) and Figure 6-14b), respectively. It can be seen that in both scales

the load resistance of the joint model is enhanced as the value of the COF increases from 0 to 0.6. The ductility of the joint also increases gradually when the COF varies from 0 to 0.5 but abrupt increase of the ductility is observed when the COF increases from 0.5 to 0.6. This is because the load level exceeds the yielding resistance of the brace members when the COF is higher than 0.5. It can be concluded that the suitable value of the COF between the steel member and the composite wrap is within 0.5~0.6 which gives good match to the joint experiments in terms of ductility and load resistance.

To justify the range of COF values concluded from the sensitivity analysis, the COF test is conducted in the tribometer Rtec MFT-5000 in Stevin Lab 2 of TU Delft, as shown in Figure 6-15. The normal contact load $P = 50 \text{ N}$ is applied through the top hydraulic and the tangential load Q is applied through the horizontal actuation. The value of Q and the horizontal displacement L is recorded by the load cell and the displacement sensor in the system, respectively. Load control is used with frequency of 0.2 Hz with loading duration of 1 min. The test coupon is shown in Figure 6-16 which is composed of the steel plate with contact surface of $25 \text{ mm} \times 10 \text{ mm}$ and composite plate cut from the uniform region of the primary bonded interface in the tested 45° X joint specimen. The fretting loops of the COF test are shown in Figure 6-17a), where the tangential load Q used to calculate COF is determined by the intersection point of the fretting loops with the dash red line crossing the origin. The slope of this line is equal to the system stiffness S [12]. Figure 6-17b) illustrates the COF values against the cycles during the loading process indicating that the average value of COF is 0.55 between composite wrap and steel which is consistent to the suitable values used in the joint model.

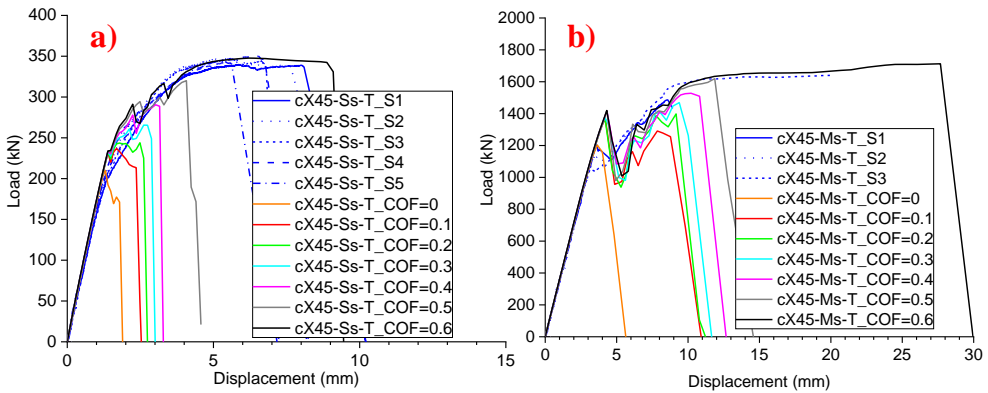


Figure 6-14 Load-displacement response of joint models in a) small-scale and b) medium-scale with variation of COF from 0 to 0.6 with 0.1 increment

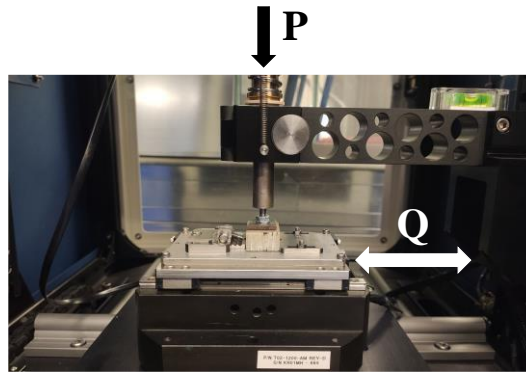


Figure 6-15 Set-up to measure the COF

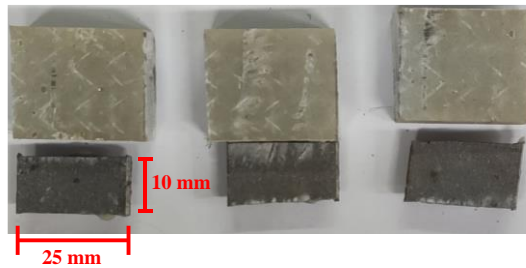


Figure 6-16 Test coupon in COF test

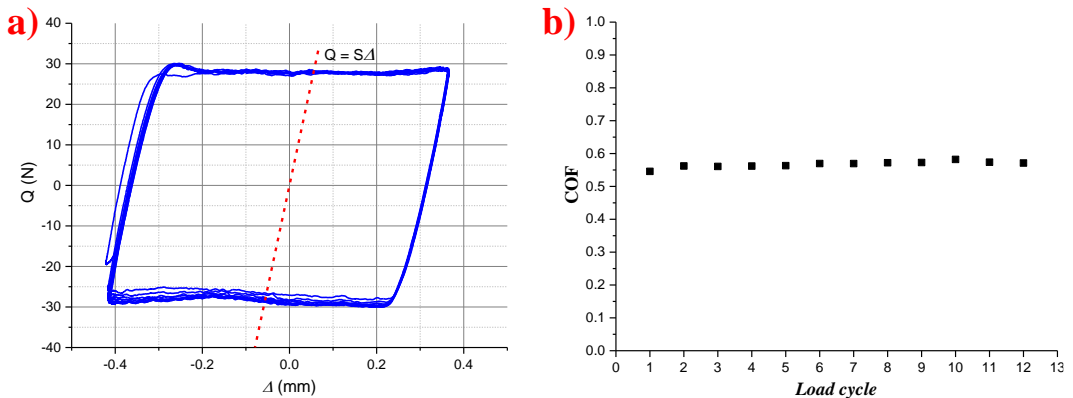


Figure 6-17 a) Explanation for calculating COF based on the fretting loops; b) COF values vs load cycles in COF test

6.6 Validation of FE models of 45° X joint

Based on the above-mentioned modelling strategy, material and interface models, as well as sensitivity analysis to physical parameters, the critical parameters in FEM of small-scale and medium-scale 45° X-joints are calibrated and summarized in Table 6-4. In addition, other parameters, e.g., mesh typology, mesh geometric order, mesh size, wrapping dimensions, joint size, etc., are investigated in a separate study shown in Section 7. In the joint FEM of this Chapter, the 4-node linear tetrahedral (C3D4) element

is used in composite wrap with interior element growth. 5% characteristic CZM based on 3ENF test are used considering the scatter of test data. COF equal to 0.55 is used to consider contribution of friction to addition debonding resistance of the bonded interface. To validate the modeling strategy and the input parameters, the static behavior of the joint models is compared to the experiment results not only in terms of the load-displacement response, but also investigating the debonding patterns, surface strains, debonding crack length, etc. The comparisons are explained thoroughly in this section.

Table 6-4 Overview of critical parameters in FE models of small/medium-scale 45° X joint models

FE model name	Composite element type	Composite mesh size (mm)	CZM	COF
cX45-Ss-T-FEM	C3D4	2→8	5%	0.55
cX45-Ms-T-FEM		8→32	characteristic 3ENF	

6.6.1 Comparison of load-displacement response

Comparing the load-displacement response between experiments and FEM is the first step to validate the compatibility of the joint FE models with the test results. Overview of comparisons of the global response in terms of initial stiffness, elastic load limit and ultimate resistance is summarized in Table 6-5, and the load-displacement curves are shown in Figure 6-18. The elastic load limit in FEM is determined by analysis of the stiffness of the load-displacement curves combined with the analysis of the damage variable (CSDMG) of the bonded interface.

It can be seen in Table 6-5 that the initial stiffness and the elastic load limit from numerical simulation match well with the average values in experiments, with the deviation within 5% and 10%, respectively. The ultimate resistance from FEA and the average test results in small-scale matches well with deviation within 1% while larger scatter is seen in the medium-scale attributed to larger scatter in ultimate load in the tested specimens resulting from acceptable variability of debonding resistance. The deviation of load resistance is only 2% when the FEA results are compared to test results of the specimen cX45-Ms-T_S3. In small-scale the numerical results show less non-linearity after the elastic stage (200~300 kN) than the test results while in medium-scale the peak value at the load drop between 3~7 mm applied displacement is larger than in the test. The reason for the less-nonlinearity and the larger load drop is underestimation of debonding.

It can be concluded that good match is reached in terms of the global response from joint FEA results and joint test results, validating that the modeling strategy and input parameters are reasonable. This provides initial motivation to compare the models and experiments on a deeper level of detail. The goal is to obtain more confidence in the validity of the model which is then used as insight to better understand the failure process and interaction of failure modes of the joints. Ultimately the validated model will be used

for parametric study in Chapter 7.

Table 6-5 An overview global response in experiments vs FEA of 45° X joints

Specimen or FE model	Initial stiffness [kN/mm]	Elastic load limit [kN]	Ultimate load [kN]
cX45-Ss-T_S1	159.0	183.9	339.5
cX45-Ss-T_S2	163.3	182.2	346.5
cX45-Ss-T_S3	160.3	180.5	347.4
cX45-Ss-T_S4	171.9	180.4	346.0
cX45-Ss-T_S5	170.3	184.9	344.9
Average (and COV [%])	164.9 (3.15)	182.4 (0.98)	345.7 (1.01)
cX45-Ss-T_FEM	173.4	182.1	346.5
Deviation (%)	5	0.1	0.2
Specimen or FE model	Initial stiffness [kN/mm]	Elastic load limit [kN]	Ultimate load [kN]
cX45-Ms-T_S1	349.2	1193	1483
cX45-Ms-T_S2	345.2	1139	1353
cX45-Ms-T_S3	341.5	1053	1640
Average (and COV [%])	345.3 (0.92)	1128 (5.11)	1492 (7.88)
cX45-Ms-T_FEM	351.4	1048	1659
Deviation (%)	2	7	11

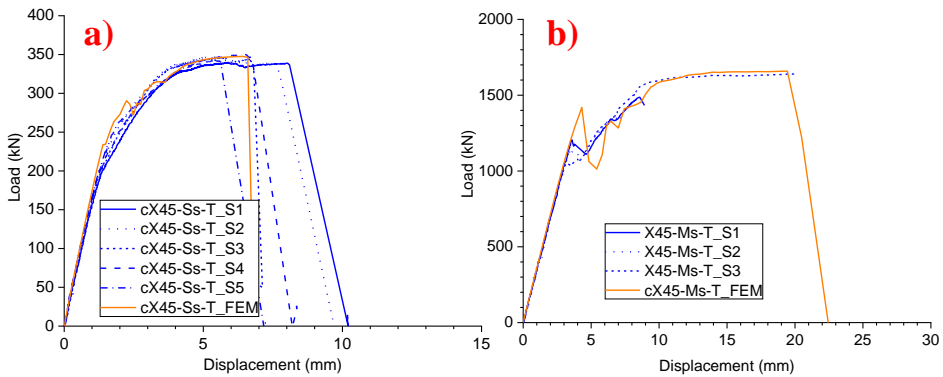


Figure 6-18 Comparison of load-displacement response of 45° X joint models vs test results in a) small-scale and b) medium-scale

6.6.2 Comparison of failure process

The motivation for comparison of failure process of joint experiments and joint FE models are: 1) to further validate the reliability of the defined modeling strategies and the input parameters used in modeling debonding behavior of wrapped composite joints;

2) to replicate and understand the debonding process of wrapped composite joints with help of FEA, which cannot be achieved explicitly from the experiments; 3) to obtain the threshold of the principle strain on the surface of composite wrap used to determine the debonding crack front in DIC analysis. Based on the experimental results and the FEA replication, 5 critical stages of the debonding process of wrapped composite joints can be defined under tensile load: stage \mathbf{l}_e – elastic load limit; stage \mathbf{i}_r – initiation of debonding from wrap root; stage \mathbf{y} – initiation of steel yielding; stage \mathbf{i}_e – initiation of debonding from wrap end; stage \mathbf{r} – rupture. They are identified in experiments through analysis of the load-displacement curves and analysis of principle strain on surface while in FEA they are specified through analysis of damage variable on the bonded interface and analysis of surface principle strain. A sketch of wrapped composite joints is illustrated in Figure 6-19 to facilitate explanation of its failure process. The following conclusions are drawn based on the comparison between experiments and FEA debonding process afterwards in this section:

1) The end of elastic behavior (stage \mathbf{l}_e) of the load-displacement curves is due to plasticity in the traction-separation behavior of the primary and the secondary bonded interface in the intersection region.

2) Debonding on braces is firstly initiated from wrap root (stage \mathbf{i}_r) attributed to shear stress concentrations on the primary bonded interface in the intersection region, and subsequently propagates steadily along the primary bonded interface. When the applied load level reaches yielding resistance of the brace members, yielding of the CHS is initiated at the wrap end (stage \mathbf{y}).

3) Steel yielding leads to contraction of the brace member at the wrap end where the peeling stress is concentrated on the bonded interface. Increase of peeling stress changes mode mixity towards the mode I with less toughness and reduces the contact pressure on the bonded interface leading to decrease of the contribution of friction to the debonding resistance.

4) Two failure modes are observed considering the differences in the amount of peeling stresses caused by the steel tube yielding / necking and the dimensions (size) of the steel members: excessive steel yielding leads to initiation of debonding from the wrap end (stage \mathbf{i}_e) which propagates along the primary bonded interface and coalesces with the debonding crack from the wrap root resulting in full debonding at the rupture stage (stage \mathbf{r}); moderate steel yielding does not result in initiation of debonding from the wrap end, so propagation of debonding from the wrap root develops consistently until reaching the wrap end (full debonding) at the rupture stage (stage \mathbf{r}).

Comparisons of the displacement and load level at the critical stages of the debonding process in experiments vs in FE models are summarized in Table 6-6 . More detailed comparisons in terms of the failure process of specific specimens are presented in Figure 6-20~Figure 6-37.

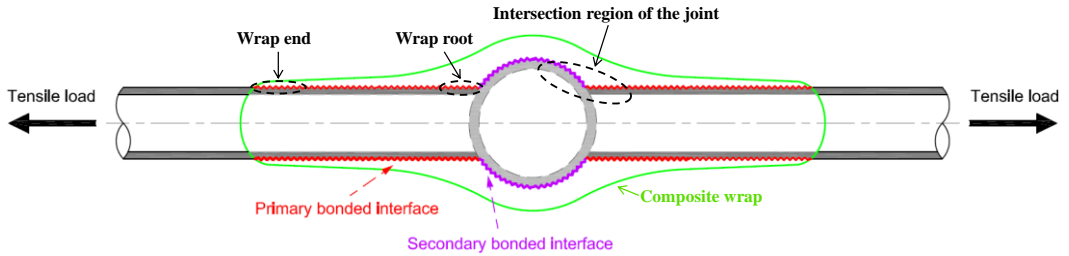


Figure 6-19 Sketch of wrapped composite joints to explain its failure process

Table 6-6 Comparisons of the displacement/load values at the critical stages of the debonding process in experiments vs in FEA

Critical stages		Small-scale		Medium-scale	
		X45-Ss-T_S4	X45-Ss-T_FEM (and deviation[%])	X45-Ms-T_S3	X45-Ms-T_FEM (and deviation[%])
Elastic load limit (stage i_e)	Disp. (mm)	1.11	1.05 [5.4]	3.31	2.98 [10.0]
	Load (kN)	180.4	182.09 [0.9]	1053	1048 [0.5]
Initiation of debonding from wrap root (stage i_r)	Disp. (mm)	1.78	1.49 [16.3]	4.64	5.82 [25]
	Load (kN)	234.4	234.2 [0.3]	1106	1108 [0.2]
Initiation of steel yielding (stage y)	Disp. (mm)	3.84	3.76 [2.1]	9.09	9.83 [8]
	Load (kN)	321.5	321.6 [0.03]	1571	1579 [0.5]
Initiation of debonding from wrap end (stage i_e)	Disp. (mm)	5.39	4.74 [12.1]	-	-
	Load (kN)	341.5	340.7 [0.2]	-	-
Rupture (stage r)	Disp. (mm)	6.75	6.60 [2.2]	20.36	19.44 [4.5]
	Load (kN)	346.0	346.5 [0.03]	1640	1659 [1.2]

6.6.2.1 Failure process of experiment vs FEA in small-scale 45° X joints

The load-displacement behavior in the FE model X45-Ss-T_FEM is compared to the behavior in specimen X45-Ss-T_S4 with critical stages marked with solid circles on the curves, as shown in Figure 6-20. It can be seen that the load and displacement values match quite well at the critical stages with the deviation all within 8% except the displacement at point i_r and point i_e due to the underestimation of debonding on the chord in the FE model, indicating the feasibility of the modeling strategy and the input parameters in the joint model.

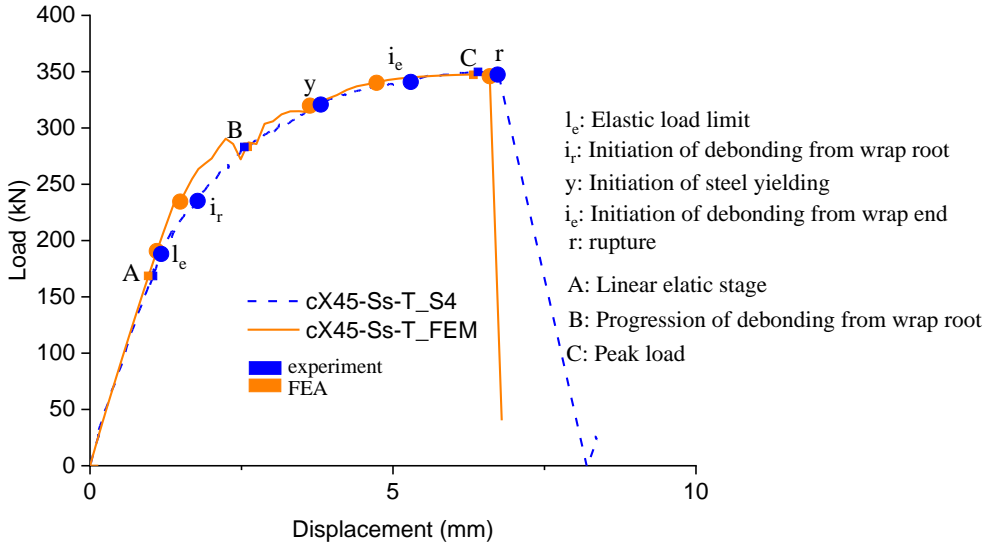


Figure 6-20 Load-displacement response of small-scale 45° X joint in FE model vs in experiment

Surface strains (principle strains) of specimen X45-Ss-T_S4 and the FE model X45-Ss-T_FEM at the marked stages in Figure 6-20 are shown in Figure 6-21~Figure 6-27 for comparison of debonding process where the damage variable output – CSDMG from FEA is also illustrated to visualize the debonding length on the bonded interface. The joint behaves elastically with low strains distributed uniformly on the joint surface as shown in Figure 6-21 – stage **A** at 170 kN. The end of the elastic behavior is reached at approximately 180 kN (stage **I_e**) attributed to plasticity of the traction-separation behavior of the bonded interface at the wrap root and the local bending of the composite wrap at the middle of the chord member. Debonding is firstly initiated on the primary bonded interface from wrap root due to shear stress concentrations indicated by the localized increase of surface strains and the occurrence of damaged region at the wrap root shown in Figure 6-22 – stage **I_r** at 234 kN. Debonding crack propagates steadily along the primary bonded interface at stage **B** – 289 kN where the high strain region on the surface and the damaged region at the bonded interface progress from the wrap root, see Figure 6-23. Crack propagation continues with further increase of high surface strain regions and the damage areas on the bonded interface illustrated in Figure 6-24 at stage **y** – 321 kN where the yielding is initiated on the braces outside the composite wrap. It can be seen from Figure 6-24 at this stage that debonding area is significantly larger in numerical results than in experiments. The possible reason is that larger yield strain in braces in experiments dissipates more external energy from the loading system such that less energy is dissipated in debonding. When the applied load reaches 341 kN, the excessive yield strain of brace leads to contraction of the cross section, resulting in mode I dominated debonding at the wrap end, see Figure 6-25– stage **I_e**. However, due to underestimation of debonding at the wrap end on the primary bonded interface, in FE model debonding crack from wrap end does not further propagate while crack from wrap

root propagates steadily at peak load (stage **C** – 347 kN, see Figure 6-26) and reaches the critical length at rupture stage (stage **r** – 346 kN, see Figure 6-27) just before full debonding. On the contrary, in the experiment, the debonding crack propagates significantly from wrap end indicated by the increase of low surface strain region in Figure 6.37 at peak load (stage **C** – 349 kN). This localizes the fracture process at the end of the composite wrap such that debonding crack stops developing from the wrap root. At the rupture stage (stage **r** – 346 kN) the debonding crack consistently propagating from wrap end coalesces with the crack from the wrap root and leads to full debonding, see Figure 6-27.

In order to better illustrate the described failure progression, stresses at surface and the damage variable at the interface are analyzed from FEM. A path is defined in the middle of the brace surface starting at the free end of the composite wrap and ending at the root connection to the chord in DIC and in FE model to extract the principal strains along the debonding path which quantifies indirectly the debonding length, see Figure 6-21a) and b). A path is also defined in the middle of the primary bonded interface in the FE model in Figure 6-21c) to extract the scalar damage variable (CSDMG) explicitly determining the debonding length. The scaled principal strain in DIC and in FEM, as well as the CSDMG in the FE model are plotted together in Figure 6-28 in solid lines, short dashed lines and dashed lines, respectively, at the critical loading stages to quantify the debonding length. The principle strains at all the loading stages are scaled to the elastic stage (stage **A**) to eliminate the linear elastic increase of surface strains such that its local increase is merely attributed to debonding. The value of CSDMG equal to 0.913 corresponding to crack initiation in 5% characteristic CZM based on 3ENF test is used to identify the debonding crack front location in the FE model thus indicating the strain threshold on the surface corresponding to crack front in the FE model and in DIC. It can be seen in Figure 6-28 that the crack front at the root and end region is determined at the location where the scaled strain increases significantly from flat line to higher strain region while in the region with uniform wrap thickness the crack front is characterized by the threshold of scaled strain equal to 0.06%. The decrease of strain from the root region to the uniform region is steadier in FE model than in DIC, which can potentially be attributed to the differences in ply drops of the FE model and the specimen.

Development of debonding in the experiment and in the FEA is compared in Figure 6-29 with respect to the applied load level at the critical stages. It can be seen that the debonding length is almost identical in DIC and in FEA until stage **y** where less yielding strain on braces in the FE model leads to longer debonding length in FEA. Debonding stops propagating from wrap root once the load reaches stage **i_e** where crack is initiated from wrap end and significantly propagates until coalescence with root debonding crack. On the contrary, debonding crack from wrap root propagates consistently in FEA until reaching the wrap end possibly due to limited length of the crack propagating from the wrap end. It can be concluded that the FE model replicates the debonding process well in terms of the debonding rate and the critical debonding length. The only difference is that crack propagates consistently from wrap root in FEA while it stops in the experiment and coalesces with the crack developed from wrap end.

Based on the above-mentioned comparisons in surface strain distribution and debonding length development between the test and the FEA, it can be concluded that the FE model of small-scale 45° X joints is decently calibrated with used modeling strategies and the selected input parameters.

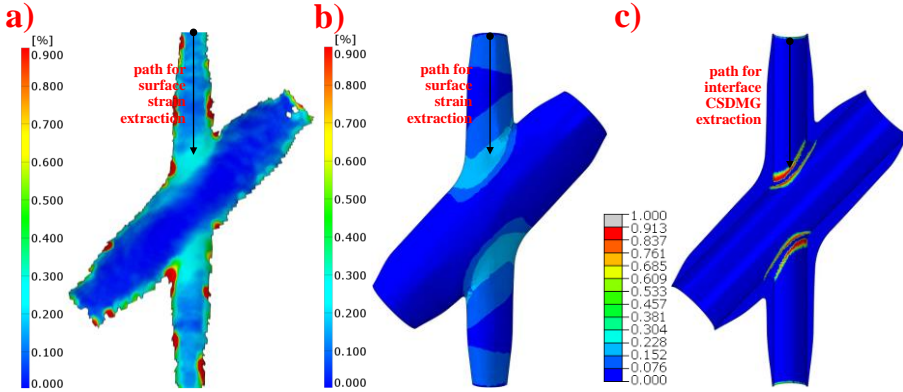


Figure 6-21 Surface strains at linear elastic stage (stage A – 170 kN) on a) test specimens and on b) FE model, and damage valuables of bonded interface of c) FE model indicating debonding length

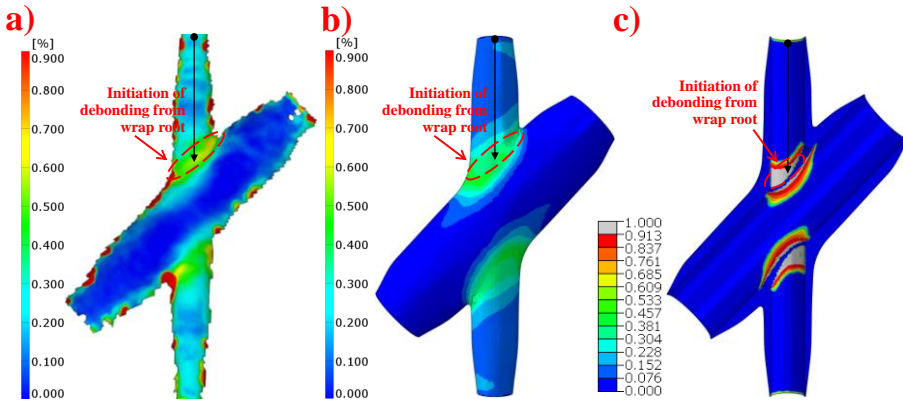


Figure 6-22 Surface strains at initiation of debonding from wrap root (stage i_r – 234kN) on a) test specimens and on b) FE model, and damage valuables of bonded interface of c) FE model indicating debonding length

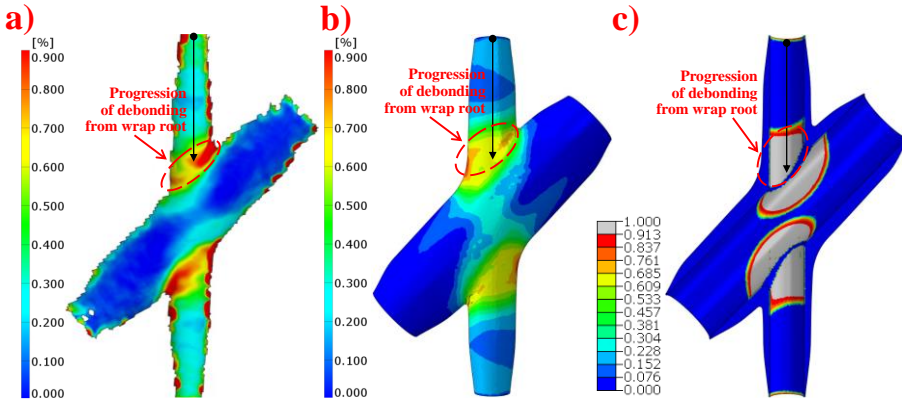


Figure 6-23 Surface strains at stage B – 289kN on a) test specimens and on b) FE model, and damage valuable of bonded interface of c) FE model indicating debonding length

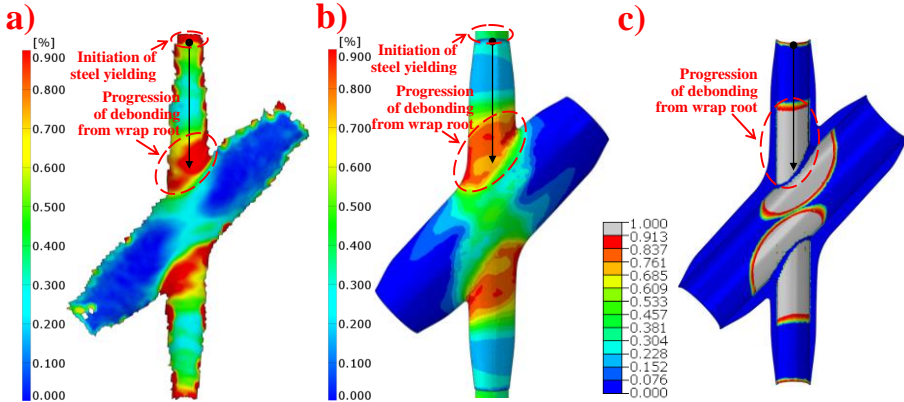


Figure 6-24 Surface strains at stage y – 321kN on a) test specimens and on b) FE model, and damage valuable of bonded interface of c) FE model indicating debonding length

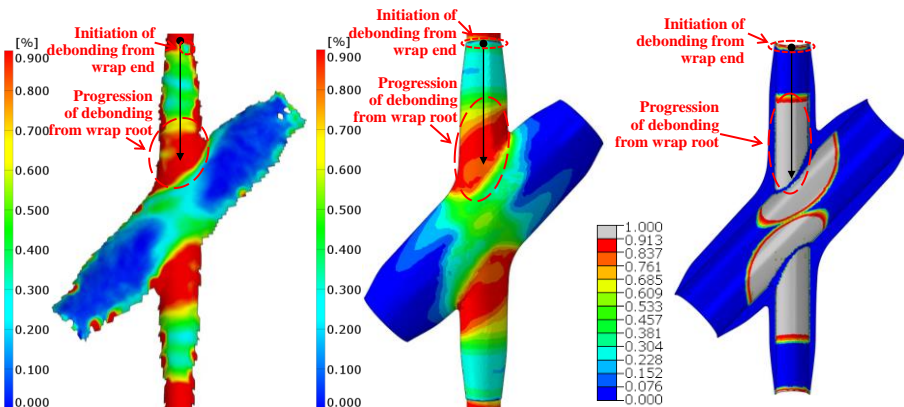


Figure 6-25 Surface strains at stage ie – 341kN on a) test specimens and on b) FE model, and damage valuable of bonded interface of c) FE model indicating debonding length

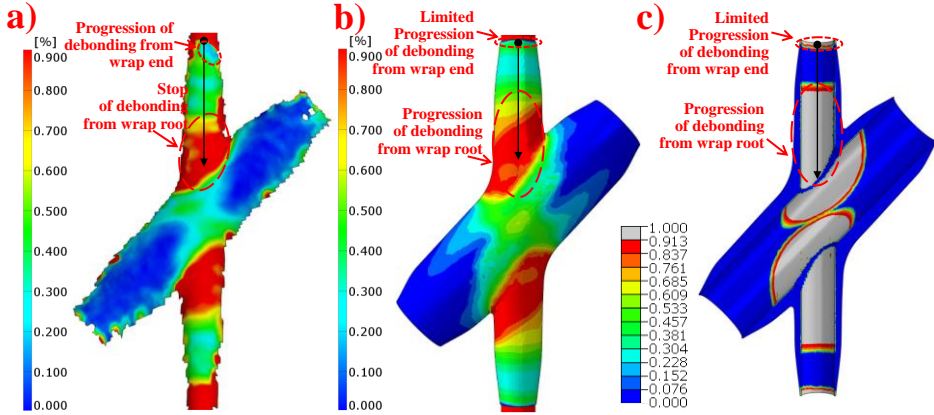


Figure 6-26 Surface strains of composite wrap at stage C – 349 / 347 kN on a) test specimens and on b) FE model, and damage valuable of bonded interface of c) FE model indicating debonding length

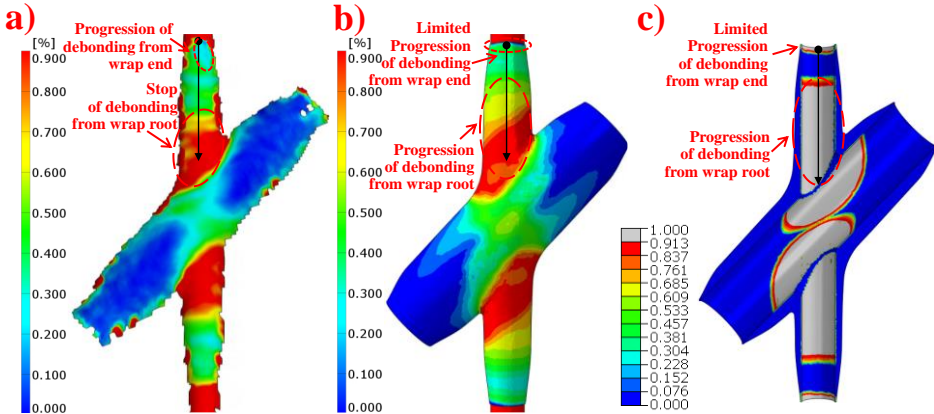


Figure 6-27 Surface strains of composite wrap at stage r – 346 kN on a) test specimens and on b) FE model, and damage valuable of bonded interface of c) FE model indicating debonding length

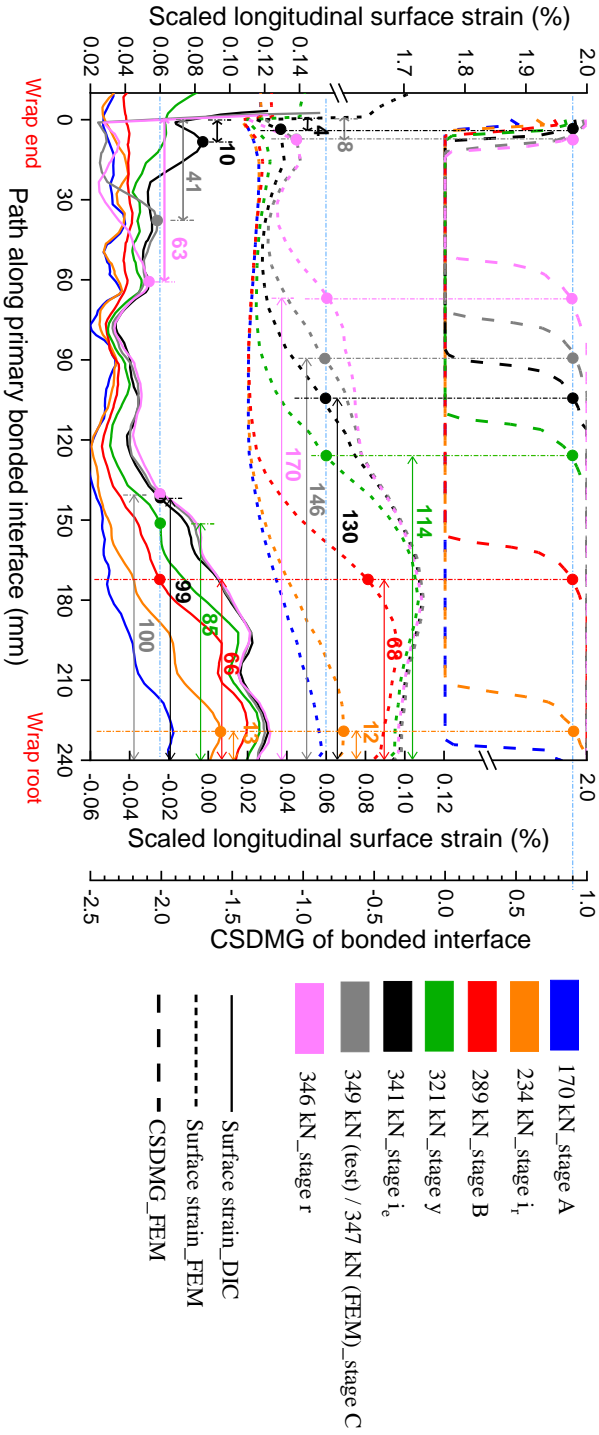


Figure 6-28 Scaled surface strains and the damage variable along the primary bonded interface at characteristic loading stages of small-scale 45° X-joints quantifying debonding length

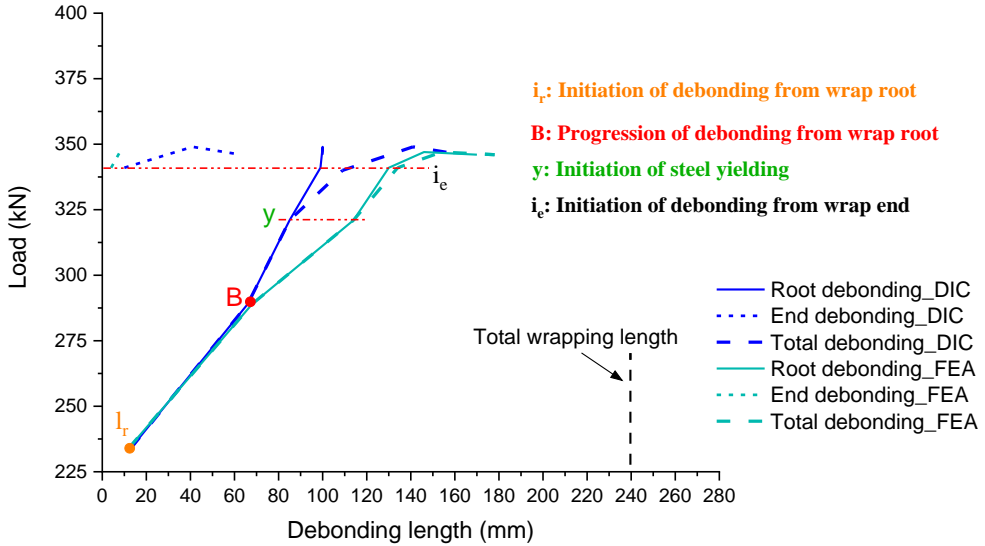


Figure 6-29 Comparison of debonding length growth in test and in FEM of small-scale 45° X joints

6.6.2.2 Failure process of experiment vs FEA in medium-scale 45° X joints

The load-displacement behavior in the FE model X45-Ms-T_FEM is compared to the behavior in specimen X45-Ms-T_S3 with critical stages marked with solid circles on the curves, as shown in Figure 6-30. It can be seen from Table 6-6 that the load and displacement values match quite well at the critical stages with the deviation all within 10% except the displacement at stage i_r due to the underestimation of debonding on the chord in the FE model, indicating the feasibility of the modeling strategy and the input parameters in the joint model.

Surface strains (principal strains) of specimen X45-Ms-T_S3 and the FE model X45-Ms-T_FEM at the marked stages in Figure 6-30 are shown in Figure 6-31~Figure 6-35 for comparison of debonding process where the damage variable output – CSDMG from FEA is also illustrated to visualize the debonding length on the bonded interface. The joint behaves elastic with low strain level distributed uniformly on the joint surface as shown in Figure 6-31 – stage A at 1000 kN. End of the elastic behavior is reached at approximately 1050 kN (stage i_e) attributed to plasticity of the traction-separation behavior of the bonded interface at the wrap root and the local bending of the composite wrap at the middle of the chord member. Debonding is initiated from wrap root of the primary bonded interface due to shear stress concentrations indicated by the localized increase of surface strains and the occurrence of damaged region at the wrap root shown in Figure 6-32 – stage i_r at 1106 kN. It can also be seen in Figure 6-32 that debonding on chord is overestimated by the FE model where the high strain region is much larger than in the DIC. This can be explained by the overestimation of the local bending of composite wrap in the model due to its limitation to simulate out-of-plane tension behavior of composite laminate. Luckily, the inaccuracy in modeling local bending of composite

wrap does not influence simulation of debonding crack on the primary bonded interface which propagates steadily with high strain region and the damaged area extending from wrap root at approximately 1570 kN – stage **y**, see Figure 6-33. At this stage yielding is initiated on braces outside the composite wrap and the yield strain increases significantly at 1618 kN – stage **B**. Different from the behavior in small-scale, in medium-scale joints the plastic strain on steel braces does not lead to initiation of debonding at wrap end while the debonding crack propagates consistently from wrap root in both test and FEM with comparable crack length, see Figure 6-34. When the applied load is increased to approximately 1650 kN – stage **r**, the debonding crack from wrap root reaches the critical value leading to full debonding, see Figure 6-35.

Similar to small-scale, in medium-scale a path is defined in the middle of the brace surface in DIC and in FE model as shown in Figure 6-31 a) and b) to extract the principal strains along the debonding path to indirectly quantify the debonding length. Another path is defined in the middle of the primary bonded interface of the model shown in Figure 6-31 c) to extract to scalar damage variable (CSDMG) determining the debonding length explicitly. The Scaled strain in DIC and in FEA, together with the CSDMG in the FE model along the debonding path at the critical stages are plotted together in Figure 6-36 in solid, short dashed and dashed lines, respectively. The principal strains at all stages are scaled to the elastic stage (stage **A**) to eliminate its elastic increase such that the local strain increase is merely due to debonding. The value of 0.913 in CSDMG is selected to identify the crack front location in FEA which corresponds to crack initiation state in 5% characteristic CZM based on 3ENF test. It can be seen in Figure 6-36 that the crack front at the wrap root is determine at the location where strains increase significantly from flat line to higher strain region while the threshold of scaled strain equal to 0.1% is used to determine the crack front outside the root region. The decrease of strain from the root region to the uniform region in FE model is more gradual than in DIC potentially due to differences in configuration of ply drops between the model and the specimen.

Development of debonding in the experiment and in the FEA is compared in Figure 6-37 with respect to the applied load level at the critical stages. It can be seen that in medium-scale the debonding length is almost identical in FEA and in DIC in every identical stage and the crack from wrap root propagates consistently without being initiated on the wrap end. In both DIC and FEA the debonding rate increase significantly after yielding of steel because it introduces peel stress to the bonded interface which would decrease the friction and therefore reduce the debonding resistance of the bonded interface.

Based on the aforementioned comparisons in terms of critical stages, surface strain distribution, debonding length and debonding rate between experiment and FEA, it can be concluded that the FE model of medium-scale 45° X joints is decently calibrated with feasible modeling strategies and the input parameters.

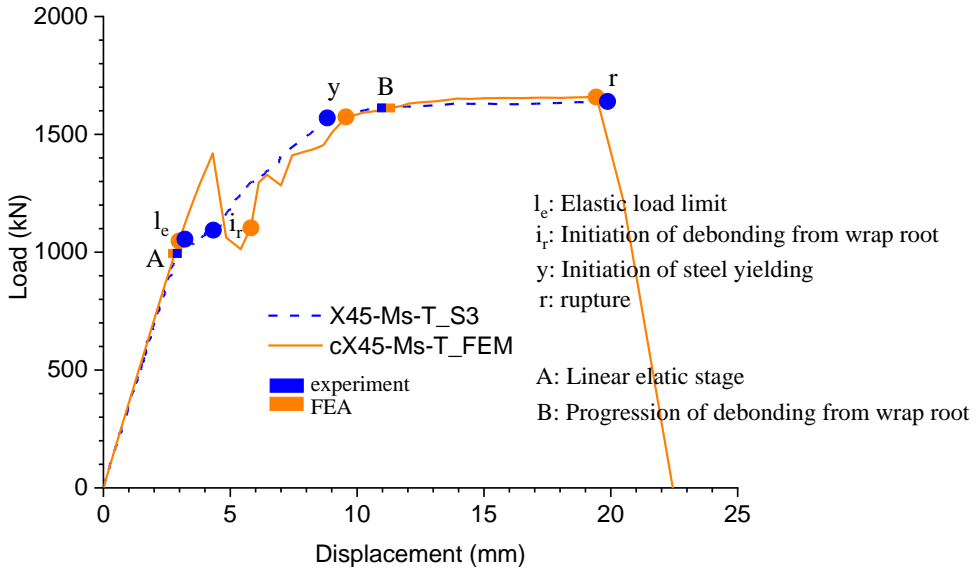


Figure 6-30 Load-displacement response of medium-scale 45° X joint in FE model vs in experiment

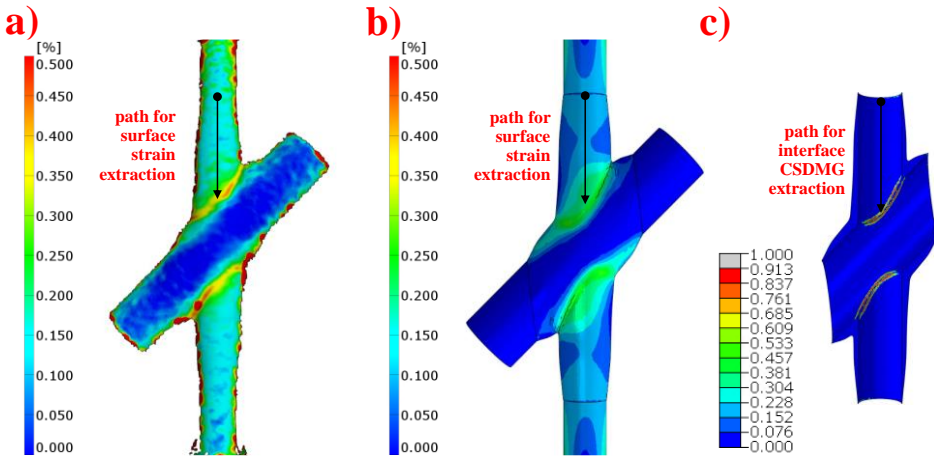


Figure 6-31 Surface strains at linear elastic stage (stage A – 1000 kN) on a) test specimens and on b) FE model, and damage valuable of bonded interface of c) FE model indicating debonding length

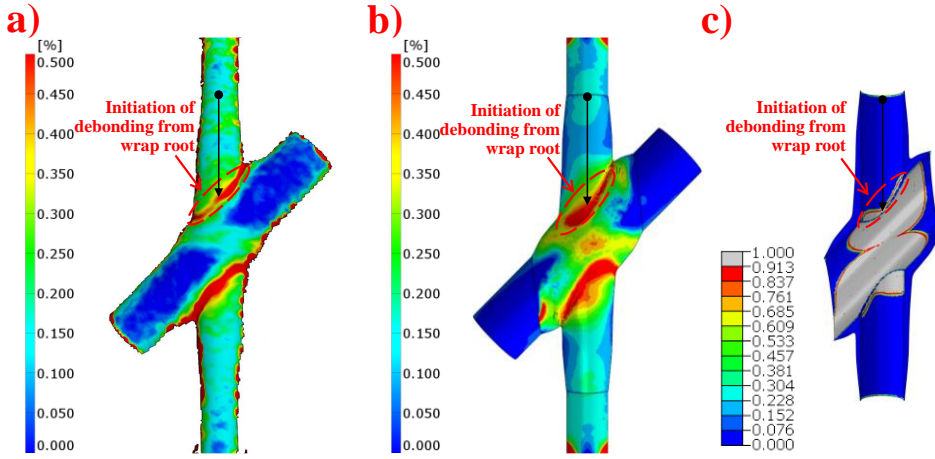


Figure 6-32 Surface strains at initiation of debonding from wrap root (stage i_r – 1106kN) on a) test specimens and on b) FE model, and damage valuable of bonded interface of c) FE model indicating debonding length

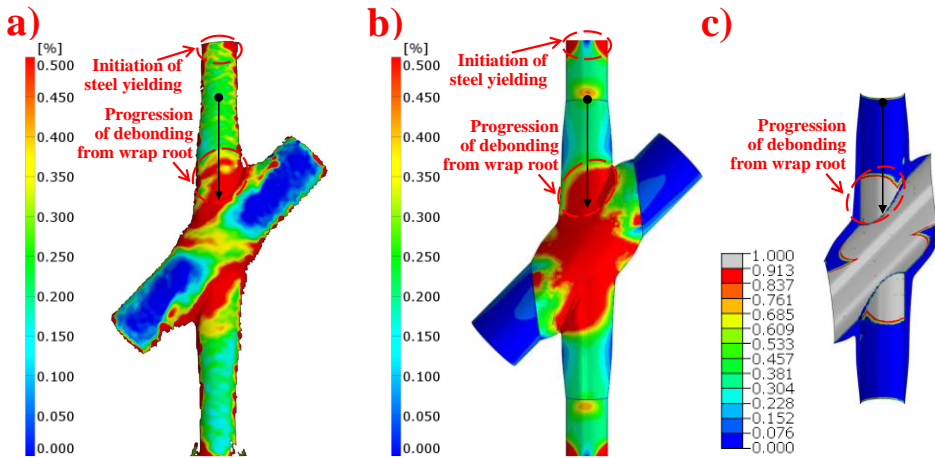


Figure 6-33 Surface strains at stage y – 1571 / 1579 kN on a) test specimens and on b) FE model, and damage valuable of bonded interface of c) FE model indicating debonding length

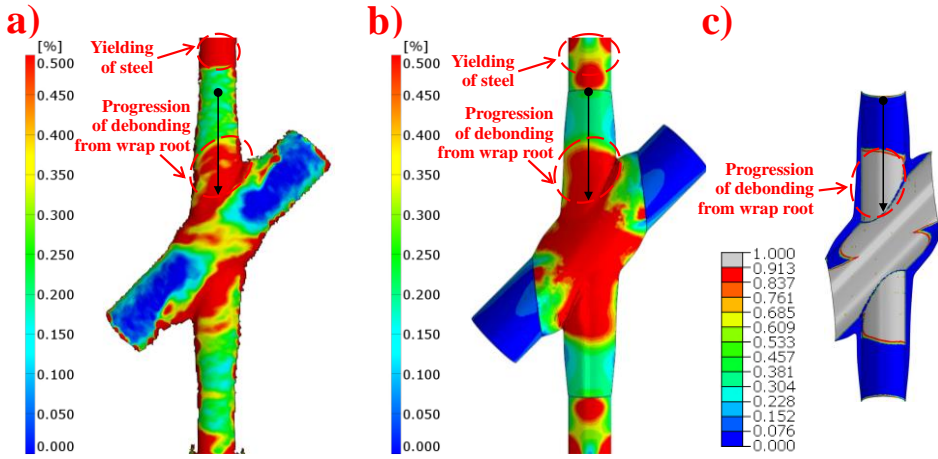


Figure 6-34 Surface strains of composite wrap at stage B – 1618 kN on a) test specimens and on b) FE model, and damage valuable of bonded interface of c) FE model indicating debonding length

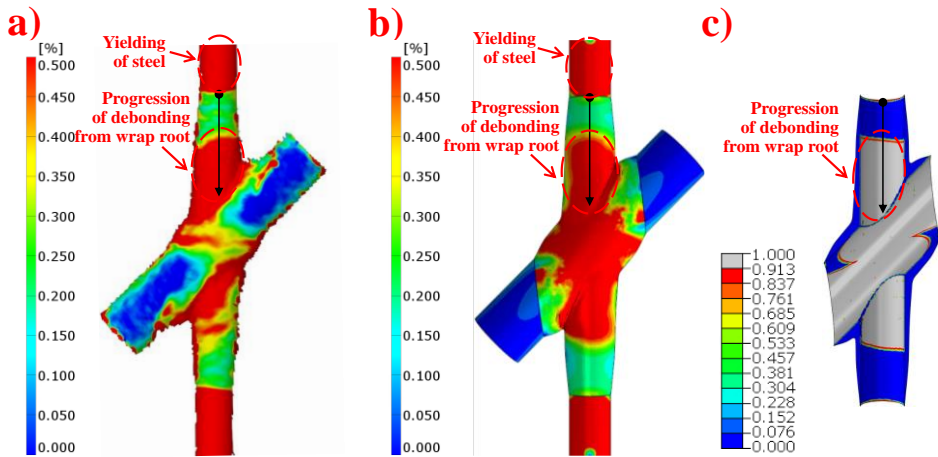


Figure 6-35 Surface strains of composite wrap at stage r – 1640 / 1659 kN on a) test specimens and on b) FE model, and damage valuable of bonded interface of c) FE model indicating debonding length

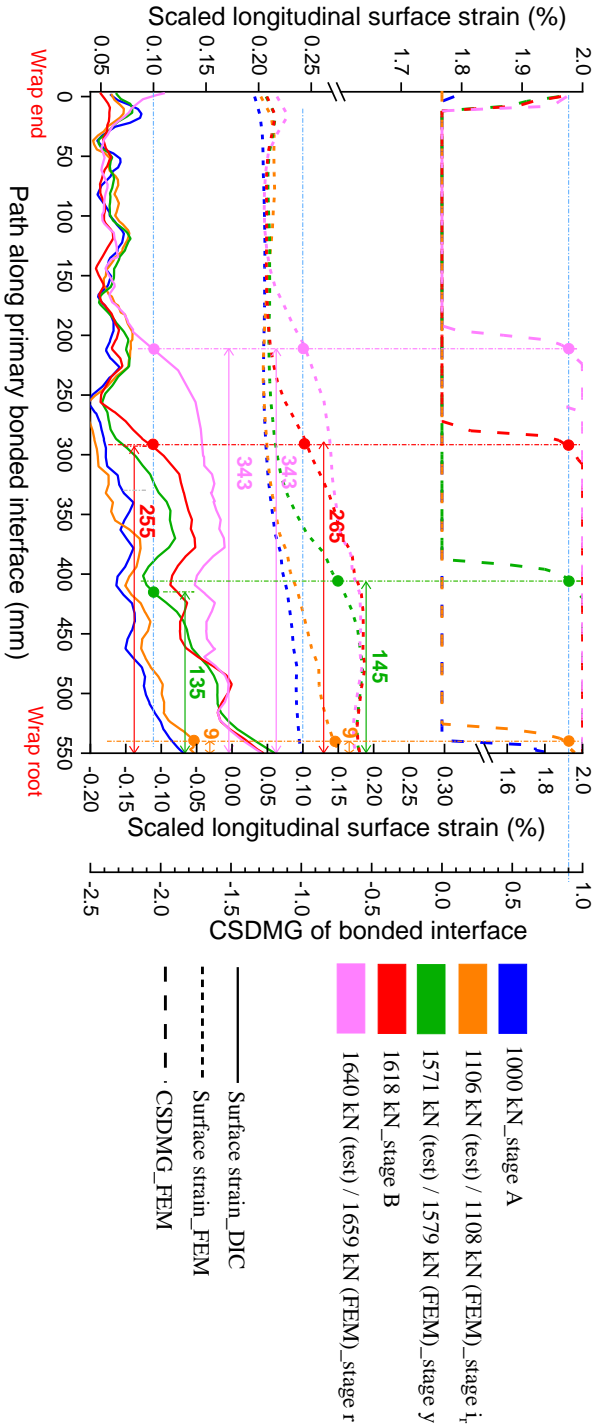


Figure 6-36 Scaled surface strains and the damage variable along the primary bonded interface at characteristic loading stages of medium-scale 45° X-joints quantifying debonding length

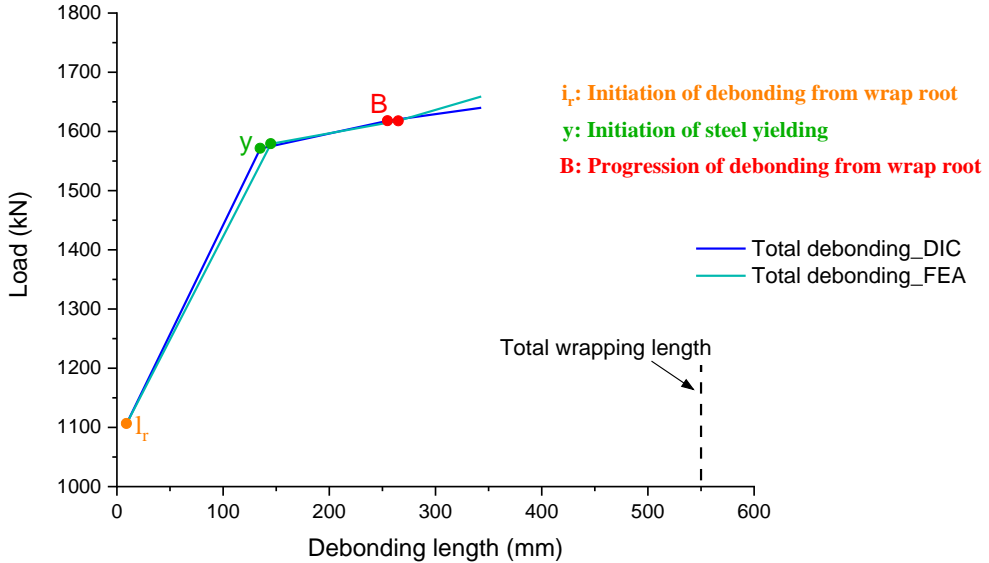


Figure 6-37 Comparison of debonding length growth in test and in FEM of medium-scale 45° X joints

6.7 Conclusions

In this Chapter, the modeling strategy and the input parameters in finite element modeling (FEM) of material and interface experiments in Chapter 5 are utilized in the joint FE models with certain changes. The joint models are validated by the good matches in terms of the global response and failure process to the small-scale and medium-scale 45° X-joints in tensile experiments presented in Chapter 3. The validated joint models gain insight into the failure process of debonding. In addition, sensitivity of joint global response to physical modeling input (CZM, COF) are investigated. The following conclusions are drawn as below:

1) The non-layered method is utilized in simulating composite wrap to avoid inputting inter-laminar fracture properties without sacrifice of the modeling accuracy considering no delamination occurred in the experiments. Variable mesh size of 4-node linear tetrahedral element (C3D4) defined by interior element growth is used in meshing composite wrap to reduce the computation cost without sacrifice of modeling accuracy, which is justified by analysis of mesh dependency.

2) The 5% characteristic cohesive zone model (CZM) obtained from 3ENF test is used in the joint modeling which considers the scatter of test data associated the number of tested specimens. It gives good matches in terms of progression of non-linearity behavior of load-displacement behavior after the initial stiffness starts to degrade.

3) Friction plays a significant role in enhancing debonding resistance of wrapped composite joints where normal pressure is applied on the bonded interface due to circumferential contraction of the composite wrap happens under tensile load under Poisson's ratio effect. The suitable value of the COF between the steel member and the

composite wrap is within 0.5~0.6 justified by COF test which gives good matches to the joint experiments in terms of ductility and ultimate resistance.

4) In wrapped composite 45° X-joints under tensile static load, debonding is initiated from wrap root and propagates along the brace which is considered as the primary bonded interface. Crack propagation rate increases when steel yielding happens on braces outside the composite wrap which introduces peel stress and decreases the fracture toughness of the bonded interface. If excessive plastic strain occurs on braces, debonding is initiated on wrap end and propagates significantly until coalescence with debonding crack from wrap root. If plastic strain is moderate on braces, debonding crack propagates consistently from wrap root until it reaches wrap end and leads to full debonding.

References

- [1] H. Herrmann and H. Bucksch, “Eurocode - Basis of structural design,” *Dict. Geotech. Eng. Geotech.*, vol. 3, no. 1, pp. 485–485, 2014, doi: 10.1007/978-3-642-41714-6_51753.
- [2] D. S. S. Corp., “ABAQUS/Explicit User’s Manual,” 2019.
- [3] R. K. Joki, F. Grytten, B. Hayman, and B. F. Sørensen, “A mixed mode cohesive model for FRP laminates incorporating large scale bridging behaviour,” *Eng. Fract. Mech.*, vol. 239, no. September 2019, p. 107274, 2020, doi: 10.1016/j.engfracmech.2020.107274.
- [4] R. K. Joki, F. Grytten, B. Hayman, and B. F. Sørensen, “Determination of a cohesive law for delamination modelling - Accounting for variation in crack opening and stress state across the test specimen width,” *Compos. Sci. Technol.*, vol. 128, pp. 49–57, 2016, doi: 10.1016/j.compscitech.2016.01.026.
- [5] A. Cameselle-Molares, A. P. Vassilopoulos, J. Renart, A. Turon, and T. Keller, “Numerical simulation of two-dimensional in-plane crack propagation in FRP laminates,” *Compos. Struct.*, vol. 200, no. April, pp. 396–407, 2018, doi: 10.1016/j.compstruct.2018.05.136.
- [6] M. Shahverdi, A. P. Vassilopoulos, and T. Keller, “Mixed-mode quasi-static failure criteria for adhesively-bonded pultruded GFRP joints,” *Compos. Part A Appl. Sci. Manuf.*, vol. 59, pp. 45–56, 2014, doi: 10.1016/j.compositesa.2013.12.007.
- [7] R. Ghanem, H. Owhadi, and D. Higdon, *Handbook of Uncertainty Quantification*. 2017. doi: 10.1007/978-3-319-12385-1.
- [8] A. Saltelli, “Making best use of model evaluations to compute sensitivity indices,” *Comput. Phys. Commun.*, vol. 145, no. 2, pp. 280–297, 2002, doi: 10.1016/S0010-4655(02)00280-1.
- [9] J. C. Helton, J. D. Johnson, C. J. Sallaberry, and C. B. Storlie, “Survey of sampling-based methods for uncertainty and sensitivity analysis,” *Reliab. Eng. Syst. Saf.*, vol. 91, no. 10–11, pp. 1175–1209, 2006, doi: 10.1016/j.ress.2005.11.017.
- [10] J. P. C. Kleijnen, “Sensitivity analysis and related analyses: A review of some statistical techniques,” *J. Stat. Comput. Simul.*, vol. 57, no. 1–4, pp. 111–142, 1997, doi: 10.1080/00949659708811805.
- [11] A. Saltelli, S. Tarantola, and F. Campolongo, “Sensitivity analysis as an ingredient of modeling,” *Stat. Sci.*, vol. 15, no. 4, pp. 377–395, 2000, doi: 10.1214/ss/1009213004.
- [12] I. Llavori, A. Zabala, A. Aginagalde, W. Tato, J. J. Ayerdi, and X. Gómez, “Critical Analysis of Coefficient of Friction Derivation Methods for Fretting under Gross Slip Regime,” *Tribol. Int.*, vol. 143, no. September 2019, 2020

7. PARAMETRIC STUDY

This chapter utilizes the validated modeling strategy and input parameters from joint modeling in Chapter 6 to reconstruct the 45° X-joint parametric study (PS) FE models in 4-scales. These models incorporate variations in interface properties and wrapping dimensions for a comprehensive parametric study. The investigation covers the influence of fracture toughness, wrapping length and thickness, as well as size effects. Based on parametric study results, a size effect law for the wrapped composite 45° X-joint is proposed which is based on the quasi-brittle size effects.

Furthermore, the mesh dependency of the joint modelling is analyzed to consider the effects of mesh typology, mesh geometric order, and mesh size.

7.1 Introduction

Validation of the modeling strategies of 45° X-joints by good matches to the joint test results in Chapter 6 gives the opportunity to perform parametric study and gives the design recommendations in terms of static resistance of wrapped composite joints. It has been found that there are two traction-separation laws in mode II of the composite-bonded interface attributed to the differences in quality of surface preparation. The cohesive law obtained from 3ENF test is used in simulation of the 45° X-joint experiments because of the nominally comparable surface preparation procedure. The cohesive law obtained from 4ENF test will be used in this Chapter because it matches production of the joints after the experimental campaign presented in this thesis with improved surface preparation to ensure more fiber bridging. It is important to quantify the influence of the interface properties on the static behavior of wrapped composite joints. On the other hand, yielding of steel braces is found in the joint experiments due to larger resistance of the bonded interface than expected. Its interaction with debonding makes it more difficult to conclude the debonding process with high level of independence. Therefore, in this chapter, linear elastic property of steel members is used in the joint model to exclude steel yielding and isolate behavior of debonding in parametric study.

Understanding size effect on the resistance of wrapped composite joints is the prerequisite for prediction of behavior of the full-scale joints. The thickness and length of composite wrap may vary in the future design to reach the balance between good resistance and expense saving. It is therefore necessary to investigate influence of wrapping length and wrapping thickness on the debonding behavior of wrapping composite joints. Therefore, parametric study into the influence of wrapping dimensions and joint size on the debonding behavior of wrapped composite 45° X-joints are conducted in this Chapter. Prior to the it, investigation into mesh dependency is indispensable because it helps reduce the computation cost in the upscaled model.

7.2 Overview of the analyzed parameters and the parametric study (PS) joint FE models

To conduct the aforementioned parametric study on static resistance of wrapped composite, this Chapter utilizes 4 parametric study (PS) joint FE models. These models are summarized in Table 7-1 and their respective geometries are shown in Figure 7-1. To understand the size effect on the debonding resistance, the joint configuration is designed with geometric similarity. The dimensions of the CHS members and composite wrap are upscaled by the size factor which is 1-4-8-12 in small-scale, medium-scale, large-scale and full-scale, respectively. The wrapping length factor f_{l_w} is 2.5 and the wrapping length is equal to the brace diameter multiplied by the wrapping length factor. The wrapping thickness is varying in the curved and complex wrap geometry, so it is described by the wrapping thickness factor f_{t_w} which is equal to 2. It means that the ratio of the current thickness of composite wrap over its reference thickness at any identical location in the joints is 2. The values of f_{l_w} and f_{t_w} will be changed in section 7.5 to investigate its influence on joint static behavior. Similar naming convention as in Chapter

6 is used here for PS FE models given in Table 7-1 and used afterwards in parametric study: cX45 – wrapped composite joint, X geometry at 45° angle; Ss, Ms, Ls, Fs – small-scale, medium-scale, large-scale and full-scale, respectively; x1, x4, x8, x12 – size factor in 4 scales.

Table 7-1 Overview of the PS FE models in parametric study of 45° X joints subjected to tensile load

Model description	Model name	Geometry in Figure number
small-scale 45° X-joint PS FE model	cX45-Ss-x1	Figure 7-1 a)
medium-scale 45° X-joint PS FE model	cX45-Ms-x4	Figure 7-1 b)
large-scale 45° X-joint PS FE model	cX45-Ls-x8	Figure 7-1 c)
full-scale 45° X-joint PS FE model	cX45-Fs-x12	Figure 7-1 d)

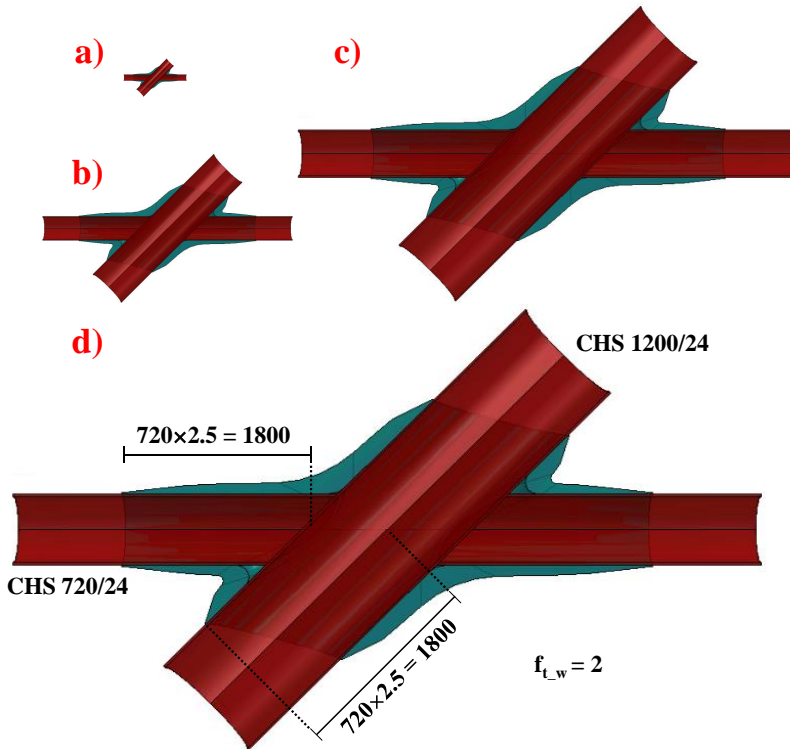


Figure 7-1 Geometries of PS FE models of wrapped composite 45° X joints in a) small-scale (x1); b) medium-scale (x4); c) large-scale (x8); d) full-scale (x12) with dimensions indicated in mm.

7.3 Mesh size and mesh type dependency analysis

The section 6.5 discusses the sensitivity of the static performance of wrapped composite joints to physical parameters, i.e., the fracture properties of the bonded

interface and the coefficient of friction (COF), which are related to the production quality. In this section the focus is on the sensitivity of the joint FEA results to the mesh set-up, a.k.a. mesh sensitivity or mesh dependency. Many researchers have conducted numerical investigation of mesh dependency for certain field of application [1]–[8] to a) help produce reliable results by FEM; b) improve effective decision making for quality product development cycle. The term mesh dependency is generally defined as the influence of element features including element type, mesh size, mesh topology and mesh geometric order, on the numerical outcome. As been discussed in Section 6.3.1, the tetrahedral element has been selected in FEM of wrapped composite joints attributed to the curved and complex shape of composite wrap. Therefore, the focus of the mesh dependency investigation of joint modeling is related to 1) mesh topology; 2) mesh size; and 3) mesh geometric order. In the mesh dependency analysis one of the PS FE models – cX45-Ms-x4, is used and loaded in monotonic tension.

7.3.1 Dependency on mesh topology

Mesh topology can be defined as the variation of node density [9], face orientation, etc., within the meshed object determining the way how the elements are structured and connected to each other. Two mesh strategies in terms of mesh topology are proposed as indicated in Section 6.3.1: 1) constant mesh size in composite wrap and 2) variable mesh size in composite wrap with definition of interior element growth. Figure 7-2 depicts the differences in the mesh topology in the PS FE model of medium-scale 45° X joints where Figure a) indicates the constant mesh size of 8 mm in the whole composite wrap and Figure b) shows the interior element growth in composite wrap where the mesh size is equal to the reference value of 8 mm close to the bonded interface and increased gradually to 32 mm until the outer surface. The load-displacement curves of the joint model with the two categories of mesh topology are compared in Figure 7-3. It can be seen that the two types of mesh topology lead to identical initial stiffness, and negligible differences in ultimate load resistance (3% deviation) and ductility (12% deviation). Figure 7-4 shows the plastic strain (PE) distribution in composite wrap at the ultimate load level where the model with constant mesh performs larger plastic deformation due to smaller size than the model with variable mesh size. Larger plastic deformation in composite wrap dissipates higher portion of energy from the loading system and requires more energy input to break the bonded interface completely leading to larger ultimate load and ductility. Considering the lower computational cost and slightly conservative values of the loading resistance for the purpose of investigating size effect, using variable mesh size with interior element growth is chosen as the optimum mesh topology in joint modeling.

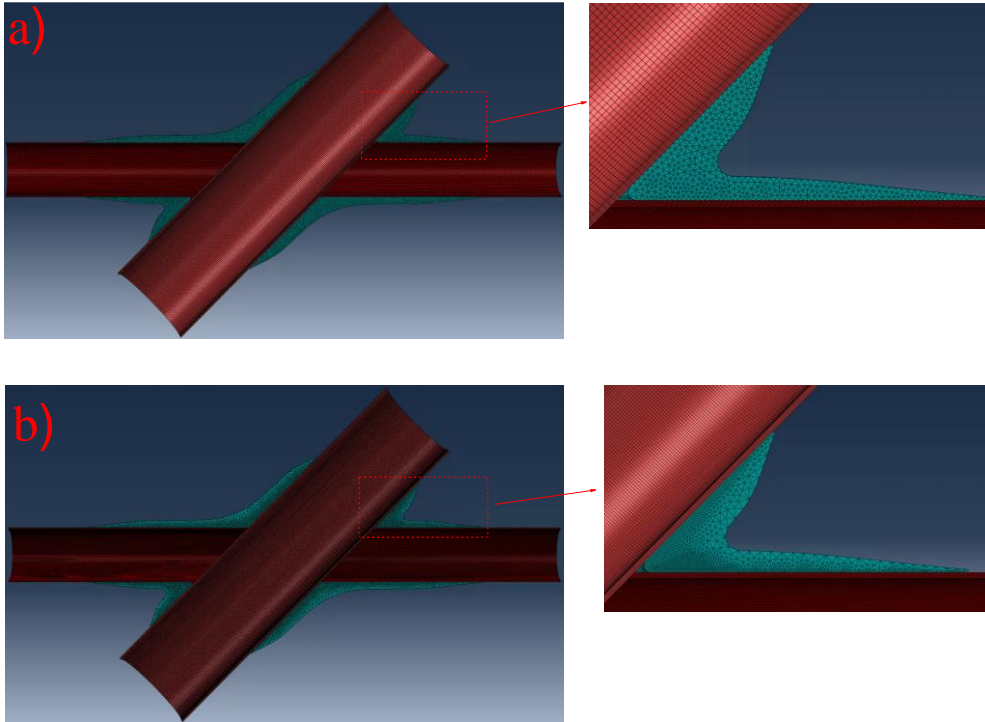


Figure 7-2 Two categories of mesh topology in PS FE model of medium-scale 45° X joints: a) constant mesh size in composite wrap; b) variable mesh size in composite wrap

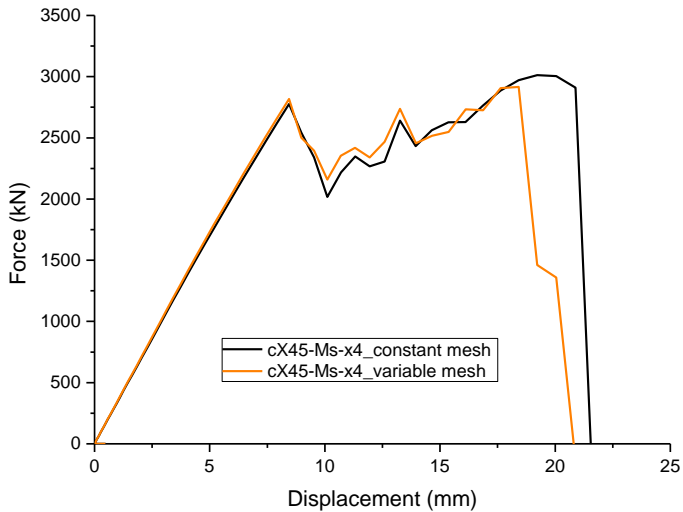


Figure 7-3 Load-displacement curves of PS FE model of medium-scale 45° X joints with constant mesh vs variable mesh in composite wrap

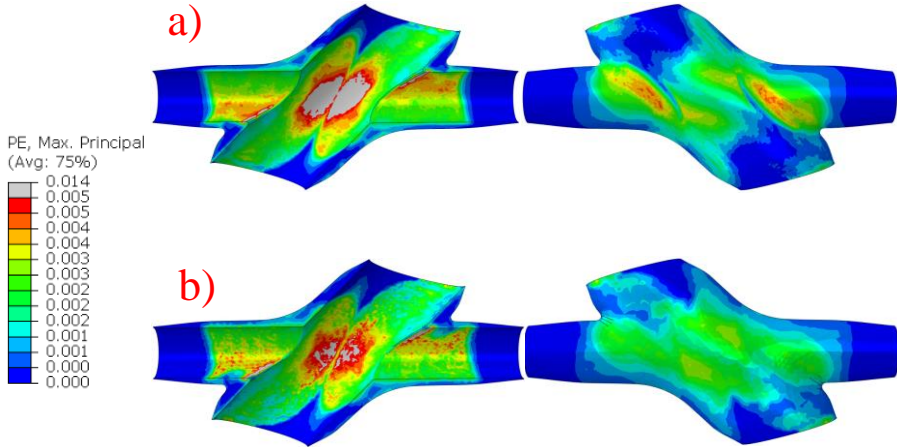


Figure 7-4 Plastic strain in composite wrap with a) constant mesh vs b) variable mesh at the ultimate load

7.3.2 Dependency on mesh geometric order

In finite element modeling the linear element is characterized by a linear shape function while in a quadratic element the displacements between the nodes are interpolated using a higher order polynomial. Quadratic element can represent curve edges and surfaces accurately but requires expensive computational cost compared to linear element. The quadratic elements have mid-side nodes and an element edge would consist of three nodes instead of two, as shown in Figure 7-5. To investigate the sensitivity of the joint behavior to geometric order of the element, the PS FE model cX45-Ms-x4 is used where the composite wrap is meshed with 4-node linear tetrahedral element (C3D4) and 10-node quadratic tetrahedral element (C3D10), respectively. The comparison of the load-displacement response of the joint model are illustrated in Figure 7-6 where linear element leads to less non-linearity, 12% lower ultimate load and 18% lower ductility. This can be explained in Figure 7-7 where the plastic strain is much larger in the composite wrap meshed with C3D10 element than meshed with C3D4 element. Accurate capture of the stress concentrations using C3D10 elements introduces more plasticity in composite wrap such that higher ultimate load and larger ductility is needed to break the bonded interface. Although the quadratic element represents more accurate stress distribution in composite wrap, it requires expensive computational cost. The focus of the FEA in the research is debonding of the bonded interface and no fracture of composite material is observed. Therefore, the nominal stress results from linear element are acceptable. Mesh with linear element also gives more conservative ultimate load resistance which is beneficial to investigation into size effect. Considering all the aspects discussed above, 4-node tetrahedral element (C3D4) is selected as the element type in the joint modeling.

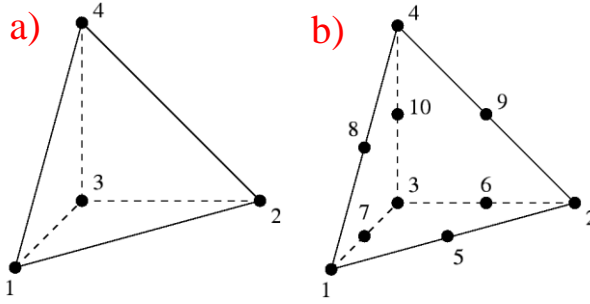


Figure 7-5 a): 4-node linear tetrahedral element (C3D4) vs b): 10-node quadratic tetrahedral element (C3D10)

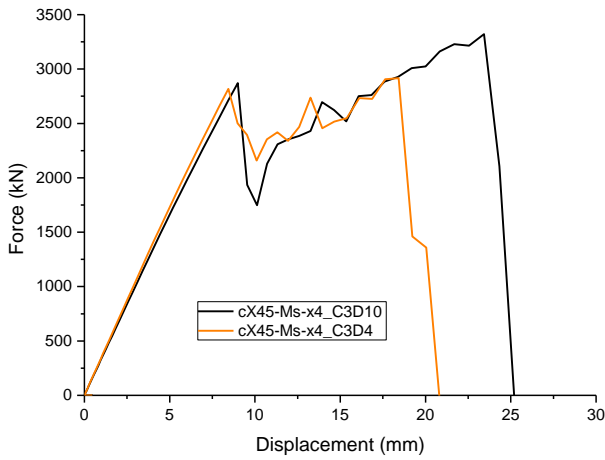


Figure 7-6 Load-displacement curves of PS FE model of medium-scale 45° X joints with linear mesh (C3D4) vs quadratic mesh (C3D10) in composite wrap

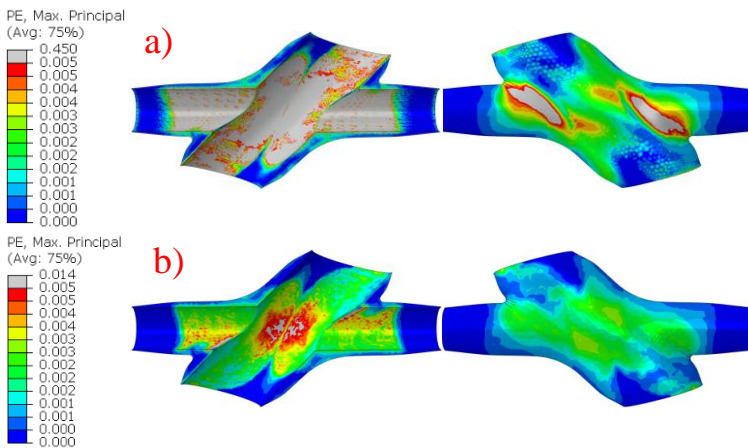


Figure 7-7 Plastic strain in composite wrap meshed with a) C3D10 vs b) C3D4 element

7.3.3 Dependency on mesh size

The dependency of the behavior of the joint model on mesh size can also be explained by the fact that differences in the plasticity of elements occur when changes in element size lead to variation of the intensity of stress concentrations. Changing from fine mesh to coarse mesh reduces the computational cost but decreases the modeling accuracy. The aim of mesh dependency study here is specifically to find the appropriate element size which increases the computational cost but still keeps reasonable accuracy. 3 sets of element size are used in the FE model of the cX45-Ms-x4 joint and are summarized in Table 7-2. The mesh size changes from fine mesh to coarse mesh by 2 times incrementally. Interior element growth is used in mesh of composite wrap where the element size close to the bonded interface is identical to size of steel element (identified as the reference mesh size) and increases gradually until by 4 times close to the outer surface. Figure 7-8 compares the load-displacement response of the joint model with the 3 reference mesh size. It can be seen that change of the mesh size has negligible influence on the initial stiffness and non-linearity of the joint but doubling the size would result in 4% decrease of ultimate load resistance and 8% reduce of ductility. This is consistent with the distribution of the plastic strain in composite wrap shown in Figure 7-9 at the ultimate load stage where smaller reference size leads to larger element plasticity such that larger external work is needed to break the bonded interface completely. It can be concluded that 8-mm reference size of element reduces the computational cost significantly and still gives acceptable modeling accuracy in terms of the debonding behavior. Therefore, it is selected as the optimal mesh size in the joint modeling.

Table 7-2 Set-up of element size used in mesh dependency analysis of the cX45-Ms-x4 joint

Number of mesh set-up	Reference element size (mm)	Element size of composites (mm)	Element size of steel (mm)	Computational cost (h)
1	2	2→8	2	17
2	4	4→16	4	5
3	8	8→32	8	1

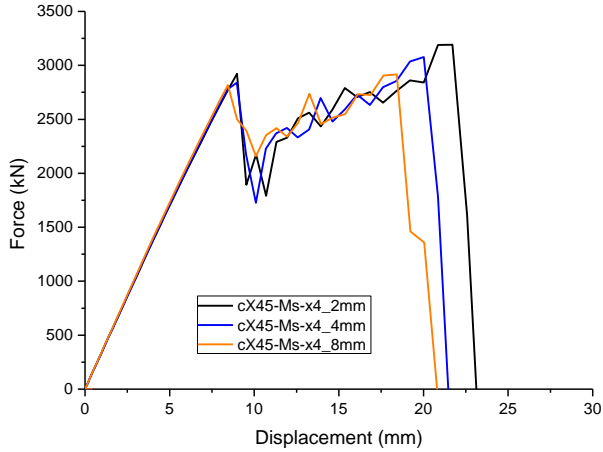


Figure 7-8 Load-displacement curves of PS FE model of medium-scale 45° X joints with reference mesh size equal to 2, 4, and 8 mm

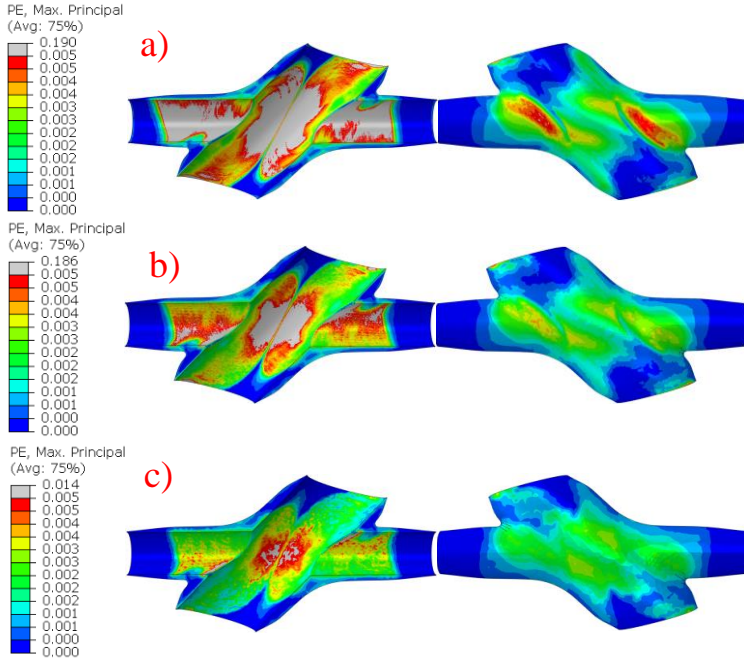


Figure 7-9 Plastic strain in composite wrap meshed with a) 2-mm; b) 4-mm and c) 8-mm reference size

In summary, 4-node linear tetrahedral (C3D4) elements with coarser mesh size varied with interior element growth is selected as the optimum mesh strategy in modeling of wrapped composite joints. It helps save computational time considerably without sacrifice in modeling initial stiffness and elastic load limit of the joints. Differences in the ultimate load and ductility are found, but they fall within a limited range. Moreover, using the optimum mesh strategy gives more conservative numerical results. Therefore,

it is used in the parametric study in this chapter.

7.4 Influence of interface properties

Based on the results of mesh dependency analysis in the previous section, the C3D4 element will be used in the parametric study with finer mesh on the bonded interface gradually increasing to coarser mesh on the outer surface by 4 times. It should be noted that the steel is simulated with linear elastic behavior in the parametric study to eliminate the influence of steel yielding on the joint resistance. The COF value equal to 0.55 is used based on the results from section 6.5.2. In this section, the 5% characteristic CZM based on 3ENF and 4ENF test are compared in each scale to quantify influence of the surface preparation on the joint static behavior. The critical parameters of the PS FE models are summarized in Table 7-3. The 5% characteristic cohesive laws in mode I and mode II based on the 3ENF production batch and the DCB/4ENF production batch are compared in Figure 7-10 and Figure 7-11. The corresponding cohesive parameters at the critical stages are summarized in Table 7-4. The comparison of the load-displacement response of the joints with cohesive laws from the two production batches in 4 scales are illustrated in Figure 7-12 and the ultimate resistance and the failure displacement are compared in Table 7-5. It can be concluded that 2.5 times larger fracture toughness at crack propagation leads to 30~50% larger load resistance and 40~70% larger ductility in all 4 scales. Therefore, the surface preparation especially the steel roughness is essential for the load resistance of wrapped composite joints.

Table 7-3 Overview of critical parameters in PS FE models of 45° X-joints

FE model name	Composite mesh size (mm)	COF	CZM
cX45-Ss-x1_5% 3ENF	2→8	0.55	5% char. 3ENF
cX45-Ss-x1_5% 4ENF			5% char. 4ENF
cX45-Ms-x4_5% 3ENF	8→32		5% char. 3ENF
cX45-Ms-x4_5% 4ENF			5% char. 4ENF
cX45-Ls-x8_5% 3ENF	16→64		5% char. 3ENF
cX45-Ls-x8_5% 4ENF			5% char. 4ENF
cX45-Fs-x12_5% 3ENF	24→96		5% char. 3ENF
cX45-Fs-x12_5% 4ENF			5% char. 4ENF

Table 7-4 5% characteristic values of critical cohesive parameters in mode I and mode II of two production batches

Prod. batch	Values	Onset of plasticity - stage "p"		Onset of cracking - stage "c"		Onset of fiber bridging - stage "b"		Failure - stage "f"		Critical SERR	
		δ_p (mm)	σ_p (MPa)	δ_c (mm)	σ_c (MPa)	δ_b (mm)	σ_b (MPa)	δ_f (mm)	σ_f (MPa)	$G_{Ic,tip}$ (N/mm)	G_{Ic} (N/mm)
3ENF	Mode I	0.0015	14.67	0.012	14.67	0.054	1.47	0.394	0	0.17	0.76
	Mode II	0.0015	14.67	0.025	22	0.069	22	0.087	0	0.45	1.6
Prod. batch	Values	δ_p (mm)	σ_p (MPa)	δ_c (mm)	σ_c (MPa)	δ_b (mm)	σ_b (MPa)	δ_f (mm)	σ_f (MPa)	$G_{IIc,tip}$ (N/mm)	G_{IIc} (N/mm)
DCB/	Mode I	0.002	20	0.015	20	0.04	2	0.687	0	0.27	1.23
4ENF	Mode II	0.002	20	0.026	30	0.089	30	0.190	0	0.61	4.03

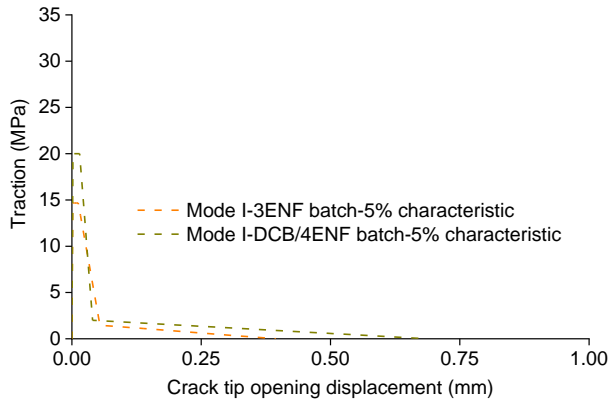


Figure 7-10 Mode I cohesive law with 5% characteristic fracture properties in 3ENF batch vs DCB/4ENF batch

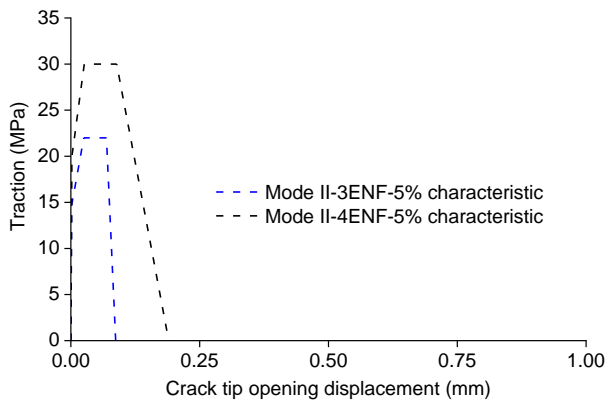
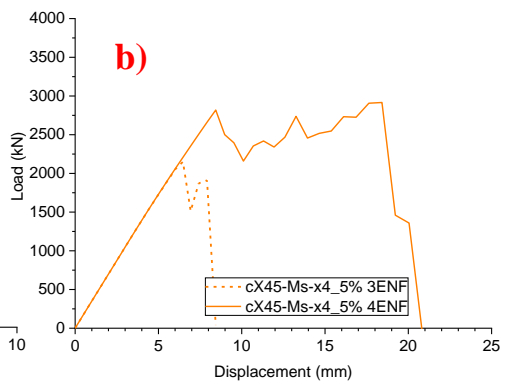
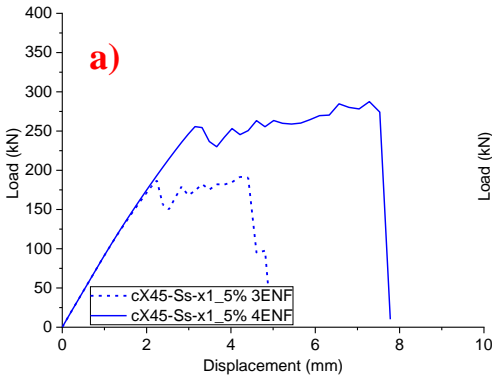


Figure 7-11 Mode II cohesive law with 5% characteristic fracture properties in 3ENF batch vs DCB/4ENF batch

Table 7-5 Comparison of global behavior of the joint with 5% characteristic 3ENF CZM vs 5% characteristic 4ENF CZM in 4 scales

FE model name	Ultimate load (kN)	Failure displacement (mm)
cX45-Ss-x1_5% 3ENF	191	4.4
cX45-Ss-x1_5% 4ENF	274	7.5
Increase of performance (%)	43	70
cX45-Ms-x4_5% 3ENF	1910	7.9
cX45-Ms-x4_5% 4ENF	2916	18.4
Increase of performance (%)	53	133
cX45-Ls-x8_5% 3ENF	6562	20.2
cX45-Ls-x8_5% 4ENF	9593	29.3
Increase of performance (%)	46	45
cX45-Fs-x12_5% 3ENF	13751	26.6
cX45-Fs-x12_5% 4ENF	18215	37.0
Increase of performance (%)	32	39



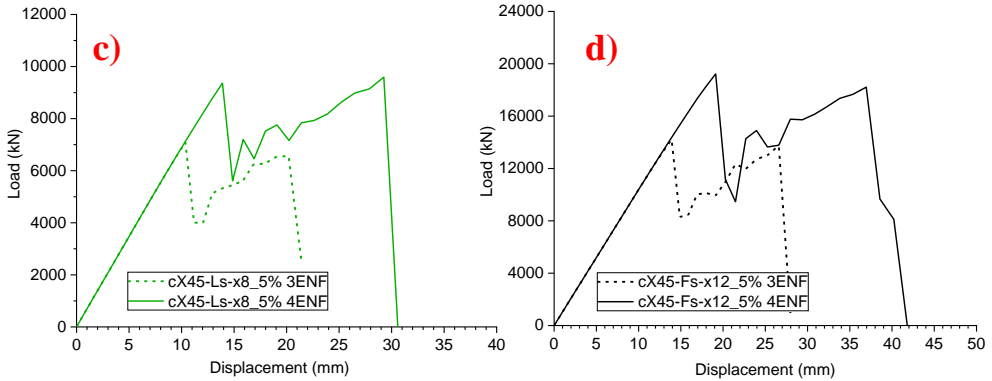


Figure 7-12 Load-displacement of joint models with 5% characteristic 3ENF CZM vs 5% characteristic 4ENF CZM in a) small-scale; b) medium-scale; c) large-scale and d) full-scale.

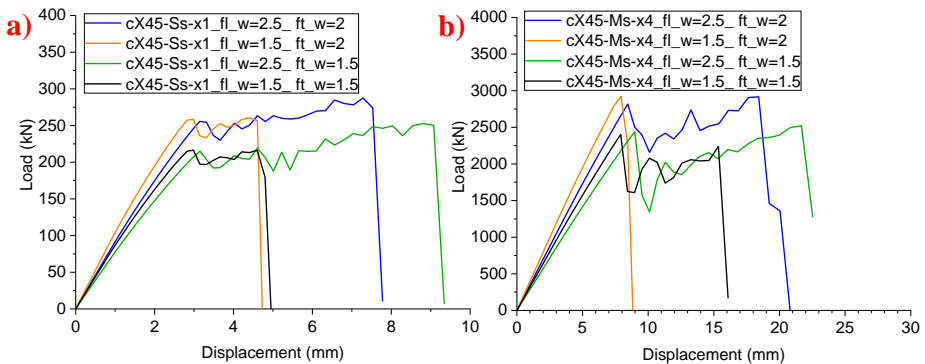
7.5 Influence of wrapping dimensions

In order to investigate the influence of wrapping length and wrapping thickness on the static behavior of wrapped composite joints, two values of wrapping length factor f_{l_w} (1.5 and 2.5) and of wrapping thickness factor f_{t_w} (1.5 and 2) are used in the PS FE models in 4 scales. It should be noted that the interface properties used in this section are based on the 5% characteristic 4ENF CZM and COF = 0.55. The comparison of the load-displacement response of the joints with different wrapping dimensions in 4 scales is illustrated in Figure 7-13 and the ultimate resistance and the failure displacement are compared in Table 7-6.

It can be seen that reducing the wrapping length on brace by 40% leads to significant decrease of the failure displacement by approximately 10~50% accompanied by slight reduction of the ultimate load within 10%. On the other hand, 25% thinner composite wrap results in 10~30% reduction of the ultimate load while the change of failure displacement in the majority of cases is within 10%. Therefore, the joint ultimate load is sensitive to the wrapping thickness while the joint failure displacement is highly dependent on the wrapping length. The possible reason is that more energy from the loading system is dissipated by out-of-plane shear plastic deformation of composite wrap with larger thickness in a certain cross-section of the joint, therefore larger ultimate load can be reached. Conversely, smaller failure displacement is found in the joint with shorter wrapping length because it reduces the length available for the crack to propagate on the braces during the debonding process. Reduction of ultimate load in this case is limited because energy dissipation in the cross-section of the joint does not alter since the thickness of composite wrap does not change.

Table 7-6 Comparison of global behavior of the joint models with different wrapping dimensions

FE model name	Ultimate load (kN)	Failure disp. (mm)
cX45-Ss-x1_f _{l_w} =2.5_f _{t_w} =2	274	7.5
cX45-Ss-x1_f _{l_w} =1.5_f _{t_w} =2	257	4.6
cX45-Ss-x1_f _{l_w} =2.5_f _{t_w} =1.5	250	9.1
cX45-Ss-x1_f _{l_w} =1.5_f _{t_w} =1.5	216	4.6
cX45-Ms-x4_f _{l_w} =2.5_f _{t_w} =2	2916	18.4
cX45-Ms-x4_f _{l_w} =1.5_f _{t_w} =2	-	-
cX45-Ms-x4_f _{l_w} =2.5_f _{t_w} =1.5	2520	21.7
cX45-Ms-x4_f _{l_w} =1.5_f _{t_w} =1.5	2239	15.4
cX45-Ls-x8_f _{l_w} =2.5_f _{t_w} =2	9593	29.3
cX45-Ls-x8_f _{l_w} =1.5_f _{t_w} =2	8544	23.9
cX45-Ls-x8_f _{l_w} =2.5_f _{t_w} =1.5	7556	32.2
cX45-Ls-x8_f _{l_w} =1.5_f _{t_w} =1.5	6990	26.5
cX45-Fs-x12_f _{l_w} =2.5_f _{t_w} =2	18215	37.0
cX45-Fs-x12_f _{l_w} =1.5_f _{t_w} =2	16203	29.2
cX45-Fs-x12_f _{l_w} =2.5_f _{t_w} =1.5	13454	35.3
cX45-Fs-x12_f _{l_w} =1.5_f _{t_w} =1.5	13501	32.2



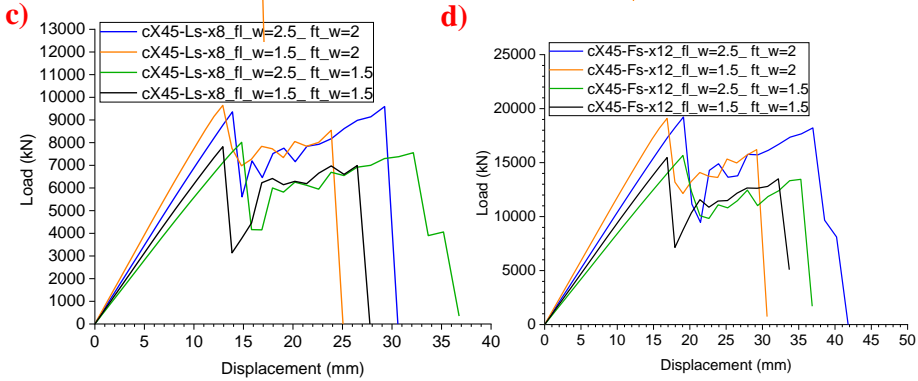


Figure 7-13 Load-displacement response of joint models with different wrapping dimensions in a) small-scale; b) medium-scale; c) large-scale and d) full-scale

7.6 Influence of the scale of the joint – Size effect

The energetic (deterministic) size effect on behavior of wrapped composite 45° X-joints is discussed in this section using the PS FE models in 4 geometric scales: small-scale, medium-scale, large-scale and full-scale. The wrapping length factor f_{l_w} is 2.5 and the wrapping thickness factor f_{t_w} is 2 in this analysis, with CZM based on the 5% characteristic 4ENF test and $COF = 0.55$. The load-displacement response of the joint models in 4 scales are illustrated in Figure 7-14 where the F_i and F_u refers to the load level at initiation of debonding on the secondary bonded interface and at the full debonding on the primary bonded interface, respectively. The sudden load drop after F_i is due to debonding on the chord which is followed by the consistent increase of load level corresponding to debonding on the brace, as explained in section 6.6. The values of F_i and F_u in all 4 scales are summarized in Table 7-7. To investigate the size effect on the full debonding resistance, F_u is considered here for further discussion. The general form of the quasi-brittle size effect law can be expressed by Equation 7-1 [10], [11]. It describe the relation of the nominal strength σ_N against the structural size D . σ_0 are the strength limit, and D_0 is the transitional size at which the power laws of plasticity and LEFM intersect [10]–[12]. In the current discussion, the nominal strength is defined as the brace nominal stress $\sigma_N = F_u/A_b$ where A_b refers to the cross-section area of the brace member, and D is defined as the brace diameter. Figure 7-15 illustrates the relation of σ_N and D with logarithmic scale, where the analytical equation of the size-effect law is derived by curve fitting to the FEA data and is shown in Equation 7-2. It indicates that $\sigma_0 = 820$ MPa and the transitional size $D_0 = 155$ mm. It can be clearly seen in Figure 7-15 that full debonding failure of wrapping composite joint follows the quasi-brittle size effect which can be considered for the bridging of plasticity and LEFM.

$$\sigma_N = \sigma_0 \left(1 + \frac{D}{D_0}\right)^{-\frac{1}{2}} \tag{Equation 7-1}$$

$$\sigma_N = 820 \times \left(1 + \frac{D}{155}\right)^{-\frac{1}{2}} \tag{Equation 7-2}$$

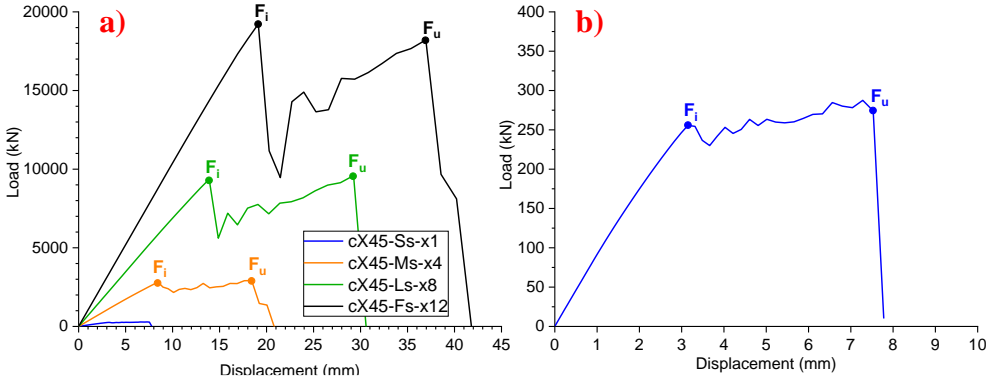


Figure 7-14 a) Load-displacement behavior of 45° X-joint models in 4 scales; b) Zoom-in view of load-displacement response in small-scale

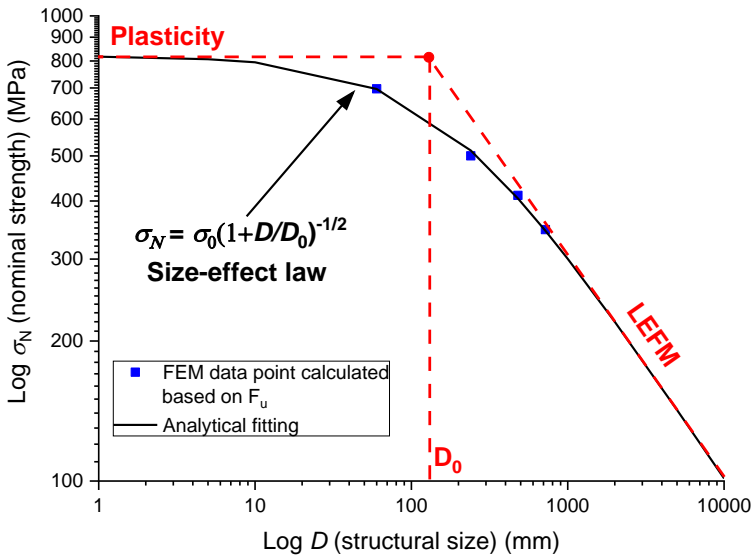
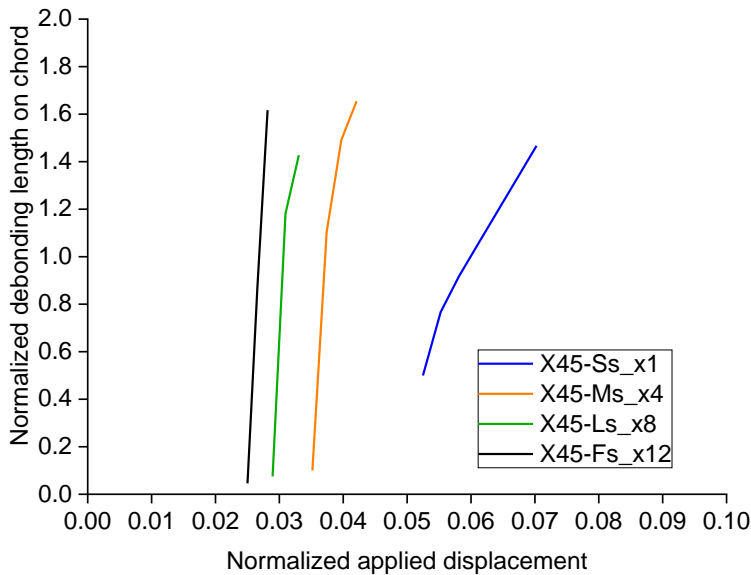


Figure 7-15 Size-effect law of wrapped composite 45° X-joints fitted with the FEM data based on 4 scales

Table 7-7 Summary of F_i and F_u values in PS FE models in 4 scales

PS FE model name	F_i (kN)	F_u (kN)
cX45-Ss-x1	254	274
cX45-Ms-x4	2819	2916
cX45-Ls-x8	9360	9593
cX45-Fs-x12	19225	18215

Except the above-mentioned size effect on the global response of wrapped composite joints, the dependency of local behavior on structural size is also investigated. It can be seen in Figure 7-14 that the load drop after F_i is more sudden when the structural size increases, indicating that debonding on chord is more instantly in larger scale. To quantify this change, the debonding rate on chord in 4 scales are compared in Figure 7-16 where the applied displacement and the debonding length on chord are normalized by the brace diameter in each scale. It can be seen that the debonding rate increases significantly from small-scale to medium-scale and slightly increases further to full-scale.

**Figure 7-16 Comparison of Debonding rate on chord in 4 scales**

7.7 Conclusions

In this Chapter, the validated modeling strategy and the input parameters in joint modeling in Chapter 6 are utilized to build the 45° X-joint PS FE models in 4-scales with variation of interface properties and wrapping dimensions for parametric study. The aim is to investigate the influence of properties of the bonded interface, mesh, geometric size and the wrapping dimensions on the static behavior of 45° X-joints subjected to tensile load. Based on the FEA results, the following conclusions can be drawn:

1) The load resistance of the full-scale joint with brace diameter of 720 mm is approximately 19000 kN. The size-effect law of 45° X-joints is proposed which is based on the quasi-brittle size effects.

2) Reducing wrapping length on the brace by 40% leads to a decrease in the failure displacement by approximately 50% in small-scale joints and 10% in full-scale joints. On the other hand, reducing wrapping thickness by 25% results in an approximately 10% reduction in ultimate load for small-scale joints and 30% for full-scale joints.

3) The load resistance of wrapped composite joints is strongly dependent on the fracture toughness of the bonded interface. 2.5 times larger fracture toughness provided by softening and fiber bridging at crack propagation in mode II leads to 30~50% larger load resistance and 40~70% larger ductility of wrapped composite joints in 4 scales.

4) In the case of debonding analysis using CZM, 4-node linear tetrahedral (C3D4) element can be used to mesh composite wrap with varied element size compared to uniform fine mesh to saving the computation cost without sacrificing the simulation accuracy. The global mesh size can be increased with the structural size of the joint.

References

- [1] Z. P. Bazant, “Imbricate continuum and progressive fracturing of concrete and geomaterials,” *Meccanica*, vol. 19, pp. 86–93, 1984, doi: 10.1007/BF01558458.
- [2] M. G. A. Tijssens, B. L. J. Sluys, and E. Van der Giessen, “Numerical simulation of quasi-brittle fracture using damaging cohesive surfaces,” *Eur. J. Mech. A/Solids*, vol. 19, no. 5, pp. 761–779, 2000, doi: 10.1016/S0997-7538(00)00190-X.
- [3] R. de Borst, “Numerical aspects of cohesive-zone models,” *Eng. Fract. Mech.*, vol. 70, no. 14, pp. 1743–1757, 2003, doi: 10.1016/S0013-7944(03)00122-X.
- [4] F. Zhou and J. F. Molinari, “Dynamic crack propagation with cohesive elements: A methodology to address mesh dependency,” *Int. J. Numer. Methods Eng.*, vol. 59, no. 1, pp. 1–24, 2004, doi: 10.1002/nme.857.
- [5] R. de Borst, J. J. C. Remmers, and A. Needleman, “Mesh-independent discrete numerical representations of cohesive-zone models,” *Eng. Fract. Mech.*, vol. 73, no. 2, pp. 160–177, 2006, doi: 10.1016/j.engfracmech.2005.05.007.
- [6] D. Xie and A. M. Waas, “Discrete cohesive zone model for mixed-mode fracture using finite element analysis,” *Eng. Fract. Mech.*, vol. 73, no. 13, pp. 1783–1796, 2006, doi: 10.1016/j.engfracmech.2006.03.006.
- [7] B. Lopes, M. R. T. Arruda, L. Almeida-Fernandes, L. Castro, N. Silvestre, and J. R. Correia, “Assessment of mesh dependency in the numerical simulation of compact tension tests for orthotropic materials,” *Compos. Part C Open Access*, vol. 1, no. July, p. 100006, 2020, doi: 10.1016/j.jcomc.2020.100006.
- [8] L. Guo, J. Xiang, J. P. Latham, and B. Izzuddin, “A numerical investigation of mesh sensitivity for a new three-dimensional fracture model within the combined finite-discrete element method,” *Eng. Fract. Mech.*, vol. 151, pp. 70–91, 2016, doi: 10.1016/j.engfracmech.2015.11.006.
- [9] K. Ho-Le, “Finite element mesh generation methods: a review and classification,” *Comput. Des.*, vol. 20, no. 1, pp. 27–38, 1988, doi: 10.1016/0010-4485(88)90138-8.
- [10] Z. P. Bažant, “Size effect on structural strength: a review,” *Arch. Appl. Mech.*, vol. 69, 1999.
- [11] Q. Yu *et al.*, “Scaling of strength of metal-composite joints-Part I: Experimental investigation,” *J. Appl. Mech. Trans. ASME*, vol. 77, no. 1, pp. 1–8, 2010, doi: 10.1115/1.3172254.
- [12] Z. P. Bažant, “Size Effect in Blunt Fracture: Concrete, Rock, Metal,” *J. Eng. Mech.*, vol. 110, no. 4, pp. 518–535, 1984, doi: 10.1061/(asce)0733-9399(1984)110:4(518).

8. CONCLUSIONS AND FUTURE WORK

This chapter offers a concise overview of this dissertation. The main conclusions are summarized for the research questions proposed in Chapter 1. Additionally, recommendations are presented for future work endeavors, with a specific emphasis on investigating multi-planar loading behavior, as well as exploring the effects of elevated temperature and moisture.

The innovative wrapped composite 45° X-joints for use in off-shore jacket structures as the competitive alternative to traditional welded joints were investigated with a focus on their debonding behavior under monotonic tensile load. Experimental works and validated FE analysis were performed to explain and predict the debonding process. The fracture properties and the constitutive model of the bonded interface were determined through fracture mechanics experiments and modeling, and were implemented into the joint model considering friction on the bonded interface. Based on the experimental and numerical results, the following conclusions are drawn:

1) Wrapped composite 45° X-joints show rather ductile debonding failure under tensile load. The elastic resistance of joints is governed by the initiation of debonding. The ductile debonding is attributed to the remaining friction along the bonded interface as a consequence of the normal pressure to the bonded interface caused by the circumferential contraction of the composite wrap and Poisson's effect. The ultimate resistance of joints governed by the debonding propagation is approximately 40% larger than the elastic load limit, and is governed by the complete debonding.

2) Debonding of wrapped composite 45° X-joints is dominated by mode II interface failure under tensile load. The primary factor that determined the overall resistance of joints is the failure of the interface on the brace. Fiber bridging develops during debonding crack propagation but has limited influence.

3) Debonding on the chord leads to loss of joint stiffness while complete debonding on the brace results in ultimate failure. In a small-scale joint, debonding starts to propagate simultaneously on the brace and on the chord. Propagation of debonding on the chord is mild and loss of joint stiffness is gradual. In the medium-scale joints, debonding firstly propagates on chord in a more pronounced manner and loss of joint stiffness is abrupt. Once propagation of debonding on the chord is developed to a steady state, debonding starts to propagate on the brace.

4) In the mode I failure of composite-steel bonded interface, the fracture toughness at crack initiation and propagation is 0.3 N/mm and 1.5 N/mm, respectively. Fiber bridging prevails as the dominant mechanism, contributing to 60% of the fracture toughness at crack propagation. On the contrary, in the mode II failure, the impact of fiber bridging is limited, accounting for a mere 6% of the fracture toughness at crack propagation. The fracture toughness at crack initiation and propagation in mode II failure is 0.56 N/mm and 3.5 N/mm, respectively. Major contribution to fracture toughness after the crack initiation is softening.

5) A new four-linear traction-separation law is developed, based on the fracture mechanics experiments, to represent the non-linear behavior of composite-steel bonded interface in mode I and mode II failure. The successful implementation of the new cohesive law has allowed for the simulation of debonding behavior of wrapped composite 45° X-joints loaded in tension. Friction on the bonded interface should be considered. The suitable value of the coefficient of friction of composite-steel bonded interface is in the range of 0.5~0.6. The energetic size-effect is modelled effectively. The numerical results indicate that friction enhances the debonding resistance of the joints by

60% in small-scale and 40% in medium-scale.

Based on the results and the discussion in this thesis, recommendations for future work are as follows:

- 1) Tensile experiments of wrapped composite joints at large-scale and full-scale should be conducted to give experimental evidence on size effects.
- 2) To further advance research on the debonding behavior of wrapped composite joints, it is necessary to extend the scope from uni-planar joint geometry to multi-planar geometry, e.g. K-K joints, and from uniaxial load conditions to multi-axial load conditions, e.g. out-of-plane bending coupled with axial tension.
- 3) It is important to optimize both the length and the thickness of the composite wrap. To facilitate the optimization of wrapping thickness, it is necessary to examine the failure of composite material in the joints.
- 4) The Fatigue performance of wrapped composite joints needs to be analyzed through physical experiments, and an appropriate numerical model should be developed to simulate it.
- 5) Effect of elevated temperature, moisture and long-term load on the debonding behavior of wrapped composite joints should be studied.

Summary

Circular hollow sections (CHS) have been extensively utilized in engineering structures, e.g., offshore jacket supporting structures, due to their advantage of high cost efficiency, aesthetic appeal, excellent mechanical properties, and durability. However, when CHS joints are traditionally formed by welds connecting the brace to the chord member and are applied in offshore jackets where long-term cyclic loading is prevalent, they encounter severe fatigue problems. The low fatigue endurance stems from high and complex stress conditions in the intersection region as a consequence of: 1) metallurgic changes occurring in the heat affected zone and the parent material; 2) the notch effect induced by the welding procedure; 3) geometric peak stresses due to the non-uniform stiffness distribution at the perimeter of the connection.

Fiber reinforced polymer (FRP) composites have gained significant attention for retrofitting concrete structures owing to their high strength-to-weight ratio, flexibility in shaping, and excellent fatigue and corrosion resistance. Over the past decade, the focus of the application of composites has shifted towards the strengthening of welded CHS joints. It has been discovered that retrofitting welded CHS joints by composites could enhance the joints' loading capacity, significantly reduce stress concentration factors (SCFs), and mitigate unfavorable failure modes such as chord ovalization and punching shear. However, in the retrofitted welded joints, a large portion of the load is still transferred through welds, which remains a source of stress concentrations and potential fatigue failure. To fully unlock applicational potential of CHS restricted by current welding joining approach, the concept of innovative wrapped composite joints was proposed by TU Delft as an alternative to traditional welded joints. The brace and the chord member in this case are bonded together and the load transfer is through the composite-steel bonded interface. The major concern of application of wrapped composite joints to offshore jackets is the uncertainty of their debonding mechanism and the difficulty in predicting their debonding resistance.

This dissertation aims to understand the debonding failure mechanism of wrapped composite joints, and to develop a reliable finite element (FE) model for predicting debonding resistance. The present study focused on wrapped composite K-K joints susceptible to tensile fatigue failure. The K-K geometry was simplified to the 45° X-joint geometry to facilitate the uni-planar load application in the laboratory. Prior to conducting ultimate load experiments on 45° X-joints, 6 series of small-scale wrapped composite A-joints were tested under monotonic tensile load to investigate effect of production parameters (bonding primer, resin toughness, steel grade) on debonding resistance. 3D digital image correlation (DIC) technique was employed to quantify the global deformation and the local strain of the joints. The results revealed that utilizing bonding primer and resin with larger fracture toughness leads to increased and less scattered joint ductility. Interaction between debonding and steel yielding is limiting utilization of debonding resistance in the mild steel joints. Main reason is initiation and propagation of debonding crack due to yielding contraction (necking) of the steel cross section at the wrap end. Monotonic tensile load on small-scale and medium-scale

wrapped composite 45° X-joints indicated that debonding on chord leads to loss of joint stiffness while full debonding on brace results in ultimate failure. In small-scale, debonding starts to propagate simultaneously on brace and on chord. Propagation of debonding on chord is mild and loss of joint stiffness is gradual. In medium-scale, debonding first propagates on chord in a more pronounced manner and loss of joint stiffness is abrupt. When propagation of debonding on the chord is developed to a steady state, debonding starts to propagate on the brace.

Identifying the fracture process and quantifying the fracture properties of the composite-steel bonded interface are prerequisites for predicting the debonding resistance of wrapped composite joints. To achieve this, composite-steel double cantilever beam (DCB) and end notched flexure (ENF) tests were carried out to acquire the mode I and mode II fracture behavior of the bonded interface, respectively. The crack length and the crack tip opening displacement (CTOD) were measured using 2D DIC, and the strain energy release rate (SERR) was calculated using the extended global method. The results showed that the fracture process of the metal-composite interface encompasses three distinct phenomena: crack tip deformation, softening and fiber bridging. Fiber bridging is governing in mode I fracture while softening contributed the most to mode II fracture resistance. A four-linear traction-separation law was proposed to describe the non-linear fracture process zone behavior of the bonded interface.

DCB and FEM FE models were developed to establish the strategy for modeling composites and the bonded interface. Solid elements were used to model composites due to their advantages in meshing complex and curved composite wrap geometries. The through-thickness shear softening of composites was phenomenologically simulated by plasticity. Debonding of the composite-steel interface was simulated using the cohesive zone modeling (CZM). A good agreement was reached between experimental and numerical results in terms of the load-displacement response, the crack extension and the crack tip opening, validating the proposed modeling strategy and the four-linear traction-separation law. They were applied in the small-scale and the medium-scale 45° X-joints FE models. The interior element growth was defined in meshing of composite wrap to save the computational costs for the exploration of size effect. Friction was defined on the bonded interface to consider the additional resistance arising from Poisson's ratio effect and the confinement of composite wrap. The joint FE models were validated through a strong agreement in load-displacement behavior and the local debonding crack progression, between experimental results and numerical predictions. The verified joint model served as the benchmark for a parametric study, where the effect of wrapping length, wrapping thickness, and joint size were investigated. The results implied that the debonding resistance of wrapped composite joints adheres to the quasi-brittle size effect law. Moreover, a prediction of the debonding resistance of the full-scale joint was made.

Samenvatting

Cirkelvormige holle secties (CHS) worden uitgebreid gebruikt in ingenieursstructuren, zoals offshore jacket-ondersteunende constructies, vanwege hun voordeel van hoge kostenefficiëntie, esthetische aantrekkelijkheid, uitstekende mechanische eigenschappen en duurzaamheid. Echter, wanneer CHS verbindingen traditioneel worden gevormd door en worden toegepast in offshore jackets waar langdurige cyclische belasting veel voorkomt, ondervinden ze ernstige vermoeidheidsproblemen. De lage vermoeiingslevensduur komt voort uit hoge en complexe spanningstoestanden in het snijpuntgebied als gevolg van: 1) metallurgische veranderingen die zich voordoen in de warmtebeïnvloede zone en het basismateriaal; 2) het kerfeffect dat wordt veroorzaakt door de lasprocedure; 3) geometrische piekspanningen als gevolg van de niet-uniforme stijfheidsverdeling aan de omtrek van de verbinding.

Vezelversterkte kunststoffen (VVK) hebben aanzienlijke aandacht gekregen voor het retrofitten van betonnen constructies vanwege hun hoge sterkte-gewichtsverhouding, flexibiliteit in vormgeving en uitstekende vermoeiings- en corrosiebestendigheid. In de afgelopen tien jaar is de focus van de toepassing van composieten verschoven naar de versterking van gelaste CHS-verbindingen. Er is aangetoond dat het retrofitten van gelaste CHS-verbindingen met VVK de draagcapaciteit van de verbindingen kan vergroten, stressconcentratiefactoren (SCF's) aanzienlijk kan verminderen en ongunstige faalmodi zoals koordovalisatie en dwarskracht pons kan verminderen. Echter, in de getroffite gelaste verbindingen wordt nog steeds een groot deel van de belasting overgebracht via lassen, wat een bron blijft van spanningsconcentraties en potentieel vermoeiing falen. Om het toepassingspotentieel van CHS dat beperkt wordt door de huidige lasverbindingmethode volledig te benutten, werd door TU Delft het concept van innovatieve composiet omwikkeling voorgesteld als een alternatief voor traditionele gelaste verbindingen. De brace en chord delen zijn aan elkaar verbonden door de composiet omwikkeling en de belastingoverdracht verloopt via de composiet-staal gebonden oppervlak. De belangrijkste zorg bij de toepassing van omwikkelde composietverbindingen in offshore jackets is de onzekerheid van hun losbreekmechanisme en de moeilijkheid om hun losbreekweerstand te voorspellen.

Dit proefschrift heeft als doel het loslaat faalmechanisme van omwikkelde composietverbindingen te begrijpen en een betrouwbaar eindige-elementen (FE) model te ontwikkelen voor het voorspellen van de losbreekweerstand. Het huidige onderzoek richtte zich op omwikkelde composiet K-K verbindingen die gevoelig zijn voor trekvermoeiing. De K-K geometrie werd vereenvoudigd tot de 45° X-verbinding geometrie om de eenvlakse belastingstoepassing in het laboratorium te vergemakkelijken. Voordat er ultieme belasting experimenten werden uitgevoerd op 45° X-verbindingen, werden 6 series van kleinschalige omwikkelde composiet A-verbindingen getest onder monotone trekbelasting om het effect van productieparameters (primer, taatheid van hars, staalkwaliteit) op de losbreekweerstand te onderzoeken. De 3D digitale beeldcorrelatie (DIC) techniek werd gebruikt om de globale vervorming en

lokale spanning van de verbindingen te kwantificeren. De resultaten toonden aan dat het gebruik van primer en hars met een grotere breuktaaiheid leidt tot een verhoogde en lagere spreiding van ductiliteit. De interactie tussen losbreek en staalvorming beperkt het gebruik van losbreekweerstand in de milde stalen verbindingen. De belangrijkste reden hiervoor is het starten en verspreiden van de losbreekkloof als gevolg van het krimpen (vernauwen) van de staalbuisdoorsnede aan het einde van de omwikkeling. Monotone trekbelasting op kleinschalige en middelgrote omwikkelde composiet 45° X-verbindingen gaf aan dat losbreek op de chord leidt tot verlies van stijfheid, terwijl volledig losbreken op de brace resulteert in het uiteindelijk falen. Bij kleinschalige verbindingen begint losbreek tegelijkertijd op de brace en de chord te verspreiden. De verspreiding van losbreek op de chord is mild en het verlies van verbinding stijfheid is geleidelijk. Bij middelgrote verbindingen verspreidt losbreek zich eerst op de chord op een meer uitgesproken manier en het verlies van verbinding stijfheid is abrupt. Wanneer de verspreiding van losbreek op de chord is ontwikkeld tot een stabiele toestand, begint losbreek zich te verspreiden op de brace.

Het identificeren van het breukproces en het kwantificeren van de breukeigenschappen van de composiet-staal gebonden interface zijn voorwaarden om de losbreekweerstand van omwikkelde composietverbindingen te voorspellen. Om dit te bereiken werden composiet-staal dubbel uitkragende balk (DCB) en eindinkeping buiging (ENF) tests uitgevoerd om het modus I- en modus II-breukgedrag van de gebonden interface te verkrijgen. De lengte van de scheur en de scheurpuntopening (CTOD) werden gemeten met behulp van 2D DIC, en de spanning-energie afgiftegraad (SERR) werd berekend met behulp van de uitgebreide globale methode. De resultaten toonden aan dat het breukproces van de metaal-composietinterface drie duidelijke fenomenen omvat: vervorming van de scheurpunt, verweking en vezelbrugging. Vezelbrugging domineert bij modus I-breuk terwijl verweking het meest bijdraagt aan de modus II-breukweerstand. Een vierlijnjige trek-opening wet werd voorgesteld om het niet-lineaire gedrag van de breukproceszone van de gebonden interface te beschrijven.

DCB- en ENF-FE-modellen werden ontwikkeld om de strategie voor het modelleren van composieten en de gebonden interface vast te stellen. Drie dimensionale elementen werden gebruikt om composieten te modelleren vanwege hun voordelen bij het meshen van complexe en gebogen geometrieën van composietomwikkelingen. De afschuifverzwakking door de dikte van de composieten werd fenomenologisch gesimuleerd door plasticiteit. Het losraken van de composiet-staalinterface werd gesimuleerd met behulp van de cohesiezone modellering (CZM). Er werd een goede overeenkomst bereikt tussen experimentele en numerieke resultaten wat betreft de belasting-verplaatsingsrespons, de scheuruitbreiding en de opening van het scheurpunt, wat de voorgestelde modelleringsstrategie en de vierlijnjige trek-scheiding wet valideerde. Ze werden toegepast in de FE-modellen van zowel de kleine als de middelgrote 45° X-verbindingen. De groei van interne elementen werd gedefinieerd in het meshen van de composietomwikkeling om de berekeningskosten te besparen bij het onderzoeken van het schaaleffect. Wrijving werd gedefinieerd op de gebonden interface om de aanvullende weerstand als gevolg van het Poisson-effect en de contractie van de

composietomwikkeling in overweging te nemen. De FE-modellen van de verbinding werden gevalideerd door een goede overeenkomst in belasting-verplaatsingsgedrag en de lokale voortgang van het losraken, tussen experimentele resultaten en numerieke voorspellingen. Het geverifieerde model diende als referentie voor een parametrische studie, waarin het effect van de omwikkelingslengte, de omwikkelingsdikte en de verbinding grootte werden onderzocht. De resultaten suggereren dat de losbreekweerstand van omwikkelde composietverbindingen voldoet aan de quasi-brosse grootte-effectwet. Bovendien werd de voorspelling van de losbreekweerstand van de volledige verbinding gedaan.

Acknowledgements

It has been almost five years since I came to TU Delft On October 19, 2018, to commence on my PhD study. And now, while I am writing the acknowledgments at the end of my PhD thesis, numerous memories flood my mind. Pursuing a PhD is a challenging yet rewarding journey, especially in the context of the COVID-19 explosion, which has significantly changed our lives. I feel very proud that I am standing at the terminal point of this journey, but I acknowledge that I could not have accomplished it alone. Many thanks are owed to my colleagues, friends and families.

Firstly, I would like to thank the China Scholarship Council (SCS) for giving me the opportunity to pursue my PhD study at TU Delft and for covering my living expenses in the Netherlands. This incredible journey has not only allowed me to gain insights from research but has also provided me with the chance to understand different cultures and to think about life from a broader perspective.

I would like to express my sincere gratitude to my promotor Prof.dr. Milan Veljkovic. Thank you for offering me this PhD position and for guiding me through the doorway of research. Although you were not extensively involved in my daily research studies, you played an important role in guiding me towards the correct research direction when I spent time on overly detailed but non-critical issues. Your suggestion of focusing my research on debonding behavior was absolutely correct when I tried to investigate into both debonding and composite material failure which is unrealistic. I learned this lesson from you that every PhD candidate should limit his or her research scopes and accept the limitations (Less is more). You also took care of our mental health by organizing monthly group meetings during the COVID-19 pandemic, where we would chat on Zoom about various topics such as life, family, health, etc., without any discussion related to research. Your consideration gave me warm and helped me get through that challenging period.

Dr. Marko Pavlovic, my copromotor and supervisor, I believe even the finest words fall short in capturing the depth of my gratitude towards you. If the PhD research is like diving, you are the diving instructor who helped me progress from a rookie without swimming skills to an experienced diver. In the beginning of my PhD study, I had rather limited knowledge of composite material and composite-steel bonding, and zero experience of ABAQUS. But you were really patient, willing to sit with me for many half days, making sketches to help me understand composites and teaching me to use ABAQUS hand by hand. These experiences laid a good foundation for my subsequent research work. You always made an effort to help foster my academic thinking and initiatives in our daily research work. “Critical thinking” is the word you mentioned most in our meetings. You also emphasized the importance to developing the routine of observing, setting hypothesis, validating, and concluding. In addition, you asked me to think about my research topic from the perspective of “the big map”, not just the research itself. I benefited a lot from these way of thinking, which greatly improved my problem-solving ability and networking awareness. You are also very considerate. In the July of

2022, when I felt quite depressed and lost confidence in successfully calibrating the cohesive zone model, you arranged a series of meetings to help me resolve the problems and regain confidence. “Pei, do not give up, no matter how difficult it may feel at some moments”. Your encouragement gave me a lot of power to get through that difficult period of time and I always appreciate it.

I truly appreciate the help from my doctoral committee (reserve) member, Prof.dr. J.R. Correia and Prof.dr.ir. M.A.N. Hendriks. You provided a large amount of very useful comments for my dissertation manuscript, which helped me improve my understanding of the PhD research. Many thanks to my doctoral committee member, Dr.ir. F.P. van der Meer, for your comments and feedback on the finite element modelling of composites in wrapped composite joints. I would like to show my deep appreciation to my research colleagues working on the development of application of wrapped composite joints. Weikang Feng, you are the person who accompanied me the longest time in terms of the research work. Our research topics are like the twin. Thank you for all your supports and help in my research studies. I really appreciate the discussions and even the complaints we had together. Jincheng Yang, thank you for your idea of using variable mesh size in modelling of composite wrap, which helped me save computational costs significantly. I also appreciate your thoughts from a different perspective during our discussions which gave me a lot of inspiration. Sincere gratitude goes towards to Mathieu Koetsier and Marcio Moreira Arouche, who offered me substantial assistance in designing, preparation, testing and data analyzing of DCB and ENF tests, as well as in revising my journal article manuscripts. Thanks to Tjeu Peeters for good alignment of my research work with the work of other colleagues. Thanks to Sigurdur Egilsson for help with DIC data analysis of DCB and 4ENF tests. Great appreciation is owed to my laboratory colleagues. Many thanks to Peter de Vries for scheduling my experiments and making appointments with lab technicians. My gratitude is extended to Giorgos Stamoulis, who provided me with great help in DIC monitoring of the test specimens. I would also like to thank you for saving my life by stopping me from plugging the air pump’s plug into the power outlet. Many thanks should also be given to Fred Schilperoort, Kees van Beek, John Hermsen, and Louis den Breejen for their great involvement in my experiments. Without your help I could not have successfully accomplished all the experiments needed for my PhD research study.

I feel super lucky to have met so many nice officemates, groupmates, and department mates during my PhD study. Deep appreciation goes toward to my (former) officemates, Lu Cheng, Fei Yang, Zhanchong Shi, and Yufei Zhang. I enjoyed the discussions with you concerning a wide range of topics including research, entertainment, cooking, traveling, and sometimes even politics, which enriched my research life. My sincere gratitude is extended to my groupmates. Many thanks to Angeliki Christoforidou for efforts in composite coupon test design and for contribution to organizing our group events. Appreciation is owed to Olena Karpenko and Trayana Tankova for the communications we had during group parties or coffee breaks that gave me inspiration for achieving work-life balance. Sincere gratitude should also be given to Rui Yan, Weijian Wu, Da Xiang, Ding Liao, Haohui Xin, Xiuli Wang, Xiaoling Liu,

Shuang Qiu, Rong Liu, Tao Yang, Florentia Kavoura, Abhijith Kamath, Linda Buecking, David Malschaert, Hagar El Bamby, and Claire de Bruin. Your support, camaraderie, and shared insights have made my PhD journey enjoyable. I am truly thankful for the collaborative spirit that each of you has brought to our work together. Many thanks to my Master students, Spyros Venetis and Zhexin Lyu, for your contribution to the wrapped composite joints modelling and DCB experiments as part of my PhD topic. I am grateful for the friendship with my department mates, Yuanchen Zeng, Li Wang, Chunyan He, Shisong Ren, Eli Assaf Martinez-Streignard, Yi Zheng, Yitao Huang, Hao Cheng, Yubao Zhou, Fengqiao Zhang, Zhenxu Qian, Jiandong Lu, Ruxin Jing, Pan Zhang, Peng Lin, Yang Jin, Bowen Li, Yunlong Guo. The communications with you in the Stevin lab II are precious memories that I would like to cherish.

I would like to express my sincere gratitude to my colleagues in Tree Composites: Maxim Segeren, Peter Bogers, Tim Kapteijn, Mees Wolters, Vasilis Mylonopoulos, Clement Waltener, Paraskevi Karatsi, Eline Spek, Anders Brodsjo, Berend van Leengoed, and Frank Sliggers. I acquired a lot of knowledge from you in terms of wind turbine, vacuum infusion, etc. Additionally, I truly enjoyed the working environment there, where everyone was willing to offer help like a big family. I do believe that the goal of the Wrap Node II project will be successfully achieved by all of your clever minds and hard work.

My deep appreciation goes towards to Zhongtian Chen, Fanxiang Xu, Zhi Wan, Ze Chang, Yuxuan Feng, Yading Xu, Minfei Liang, Hu Shi, Shi Xu, Ali Ghaderiaram, Shan He, Jinbao Xie, Xuhui Liang, Chen Liu, Zhaozheng Meng, Yu Chen, Yun Chen, Lubin Huo, Maimai Ma, Xiaohui Liang, Zheng Li, Bo Li, Chi Jin, Rong Yu, Shuo Zhang, Dengxiao Lang, Linghan Chen, Rudy de Lange, Langzi Chang, Yi Xia, Mengmeng Gao, Jian Shen, Jiewei Gao, Wenxuan Huang, Wenkan Chen, Yuanchao Zhao, Yuchuan Ouyang, Xiaofan Feng, Xiaoying Wu, Jingwen Yu, Yiqiao Wang, Cheng Huang, Congzhe Wang, Peng Qin. The time that we spent together, whether at X TU Delft, in offices, at parties, while traveling, at conferences, during phone calls, are valuable experiences that I would like to treasure for my whole life. I truly appreciate your friendship with me.

Special thanks should be given to my teachers and friends in China: Jianyuan Sun, Shengai Cui, Lanming Duan, Xin Li, Jiahui Li, Zexi Yan, Baorui Dai, Kunkai Tu, Qi Hu, Zhe Liu, Yezhan Li, Gang Shen, Yinghao Luo, Liang Zheng, Shiyu Zhao, Yalin Zou, Hao Su, Zhuo Dang, Yanming Tang, Yanqiu Zhang, Heyu Chen. You mean a lot to me, and I always cherish the support, encouragement, and consideration that you have given to me.

I would like to express my heartfelt gratitude to my family and relatives for their unwavering support during my PhD journey. Your encouragement and love have been my pillars of strength, even from miles away. Your belief in me and constant reassurance have kept me motivated to overcome challenges and to strive for excellence. During the COVID-19 pandemic, all late-night calls and early morning messages between us bring me warmth and courage to face all the difficulties in research and in life. Your unwavering dedication to staying connected has provided me not only with a source of

emotional strength but also a sense of belonging during these uncertain times.

Pei He

Delft, August 2023

List of publications

Journal articles

1. **P. He**, W. Feng, and M. Pavlovic, “Influence of steel yielding and resin toughness on debonding of wrapped composite joints”, *Compos. Struct.*, vol. 312, no. February, p. 116862, 2023, doi: 10.1016/j.compstruct.2023.116862.
2. **P. He** and M. Pavlovic, “Failure modes of bonded wrapped composite joints for steel circular hollow sections in ultimate load experiments”, *Eng. Struct.*, vol. 254, no. August 2021, p. 113799, 2022, doi: 10.1016/j.engstruct.2021.113799.
3. **P. He**, M. Arouche, M. Koetsier, M. Pavlovic, “Mode I fracture behavior of glass fiber composite-steel bonded interface – experiments and CZM”, *Compos. Struct.*, 2023. (Minor revision)
4. **P. He**, M. Koetsier, V. Mylonopoulos, M. Pavlovic, “Mode II fracture behavior of glass fiber composite-steel bonded interface – experiments and CZM”, *Compos. Struct.*, 2023. (Under review)
5. **P. He**, W. Feng, M. Arouche, M. Pavlovic, “Debonding behavior of non-welded wrapped composite X-joints subjected to monotonic tensile load – an experimental and numerical study”, *Compos. Struct.* (In preparation)
6. **P. He**, J. Yang, M. Arouche, M. Pavlovic, “Size effect on debonding behavior of wrapped composite X-joints subjected to monotonic tensile load”, *Compos. Struct.* (In preparation)
7. M. Arouche, Z. Lyu, **P. He**^{*}, M. Pavlovic, “Influence of steel surface roughness on mode I fracture behavior of glass fiber composite-steel bonded interface”, *Compos. Struct.* (In preparation)
8. **P. He** and M. Pavlovic, “Long-term behavior of non-welded wrapped composite X-joints under tensile creep load”, *Eng. Struct.* (In preparation)
9. W. Feng, **P. He**, and M. Pavlovic, “Combined DIC and FEA method for analysing debonding crack propagation in fatigue experiments on wrapped composite joints,” *Compos. Struct.*, vol. 297, no. March, p. 115977, 2022, doi: 10.1016/J.COMPSTRUCT.2022.115977.

Conference proceedings

1. **P. He** and M. Pavlovic, “Feasibility of Wrapped FRP Circular Hollow Section Joints,” in *Proceedings of the 17th International Symposium on Tubular Structures*, 2019, pp. 292–299. doi: 10.3850/978-981-11-0745-0_043-cd.dsff452424
2. W. Feng, **P. He**, M. Koetsier, M. Pavlovic, “Interfacial friction effect on fatigue debonding behavior of wrapped composite joints”, *In Proceedings of the 20th European Conference on Composite Materials*, 2022.

Curriculum Vitae

Pei HE
何培



Dec. 2nd 1992 Born in Chongqing, China

Education

	B.Sc. student
Sep. 2011 – June. 2015	Civil Engineering Southwest Jiaotong University, Chengdu, China
	M.Sc. student
Sep. 2015 – June. 2018	Architectural and Civil Engineering Tongji University, Shanghai, China
	PhD. candidate
Oct. 2018 – Present	Civil Engineering and Geosciences Delft University of Technology, The Netherlands

